Interannual Variability in Atmospheric Water Vapor Transport Over North European and West African Regions

by

Marybeth Long

Submitted to the Department of Civil and Environmental Engineering
in partial fulfillment of the requirements for the degree of

Master of Science

at the

MASSACHUSETTS INSTITUTE OF TECHNOLOGY

February 1996

Author .....
Department of Civil and Environmental Engineering
January 19, 1996

Certified by .....
Dara Entekhabi
Associate Professor
Thesis Supervisor

Accepted by ....
Joseph M. Sussman
Chairman, Departmental Committee on Graduate Students

Interannual Variability in Atmospheric Water Vapor Transport Over North European and West African Regions

by

Marybeth Long

Submitted to the Department of Civil and Environmental Engineering
on January 19, 1996, in partial fulfillment of the
requirements for the degree of
Master of Science

Abstract

Water vapor transport is closely linked to energy transfer and the regional water balance. Thus, knowledge about water vapor movement is necessary for understanding regional and global climate systems. This thesis presents two regional studies of water vapor transport. The first study focuses on seasonal and interannual variability of water vapor flux over Northern Europe. A mean climatology for years 1974 through 1989 allows intra-annual analysis of total motion, mean motion, and transient eddy water vapor flux; wind; humidity; and annual convergence. Yearly data for the 1974 to 1989 period provide time series of vapor flux and convergence over the region.

The second study examines water vapor transport over West Africa during drought and non-drought years. A thirty-one year dataset spanning 1959 through 1989 facilitates analysis of rainfall, water vapor flux, and general circulation variability. Total motion moisture flux calculations yield time series of zonal and meridional vapor transport. Empirical orthogonal function (EOF) analysis applied to vertical wind velocity fields provides a scalar index of the general circulation. Correlations between rainfall and EOF time series reveal that large-scale forcing impacts rainfall anomalies. Relationships between rainfall and vapor flux indicate seasonal and regional variations important for understanding West Africa's drought problem.

Thesis Supervisor: Dara Entekhabi
Title: Associate Professor

Acknowledgments

Research for this thesis was supported by a National Science Foundation Graduate Research Fellowship and NASA Research Grant No. NAGW-4163.

I wish to thank Professor Sharon Nicholson of Florida State University; Abraham Oort of the National Oceanic and Atmospheric Administration (NOAA) Geophysical Fluid Dynamics Laboratory; and Richard Rosen and Peter Nelson of Atmospheric and Environmental Research, Inc. for their data contributions and insight.

I am very grateful to Professor Dara Entekhabi for his invaluable guidance throughout the development of this thesis.

Contents

List of Figures

List of Tables

Chapter 1

Introduction

". . .Flow of water across the boundaries of a watershed through the atmosphere is just as much a part of the hydrologic balance of that watershed as flow of water out of the area through river channels or by subsurface seepage" (Benton 1950).

As George S. Benton pointed out in 1950, the atmosphere is a critical component of the Earth's hydrologic cycle. The atmosphere transports water in the condensed or vapor phases. After an estimated nine-day residence time in the atmosphere, water falls on continents in various forms of precipitation and then runs off over the land, infiltrates into the subsurface, or returns to the atmosphere via evaporation or evapotranspiration (Peixoto and Oort 1992). Water vapor's mobile and regenerative qualities make it an important factor in the Earth's water and energy budgets (Peixoto *et al.* 1981). Water and water vapor, for example, allow functioning of the biosphere. In addition, phase changes of water release and absorb large amounts of latent heat. Atmospheric water vapor in the form of clouds, snow, and sea ice affects the amount of solar radiation that reaches the Earth, as well as the amount of longwave radiation that is re-radiated after emission from the Earth's surface (Rosen and Omolayo 1981).

Processes involving water and energy are vital for the operation of the global climate system. As water changes phase it transports energy in and out of the atmosphere. This transfer of energy, along with associated atmospheric dynamics, deter-

mine the air temperature. For example, when solar radiation evaporates water, the atmosphere loses energy. Conversely, latent heat enters the atmosphere when condensation occurs. Latent heat released via rainfall supplies 85% of the atmospheric energy balance. However, the atmosphere loses even more of its energy via infrared radiation from water vapor (Newell 1983, p. ix).

Important energy/water linkages mean that global water cycle variability impacts changes in the general circulation and regional climates. Atmospheric fluctuations are the biggest source of hydrologic cycle variability. Variability in the Hadley cell is a good example. As the intensity and position of the Hadley cell vary, so do the amount and location of the precipitation the cell generates. Thus, an understanding of the global water cycle provides insight into the global climate system. This insight derives from knowledge about the global distribution of water, its movement, its phase changes, and the mechanisms governing its evaporation and precipitation (Newell 1983, p. xi).

This thesis focuses on interannual variability in the regional movement of water vapor. Water vapor transport involves the advection of moist air by wind. The two components of water vapor transport are specific humidity and wind velocity. These variables significantly impact the general circulation and land-atmosphere interaction. Chapter 2 presents a brief overview of the theory underlying our understanding of the atmospheric branch of the hydrologic cycle. This chapter discusses the integrated water vapor flux vector, atmospheric and soil water balance, and vertical wind velocity.

Chapter 3 contains a study of water vapor transport over a region of Northern Europe. This study analyzes zonal and meridional water vapor movement at region boundaries and reveals seasonal and interannual variations in convergence and in the various components of water vapor flux. A mean monthly climatology for years 1974 through 1989 allows intra-annual analysis of total motion, mean motion, and transient eddy water vapor flux; wind; humidity; and annual convergence. Yearly data provide time series of vapor flux and convergence over the region.

Chapter 4 is a regional study of water vapor-related variables over West Africa

during drought and non-drought years. A thirty-one year dataset spanning 1959 through 1989 allows analysis of rainfall, water vapor transport, and general circulation variability. This variability is examined within the rainy season and over the thirty-one year period. Total motion moisture flux calculations yield time series of zonal and meridional vapor transport. Empirical orthogonal function (EOF) analysis applied to vertical wind velocity fields provides a scalar index of the general circulation and time series of EOF multipliers. Correlations between rainfall and EOF time series reveal that large-scale forcing impacts rainfall anomalies. Relationships between rainfall and vapor flux indicate seasonal and regional variations important for understanding West Africa's drought problem.

Chapter 5 presents concluding remarks and suggestions for future research.

Chapter 2

The Atmospheric Branch of the Hydrologic Cycle

The Europe and Africa studies in Chapters 3 and 4 focus on water vapor movement across designated borders. The Europe study also includes convergence and precipitable water results. Peixoto and Oort (1992) and Brubaker *et al.* (1993) present the theoretical basis for many of the calculations used in these analyses. Below is an overview of the theory that addresses vertically integrated water vapor flux, soil water balance, precipitable water, and vertical wind velocity.

2.1 Theory

Atmospheric transport occurs via turbulent and molecular diffusion, convection, and advection. Diffusion mechanisms associated with evaporation transport water from land and ocean surfaces into the atmospheric boundary layer where diffusion and advection mix the vapor (Brubaker *et al.* 1993). Diffusion, alone, however, dominates lateral transport. On the time and space scales of horizontal vapor transport, lateral wind advects a scalar admixture of water vapor . The discussion below addresses the flux, wind, specific humidity, precipitable water, and convergence associated with this horizontal vapor transport.

2.1.1 Vertically integrated vapor flux vector

Specific humidity and wind vary spatially and temporally. These parameters are defined in a four-dimensional domain of ϕ (latitude), λ (longitude), p (pressure), and t (time). At a particular point in space, the vector describing lateral water vapor transport is expressed as:

$$q\vec{V}(\lambda, \phi, p, t) = (qu)\vec{i} + (qv)\vec{j} \tag{2.1}$$

where q is specific humidity (mass of water per mass of moist air), $\vec{V}$ is the horizontal wind vector (LT^{-1}), u is zonal wind (positive in the eastward direction), and v is meridional wind (positive in the northward direction) (Brubaker *et al.* 1993, p. 410).

The zonal and meridional horizontal transport vectors may be expressed in terms of a time mean and a deviation from that mean. An example is:

$$q(\lambda, \phi, p, t) = \overline{q}(\lambda, \phi, p) + q'(\lambda, \phi, p, t) \tag{2.2}$$

where the overbar indicates a time mean and the prime denotes a perturbation. The time-averaged product of specific humidity and wind is, therefore:

$$\overline{qu}(\lambda, \phi, p) = \overline{(\overline{q} + q')(\overline{u} + u')}. \tag{2.3}$$

As shown in Peixoto and Oort (1992), Equation (2.3) reduces to:

$$\overline{qu}(\lambda, \phi, p) = (\overline{q})(\overline{u}) + \overline{q'u'}. \tag{2.4}$$

Equation (2.4) also applies to the meridional direction when the u term is replaced with a v variable. The terms on the right hand side of Equation (2.4) are mean motion and transient eddy terms, respectively. The mean motion term reflects the advection of mean specific humidity by mean zonal wind. The transient eddy term is a correlation term. Its value is positive, for example, if winds at a particular location are simultaneously more westerly and moister than average (Peixoto and Oort 1992).

On a global scale, the zonal component of vapor flux generally exceeds the merid-

ional component. Mean motion dominates moisture flux in the zonal direction, whereas the mean and transient eddy components in the meridional direction have comparable magnitudes (Brubaker *et al.* 1993, p. 413).

It should also be noted that a correlation term of spatial perturbations (transport by standing eddies) is sometimes included as part of the total motion quantity. This correlation is determined by evaluating deviations from mean values calculated along belts of constant latitude. However, the spatial scale considered in this analysis is too small to warrant consideration of deviations from a spatial mean.

The vertically integrated horizontal vapor flux vector $\vec{Q}$ is obtained by vertically integrating the meridional and zonal versions of Equation (2.4) over pressure levels. These meridional and zonal $\vec{Q}$ components can be time-averaged to yield:

$$\overline{Q}_\lambda = \int_0^{p_o} \overline{qu}\frac{dp}{g} = \int_0^{p_o} (\overline{q})(\overline{u})\frac{dp}{g} + \int_0^{p_o} \overline{q'u'}\frac{dp}{g} \tag{2.5}$$

and

$$\overline{Q}_\phi = \int_0^{p_o} \overline{qv}\frac{dp}{g} = \int_0^{p_o} (\overline{q})(\overline{v})\frac{dp}{g} + \int_0^{p_o} \overline{q'v'}\frac{dp}{g} \tag{2.6}$$

In Equations (2.5) and (2.6), p_o is surface pressure, g is gravitational acceleration, and Q_λ and Q_ϕ are the zonal and meridional components of $\vec{Q}$. $\vec{Q}$ has dimensions $MT^{-1}L^{-1}$. This quantity reflects the net water vapor transport above a point on the Earth's surface (Brubaker *et al.* 1993, p. 413).

2.1.2 Atmospheric Water Balance

$\vec{Q}$ plays an important role in the atmospheric water balance. For an atmospheric column surrounded by a vertical wall and situated above a region of area A on the Earth's surface, the spatially averaged mass conservation equation for water vapor is:

$$[\frac{\partial W}{\partial t}] + [\nabla \cdot \vec{Q}] = [E - P]. \tag{2.7}$$

In the above equation, W is precipitable water and has units of ML^{-2} or L. E is the evapotranspiration rate into the base of the column. P is the precipitation rate

from the column. $\nabla \cdot \vec{Q}$ is the divergence of lateral moisture flux. Positive divergence indicates an atmospheric water vapor source, while negative divergence (convergence) denotes an atmospheric water vapor sink. The brackets in Equation (2.7) indicate space averages.

By applying Green's Theorem Equation (2.7) becomes:

$$[\frac{\partial W}{\partial t}] = [E - P] - \frac{1}{A} \int \vec{Q} \cdot \vec{n_\gamma} d_\gamma \tag{2.8}$$

In Equation (2.8), $\nabla \cdot \vec{Q}$ is expressed in terms of lateral outflow through vertical boundaries of a control volume. This equation represents the mass balance of water in the atmospheric branch of the hydrological cycle. The time rate of change of water vapor storage in the atmospheric volume equals the evapotranspiration minus precipitation and minus the net lateral outflow through the control volume's vertical boundaries. A change in the atmospheric volume's water vapor content coupled with vapor outflow across region boundaries balances an excess of evapotranspiration over precipitation (Brubaker *et al.* 1993, p. 411).

2.1.3 Soil Water Balance

An expression similar to Equations 2.7 and 2.8 describes the soil water balance for the terrestrial component of the hydrologic cycle:

$$[\frac{\partial S}{\partial t}] = -[E - P] + [R_{in} - R_{out}] \tag{2.9}$$

In Equation (2.9), S is water mass storage in surface and subsurface reservoirs of the region. R_{in} and R_{out} are lateral influx and efflux across the region's horizontal boundaries. If these boundaries are drainage divides, $[R_{in}] = 0$, and $[R_{in} - R_{out}]$ is the runoff rate per unit area.

Equating the common $[E - P]$ terms in Equations (2.7) and (2.9) yields:

$$[R_{out} - R_{in}] + [\frac{\partial S}{\partial t}] = -[\nabla \cdot \vec{Q}] - [\frac{\partial W}{\partial t}] \tag{2.10}$$

Equation (2.10) links the atmospheric and land components of hydrologic cycle. For sufficiently long time periods (a year or more) the precipitable water and water storage terms in Equation (2.10) can be neglected. The resulting equation indicates that aerological data can be used to estimate land liquid runoff (Brubaker *et al.* 1993, pp. 411-2).

2.1.4 Precipitable Water

The amount of water vapor in a unit atmospheric column is given by:

$$W(\lambda, \phi, t) = \int_{p_o}^{0} q \frac{dp}{g} \tag{2.11}$$

Precipitable water represents the amount of water that would result from condensation of all the water vapor in a unit atmospheric column. Precipitable water has units of ML^{-2} or L when normalized by liquid water density (Peixoto and Oort 1992, pp. 274-5).

2.1.5 Vertical Wind Velocity

Omega is the wind component along the pressure axis. Values of ω at 500 mb were used in this analysis as an index of vertical and large-scale motion. According to Peixoto and Oort (1992), maximum omega values in the vertical dimension occur between approximately 400 and 500 mb. Consequently, ω values at 500 mb were analyzed. Omega values provided in the Oort (1983) dataset were estimated by using the continuity equation and were derived from horizontal wind fields.

Omega is approximated as

$$\omega \approx \frac{dP}{dt} \approx -\rho g w \tag{2.12}$$

where ω is in mb/s, P is pressure (mb), t is time (s) , ρ is air density (kg/m^3), g is acceleration due to gravity (m/s^2), and w is vertical wind velocity (m/s).

The above expression is derived from:

$$\frac{dp}{dt} = \frac{\partial p}{\partial t} + \vec{v} \cdot \nabla P + w\frac{\partial p}{\partial z} \tag{2.13}$$

where:

$\vec{v}$ is the horizontal wind vector (m/s), ∇P is the pressure gradient, and z is elevation (m).

Since the first two terms are much smaller than the last,

$$\omega \approx w\frac{\partial p}{\partial z} \tag{2.14}$$

Assuming hydrostatic equilibrium this equation becomes

$$\omega \approx -\rho g w \tag{2.15}$$

The concepts presented above provide a basis for the calculations explained in the following chapters.

2.1.6 Aerological and Surface Pressure Data

The humidity, wind and omega data used in this analysis were provided by Dr. Abraham Oort of the National Oceanic and Atmospheric Administration (NOAA) Geophysical Fluid Dynamics Laboratory (GFDL). The dataset contains monthly mean climatologic fields of zonal wind ($\overline{u}$) (m/s), meridional wind ($\overline{v}$) (m/s), specific humidity ($\overline{q}$) (g/kg)[1], zonal transient eddy flux ($\overline{u'q'}$) ($m/s{\cdot}g/kg$), meridional transient eddy flux ($\overline{v'q'}$) ($m/s{\cdot}g/kg$), and vertical wind velocity ($\overline{\omega}$) (m/s). The fields con-

[1]Specific humidity is the ratio of the mass of water vapor to the mass of moist air for the same volume of moist air.

tain monthly mean values for the years 1959 through 1989, inclusive. The data are based on radiosonde measurements taken between two and four times per day at eight pressure levels: 1000, 950, 900, 850, 700, 500, 400, and 300 millibars (mb) and interpolated onto a 2.5° latitude by 5° longitude grid using CRAM (Conditional Relaxation Analysis Method), an objective analysis scheme detailed in Oort (1983).

Peter Nelson of Atmospheric and Environmental Research, Inc. (AER) provided surface pressure data. The AER dataset contains monthly mean values of surface pressure, in millibars, for a 2.5° latitude by 5° longitude grid.

Chapter 3

North European Study

Analysis of water vapor over Northern Europe provides insight into the hydrologic cycle and its linkages to the general circulation. On a regional scale water vapor flux and convergence reflect information about the water budget and hydrological forcing mechanisms associated with the Atlantic Ocean and Mediterranean Sea. On a larger scale, water vapor transport serves as an indicator of circulation features such as the Jet Stream and the Polar Front. Interannual analysis can be used to relate these features to phenomena such as El-Nino and the Southern Oscillation Index.

The goal of the study is to gain a better understanding of intra-annual and interannual variability of water vapor transport and convergence over the European region. Results indicate seasonal variation in water vapor flux, wind, and humidity. The interannual study shows large variations in moisture flux magnitudes across region borders and in the transport modes that comprise vapor movement.

Water vapor flux at a boundary surrounding a portion of Europe is the focus of the study. Figure 3-1 illustrates the region of Europe considered. This area extends from the Prime Meridian to 25° East (E) longitude and from 45° North (N) to 70.5° N latitude. Three boundary segments in Figure 3-1 indicate three regions defined for comparative analysis. The Mediterranean boundary extends from the Prime Meridian to 25° E longitude along 45° N latitude. The South Atlantic boundary reaches between 45° and 51° N latitude along the Prime Meridian. The North Sea boundary covers 51 ° to 70.5° N longitude along the Prime Meridian. The region excludes Italy and

the Iberian Peninsula because the data quality limits the physical significance of variations at small scales and along irregular boundaries. For the excluded region, the Mediterranean is clearly an important source of moisture and energy.

The intra-annual portion of the analysis is based on a monthly mean climate for years 1974 through 1989, inclusive. Annual and seasonal moisture flux is calculated at the European region boundaries and is separated into its various components. One decomposition involves the modes of motion: total motion, mean motion, and transient eddies. The other decomposition involves separation into pressure-weighted values of wind and humidity. In addition, total motion boundary flux is used to estimate convergence over the region.

The interannual study is based on monthly mean data for the years 1974 through 1989 inclusive. Water vapor flux calculated at the European boundary is used to produce a time series of convergence and to compare the magnitude of vapor flux crossing specified boundary segments.

Section 3.1 discusses the aerological data used in this study. Section 3.2 presents the methodology employed in estimating water vapor flux, convergence, and vertically averaged specific humidity and wind. Section 3.3 details the intra-annual results. These results include zonal and meridional transport, specific humidity and wind, and convergence for the mean climatology. Section 3.4 contains interannual results. This section presents time series of convergence and regional flux.

Figure 3-1: European Region

3.1 Radiosonde Data

Chapter 2 addresses aerological and surface pressure data. The North European dataset contains monthly mean climatologic fields and monthly mean anomaly fields for the period 1974 through 1989. Actual climatology for this time period is obtained by adding the mean climatology and anomaly field values.

Observational errors associated with the data relate to instrument variability and calibration, the diurnal cycle, and resolution of the boundary layer. Radiosonde instrumentation errors can result from manufacturing variability and calibration loss Elliot and Gaffen (1991). In addition, the limited number of daily soundings do not sufficiently capture the diurnal cycle and and fail to reflect variations during unsampled hours. Brubaker *et al.* (1993) points out that radiosonde measurements do not resolve the planetary boundary layer - the layer containing most of the Earth's water vapor. Furthermore, data at 1000 mb is generally less reliable than data at other pressure levels (Fontaine *et al.* 1995, p. 1504).

3.2 Methodology

Much of the estimation methodology used in the analysis is based on Brubaker *et al.*'s (1993) study of horizontal advective transport. As indicated in this study, the movement of moisture by wind is represented by the zonal and meridional components of the vapor flux vector. Each of these components can be further decomposed into its mean motion and transient eddy terms. Vectors of total, mean, and transient eddy motions are integrated over discrete segments of the European region boundary to create graphical fluxbar representations of the mass per unit time flux of water vapor crossing the boundary. Summation of influx and efflux values around the boundary produces an estimate of water vapor flux convergence.

3.2.1 Flux Calculations

All flux calculations carried out in this analysis begin with vertical trapezoidal-rule integration of the vapor flux vector field, $\vec{Q} = \overline{Q}_\lambda \vec{i}_\lambda + \overline{Q}_\phi \vec{j}_\phi$. Integration begins at the actual surface pressure level.

Flux vectors are then integrated horizontally across discrete European boundary segments. As shown in Equation (3.1) the closed-path integral can be expressed as a sum of smaller integrals around segments of the boundary:

$$\int \vec{Q} \cdot \vec{n_\gamma} d_\gamma = \sum_{k=1}^{m} \int_{x_k}^{x_{k+1}} \vec{Q} \cdot \vec{n}_\gamma d_\gamma \tag{3.1}$$

In Equation (3.1), $\vec{n}_\gamma$ is the outward unit vector normal to the horizontal boundary, γ, of the region, and x_k and x_{k+1} are gridpoints around the boundary. These gridpoints bound each segment. The sub-integral over each segment has units of kg/s. Thus, sub-integral calculations determine the mass of water passing across each sub-interval per unit time.

The average flux across several boundary segments (the Mediterranean boundary, for example) provides an estimate of "regional flux". Regional flux is obtained by summing a number of the sub-integrals flux values and dividing by the sum of segment lengths. Regional flux is expressed in Equation (3.2) and has units of $MT^{-1}L^{-1}$.

$$\frac{\sum_{k=1}^{m} \int_{x_k}^{x_{k+1}} \vec{Q} \cdot \vec{n_\gamma} d_\gamma}{\sum_{k=1}^{m} \int_{x_k}^{x_{k+1}} d_\gamma} \tag{3.2}$$

3.2.2 Vertically Averaged Specific Humidity and Wind

Total atmospheric column values of specific humidity and wind are obtained by vertically integrating over pressure intervals and dividing by the gravitational acceleration.

Equation (3.3) is the continuous form of the expression for pressure-weighted specific humidity. If $\overline{q}$ in Equation (3.3) is replaced with $\overline{u}$ or $\overline{v}$, the equation becomes an expression for pressure-weighted wind velocity.

$$\overline{q}_{pressure-weighted} = \frac{\int_{p_o}^{300mb} \overline{q} \frac{dp}{g}(g)}{\int_{p_o}^{300mb} dp} \tag{3.3}$$

In Equation (3.3), p_o is surface pressure, g is gravitational acceleration, and dp is the pressure interval.

3.3 Intra-annual Variations in Vapor Flux

Results based on analysis of the mean climatologic data illustrate seasonal behavior of atmospheric moisture fields. In addition, these results reveal interesting relationships between the modes of atmospheric water vapor transport and their wind and humidity components. The four seasons considered in this study are December/January/February (DJF), March/April/May (MAM), June/July/August (JJA), and September/October/November (SON) (see Figures 3-2 through 3-10).

3.3.1 Zonal Flux

The Earth's rotation and pole-equator temperature gradients result in the dominance of zonal over meridional circulation (UNESCO 1978). Zonal flux is generally two to three times larger than meridional flux (Peixoto *et al.* 1981) and is westerly in the mid-latitudes and easterly in the tropical belt.

Dominant westerly zonal flux is evident in Figures 3-2, 3-3, and 3-4. These figures contain fluxbar representations of annual total, mean motion, and transient eddy flux. The fluxbars are determined by integrating water vapor flux vertically and horizontally as described above. Each fluxbar indicates the magnitude and direction of the time rate of moisture flux across each boundary segment.[1] Appendix A contains a full set of annual and seasonal flux figures for total, mean, and transient eddy motion over the European region. The results in this section are summarized using a select subset of figures.

[1]It should be noted that the European region outline in these figures is distorted and does not accurately reflect actual boundary dimensions.

Westerlies in the mid-latitudes are associated with circulation along the polar fronts and borders of the subtropical anticyclones (Peixoto and Oort 1992). The westerlies themselves reflect what is known as the Jet Stream in the upper altitudes (maximum around 300 mb) and Polar Front at lower altitudes. The Jet Stream/Polar Front phenomenon results from energy and pressure gradients that stretch from southwest (high pressure) to northwest (low pressure) across Europe (Wallen 1970). Westerlies aid in maintaining the relatively temperate European climate. The Gulf Stream's warm poleward current carries warm air from the waters east of the United States to the North Atlantic, North Sea, and Norwegian Sea. The westerlies may then transport warm, moist air across Europe.

A comparison of the total, mean, and transient eddy components of annual zonal flux reveal the relative importance of these transport modes. Magnitudes of total annual zonal flux range between 7.4 x 10^6 and 2.2 x 10^7 kg/s across each 1.5° latitude segment. Mean motion clearly drives zonal flux with annual values between 7.0 x 10^6 to 2.0 x 10^7 kg/s, compared to an annual westerly transient eddy flux between 4.0 x 10^5 and 2.5 x 10^6 kg/s.

Figures 3-5 and 3-6 show that total vapor flux across the region boundaries exhibits notable seasonal variation. Flux is smallest in winter and spring and largest in summer (Figure 3-6) and autumn. Total zonal flux during the winter season (Figure 3-5) ranges between approximately 6.7 x 10^6 and 2.2 x 10^7 kg/s, while flux during the summer ranges between 8.4 x 10^6 and 2.6 x 10^7 kg/s across each 1.5° latitude grid. Mean motion flux undergoes a similar seasonal change (Figures 3-7 and 3-8). This reflects the shift of maximum eastward movement to higher latitudes in the summer following solar declination shifts. These findings also agree with Rosen and Omolayo (1981) who maintain that cross-coastal flux in the northern hemisphere tends to be largest in the summer.

Throughout the year, westerly transient eddy flux varies with the largest values occurring in winter (Figure 3-9) and autumn. However, during summer, transient eddy zonal flux along the eastern boundary becomes small and easterly. Transient eddy zonal flux in summer (Figure 3-10) is considerably smaller (between 2 x 10^3 and

1 x 10^6 kg/s per 1.5° latitude) along both the eastern and western boundaries.

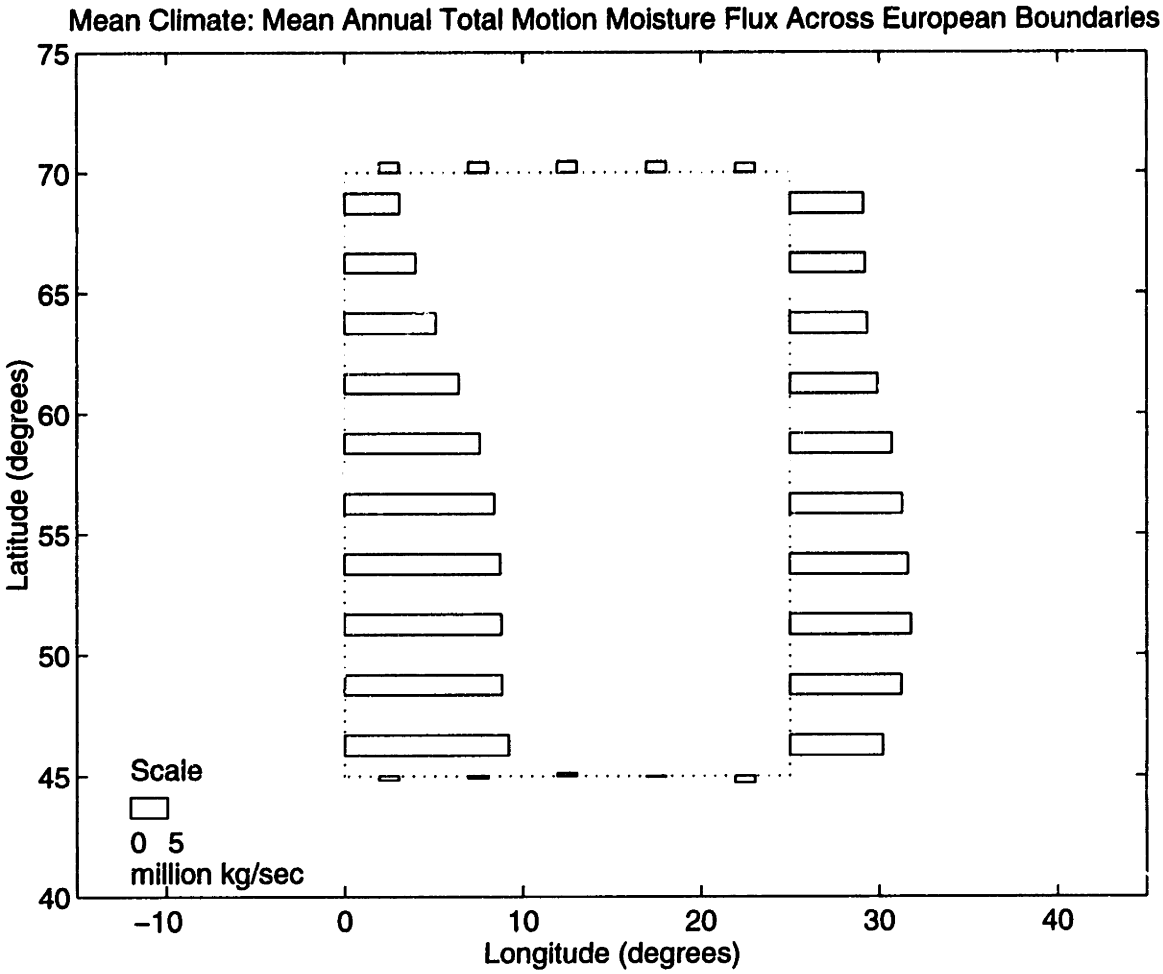

Figure 3-2: Annual Mean Climate Total Motion Water Vapor Flux

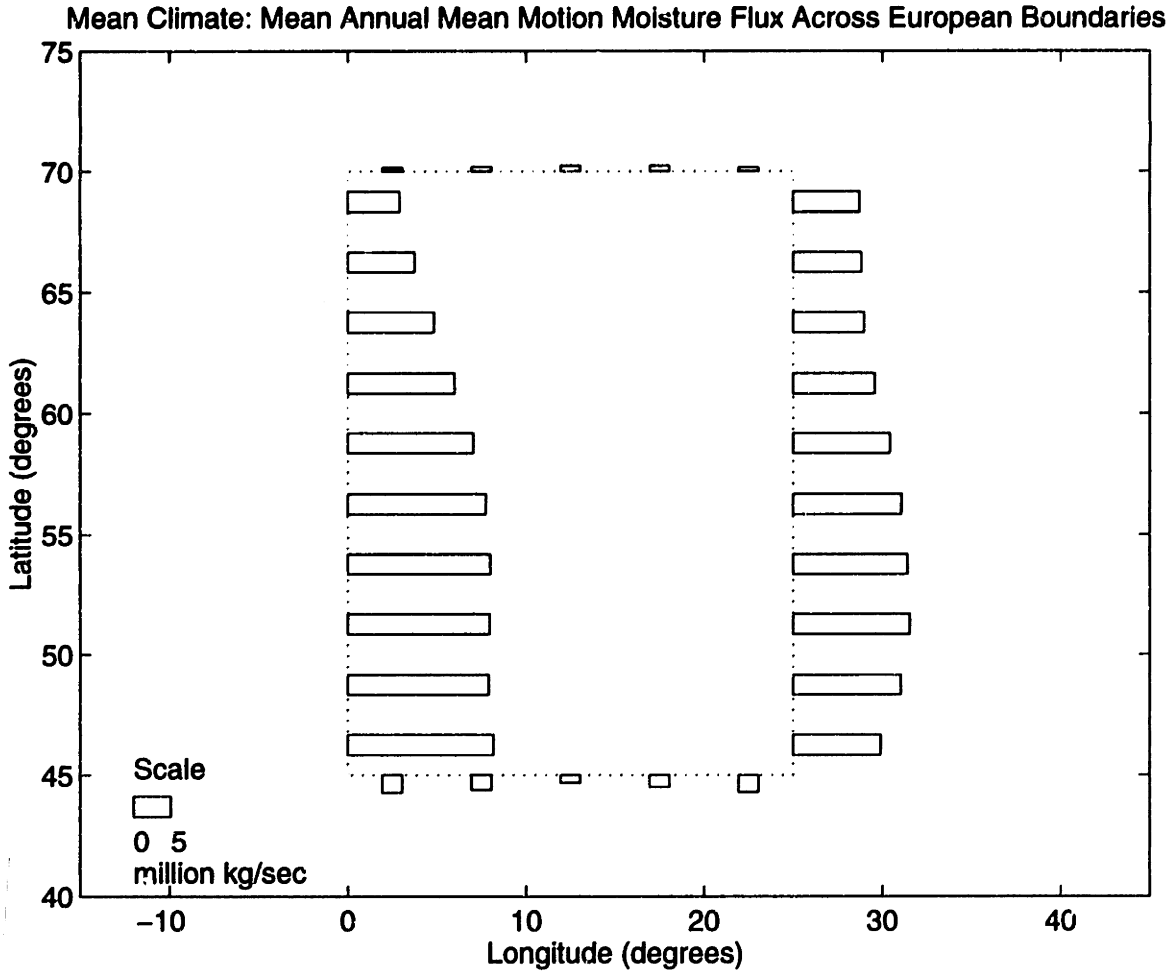

Figure 3-3: Annual Mean Climate Mean Motion Water Vapor Flux

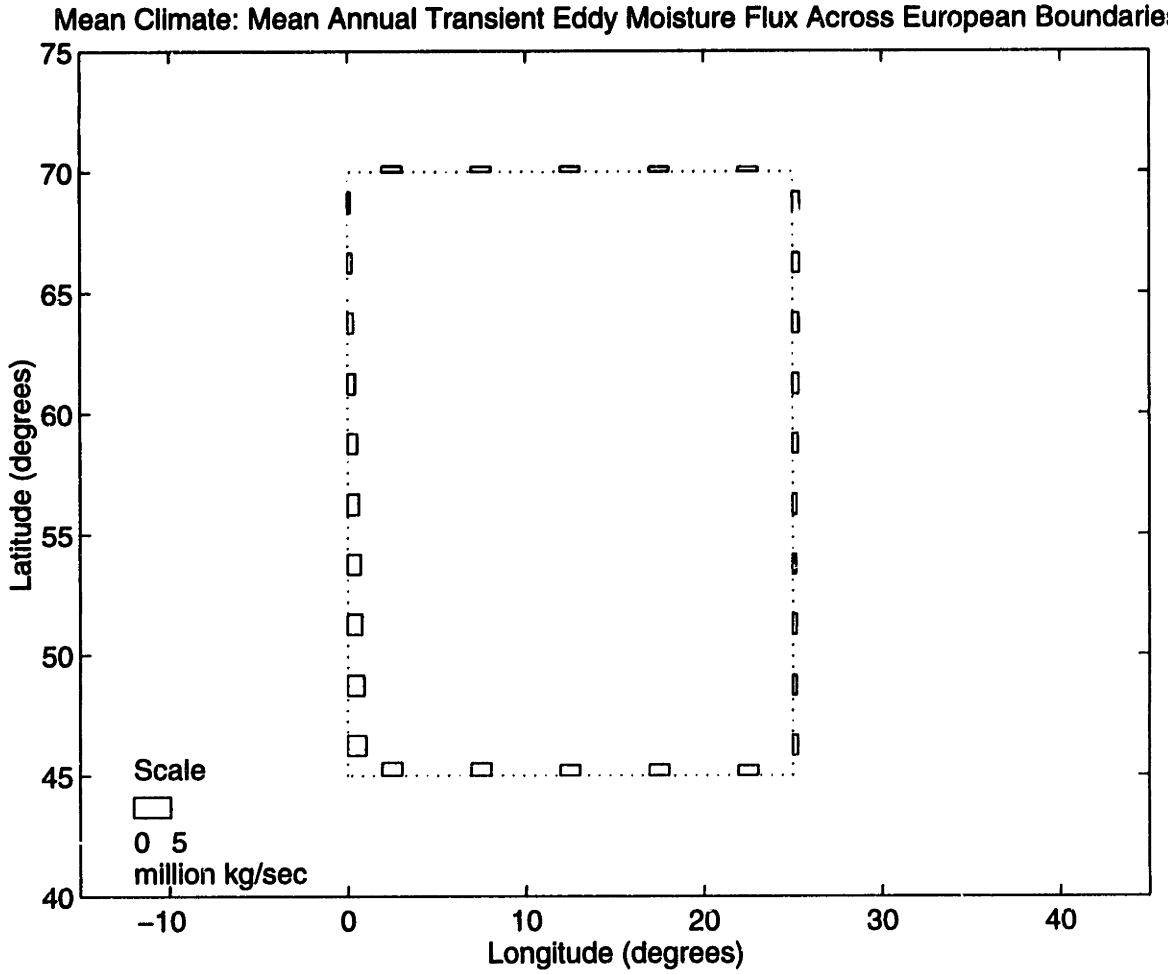

Figure 3-4: Annual Mean Climate Transient Eddy Water Vapor Flux

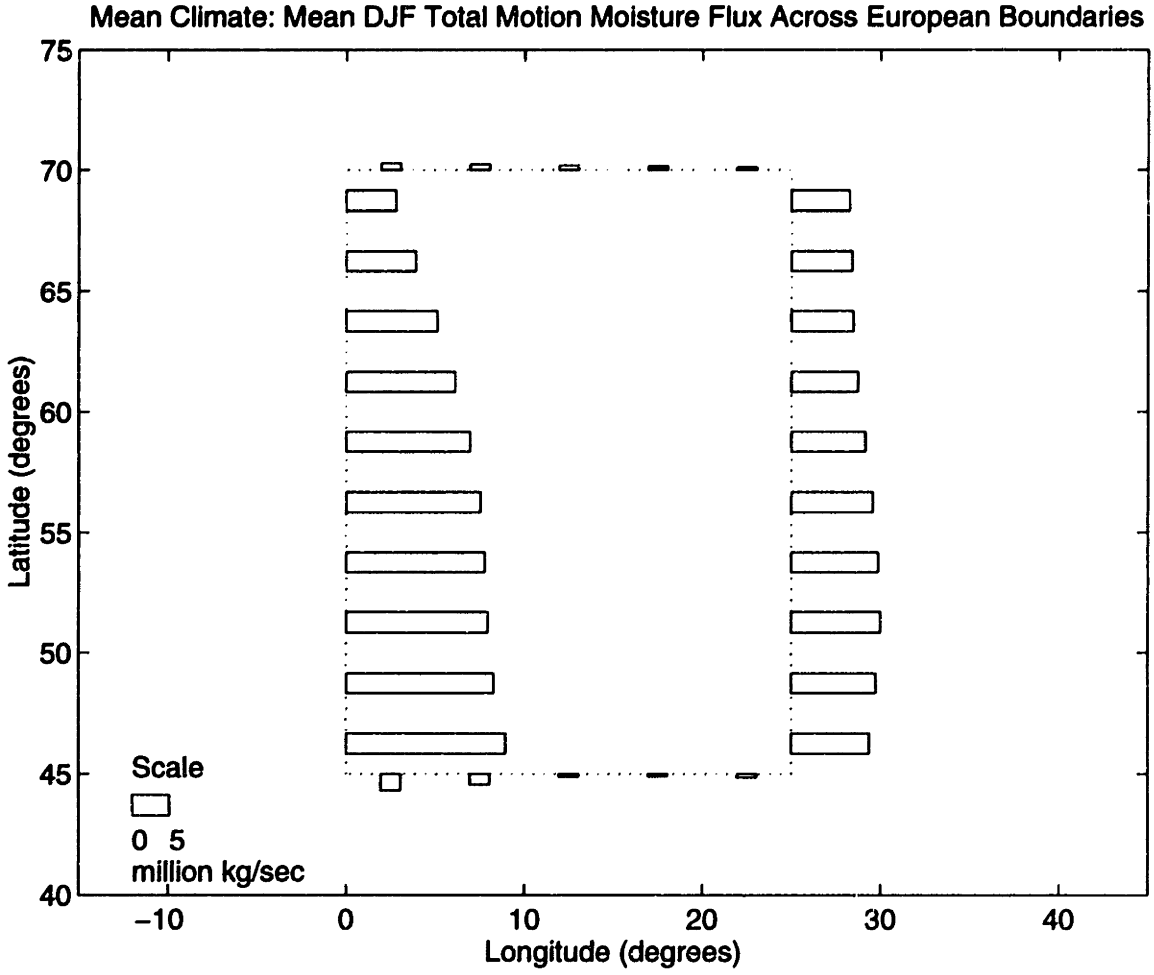

Figure 3-5: DJF Mean Climate Total Motion Water Vapor Flux

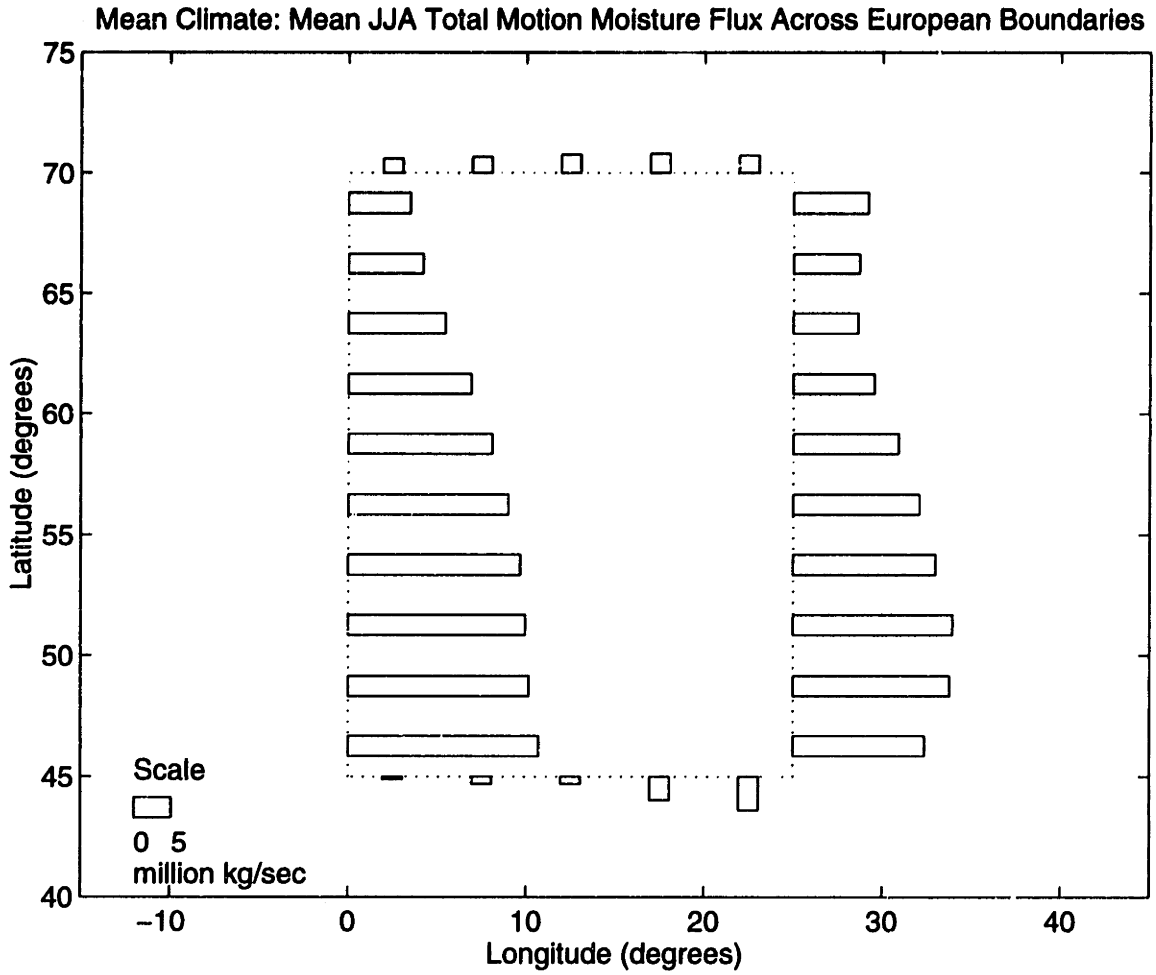

Figure 3-6: JJA Mean Climate Total Motion Water Vapor Flux

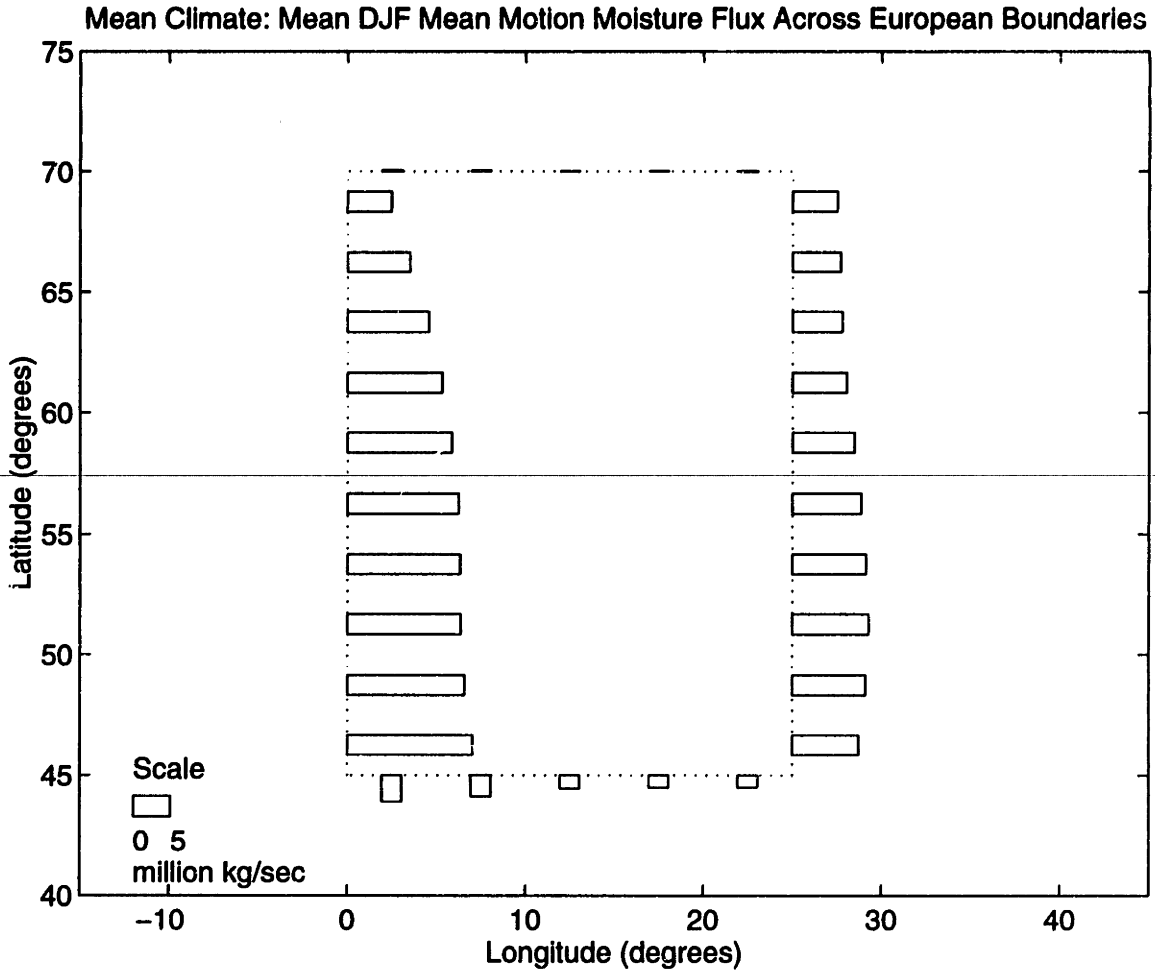

Figure 3-7: DJF Mean Climate Mean Motion Water Vapor Flux

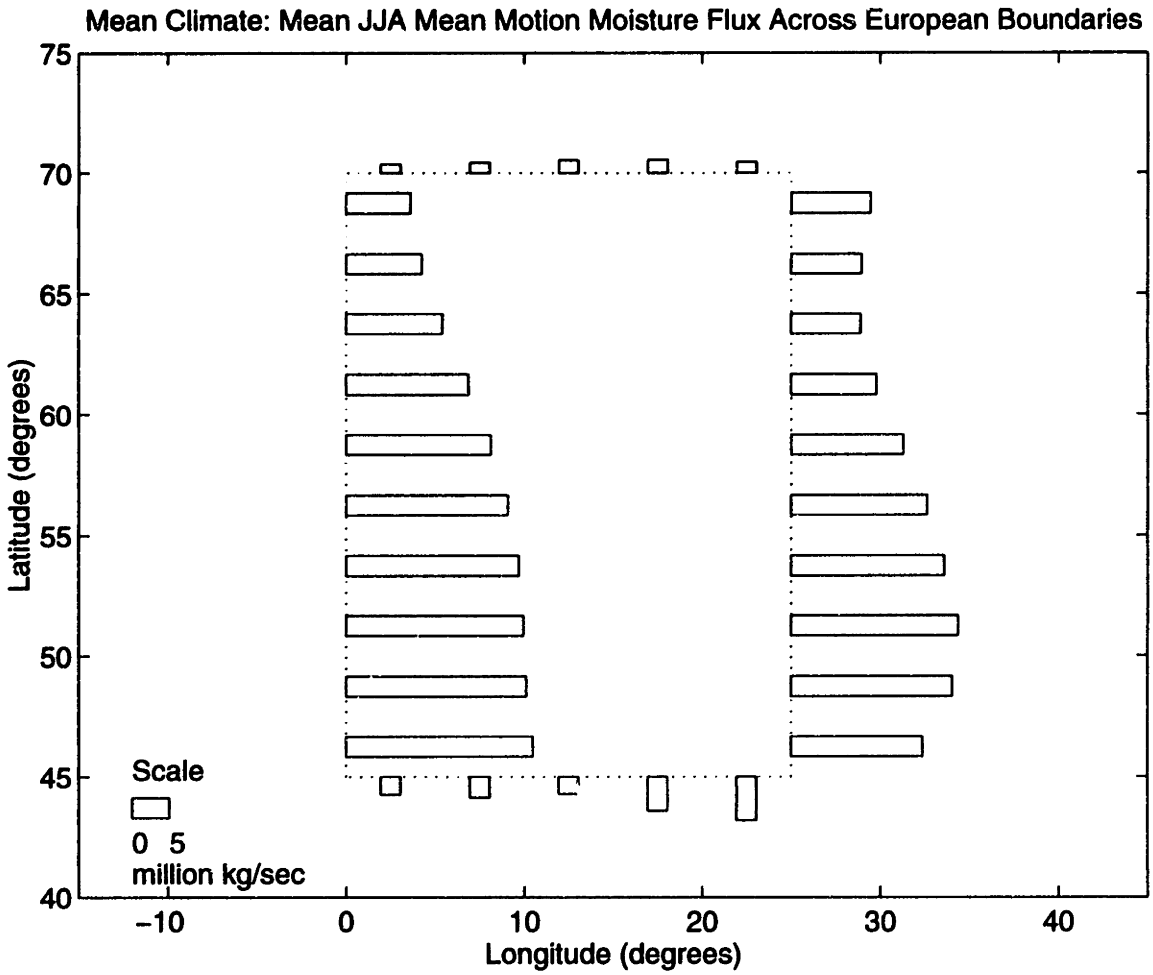

Figure 3-8: JJA Mean Climate Mean Motion Water Vapor Flux

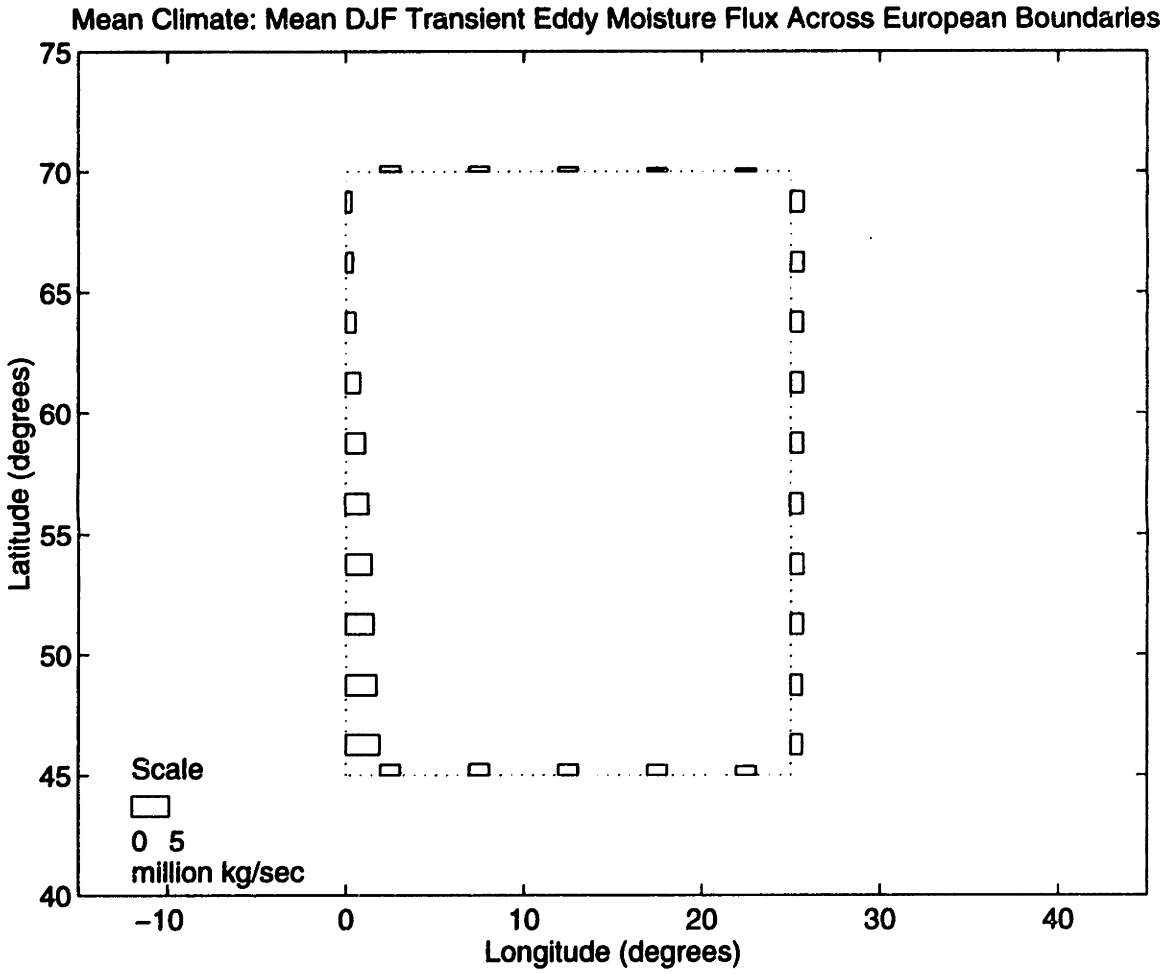

Figure 3-9: DJF Mean Climate Transient Eddy Water Vapor Flux

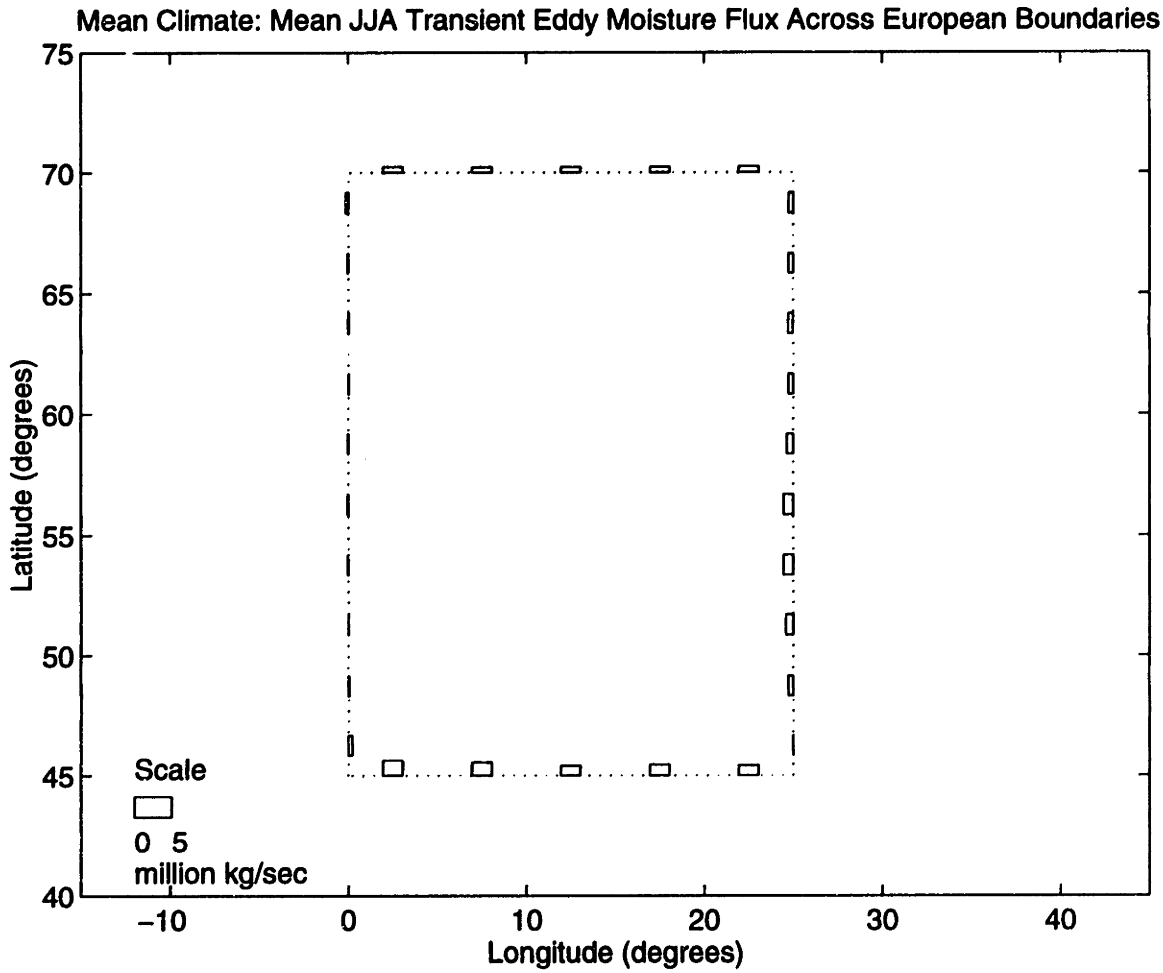

Figure 3-10: JJA Mean Climate Transient Eddy Water Vapor Flux

3.3.2 Meridional Flux

Although the meridional flux field is smaller and less regular than the zonal flux field, it is important for maintaining the Earth's water and energy balance (Peixoto and Oort 1992). On a global scale, meridional motion generally transports water and energy poleward (Peixoto *et al.* 1981). Meridional flux accounts for a large fraction of latent heat flux from the tropics and exhibits large seasonal variation associated with seasonal changes in radiation (Peixoto *et al.* 1981). Baroclinic disturbances, quasi-stationary lows, and subtropical highs are also associated with meridional transport. These eddies carry moisture northward because the southerly component of the flow is moister than the northerly component (Peixoto and Oort 1992). Zonal flux is especially important for the European region because of the pool of warm water directly to the south, the Mediterranean Sea. If the European region were to include Italy and the Iberian peninsula, the Mediterranean would constitute an even greater source of moisture and energy.

Total meridional flux varies with location and season. Annual total flux (Figure 3-2) along the northern boundary is poleward and ranges between 3.0 x 10^6 and 3.5 x 10^6 kg/s. This flux is smallest in winter (Figure 3-5) and spring and maximum in summer (Figure 3-6). Total meridional flux along the Mediterranean varies seasonally in magnitude and direction. Annual total poleward flux between 10° and 15° E longitude is small since the Alps suppress low altitude transport by mean motion. These small annual flux values reflect the net impact of opposite positive and negative seasonal fluxes. Winter and and summer total meridional Mediterranean flux is equatorward (Figure 3-5 and 3-6), whereas spring and autumn meridional flux is generally poleward (see Appendix A).

A comparison of the total, mean motion, and transient eddy components of meridional flux at the European boundary indicates that transient eddies are an important component of meridional flux. This is best illustrated by the magnitude and direction of the flux components along the northern and Mediterranean boundaries of the region. Along the northern boundary, very small negative or positive mean motion

flux combines with a relatively strong poleward transient eddy flux to produce a net poleward total motion flux (compare Figures 3-7 and 3-9 with 3-5 for the winter season).

Along the Mediterranean boundary, mean motion clearly influences seasonal variability. However, the total flux also contains significant transient eddy contributions. The poleward transient eddies substantially decrease the equatorward mean motion flux contribution to total flux along the Mediterranean boundary. The resulting total moisture flux is very small. This effect is most dramatic in spring and autumn

3.3.3 Specific Humidity and Wind

Figures 3-11 through 3-15 present vertically pressure-weighted specific humidity at grid midpoints around the boundary. These figures indicate the relative influence of humidity on moisture flux. Specific humidity varies around all segments of the boundary and throughout the year. As expected, it is generally maximum at the sourthernmost latitudes. Annual values of specific humidity along the east and west boundaries, for example, range between 1.2 and 2.4 g/kg with maximum values in the south. Along the north and Mediterranean boundaries, specific humidity is approximately 1.2 and 2.4 g/kg, respectively. High specific humidity along the Mediterranean boundary reflects higher temperatures coupled with the moisture availability over the Mediterranean Sea. In winter, minimum specific humidity values are approximately 1 g/kg, while in summer the maximum values are approximately 4 g/kg. Spring values are similar, although slightly larger, than winter values and autumn values are similar, although slightly smaller, than summer values.

Figures 3-16 through 3-20 show vertically averaged and pressure-weighted annual and seasonal wind fields. Seasonal variation in the wind fields resembles seasonal variation in mean motion flux patterns. Vertically averaged annual mean zonal winds are westerly with speeds ranging between 3.3 and 5.3 m/s. Vertically averaged annual mean meridional winds along the northern boundary are generally northward with velocities between 0.0 and -0.5 m/s. Along the Mediterranean boundary, annual wind is uniformly northerly, with velocities between -0.5 and -1.2 m/s. Zonal winds

decrease in spring and summer and increase in autumn and winter. Meridional winds vary in direction throughout the year, but tend to be largest in winter and summer.

It is interesting to compare vertically averaged humidity and wind diagrams (Figures 3-11 through 3-20) with mean motion fluxbar plots (Figures 3-3, 3-7, 3-8, and Appendix A). The subtle effects of humidity variations along the boundary and throughout the seasons are evident. For example, annual mean motion moisture influx is maximum in the southern half of the western boundary. Humidity at this location is relatively large and compensates for the smaller wind speed.

Seasonal fluctuations in mean motion along the Mediterranean boundary are significantly influenced by seasonal variations in wind. Comparison of summer and autumn total and mean motion zonal flux with corresponding humidity and wind data indicate that the large zonal moisture flux in summer results from larger than average humidity. Alternatively, large zonal autumn moisture flux values reflect larger than average zonal wind speeds.

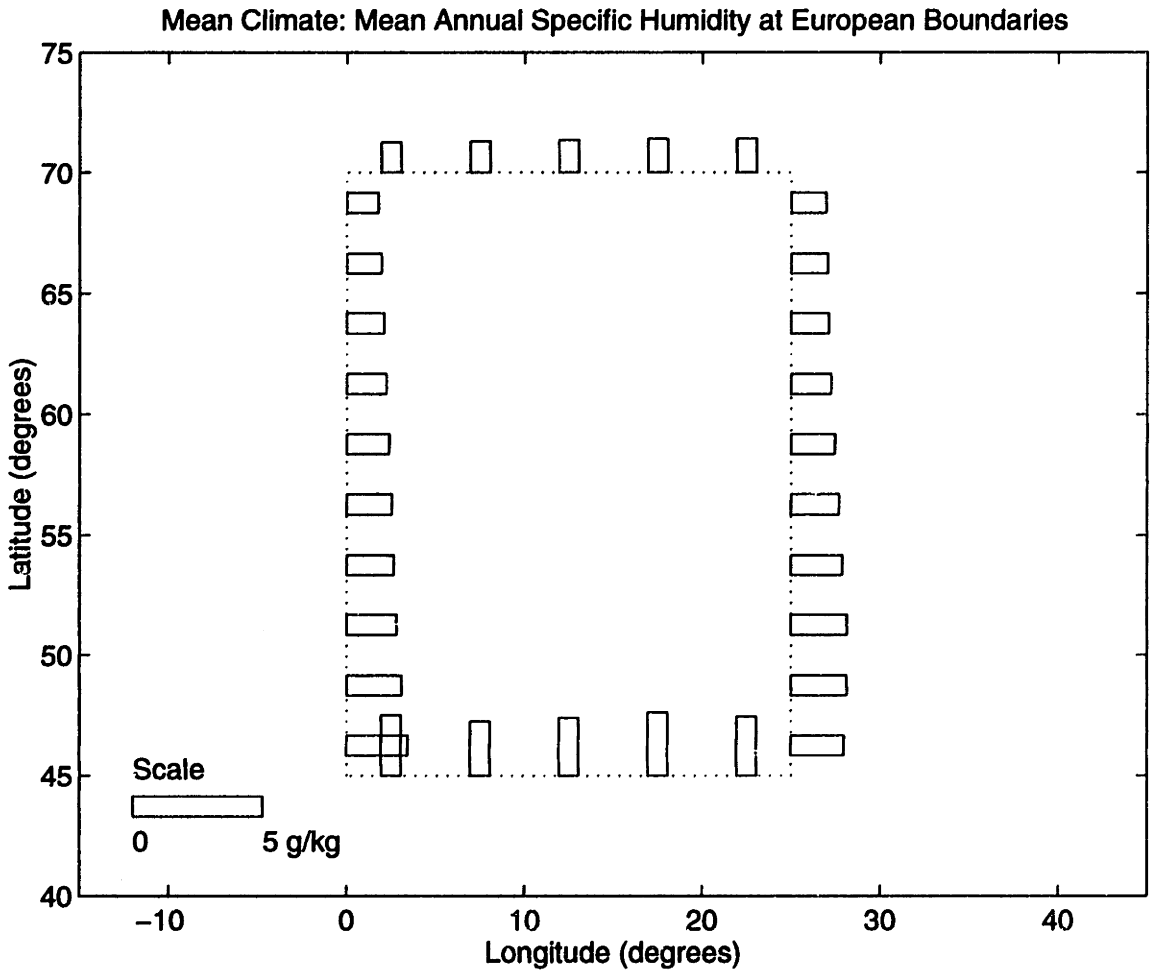

Figure 3-11: Vertically Averaged Annual Specific Humidity

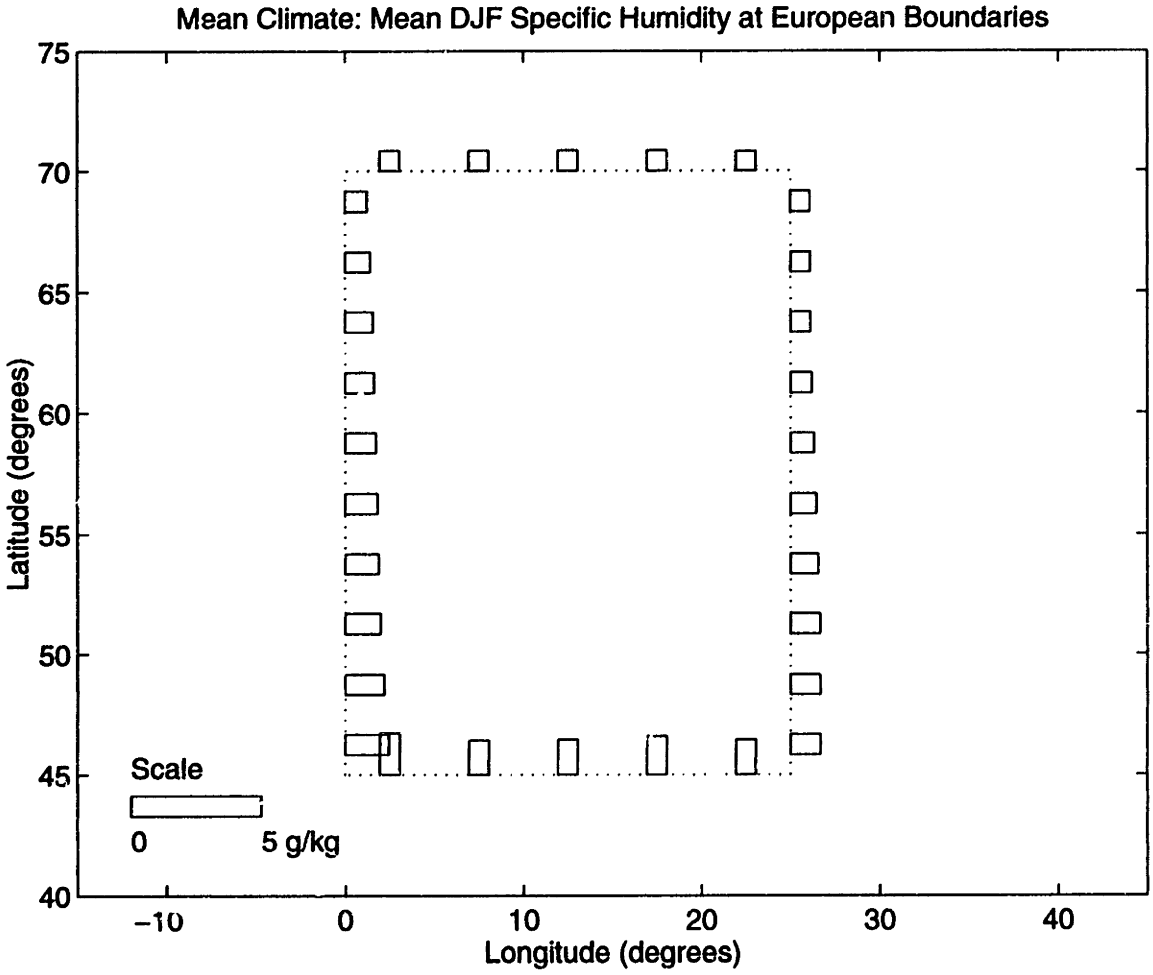

Figure 3-12: Vertically Averaged DJF Specific Humidity

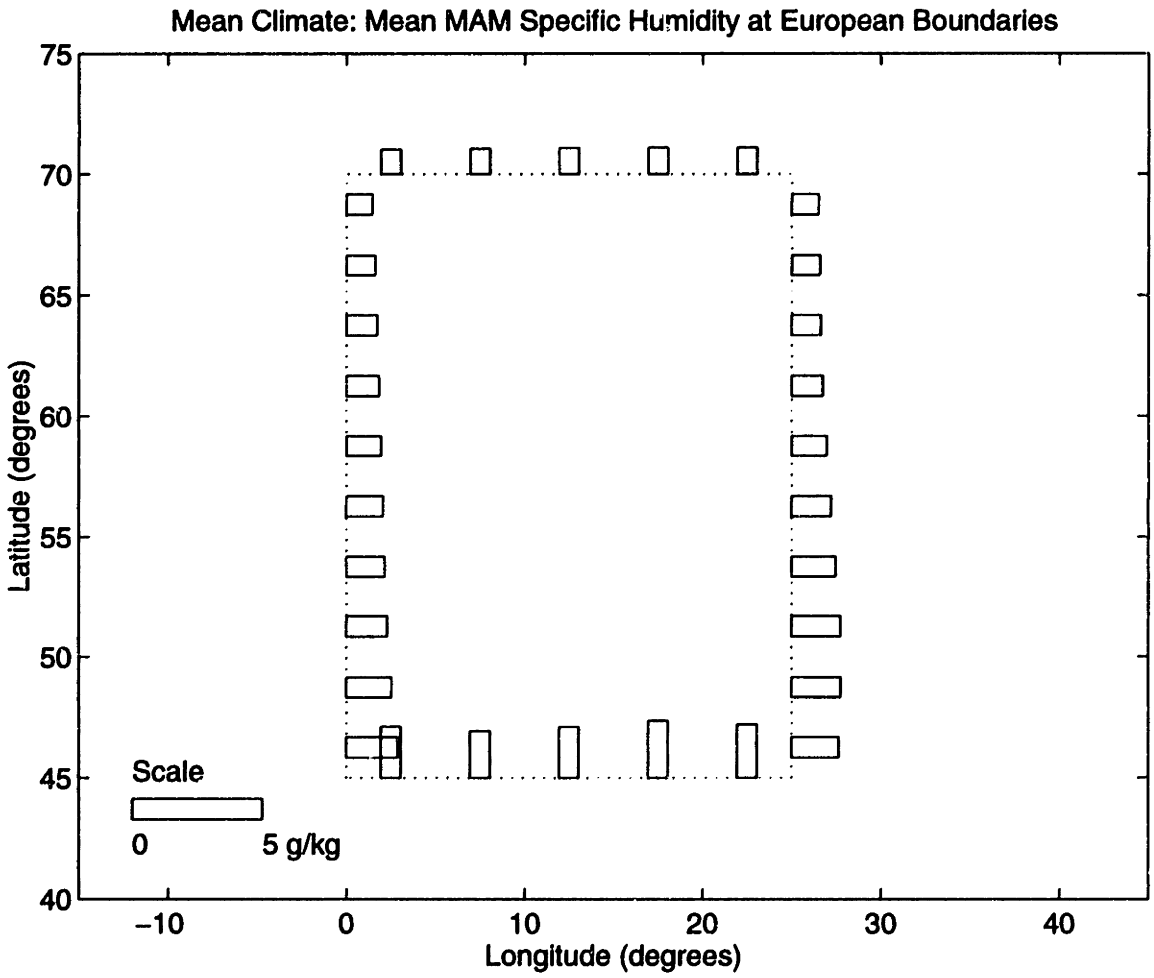

Figure 3-13: Vertically Averaged MAM Specific Humidity

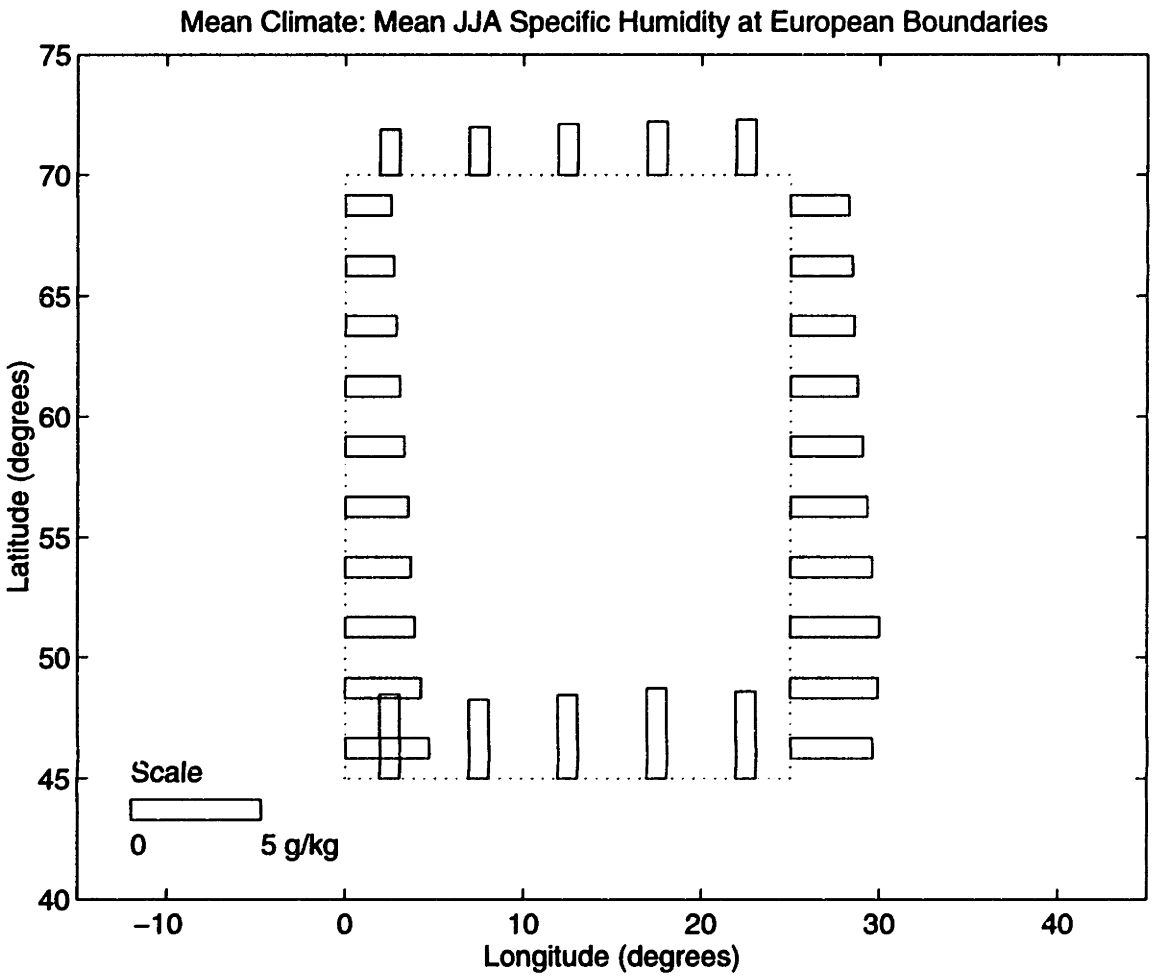

Figure 3-14: Vertically Averaged JJA Specific Humidity

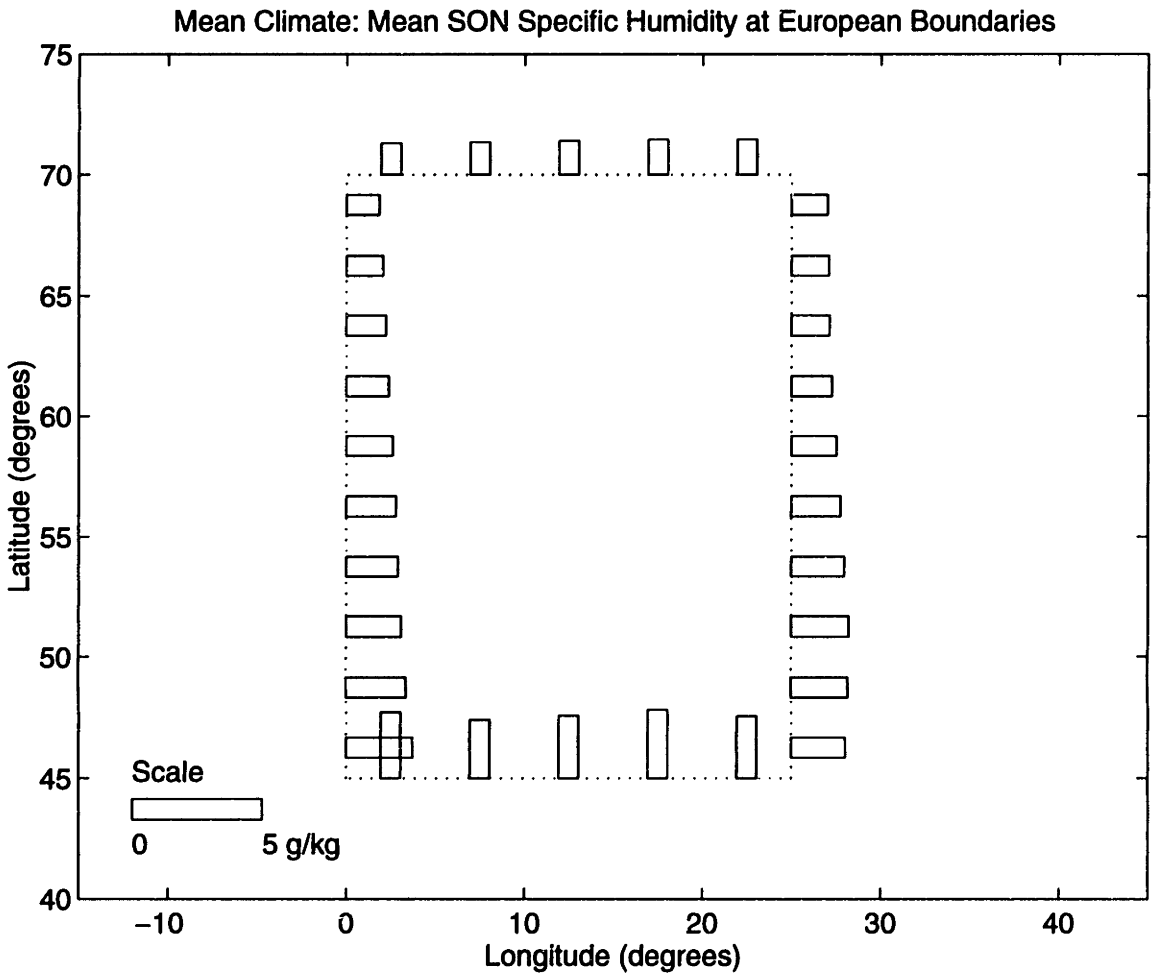

Figure 3-15: Vertically Averaged SON Specific Humidity

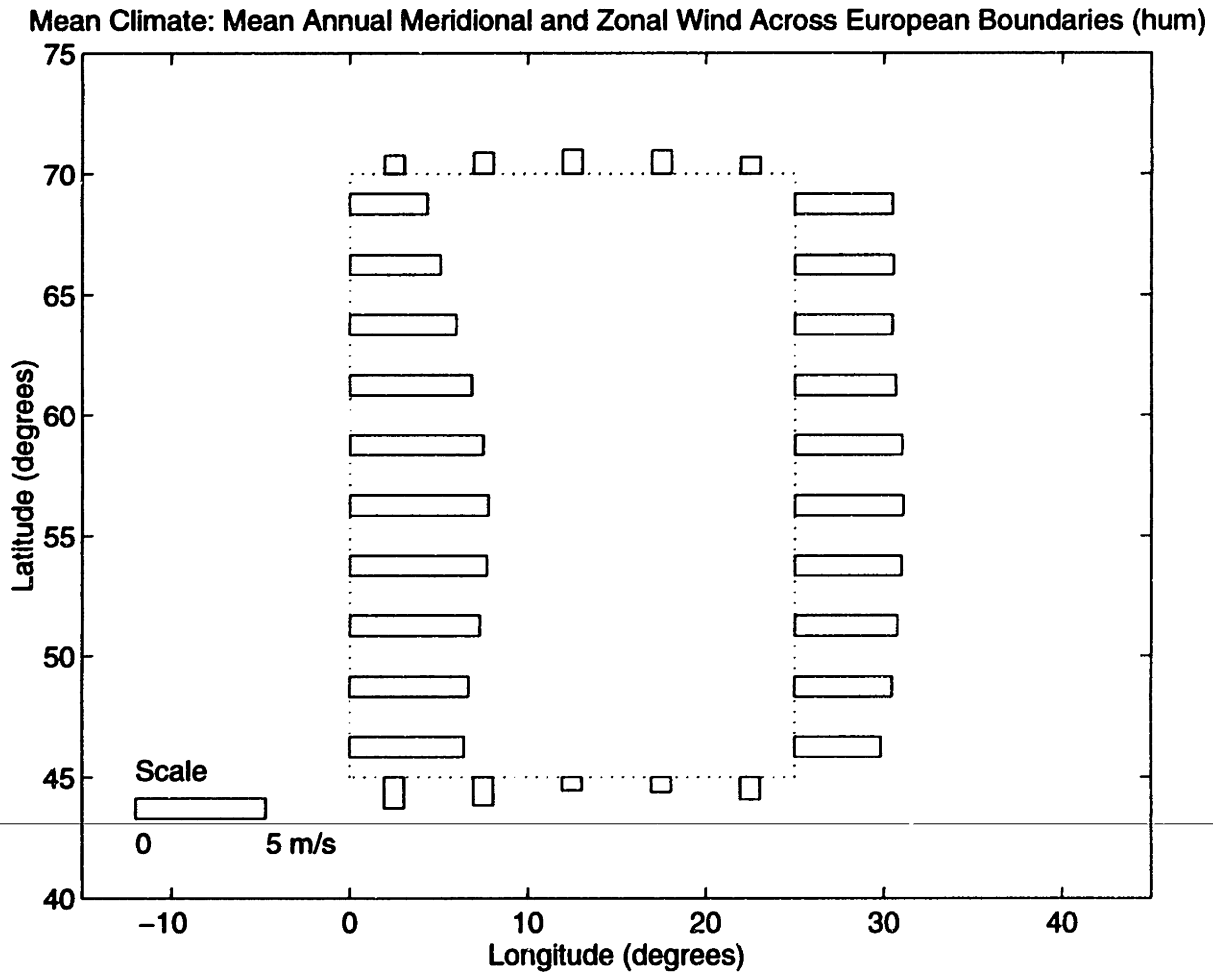

Figure 3-16: Vertically Averaged Annual Wind Velocity

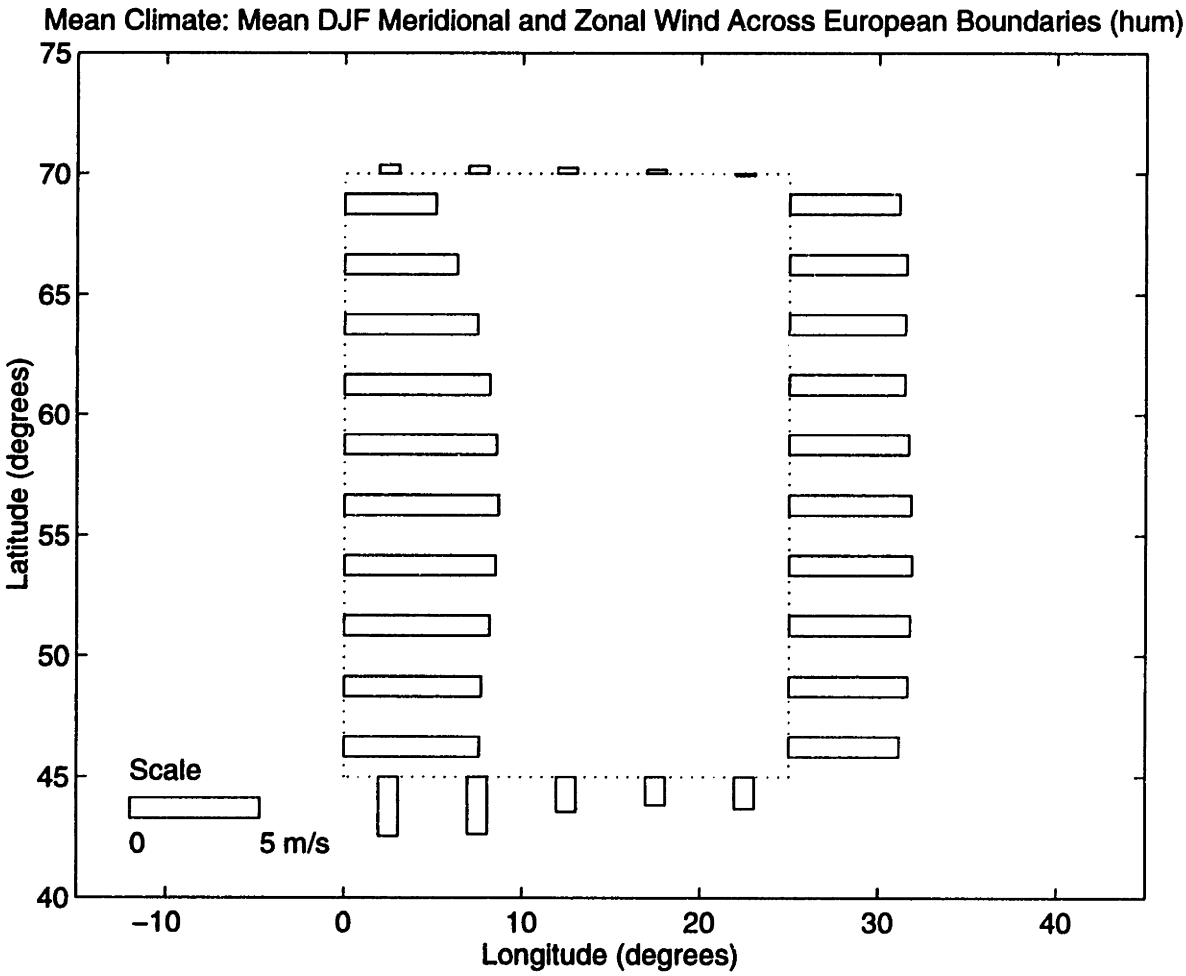

Figure 3-17: Vertically Averaged DJF Wind Velocity

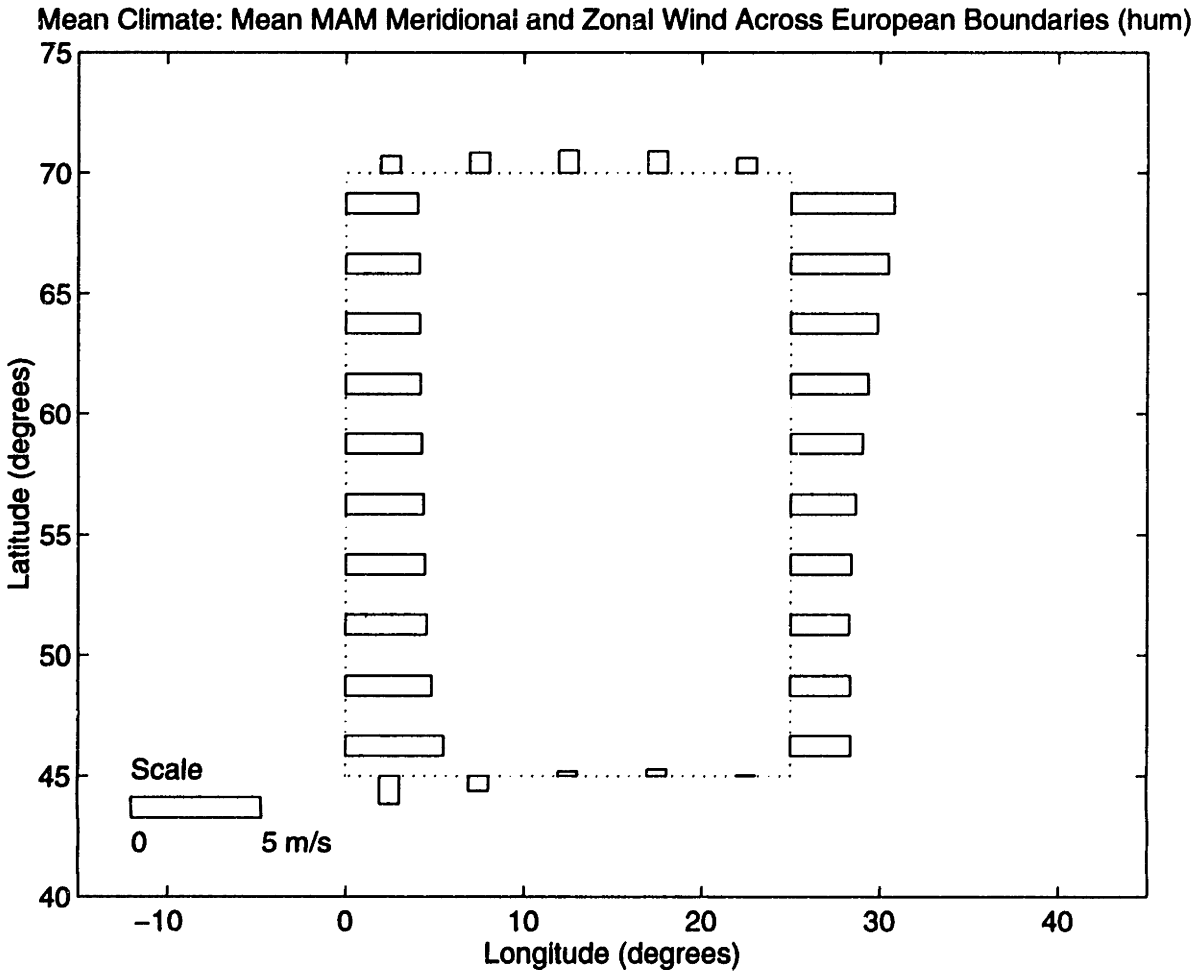

Figure 3-18: Vertically Averaged MAM Wind Velocity

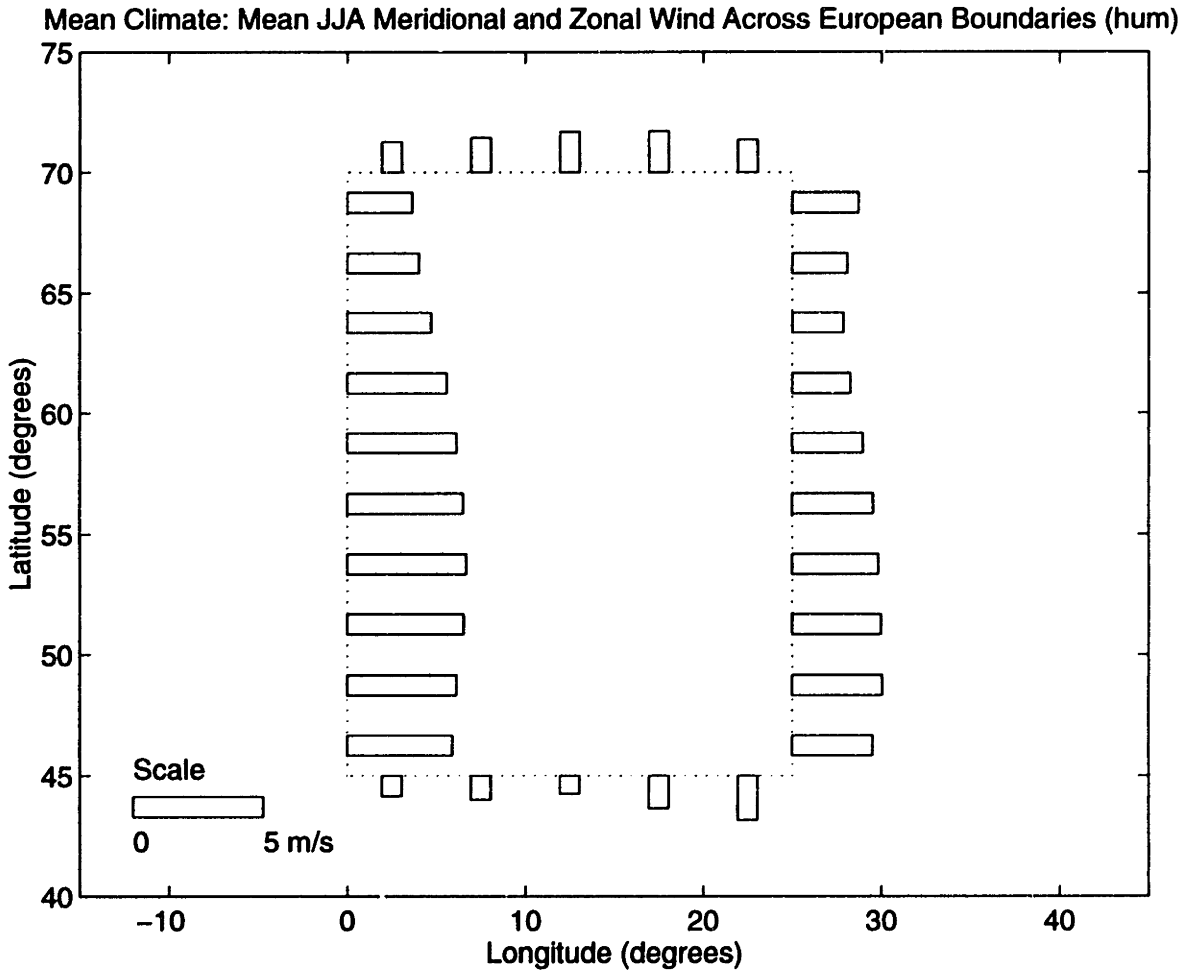

Figure 3-19: Vertically Averaged JJA Wind Velocity

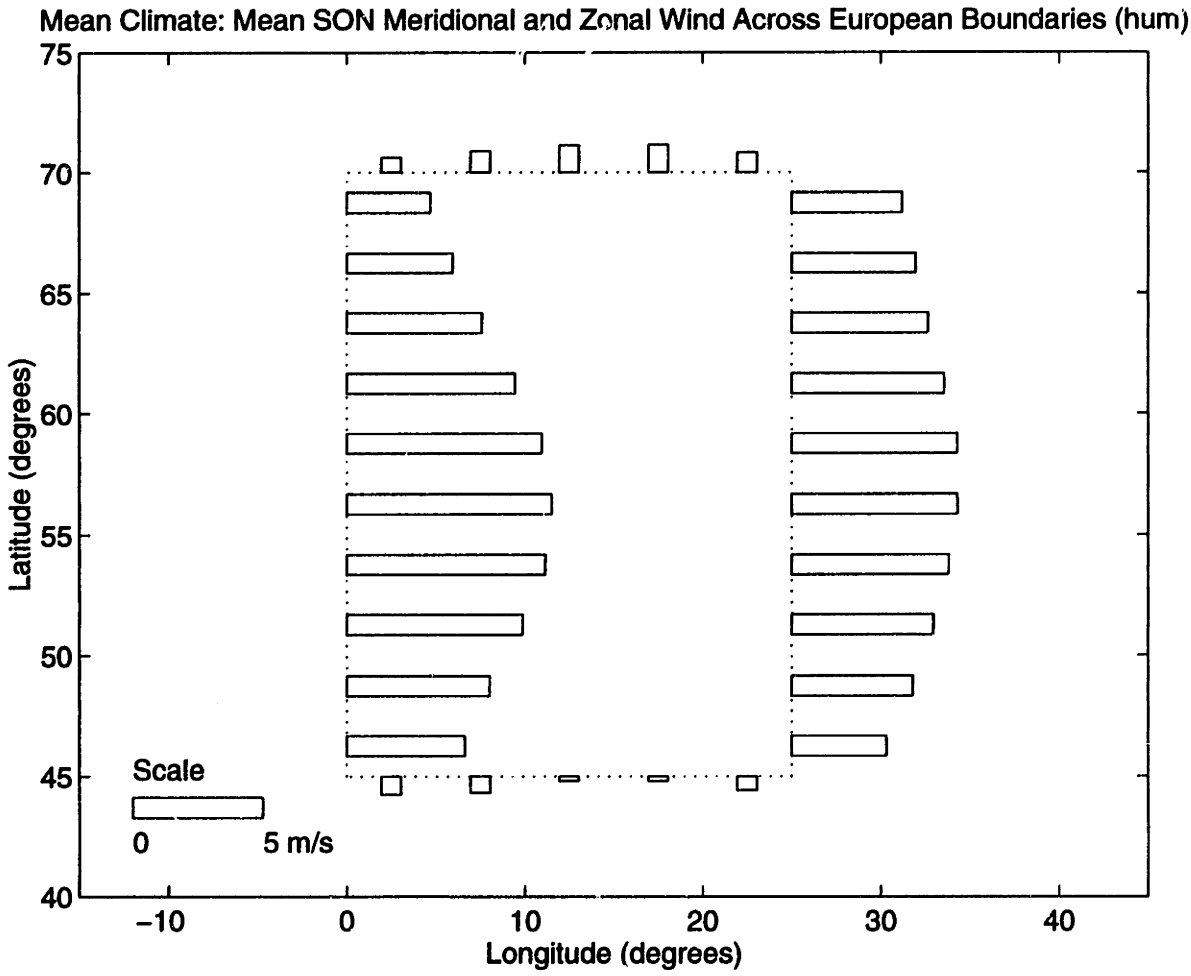

Figure 3-20: Vertically Averaged SON Wind Velocity

3.3.4 Convergence

By adding and subtracting influx and efflux into and out of the European region, annual convergence over the region is estimated at approximately 16 cm/yr. In the long-term this is equivalent to river runoff. UNESCO (1978) estimates annual European runoff for the entire European continent (excluding islands) (Region A) at 25.9 cm/yr. This estimate is based on streamflow data collected at stations throughout Europe between 1918 and 1967. Alestalo (1983) extracts long-term averages of $\overline{P}$ and $\overline{E}$ in order to compute the differences in these values. Alestalo (1983), Budyko (1963), and Baumgartner and Reichel (1975) suggest $\overline{P}$-$\overline{E}$ estimates of 23 cm/yr and 27.5 cm/yr respectively. In addition, $\overline{P}$-$\overline{E}$ values for a portion of Europe extending roughly from 45° to 55° N latitude and between the Prime Meridian and 45° E longitude (Region B) are 37.5 and 41 cm/yr, respectively.

Alestalo (1983) also performs an analysis similar to the one discussed in this paper to arrive at a convergence value of 23.5 cm/yr for his Region A and 42 cm/yr for his Region B. Alestalo (1983) contains an analysis of two sets of radiosonde measurements at several pressure levels. One set was collected from approximately 90 stations between 1974 and 1976, and the other was obtained from about 60 stations between 1969 and 1977. Using a triangular computational element, the Alestalo (1983) methodology vertically integrates divergence of specific humidity and wind, assuming that flux components vary linearly between different stations and pressure levels. The study also assumes that specific humidity is zero at 300 mb. The total divergence at each pressure level is calculated as:

$$\nabla \cdot \overline{q}\overline{\vec{v}}_{corrected} = \nabla \cdot \overline{q}\overline{\vec{v}}_{computed} - \overline{q}\nabla \cdot \overline{\vec{v}}_{verticalaverage} \tag{3.4}$$

In the above equation, the correction factor, $\nabla \cdot \overline{v}_{verticalaverage}$ ensures mass balance in the atmospheric column and comprises 87 percent of the uncorrected annual mean convergence value for Region A. The Alestalo (1983) analysis yields runoff estimates of 23.5 cm/yr for Region A and 42 cm/yr for Region B.

In comparison to all of the above studies, this analysis underestimates convergence.

Differences in areas analyzed and watershed boundaries, limited spatial coverage of the radiosonde network, an uncorrected mass balance, and underestimation of the boundary layer may result in this study's lower convergence values.

3.4 Interannual Results

Interannual analysis results form a time series of annual convergence over the region and of water vapor flux across regional boundaries. The regional boundary flux estimates are further decomposed into time series of the total motion, mean motion, and transient eddy regional flux components. These time series suggest that Atlantic Ocean and Global El-Nino-Southern Oscillation (ENSO) signatures may exist in the convergence time series. Results also facilitate comparison of regional flux magnitudes.

3.4.1 Convergence

Figure 3-21 is a times series of annual convergence due to total motion. Convergence values are positive in all years. This reflects the fact that precipitation exceeds evaporation in the mid-latitudes (Peixoto and Oort 1992).

Local minima appear to exist around years considered to contain an El Nino/ Southern Oscillation (ENSO) event (chiefly 1975/76 and 1982/83). ENSO is a global-scale climatic oscillation that occurs with quasi-periodicity near 3 and 5 years. ENSO has an oceanic and an atmospheric component. El Nino is the oceanic component and has historically been linked to anomolous warming in the east Pacific along the coast of Ecuador and Peru. Under normal conditions, a westward surface wind and other heating factors maintain a temperature gradient between the cold tropical east Pacific and warm west Pacific. During El Nino, tropical east Pacific sea surface temperature (SST) increases, while the west Pacific SST decreases. The atmospheric component of ENSO is called Southern Oscillation. Under normal conditions a pressure gradient exists between east Pacific (high pressure) and west Pacific (low pressure). This gradient is accompanied by convective atmospheric rising motion in the west and

sinking motion in the east. During the Southern Oscillation, the east-west pressure gradient diminishes, disappears, or reverses, and the area of rising motion moves eastward. Together El Nino and Southern Oscillation are referred to as ENSO. One of the major effects of ENSO is the change in global precipitation patterns. Relative drought conditions occur in the tropics and northeastern America. Mid-latitudes exhibit a weak rainfall increase over North America and southeast South America.

ENSO years covered by this study include 1976, 1982-3, and 1987 (Yulaeva 1993). It is interesting to look for an ENSO signature in the convergence time series for the European region. Local minima appear in the convergence time series at 1976, between 1982 and 1983, and in 1987. This may suggest a relationship between convergence and ENSO.

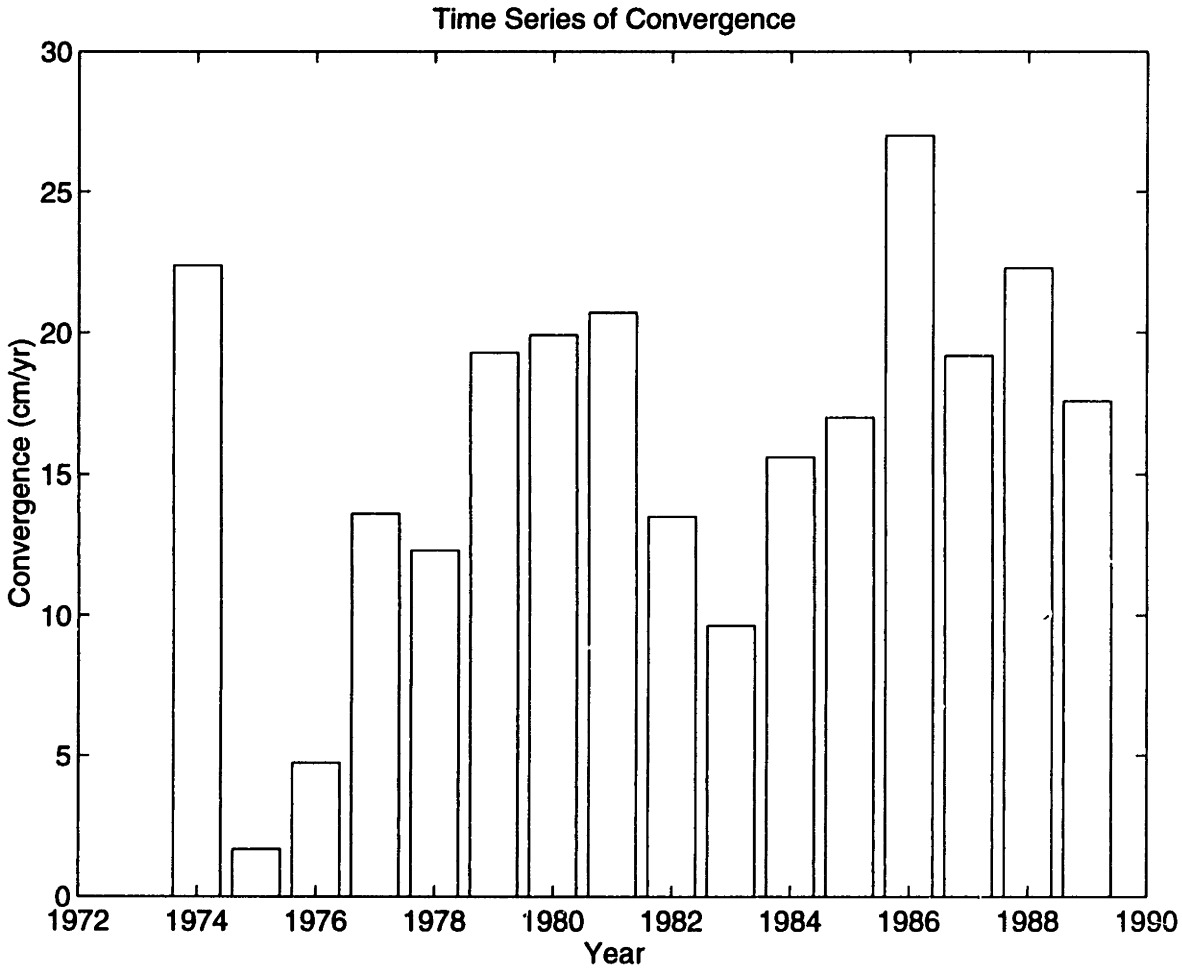

Figure 3-21: Time Series of Annual Convergence Due to Total Motion

3.4.2 Regional Flux

Figure 3-22 shows time series of flux across the Mediterranean, South Atlantic, and North Sea boundaries. It is clear from this figure that the largest flux occurs across the South Atlantic boundary (between 45° and 51° N latitude). This flux ranges between 43 kg/ms (1975) and 100 kg/ms (1974). Flux across the North Sea boundary (between 51° and 70.5° N latitude) ranges between 52 (1977) and 84 (1983) kg/ms. Flux across the Mediterranean boundary (between the Prime Meridian and 25° E longitude along 45° N latitude) is smallest and ranges between -0.2 (1975) and 8 (1977). At this boundary the Alps provide an effective barrier to meridional vapor flux. The barrier limits the Mediterranean influence on this part of the European region.

The relative magnitude of the regional flux estimates support results shown in mean climatology fluxbar plots. Atmospheric water vapor transport occurring across the South Atlantic and North Sea are driven by the strong zonal winds of the mid-latitudes. The winds carry more humidity across the South Atlantic boundary. Both zonal fluxes are large in comparison to the Mediterranean region flux which is generally dominated by the smaller transient eddy component. The interannual variability also shows that the convergence anomaly over Europe during ENSO episodes (Figure 3-21) is chiefly forced by anomalously low zonal vapor flux from the South Atlantic border. Evidence of this forcing appears in negative South Atlantic flux anomalies during 1975-76 and 1982-83 in Figure 3-22.

Decomposition of the three regional fluxes (Figures 3-23 through 3-25) supports the above-mentioned conclusions regarding relative regional flux magnitude. When the South Atlantic and North Sea fluxes are decomposed into total, mean motion, transient eddy modes of transport it is clear that mean motion dominates zonal flux. Transient eddies, although also westerly, are much smaller in magnitude. Decomposition of the Mediterranean flux, however, shows that, although total and mean motion flux exhibit the same shape, transient eddies exceed both of these modes in magnitude.

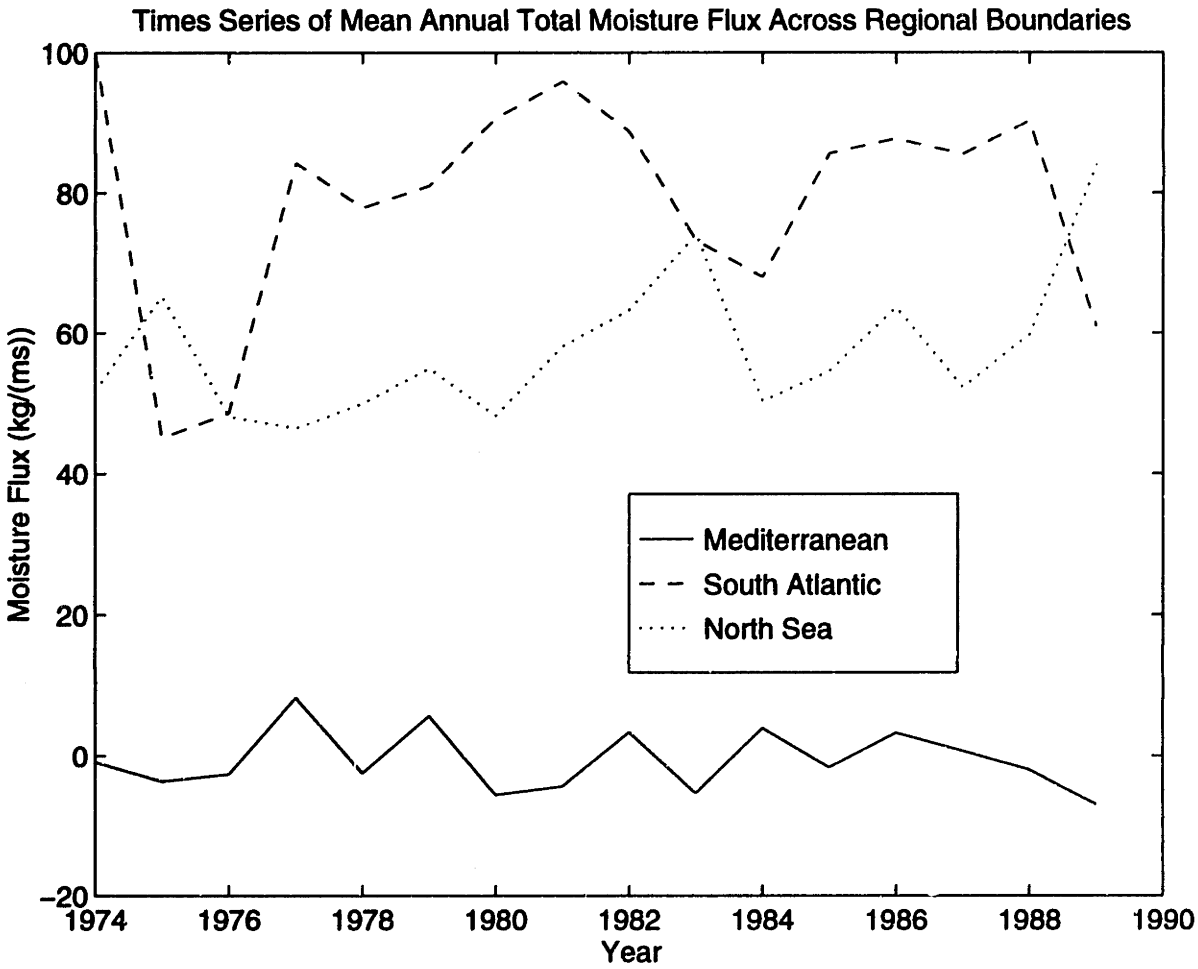

Figure 3-22: Time Series of Flux Across Regional Boundaries

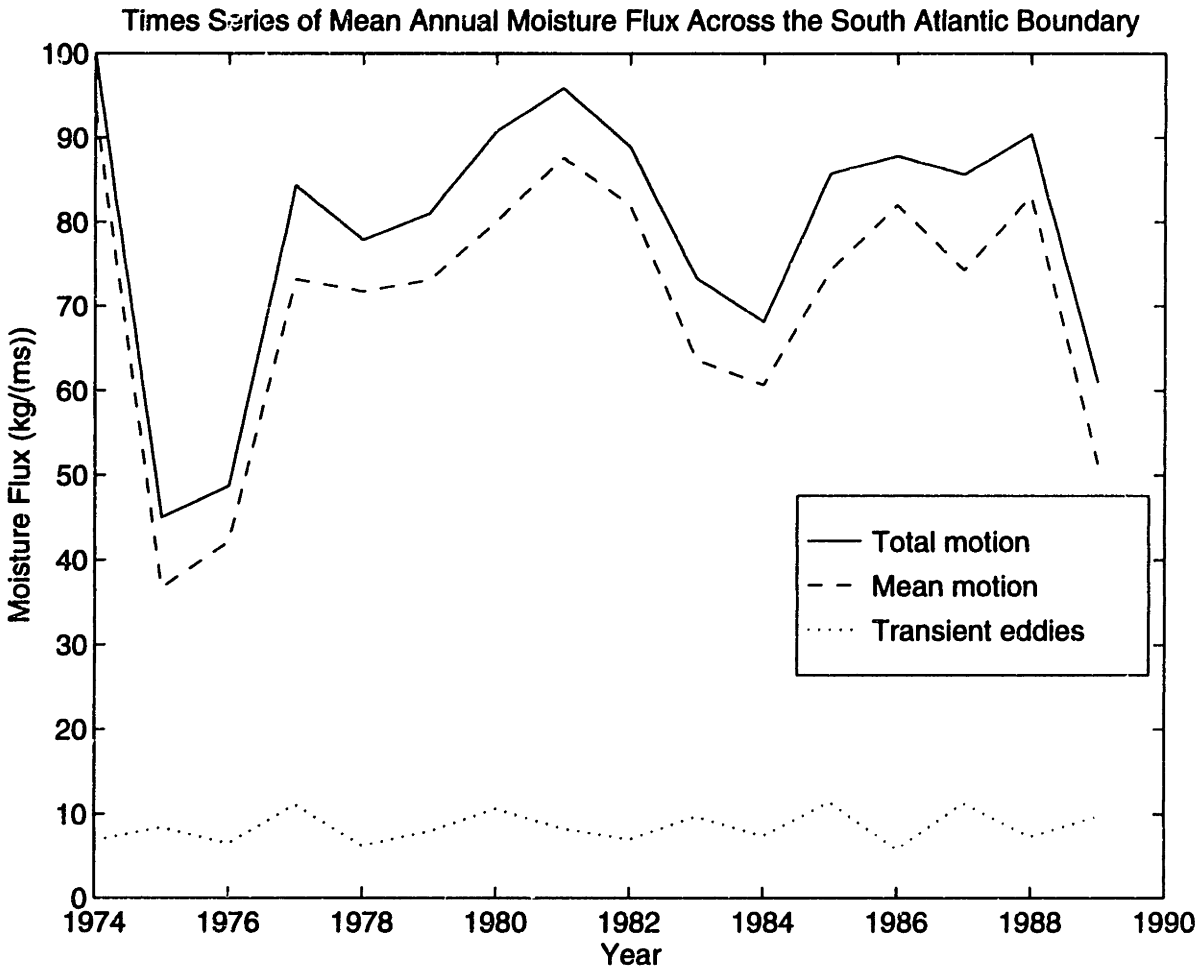

Figure 3-23: Time Series of Flux Across the South Atlantic Boundary

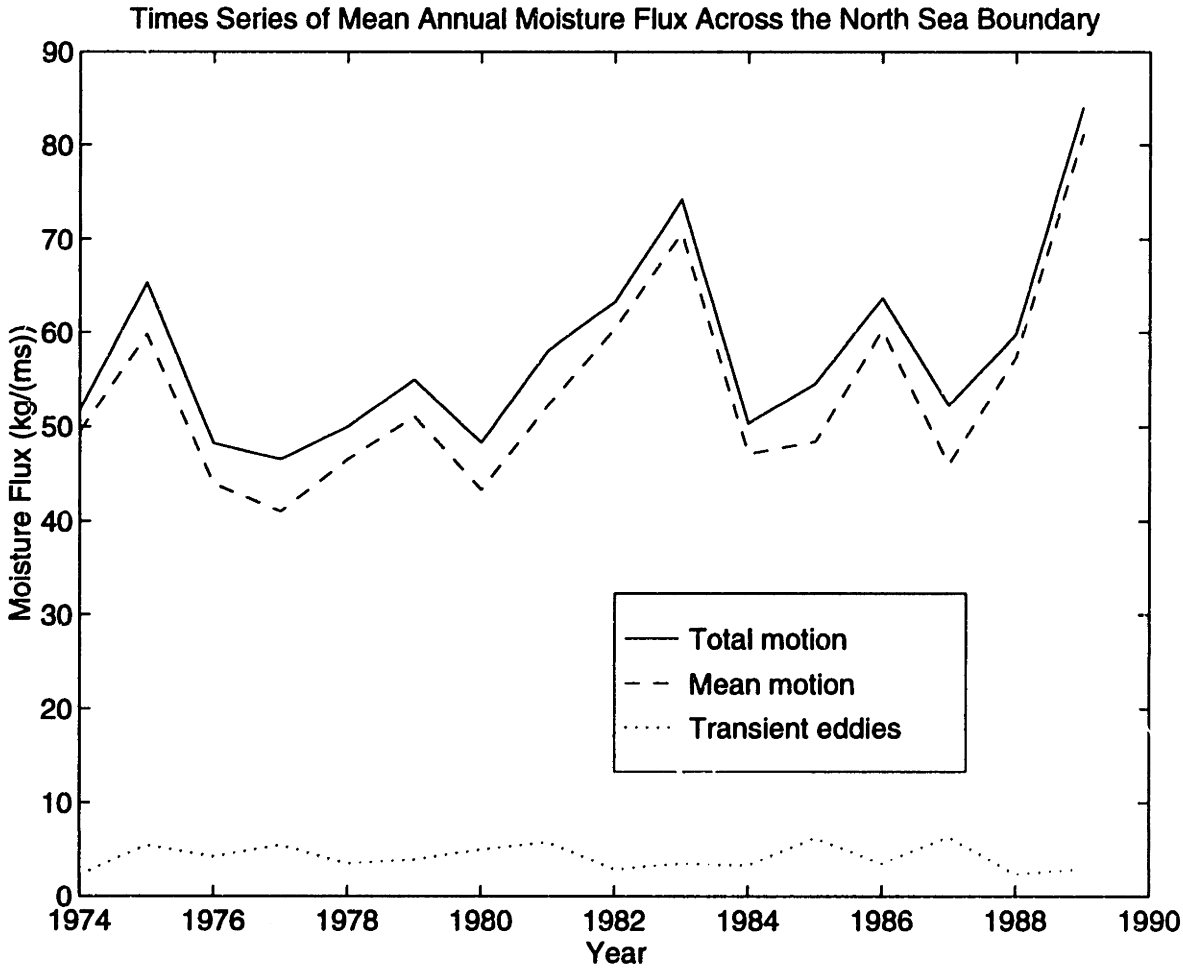

Figure 3-24: Time Series of Flux Across the North Sea Boundary

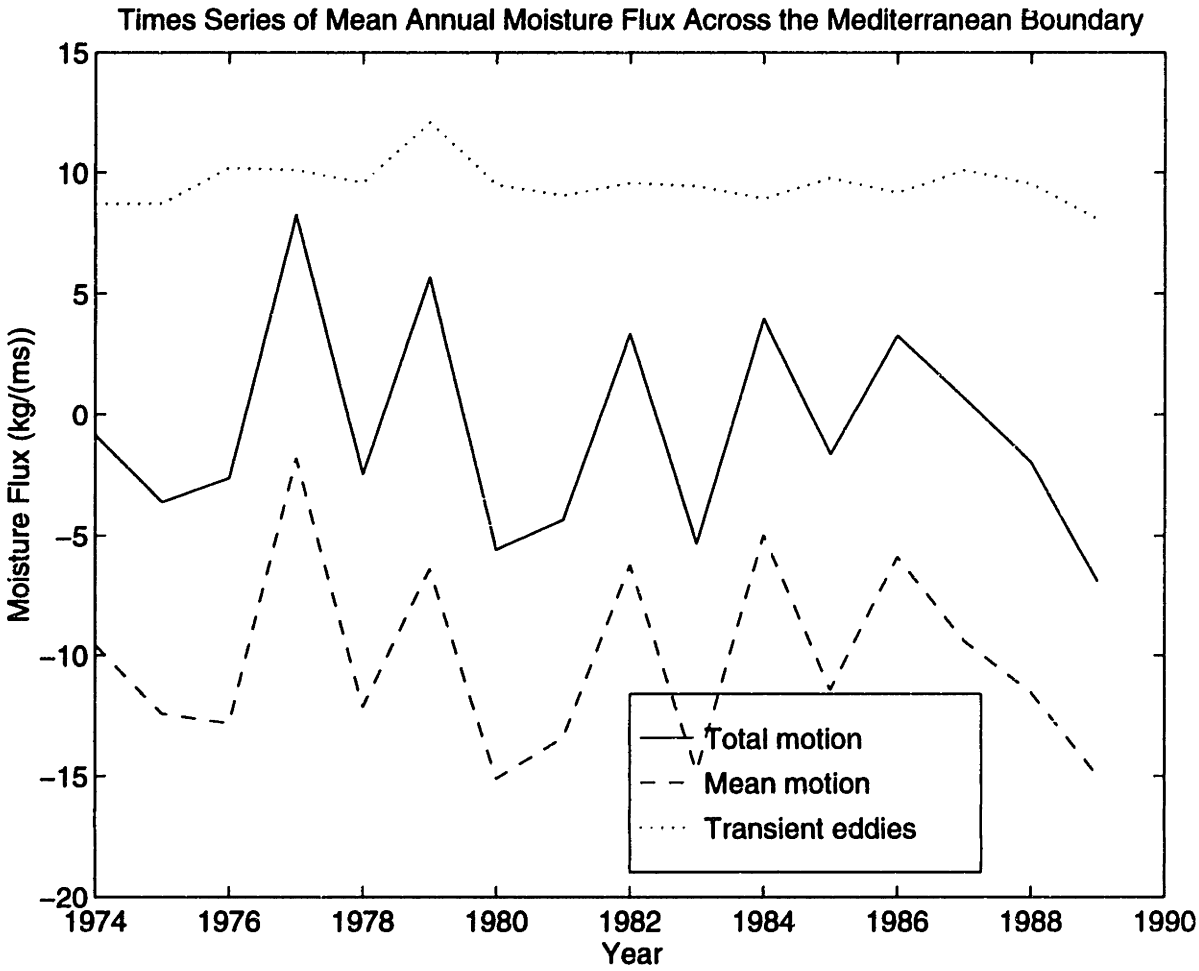

Figure 3-25: Time Series of Flux Across the Mediterranean Boundary

3.5 Conclusions

This study examines aspects of atmospheric moisture flux over the European region bounded by the 25° E, the Prime Meridian, 70.5° N, and 45° N over a sixteen year period. The mean climatology analysis reveals intra-annual relationships between different modes of water vapor transport, wind, and specific humidity, and relates these parameters to the general circulation. This analysis emphasizes the importance of mean motion in the zonal plane and transient eddy transport in the meridional direction. In addition, examination of the mean climatology also indicates the seasonality associated atmospheric water vapor transport.

This analysis reveals the relative magnitudes of moisture flux around different segments of the European boundary and compares the modes of transport that comprise these regional fluxes. Study results indicate that, as expected, fluxes of larger magnitude enter Europe across its Atlantic and North Sea boundaries. In addition, relative wind and specific humidity contributions to the zonal and meridional transport from year to year correspond to those determined in the mean climatology investigation. During ENSO years, an anomalously small water vapor convergence rate dominates the European region. Principal forcing for this scenario derives from anomalous zonal vapor transport over the tropical Atlantic.

Chapter 4

West African Drought and Theories Regarding its Forcing

The West African drought of the past three decades has had devastating social and economic impacts. Yet, debates regarding the causes of this persistent drought continue. Numerous studies analyze the role of certain climate parameters in contributing to drought. However, the role of the general circulation and land-surface feedbacks in promoting drought remain elusive, as do improved drought and flood predictions techniques (Rowell and Milford 1993, p. 699). Some research attempts to explain drought forcing by characterizing spatiotemporal patterns of rainfall behavior. Other work examines rainfall fluctuations in light of wind regimes and moisture flux, Hadley and Walker circulations, and sea surface temperatures (SSTs) (Nicholson 1993).

This study aims to identify relationships between rainfall, water vapor transport, and an index of the general circulation. Time series of rainfall anomalies, vertically integrated moisture flux, and empirical orthogonal function (EOF) patterns of the 500mb vertical wind velocity (ω) are the focus of the study. These time series are constructed such that they distinguish between the first and second halves of the rainy season and between the northern and southern regions of sub-Saharan Africa. Linear correlation coefficients derived from the time series reveal direct relationships between rainfall variability and variability in the general circulation features.

This chapter is comprised of seven sections. Section 4.1 overviews features of

the general circulation above West Africa and summarizes research that links these features to drought. Section 4.2 identifies the West African regions studied, discusses rainfall behavior in these regions, and addresses rainfall anomaly persistence and continent-wide anomaly patterns. Sections 4.3, 4.4, and 4.5 describe the water vapor flux and ω components of the present study. Section 4.3 begins with a discussion of study objectives and a description of the data used. Section 4.4 goes on to present results for zonal flux, meridional flux, and interannual flux variability. Section 4.5 presents EOF analysis of vertical wind velocity. This includes discussions of EOF methodology, EOF patterns, eigenvalues, and time series. Section 4.6 presents correlations between rainfall, vapor flux, and EOF time series. Section 4.6 also addresses correlation scale results for these parameters, and the land surface feedback implications associated with these findings. Section 4.7 closes with a summary of conclusions.

4.1 General Circulation Features and Their Relevance to Sahelian Drought

The devastating impacts of West African drought and the uniqueness of rainfall persistence in the Sahel prompt many intriguing questions. Researchers approach these questions from a number of different angles. Often they seek to gain a better understanding of rainfall behavior by correlating rainfall time series with wind, moisture transport, vertical motion, and SSTs. Such research aims to fit West African drought into the context of the general circulation with the ultimate goal of identifying drought-forcing mechanisms. The following sections describe major features of the general circulation over West Africa. They also discuss drought theories associated with these features. Section 4.2.1 outlines prominent features of the West African climate. Section 4.2.3 overviews research that attempts to link these features to African drought.

4.1.1 Major Circulation Features

Before discussing findings of the present research, it is helpful to review current understanding of the general circulation features over West Africa and the studies that relate these features to rainfall variability. Below is a brief description of atmospheric systems over the Sahel. This description addresses the main upper-level wind regimes, precipitation-generating disturbances associated with these regimes, pressure distributions, lower-level wind systems, and Hadley and Walker circulations.

The wind patterns at higher levels are simpler than those near the surface. The dominate equatorial wind patterns are easterly. Overall, three jet systems characterize the West African zonal wind regime during summer months. These three jets are: the Tropical Easterly Jet (TEJ) at 200 mb, the African Easterly Jet (AEJ) at 650 mb, and the subtropical westerly jets near 200 mb (Nicholson *et al.* 1988, p. vi). The TEJ is related to a meridional thermal gradient which exists during northern hemisphere summer between the Tibetan highlands and the Indian Ocean (Fontaine *et al.* 1995, p. 1503). The AEJ arises from a temperature contrast between the Sahara and the Atlantic Ocean. A similar wind flow exists in the southern hemisphere above 5° S latitude. All three jet systems are important for understanding African climate. They provide the energy for weather disturbances and direct these disturbances across the continent (Nicholson *et al.* 1988, p. vi).

In sub-Saharan Africa most precipiation arises from pressure disturbances (easterly waves) associated with the AEJ. These rain-carrying disturbances are also known as squall lines (SLs). According to Rowell and Milford (1993), an SL is an "organized line of convective cells." This line can extend up to 1000 kilometers in length, has a North/South orientation, and generally travels westward. Squall lines involve diabatic heating that plays an important role in North African circulation. SL generation requires dry desert air above a potentially unstable low-level moisture supply. Generation also requires vertical wind shear below the African Easterly Jet. Surface evaporation, topography, and surface heating can trigger instability. Rowell and Milford (1993) found that above-average low-level westerly flow and topography were

the most influential factors affecting SL generation. African waves and AEJ strength, however, do not impact SL generation (Rowell and Milford 1993, p. 1181).

At lower levels the wind activity is more complex. Pressure distribution plays a central role in dictating this activity. Major pressure features include a low pressure trough above the equator and two high-pressure cells located to the north and south of this trough. The low pressure trough moves northward during northern hemisphere summer. During this time, low pressure pervades much of northern-hemisphere Africa. The high pressure cells also exhibit seasonal variation. In the summer hemisphere they tend to be wider, stronger, and further poleward (Nicholson *et al.* 1988, p. vi).

These pressure patterns result in several wind systems. Northeast and southeast trade winds along with southwesterly monsoon flow converge near the surface at the equatorial trough. Consequently, air at the point of convergence moves upward and produces rainfall thus creating the Intertropical Convergence Zone (ITCZ).

Cadet and Nnoli (1987) examined moisture transport over West Africa. Their findings provide insight into relationships between monsoonal flow, the ITCZ, and the AEJ. Cadet and Nnoli (1987) examined vertically integrated water vapor flux over Africa and the eastern Atlantic Ocean during the summer of 1979. Results reveal the northward movement of the African monsoonal flow and the attendant ITCZ during the northern hemisphere summer. Findings also suggest the importance of the AEJ and its relationship with water vapor originating in the Gulf of Guinea. Budget calculations and the large vapor flux exiting West Africa and entering the Atlantic Ocean suggest that moisture from the Gulf of Guinea moves upward and is advected toward the West by the AEJ. The relatively large divergent component of this flux indicates that it is not an important rainfall source for sub-Saharan Africa (Cadet and Nnoli 1987, p. 581).

The zonal circulation is another important feature of the African climate. The east/west circulation associated with the Hadley circulation is called the Walker circulation. The Walker cell is characterized by upward motion in the eastern regions of the African continent and falling motions in the west (Nicholson *et al.* 1988, p.

vi). According to Fontaine and Janicot (1992), the westerly monsoon flow constitutes the low-level branch of the Walker cell over West Africa, while the TEJ comprises the easterly, upper level branch of this cell. The effects of the Walker circulation on rainfall are prominent in southern Africa where the southeast experiences greater rainfall than the southwest (Nicholson *et al.* 1988, p. i).

4.1.2 Studies Linking Atmospheric Circulation and Drought

Several studies compare wet and dry-year behavior of various African climate features. Each reference discussed here is presented as part of three categories: (1) horizontal wind and water vapor transport, (2) vertical motion patterns, and (3) rainfall and SST relationships. Studies addressing horizontal wind and water vapor flux include work by Kidson (1977), Newell and Kidson (1984), Lamb (1983), and Fontaine *et al.* (1995). Newell and Kidson (1984) and Kidson (1977) concentrate on easterly flow while Lamb (1983) addresses monsoonal features. Fontaine *et al.* (1995) confirms and builds upon aspects of the Kidson (1977), Newell and Kidson (1984), and Lamb (1983) studies. Research into vertical motion regimes includes work done by Nicholson (1981), Fontaine and Janicot (1992), and Fontaine *et al.* (1995). A brief review of SST/rainfall studies highlights work by Lamb (1978a and 1978b), Folland *et al.* (1986a and 1986b), and Rowell (1995).

Horizontal Wind and Water Vapor Transport

Some of the earliest research linking drought to general circulation features addresses pressure, wind, and moisture flux associated with wet and dry years. Kidson (1977) related African rainfall to upper air circulation and concluded that a weakening of the northern hemisphere circulation accompanied downward trends in rainfall. Specifically, Kidson (1977) found that near-disappearance of the 850 mb trough around 8° N latitude and weakening of the TEJ occurred during periods of anomalously low Sahelian rainfall (Kidson 1977).

In 1984, Newell and Kidson (1984) built upon Kidson (1977) findings when they

examined wind velocity data for wet and dry periods over the Sahel. These authors determined that the AEJ, the 850-700 mb temperature gradient, and the wind shear strengthen during dry years. In addition, the 200 mb TEJ weakens. During wet years the easterly jet south of the equator shows greater vertical shear (Newell and Kidson 1977). Newell and Kidson (1977) suggested two possible explanations for their findings. One explanation states that a decrease in rainfall results in decreased evapotranspiration, increased heat loss via sensible heat, a warmer surface boundary layer of air, and increased thermal wind and zonal wind shear. Increased shear, in turn, enhances the thermal wind's easterly component. This scenario, however, does not explain the wet-year increase in the southern easterly jet's shear. The second explanation involves variability in subsidence due to changes in the general circulation. However, global teleconnections affecting subsidence variability require further study (Newell and Kidson 1977, p. 32).

Other studies focus on monsoonal flow over West Africa. For example, Lamb (1983) is one of the first notable studies relating moisture flux and drought. Results show that below-average moisture flux does not necessarily accompany below-average rainfall. Lamb (1983) examined the interannual and intraseasonal variability of the thickness and moisture content of the southwest monsoon layer over West Africa. He compared below-average rainfall years (1968, 1971, and 1972) to near-average rainfall years (1967,1969, and 1975). Lamb (1983) found that drought years did not appear in conjunction with unusually dry southerly surface air. In fact, southwest monsoon flows showed higher-than-average specific humidity at the surface. Specific humidity was actually below average during years of more normal rainfall (Lamb 1983, p. 210). In addition, the 1972 rainy season corresponded to an especially shallow southwesterly monsoon flow across the Gulf of Guinea coast and a less shallow flow for more abundant rainfall years. However, monsoon depth during non-drought years did not always exceed that observed during drought years (1969 is an example). Analysis of the drought and non-drought monsoon layer at 13° N latitude displayed minimal interannual and intraseasonal variation (Lamb 1983, p. 211).

Most recently Fontaine *et al.* (1995) investigated rainfall variability in relation

to tropospheric wind anomalies for 1958 through 1989. Their results confirm and further illuminate the observations of Newell and Kidson (1984) and Lamb (1983). Fontaine *et al.* (1995), for example, found that increases in the AEJ, decreases in the TEJ, and decreases in the southwesterly monsoon flow accompany below-average rainfall in the central Sahel. Persistent drought periods were also associated with a less southward extension of the upper easterlies and a weakening of the upper branch of the Hadley circulation (Fontaine *et al.* 1995, p. 1503). Correlations between an index of Sahelian rainfall and the zonal wind field reveal two major coherent wind field domains related to Sahelian rainfall. These domains are: the 200 mb easterly flow related to the monsoon and the AEJ's southern edge. The AEJ is most closely related to monsoon flow near the "meteorological equator", and is, therefore, most affected by displacements of its southern edge. Because such displacements have their biggest impact below 700 mb, monsoonal flow and rainfall affect the AEJ through sensible/latent heat partitioning (Fontaine *et al.* 1995, p. 1506). This explanation is very similar to Newell and Kidson's (1984) thermal wind argument. According to Fontaine *et al.* (1995), a weak West African monsoon, results in a lower-than-average moisture supply, and, therefore, lower Sahelian rainfall. Lower rainfall means less evaporation and thus, less latent heat flux. As latent heat transfer decreases, sensible heat flux increases and warms lower level air in the North. This warming increases the West African temperature gradient and consequently increases the thermal wind (Fontaine *et al* 1995, p. 1506). Strengthening of the thermal wind is evident in the stronger AEJ observed during dry years.

Fontaine *et al.* (1995) investigated wind field changes associated with opposite rainfall anomalies patterns in the Sahel and Guinean regions. Results from this investigation provide insight into Lamb's (1983) monsoon layer depth findings. Fontaine *et al.* (1995) found that rainfall anomalies in the Sahel and Guinea Coast are often of opposite sign. This characteristic is especially prevalent between 1958 and 1989. To relate this phenomenon to wind fields, Fontaine *et al.* (1995) produced three rainfall patterns: Sahel drought/Guinea flood, Sahel flood/Guinea drought, and Sahel drought/Guinea drought. Fontaine *et al.* (1995) concluded that the first scenario

corresponded to increased southward low-level meridional temperature gradients and stronger wind velocity of the AEJ's southern border. This scenario was also found to occur in conjunction with reduced upper level zonal monsoon flow. (Opposite relationships characterized scenario 2). Drought in both regions corresponded to little AEJ variation (Fontaine *et al.* 1995, p. 1509).

The Fontaine *et al.* (1995) conclusions support Lamb's (1983) findings of thicker monsoonal flow at 13° N during non-drought years. They may also explain Lamb's (1983) discovery that a 5° N monsoon layer depth was not always thicker in non-drought years than in drought years. At this lower layer, the Sahel/Guinea relationships investigated in Fontaine *et al.* 1995 may play a role. Fontaine *et al.* (1995) showed that the years that Lamb (1983) examined did not all reflect the same Sahel/Guinea rainfall patterns. For example, the dry Sahelian years 1968 and 1972 showed Guinean flood and Guinean drought. The years 1969 and 1972 were both Guinea drought years. This could explain why Sahel rain and monsoon layer depth along the Guinea Coast do not always exhibit the same relationship. This also suggests that, in some cases, it may be beneficial to study the entire West African region instead of the Sahel alone (Fontaine *et al.* 1995, p. 1509).

As the above-mentioned studies indicate, consistent findings exist regarding easterly jet strength and drought. In addition, they suggest possible explanations for jet variability. Monsoon behavior associated with drought/non-drought years and with regional differences, however, appears more complex. Further study is necessary before full explanations of monsoon variability can evolve.

Vertical Motion Features

The Hadley and Walker circulations heavily influence West African climate. Early hypotheses suggested that a southward displacement of the ITCZ caused West African drought. Numerous studies refute this explanation (Nicholson 1988, p. 53), but few provide definitive pictures of exactly how Hadley and Walker circulation varies with rainfall. Some of the clearest findings are found in work by Nicholson (1981) and Fontaine and Janicot (1992).

Wetter-than-normal years result from a northward displacement of the ITCZ, while drought years are not a product of an anomalous ITCZ position, but rather result from changes in the nature of Hadley circulation. A high-sun rainfall minimum along the Guinea Coast reflects northward displacement of the ITCZ (Nicholson 1981). Furthermore, intensification of the rainy season and earlier ITCZ excursion to the North are also factors. Nicholson (1981) identified a narrowing of the belt of maximum rainfall during drought years and also supplied historical evidence of simultaneous negative rainfall anomalies to the north and south of the ITCZ. In addition, she showed that decreased sub-Saharan rainfall during drought accompanies increased rainfall in equatorial regions. These observations suggest that drought is associated with an expansion of the Hadley cell's descending branch and a contraction of its ascending branch (Nicholson 1981).

Fontaine and Janicot (1992) also studied Hadley and Walker circulation. They used wind field coherence over West Africa to confirm the existence of Hadley and Walker cell intensities and positions. They also noted that dry periods, correspond to a weakened coherence accompanied by a more southward location of the Intertropical Convergence Zone (ITCZ), a decrease in monsoonal flow, a higher AEJ velocity and a lower TEJ velocity. In regard to north/south dynamics, Fontaine and Janicot (1992) concluded that the HCS weakens over West Africa during dry years. In terms of the HCN, however, the only distinct dry-year characteristic is an increase in its upper-level southerly flow, a finding first presented by Nicholson (1981). This generally supports the association between drought years and the near-disappearance of the 850 mb trough and weakening of the TEJ. This finding led to the conclusion that the decreasing trend in Sahelian rainfall occurs in conjunction with a weakening of northern hemisphere circulation (Kidson 1977).

The Fontaine *et al.* (1995) analysis of Sahelian and Guinean rainfall anomalies in relation to zonal and meridional wind components revealed vertical relationships linking the upper and lower troposphere. These relationships reflect West African monsoon circulation and its notable relationships to Sahelian rainfall. In particular, Fontaine *et al.* (1995) found that the Sahel drought/Guinea flood pattern occurred

in conjunction with a weak east-west circulation

Vertical motion studies are inconclusive and, in some cases, contradictory. Although researchers tend to agree on jet variability, in relation to drought, their findings regarding the location and strength of the vertical motion cells are less definitive.

Sea Surface Temperatures

Discussion of Walker and Hadley circulation alludes to SST variability and its relation to West African rainfall. Many investigations attempt to relate SSTs to West African rainfall. Often, however, the dynamics responsible for the observed SST relationships are not understood (Nicholson 1989, p. 84). Early studies focus on Atlantic Ocean SSTs, while more recent research considers SSTs on a global scale. A brief overview of SST studies is presented in Nicholson (1989) and is summarized below.

Sahelian wet years are associated with abnormally high temperatures across much of the tropical Atlantic, but anomalously low SSTs to the north and west of the convergence zone over the Atlantic. This anomalous SST pattern forces a southward movement of the wind convergence zone and equatorial trough, and a lower Sahel rainfall (Lamb 1978a). Although the SST pattern detected by Lamb (1978a) is the most commonly identified SST pattern, it is unlikely to reflect a unique drought cause (Nicholson 1989).

Observed trends and modelling studies suggest that global interhemispheric SST differences are more influential than interhemispheric differences in the Atlantic alone. For example, the downward trend in interhemispheric SST differences accompanies the downward rainfall trend in the Sahel. Modelling results reveal that global, Pacific Ocean and Indian Ocean SSTs have a greater influence on Sahel rainfall than Atlantic SSTs. As Nicholson points out, this makes more sense in terms of African climatology because the weather systems that fail in the Sahel during dry years originate in pressure perturbations in the eastern Sahel and traverse to the west. Thus, the Indian Ocean SSTs, nearer to the source of these perturbations, are more likely to influence Sahel rainfall (Nicholson 1989, p. 86). In addition, Rowell *et al.* (1995) combined observational and modeling data to determine that global SST variations

are responsible for much seasonal rainfall variability.

4.2 Rainfall

West African rainfall studies generally involve traditional time series analysis. These studies often investigate rainfall interannual variability and its relationship to other atmospheric and oceanic parameters. Researchers also use rainfall time series to examine rainfall behavior throughout the African continent (Nicholson and Palao 1993). Some studies focus on temporal variability of rainfall within specific regions. Other work identifies spatial coherence and common continent-wide anomaly patterns (Nicholson 1988; Nicholson 1989).

4.2.1 Regions and Rainfall Time Series

The geographical areas studied in this analysis roughly correspond to those identified by Nicholson as: (1) Sahelo-Sahara, (2) Sahel, (3) Sudan, and (4) Sudano-Guinean (Nicholson 1993). These areas are pictured in Figure 4-1 and span between approximately 7.5° N latitude and 25° N latitude. These regions generally experience a high-sun rainy season between June and September with the maximum rainfall occurring in August (Nicholson 1993).

For the purposes of this study, the four areas discussed above are grouped into two regions: North and South. The Sahelo-Sahara and Sahel comprise the North and the Soudan and Soudano-Guinean constitute the South. As explained below, each pair of regions comprising North and South exhibit similar rainfall and water vapor flux patterns. Thus, pairing the four regions into two simplifies the analyses.

Figures 4-2 and 4-3 show rainfall time series for the North and South. There are two time series for each region: one for June/July (JJ) and one for August/September (AS). These time series extend from 1959 to 1989 and show regionally-averaged departures from regionally-averaged long-term means determined from the entire thirty-one year period.

Professor Sharon Nicholson, of Florida State University, provided the data used to

construct the time series. Professor Nicholson provided yearly JJ and AS rainfall totals for twelve subregions. The North and South are comprised of six subregions each. North and South JJ and AS average rainfall values were calculated from subregion totals.

Distinctions between JJ and AS and between North and South in these time series suggest that different forcing mechanisms operate during the first and second halves of the rainy season and within different sub-Saharan areas. Figures 4-2 and 4-3 show that the JJ season in both the North and South experiences less persistent rainfall anomalies than AS. In addition, these figures show that JJ/AS and North/South differences exist regarding contributions to the overall interannual variability of rainfall. Many of these observations support the findings of Nicholson and Palao (1993).

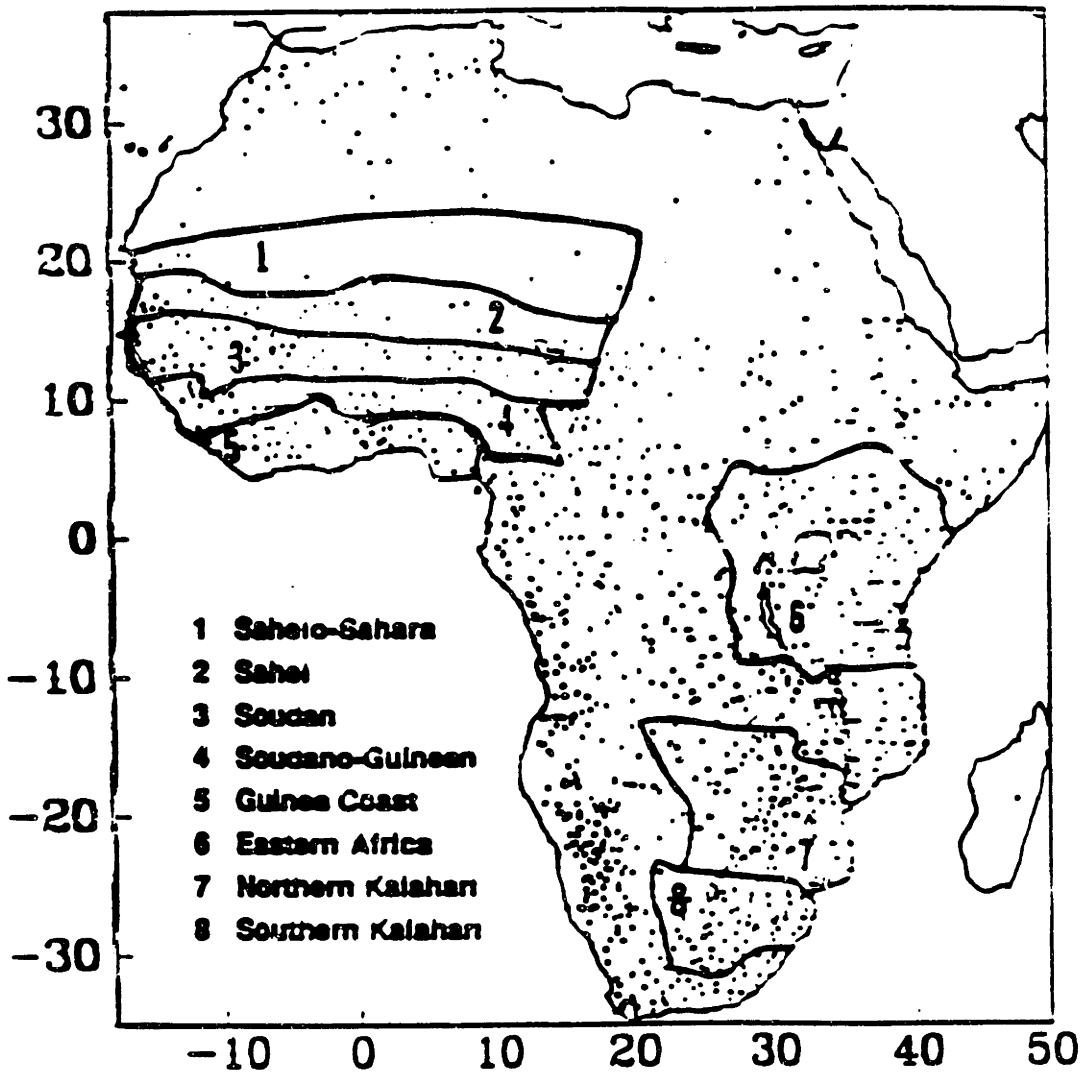

Figure 4-1: West African Regions

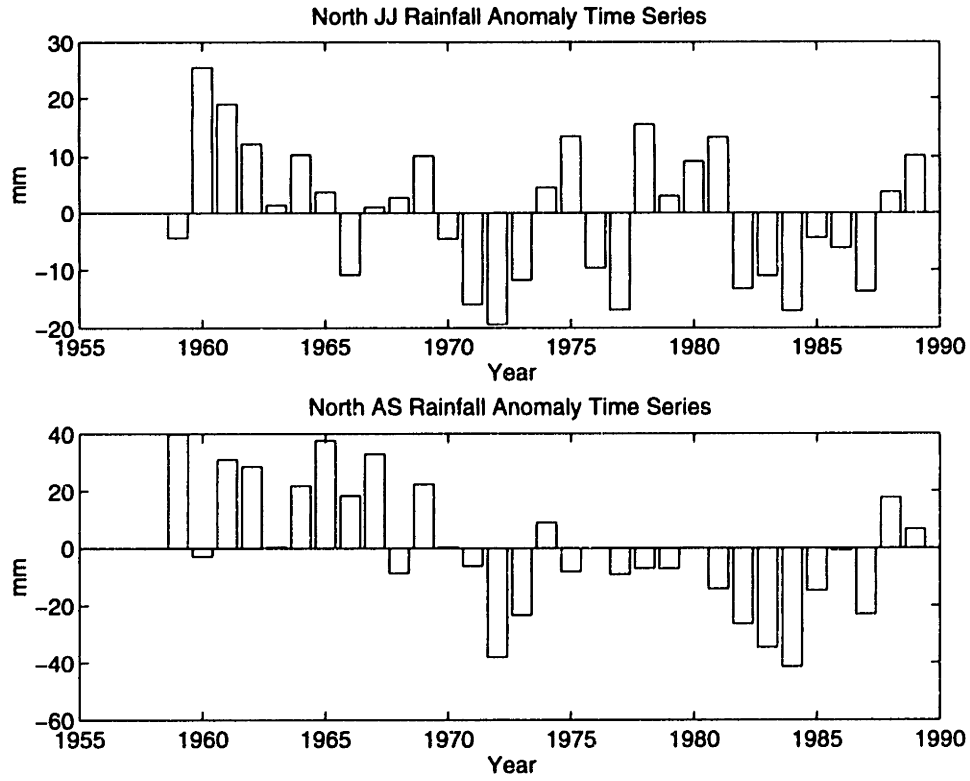

Figure 4-2: North Rainfall Anomaly Time Series

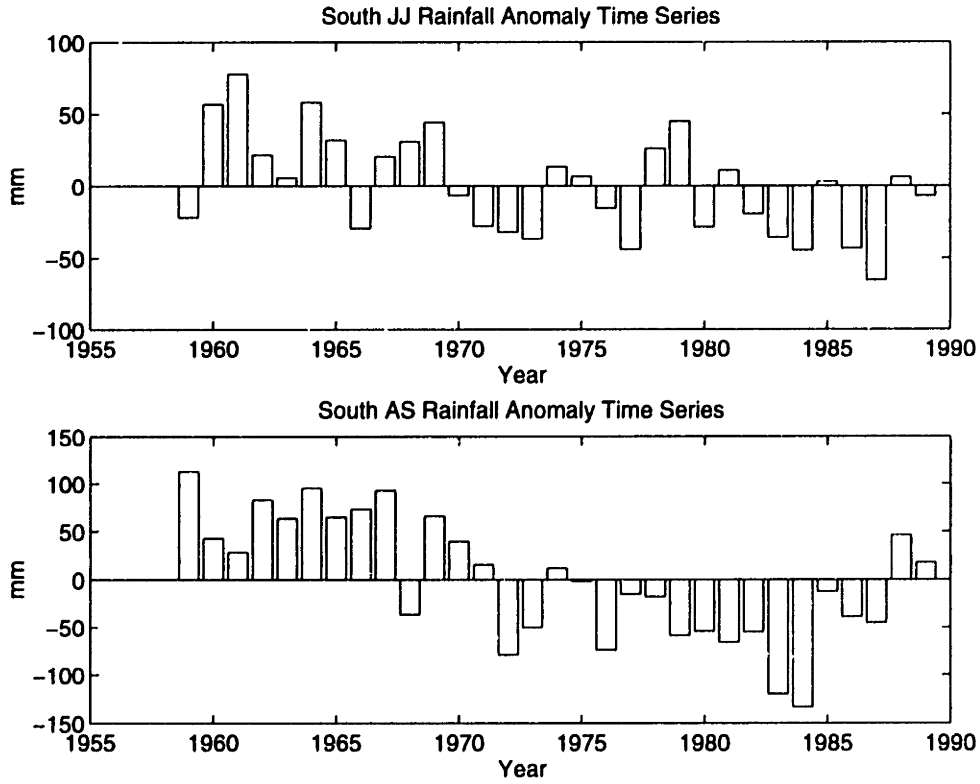

Figure 4-3: South Rainfall Anomaly Time Series

JJ and AS Rainfall as a Percent of Annual Rainfall		
	North	South
JJ	32	32
AS	55	45
JJ + AS	87	77

Table 4.1: Percent Annual Rainfall

Nicholson and Palao (1993) analyzed JJ and AS rainfall in regions approximately equivalent to the four regions shown in Figure 4-1. They found that AS contributes more to annual rainfall than does JJ. Table 4-1 was derived from the Nicholson and Palao (1993) and shows JJ and AS rainfall as a percentage of mean annual rainfall for North and South. Nicholson and Palao determined that the contribution of AS rainfall to the annual mean varies little with latitude across the four areas they studied. AS rainfall constitutes approximately 60% of the annual mean around the Sahelo-Sahara, 50% in the Sahel and Soudan, and about 40% in the Soudano-Guinean area (Nicholson and Palao 1993, p. 374). The contribution of JJ rainfall to the annual mean is more consistent throughout the Sahel. This contribution ranges from 27% to 36% throughout most of the four regions. However, the extreme northwest and southeast show a JJ contribution to annual mean of 11% to 22% (Nicholson and Palao 1993, p. 374).

Nicholson and Palao (1993) also correlated sub-Saharan AS and JJ rainfall to annual rainfall in order to approximate the contribution of JJ and AS rainfall to interannual variability. They found AS accounts for 65 to 80% of the interannual variability. JJ/annual rainfall correlations are insignificant in much of the northern Sahel. However, in other areas, JJ rainfall accounts for 40 to 60% of the interannual variability. JJ and AS rainfall are not significantly correlated except, perhaps, in the extreme northwest region of the Sahel (Nicholson and Palao 1993, p. 374-5).

4.2.2 Anomaly Persistence in Sub-Saharan Africa

Rainfall time series suggest that North/South and JJ/AS contributions to annual rainfall and to interannual variability differ significantly. Time series also show that similar distinctions apply to persistence behavior. As revealed in Figures 4-2 and 4-3, rainfall persistence differs between the North and South and between JJ and AS. AS rainfall persistence exceeds JJ rainfall persistence in both the North and South. Overall, persistence is greatest in the South during AS. This section addresses differences in rainfall persistence as evidenced via visual inspection of the time series and via correlation scale calculations. These results support findings by Nicholson and Palao (1993) who also note stronger AS persistence.

Before discussing rainfall anomaly persistence further, it is helpful to define "wet" years and "dry" years reflected in both time series. Wet years are those years exhibiting predominantly above-average rainfall anomalies, while dry years are those years showing predominantly below-average rainfall anomalies. In North JJ and AS and in the South JJ, wet years extend from 1959 to 1969, while dry years include 1970 to 1989.[1] In South AS, the wet year period is longer. The wet period extends from 1959 to 1971, while the dry year period lasts from 1972 to 1989.[2]

The persistence of negative rainfall anomalies is greatest in AS in both the North and the South. This is evident from visual inspection of the time series. During the wet period, JJ and AS show roughly the same number of years with above-average rainfall. The dry period scenario is similar. During the dry period, JJ and AS contain approximately the same number of years with anomalously low rainfall. However, the strength of the wet and dry-year anomalies in JJ and AS differ considerably. Above-average wet-year anomalies and below-average dry-year anomalies in AS are clearly stronger than those in JJ.

Correlation scale results (Table 4-2) further indicate rainfall anomaly persistence.

[1] 1988 and 1989 do show positive rainfall anomalies, however, these anomalies reflect only a temporary departure from the negative anomaly trend.

[2] See above footnote.

North Correlation Scale Values*		
Parameter	JJ	AS
Rain (North)	1.3	2.8
Rain (South)	1.3	4.1

Calculated at a maximum of 8 lag

Table 4.2: Rainfall Correlation Scale Values

Correlation scale values are defined as follows:

$$\theta = \int_{\tau=0}^{\infty} \rho(\tau) d\tau \tag{4.1}$$

where $\rho(\tau)$ is the autocorrelation function at lag τ. For example, if an exponential correlation function with scale parameter T is used, then

$$\rho(\tau) = e^{-\tau/T} \tag{4.2}$$

and $\theta = T$

Thus, the larger the correlation scale, the more persistent the time series. Correlation scales shown in Table 4-2 were calculated up to a maximum lag of 8 years beyond which there is no significant serial correlation. As can be seen in this table, rainfall exhibits more persistence in AS than in JJ. This is true for both the North and South and supports Nicholson and Palao (1993) who also note higher AS rainfall persistence.

Lack of persistence during JJ may result from a random onset of the rainy season. During these rainy season months, random onset of rain events becomes important in determining rainfall variability. Stronger persistence during AS may reflect the enhanced effects of land surface feedbacks during the later rainy season. In AS, the general circulation features that govern rainfall variability are well established. Such feedbacks are discussed further in Section 4.3.6. In summary, JJ and AS exhibit different rainfall behavior. AS provides a greater contribution to annual rainfall, a greater contribution to interannual variability, and stronger anomaly persistence.

4.2.3 Temporal and Spatial African Rainfall Patterns

It is interesting to relate the spatial and temporal characteristics of West African rainfall to those found elsewhere in the continent. Variations in rainfall fluctuation frequency and spatial coherence in common patterns of rainfall anomalies provide information important for understanding drought-forcing mechanisms. The discussion below addresses differences in rainfall variability throughout Africa and common

modes of spatial coherence in rainfall anomalies.

As noted above, persistent anomaly trends characterize rainfall in much of West Africa. This persistence is not found in other areas of the African continent. In the Kalahari region, as in most of the rest of the continent, the longest dry periods generally last only five or six years. This higher frequency variability occurs on time scales of 2.3, 3.5, and 5 to 6 years and corresponds to time scales characterizing the quasi-biennial oscillation, SST fluctuations, and ENSO (Nicholson 1988). Unusual temporal coherence in West Africa, is believed to reflect local, positive feedback mechanisms in this region (Nicholson 1988). Nicholson contends that large-scale forcing initiates drought, while local feedback mechanisms are responsible for rainfall anomaly persistence (Nicholson 1989, p. 81).

Some researchers have identified a relatively small number of commonly occurring large-scale rainfall anomaly spatial patterns. These patterns are useful in relating the drought to rainfall intensity, the position of the ITCZ, and the general circulation. According to Nicholson, the most common spatial mode shows negative rainfall anomalies in the subtropics with positive rainfall anomalies in the equatorial latitudes. This pattern occurred during seven years between 1910 and 1967, all years between 1968 and 1973, and somewhat in 1982. Another frequently-occurring pattern is below-average rainfall continent-wide. A good example of this is found in 1983. The inverse of these patterns comprises the remaining common patterns: above-average rainfall in the subtropics with below-average rainfall at the equator (1950-59) and above-average rainfall throughout the continent (1961) (Nicholson 1988, p. 53).

Overall, researchers such as Nicholson maintain that the unique spatial and temporal coherence that characterizes rainfall over the African continent indicates that "large-scale circulation changes, and not regional-scale phenomena, impose the dominant control on rainfall variability" (Nicholson 1989, p. 81).

4.3 Vapor Flux and Wind Data

As documented above, the climate system over West Africa is complex and the studies aimed at understanding this system and how it relates to drought are largely inconclusive. Each researcher contributes a piece of the puzzle. But sometimes the pieces are contradictory and the puzzle has yet to come together to form a coherent picture of drought-forcing mechanisms. This research aims to relate local parameters such as rainfall and water vapor flux, to an index of the general circulation (EOF time series of the 500 mb ω field). The remaining sections describe the data, methodology, and results obtained from the analysis. Findings reveal interesting relationships between climate parameters and also highlight important differences between North and South regions and between JJ and AS periods.

This section describes the parameters analyzed and the data used in the investigation. Section 4.3.1 discusses water vapor flux. Section 4.3.2 addresses vertical wind velocity, and Section 4.3.3 describes the dataset used in the analysis.

4.3.1 Vertically integrated vapor flux vector

As mentioned in Chapter 2, the vertically integrated horizontal vapor flux vector $\vec{Q}$ is obtained by vertically integrating the meridional and zonal flux over pressure levels. These meridional and zonal $\vec{Q}$ components can be time-averaged to yield:

$$\overline{Q}_\lambda = \int_0^{p_o} \overline{qu}\frac{dp}{g} = \int_0^{p_o} (\overline{q})(\overline{u})\frac{dp}{g} + \int_0^{p_o} \overline{q'u'}\frac{dp}{g} \tag{4.3}$$

and

$$\overline{Q}_\phi = \int_0^{p_o} \overline{qv}\frac{dp}{g} = \int_0^{p_o} (\overline{q})(\overline{v})\frac{dp}{g} + \int_0^{p_o} \overline{q'v'}\frac{dp}{g} \tag{4.4}$$

In Equations (4.3) and (4.4), p_o is surface pressure, g is gravitational acceleration, and Q_λ and $Q\phi$ are the zonal and meridional components of $\vec{Q}$. $\vec{Q}$ has dimensions $MT^{-1}L^{-1}$. This quantity reflects the net water vapor transport above a point on the Earth's surface (Peixoto and Oort 1992).

4.3.2 Radiosonde Data

Chapter 2 discusses aerological data used in the Africa study. This section briefly overviews possible errors or discrepancies arising from observation, spatial distribution, and analysis of the data.

Observational errors associated with the data relate to instrument variability and calibration, the diurnal cycle, and resolution of the boundary layer. Radiosonde instrumentation errors can result from manufacturing variability and calibration loss Elliot and Gaffen (1991). In addition, the limited number of daily soundings do not sufficiently capture the diurnal cycle and fail to reflect variations during unsampled hours. Brubaker *et al.* (1993) points out that radiosonde measurements do not resolve the planetary boundary layer - the layer containing most of the Earth's water vapor. Furthermore, data at 1000 mb is generally less reliable than data at other pressure levels (Fontaine *et al.* 1995, p. 1504).

Data scarcity poses the biggest data problems for Africa. Station coverage, as displayed in Figure 4-4, is limited. Figure 4-4 shows the maximum possible number of radiosonde station locations. Many of these station locations represent partial or no coverage for many of the years studied.

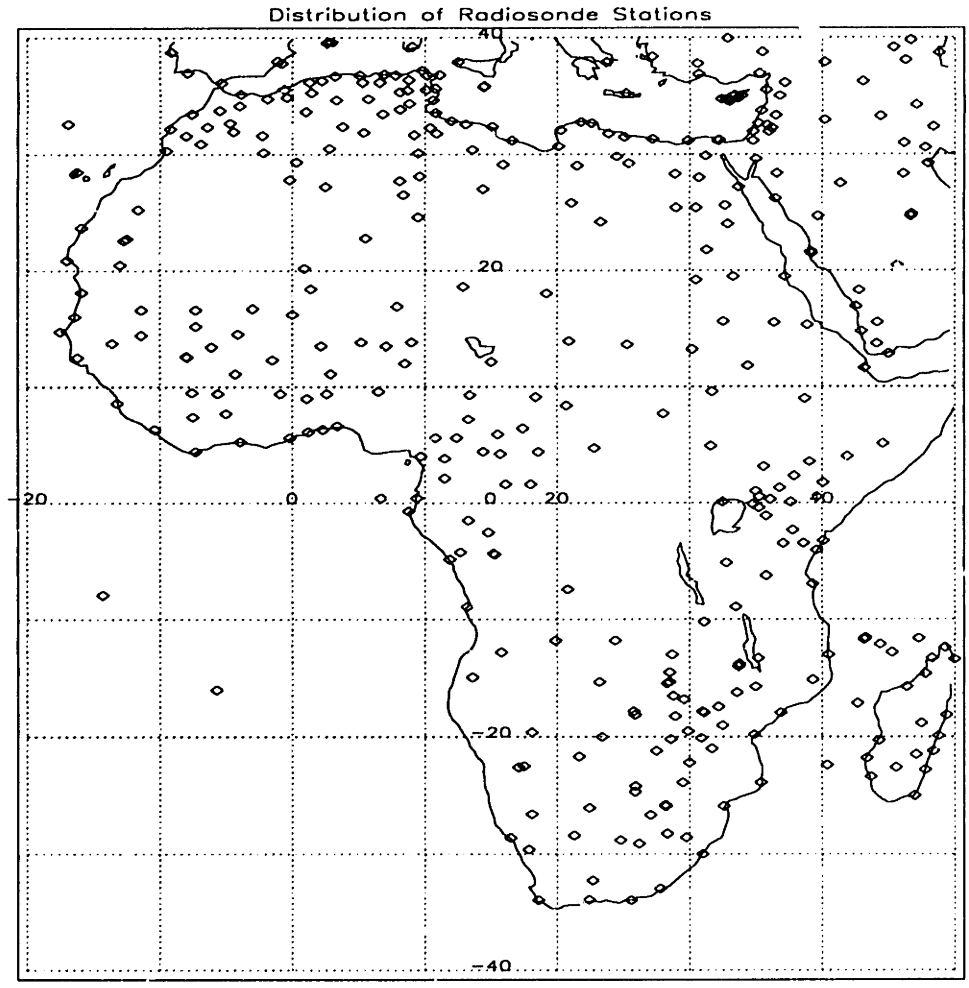

Figure 4-4: Radiosonde Station Locations

4.4 Water Vapor Flux Analysis

Analysis of water vapor transport over West Africa provides insight into features of the general circulation and their relationship to West African drought. This section discusses, zonal and meridional water vapor flux characteristics as well as the interannual variability of water vapor transport over West Africa. Sections 4.4.1 and 4.4.2 present wet and dry-year differences in zonal and meridional vapor flux, respectively. Section 4.4.3 examines interannual variability in zonal and meridional vapor flux.

4.4.1 Wet/Dry Comparisons of Zonal Vapor Flux

Figures 4-5 and 4-6 illustrate JJ and AS water vapor flux at region borders for wet and dry years. The dotted line represents the border of the North and South regions combined while the bars indicate the magnitude and direction of water vapor flux at region boundaries.

To determine the magnitude of each of the "fluxbars" pictured in figures 4-5 and 4-6, total motion vectors were integrated vertically using trapezoidal rule integration at all node points surrounding region boundaries. Meridional components were evaluated along northern and southern boundaries, while zonal components were evaluated along east and west boundaries. This integration yielded flux vectors in units of $M/(T * L)$. Flux vectors were then integrated horizontally over discrete segments of the region boundary to yield a mass-per-unit time value of water vapor traversing each boundary segment. These calculations were carried out for each year of the study. Mean wet and dry-year fluxbars were determined by averaging fluxbars over wet and dry years. Wet and dry years in this case were not based on the anomaly time series discussed in Section 4.2. Instead, wet and dry-year designations were based on the conventional dry-year period assumed to begin in 1968 (Nicholson 1988). In this dataset, wet years extend from 1959 through 1967. Dry years extend from 1968 to 1989.

Fluxbar diagrams build upon previous research by revealing important differences between JJ and AS periods. These figures also illustrate several wet and dry-year

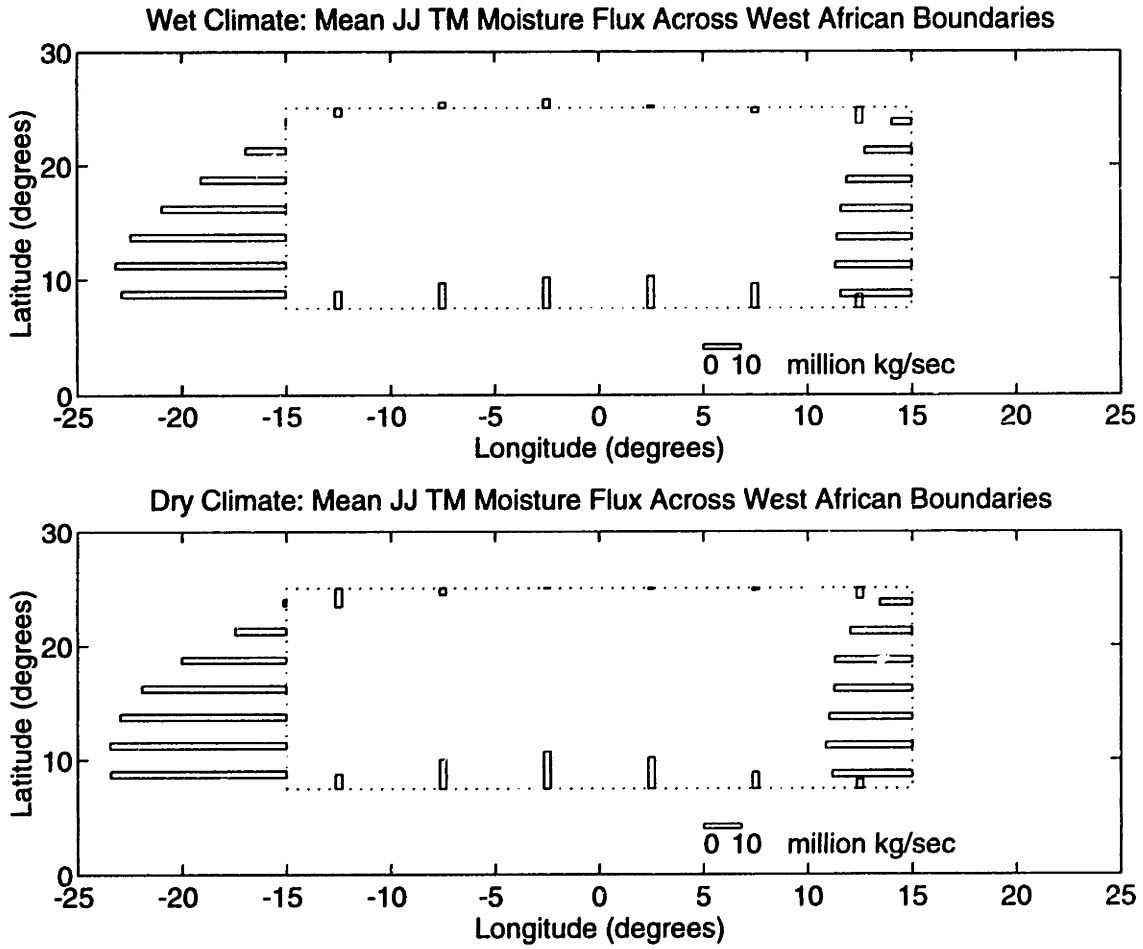

Figure 4-5: JJ Moisture Flux

contrasts in the general circulation features discussed above. Figures 4-5 and 4-6 clearly show that easterly flow dominates motion patterns over sub-Subsaharan Africa. Given that atmospheric moisture is concentrated at lower altitudes, it appears that the easterly motion pictured in Figures 4-5 and 4-6 reflects water vapor carried by systems embedded in the AEJ. It is evident from Figures 4-5 and 4-6 that the magnitude of easterly flux is generally greatest in the South and in AS. Stronger zonal flux in later summer months is also noted in Cadet and Nnoli (1987). These authors observed that, as the summer progresses, the moisture carried by the trade winds north of the equator increases. In addition, both JJ and AS zonal flux is greater in dry years than in wet years. This finding of a stronger AEJ during dry years supports the thermal wind and subsidence arguments presented by Newell and Kidson (1984).

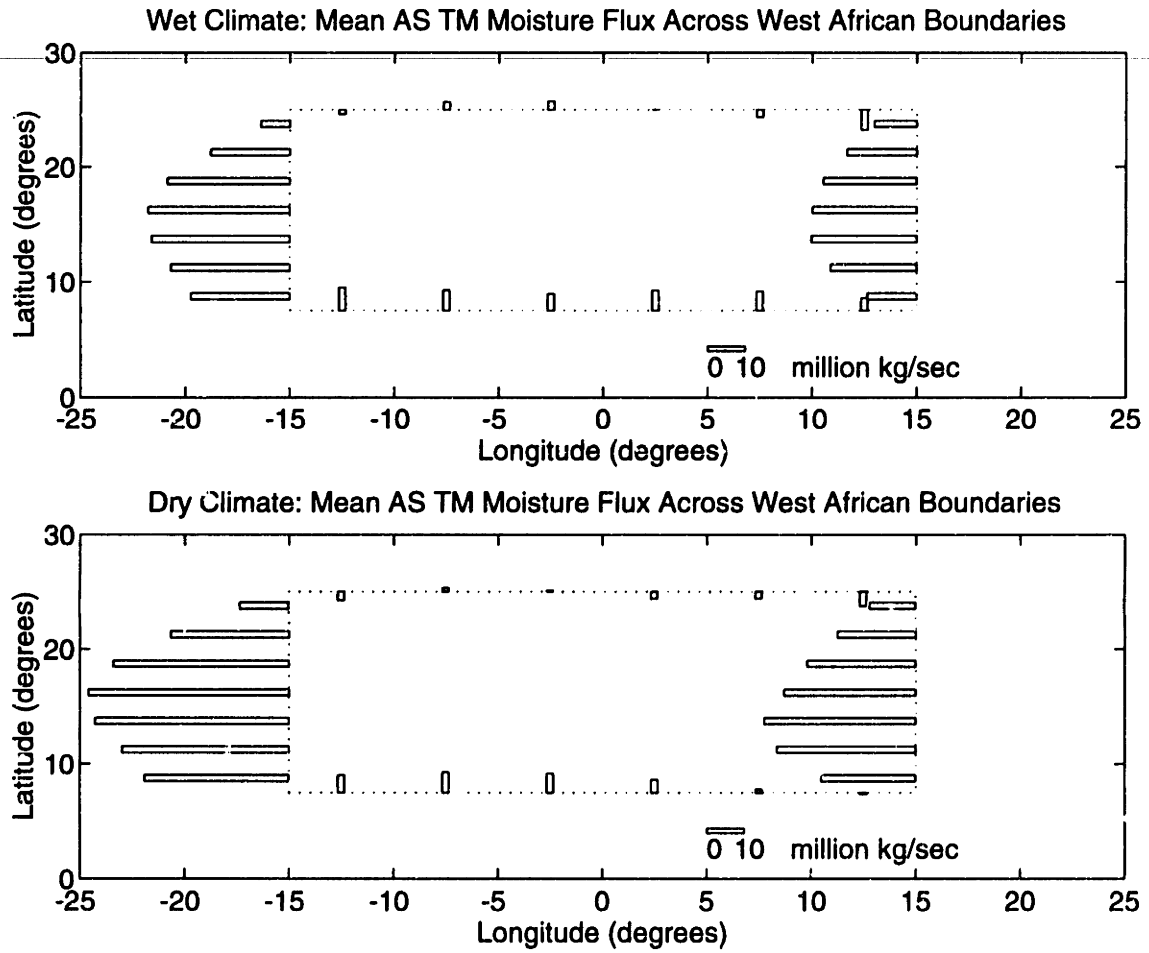

Figure 4-6: AS Moisture Flux

4.4.2 Wet/Dry Comparisons of Meridional Vapor Flux

Figures 4-5 and 4-6 also reveal important characteristics of meridional vapor flux. A JJ/AS contrast, for example, characterizes meridional flux at southern border of the region studied (around 7.5° N latitude). This flux is larger in JJ than in AS (a finding similar to those by Cadet and Nnoli (1987)). Cadet and Nnoli (1987) studied water vapor flux along an equatorial section parallel to the Gulf of Guinea Coast. They found that the vertically integrated flux magnitude between the surface and 850 mb decreases during the summer. This decrease in meridional flux magnitude between JJ and AS probably reflects northward movement of the southerly branch of the Hadley cell as the rainy season progresses (Cadet and Nnoli 1987, p. 599-600).

Figures 4-5 and 4-6 also indicate that both JJ and AS meridional flux weaken slightly between wet and dry years. Originally this type observation may have been explained as southward displacement of the ITCZ. This explanation, however, does not account for the continent-wide coherence of rainfall anomalies and has been refuted by several authors (Nicholson 1988, p. 53). Instead, the decrease in meridional flux between wet and dry years may indicate a weakening or contraction of the ascending branch of the Hadley cell as noted in Nicholson (1981).

4.4.3 Interannual Variability of Water Vapor Flux

Figure 4-7 shows a time series of JJ and AS meridional flux at 7.5° N latitude. The lines overlaying the graphs represent the wet-year and dry-year means in each season. The meridional flux shown in these time series was determined by finding the total meridional flux of water vapor passing the 7.5° N latitude boundary per unit time and dividing by the length of this boundary.

Notable features of Figure 4-7 involve JJ and AS differences as well as wet/dry year differences in meridional vapor flux. The decrease in meridional flux magnitude between JJ and AS probably reflects northward movement of the southerly branch of the Hadley cell. Once again, this agrees with the findings of Cadet and Nnoli (1987). As mentioned above, their analysis of water vapor flux fields at different

sections near the Gulf of Guinea decreased over the summer months, thus, reflecting the northward movement of the Intertropical Convergence Zone (ITCZ) (Cadet and Nnoli 1987, p. 581). Furthermore, in both JJ and AS the mean flux decreases between wet and dry years. The difference in mean values between wet and dry periods is statistically significant at a 95% confidence interval and corresponds to the wet/dry contrast pictured in Figure 4-6. Differences in meridional flux mean values may reflect contraction of the ITCZ during drought years as suggested by Nicholson (1981).

Figure 4-8 shows JJ and AS meridional flux at 15° N latitude. As found in Figure 4-7, the differences between JJ and AS most likely reflect northward movement of the ITCZ during summer months. During JJ, the convergence zone is to the south of 15° North and northerly flux dominates the meridional motion. During wet AS years, the northward movement of the ITCZ is apparent as southerly flux is the dominant motion. This process is similar to that observed by Cadet and Nnoli (1987). At 22° N Cadet and Nnoli (1987) found that water vapor flux is generally northerly at the beginning of the summer, but gradually becomes more southerly as the summer progresses and the southerly monsoon movement dominates.

Figures 4-7 and 4-8 contrast wet and dry-year behavior. Wet and dry-means for both JJ and AS differ significantly at a 90% confidence level. A prominent wet/dry year difference concerns changes in the strong wet-year southerly flux at 15°. This flux notably weakens during dry years and may provide another example of the ITCZ contraction that Nicholson (1981) suggests.

Figures 4-9 and 4-10 show time series of mean JJ and AS zonal flux in the North and South. Total zonal flux is averaged across seven north-south transects that extend between 7.5° N latitude to 25° N latitude and are located at 5° degree intervals between 15° E longitude and 15° W longitude. The magnitude of mean zonal flux increases between wet and dry years in both the North and South AS. However, only the South AS wet and dry means show a significant difference at the 95% confidence level. Zonal flux increases during dry years provide further evidence to support evidence of increased AEJ flow during drought Newell and Kidson (1984).

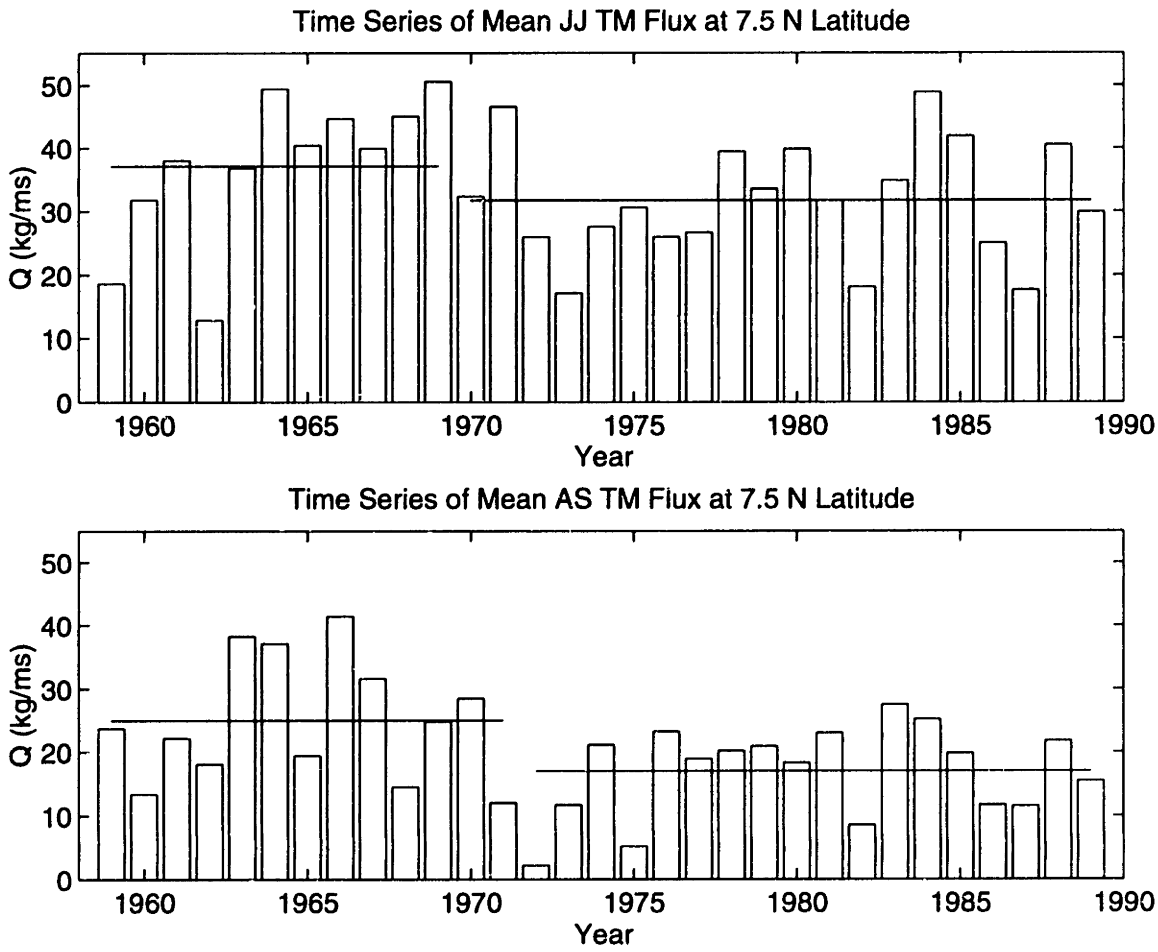

Figure 4-7: Time Series of Meridional Moisture Flux at 7.5° North

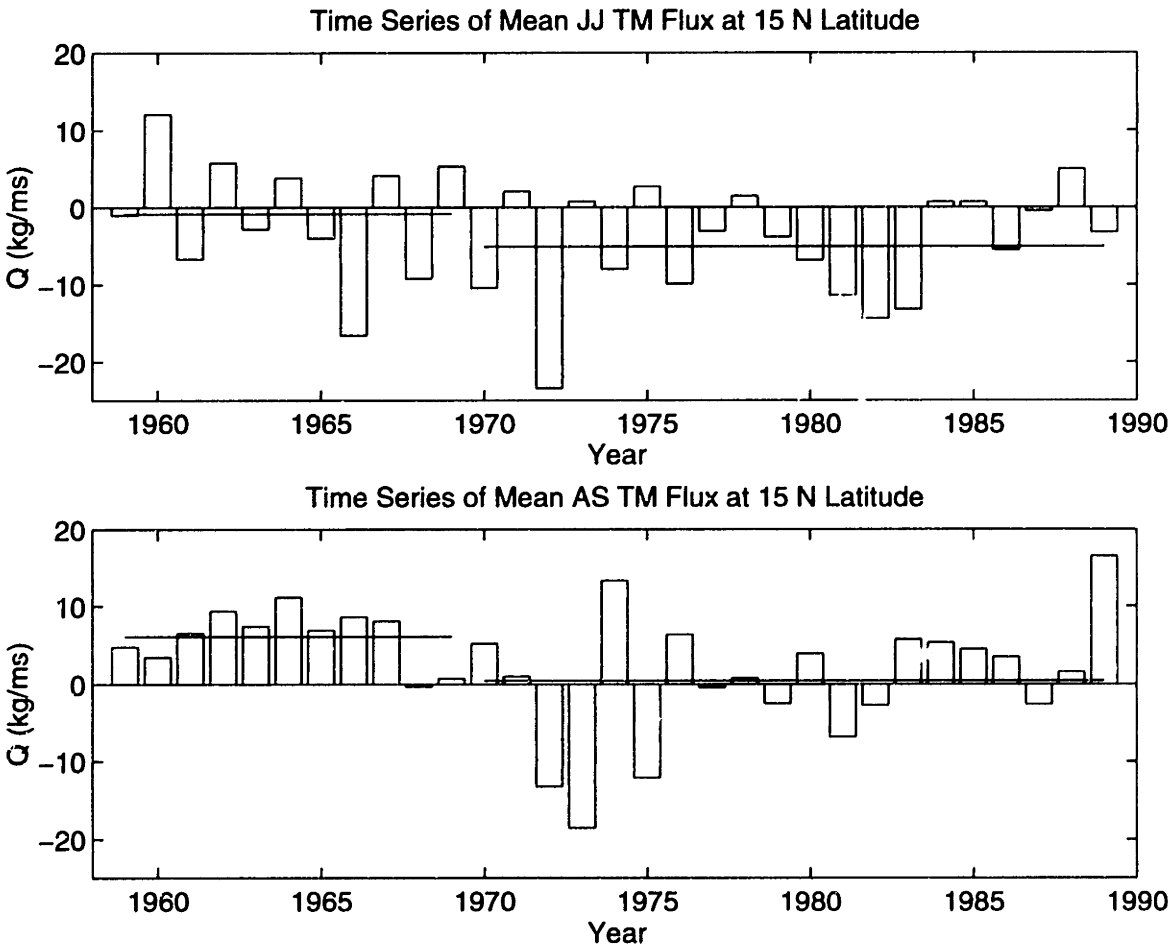

Figure 4-8: Time Series of Meridional Moisture Flux at 15° North

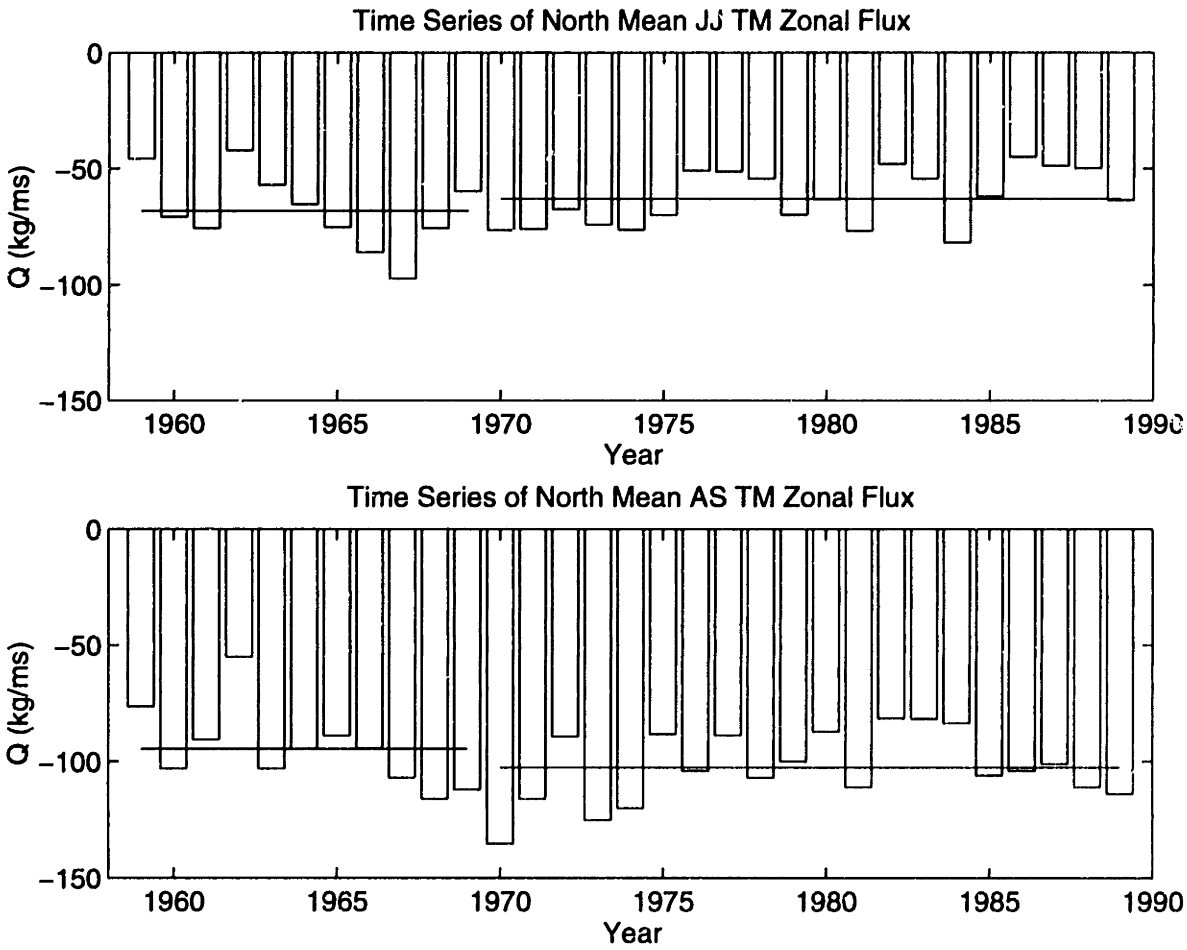

Figure 4-9: Time Series of Zonal Vapor Flux in the North

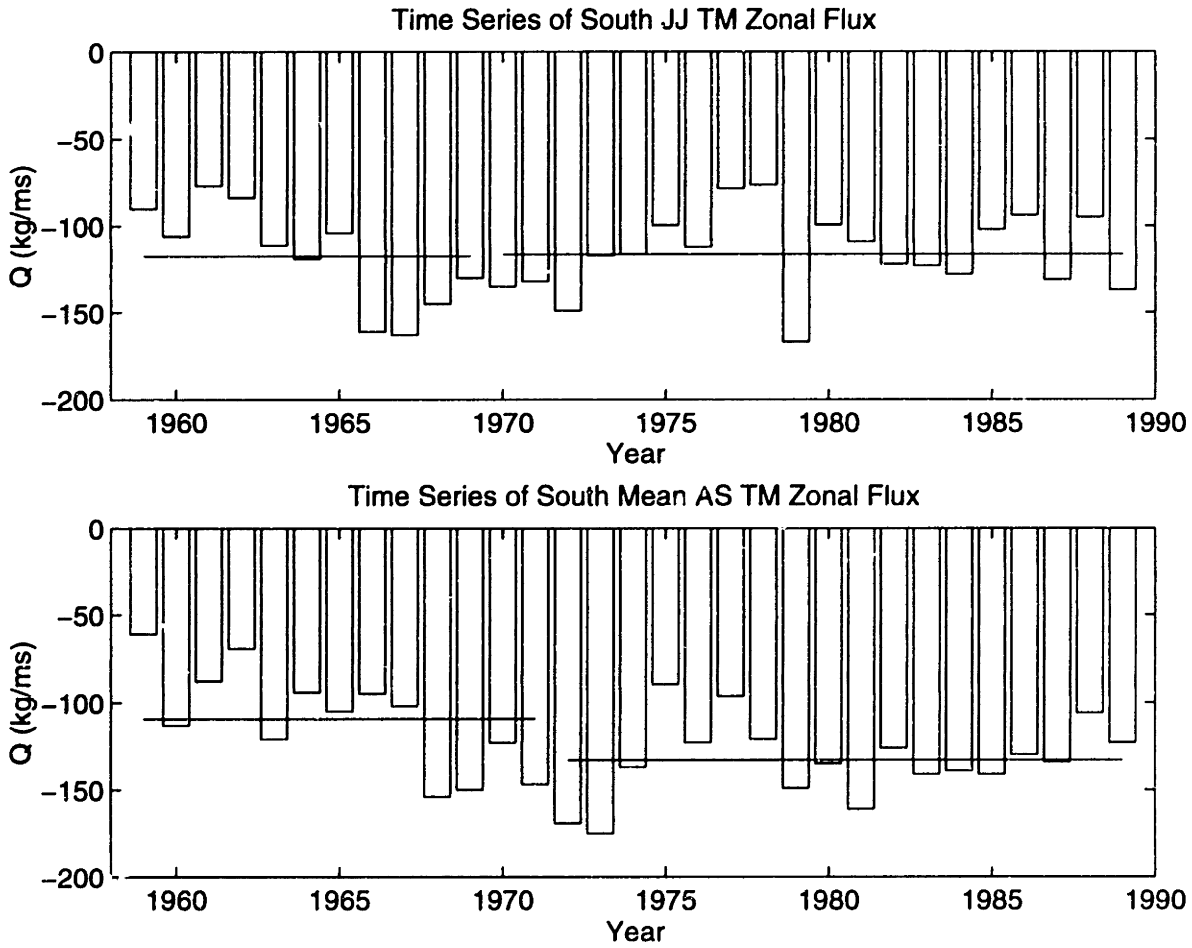

Figure 4-10: Time Series of Zonal Vapor Flux in the South

4.5 EOF Analysis of Vertical Wind Velocity

Empirical orthogonal function (EOF) (or eigenvector) analysis was used to derive a scalar index of the general circulation field from the gridded vertical velocity (ω) field. Eigenvectors were calculated from the covariance matrix of 500 mb omega values between 20° E and 50° W longitude and between 5° S and 40° N latitude.

Eigenvectors can be used in the same way as polynomials to describe patterns of data. Eigenvectors are orthogonal sets of linear coefficients that can be arranged such that the first eigenvector is the most dominant spatial pattern. The remaining patterns are orthogonal or uncorrelated.

In this analysis, eigenvectors were constructed for 31 omega arrays, one array for each of the 31 years of the study. Each array contains omega values corresponding to 285 grid node locations. Each 285 x 1 array is represented by a column vector, $\mathbf{p}_n$. where n = 1 to 31. The 31 vectors were combined to form a 285 x 31 matrix, **P**. Thirty-one year means were removed from each element of the matrix to form matrix **F**. EOF calculations were performed on the covariance matrix formed from matrix **F** and its transpose. These calculations are presented in Appendix B.

Varimax rotation results show that the EOF patterns shown below are robust. Varimax rotation is an orthogonal rotation method. Rotation analysis based on Reymont and Jöreskog (1993) produced patterns which are very similar to those obtained from the unrotated analysis. Rotation was performed on the first 3, 5, 10, and 80 eigenvectors. Appendix C contains the resulting patterns. The rotated AS-EOF1 and JJ-EOF2 patterns show negative and positive signs opposite to those in the original figures. However, such sign changes are arbitrary and do not impact the patterns' robustness.

4.5.1 EOF Results

Eigenvector calculations yielded the JJ and AS EOF patterns shown in Figures 4-11 through 4-16. Figure 4-17 shows the percentage of the total variance associated with each eigenvector. Figures 4-14 and 4-15 show the first eigenvector patterns for JJ and

AS, respectively. The AS EOF1 pattern represents about 15% of the variance in JJ and about 17% of the total variance in AS. The patterns for JJ and AS EOF1 are similar and exhibit a strong southeast/northwest dipole. This dipole moves slightly northward between JJ and AS. The EOF2 patterns (Figures 4-13 and 4-14) reflect roughly 14% of the total variance in JJ and approximately 15% of the total variance during AS. The JJ and AS EOF2 patterns are also similar and exhibit adjacent positive and negative regions that extend from east to west across the north of the continent. The JJ EOF3 patterns (Figures 4-15 and 4-16) represent approximately 8% of the total variance while the AS EOF3 pattern reflects roughly 10% of this variance. In JJ, the EOF3 pattern shows an east/west dipole pattern, while the AS EOF3 pattern exhibits a central area of negative loading centered around 20°N latitude and 12° E longitude. This negative region is surrounded by areas of positive loading. On the other hand, the most prominent feature of AS EOF3 is the strong east/west dipole centered around 25° N latitude.

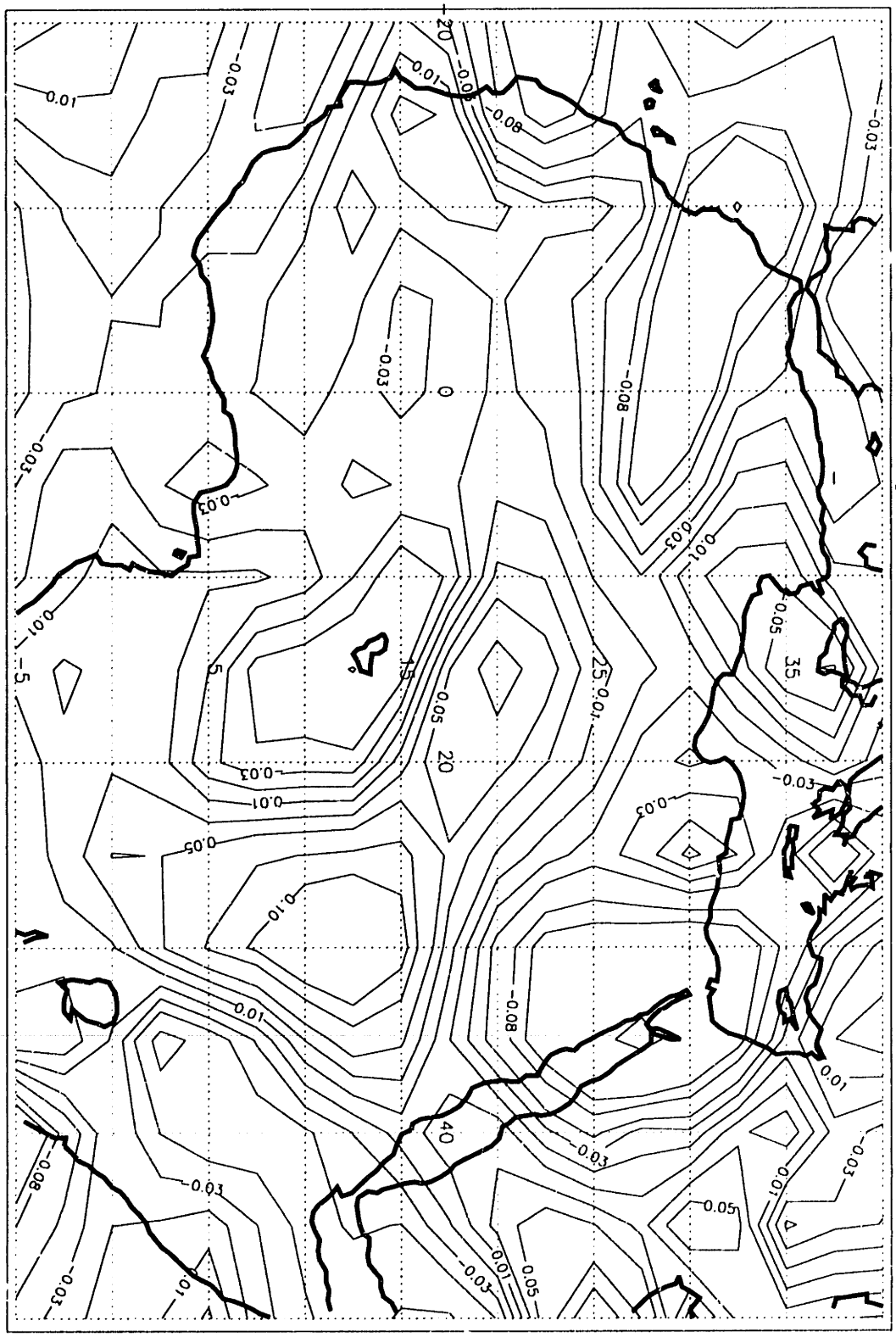

Figure 4-11: First JJ Eigenvector Pattern

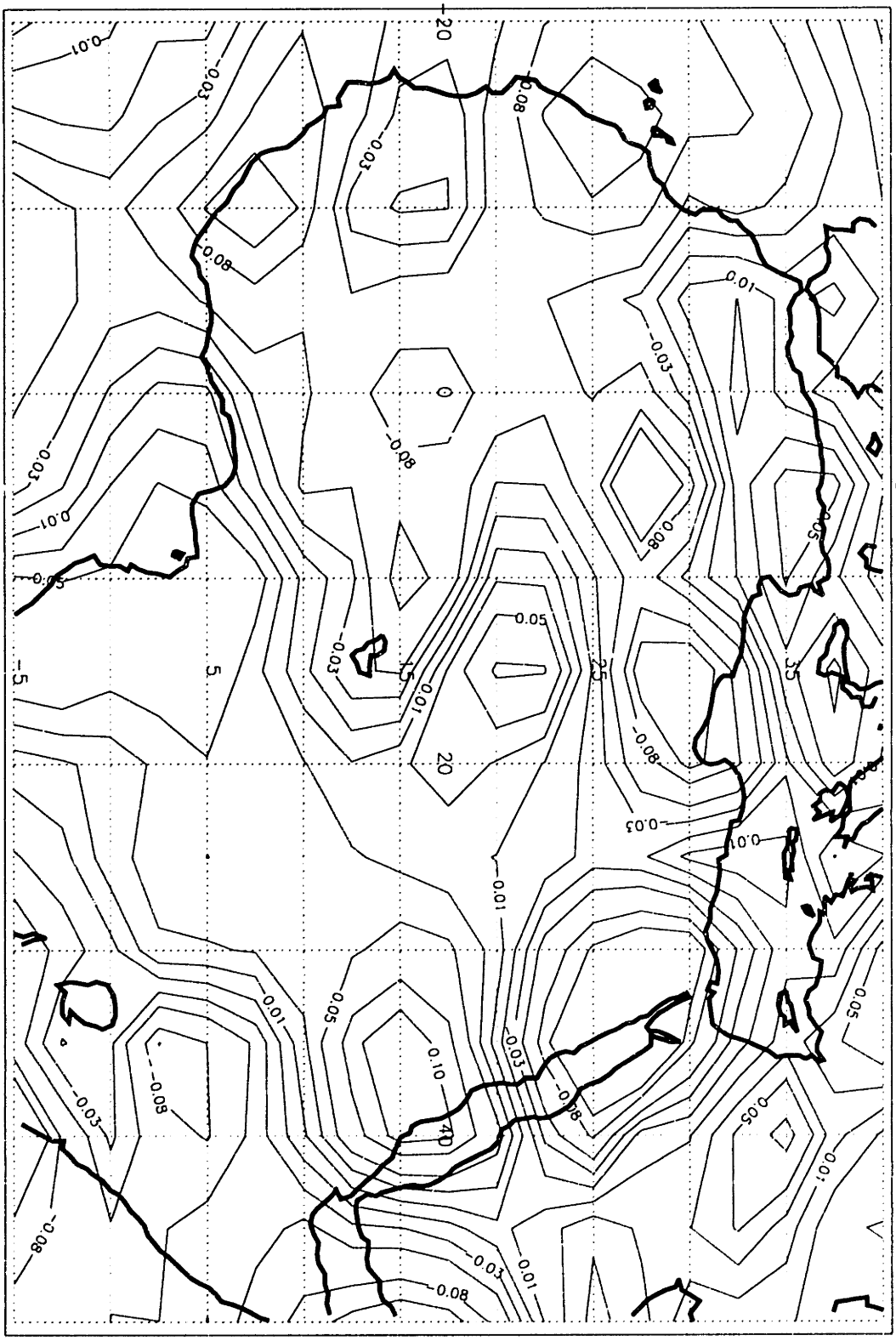

Figure 4-12: First AS Eigenvector Pattern

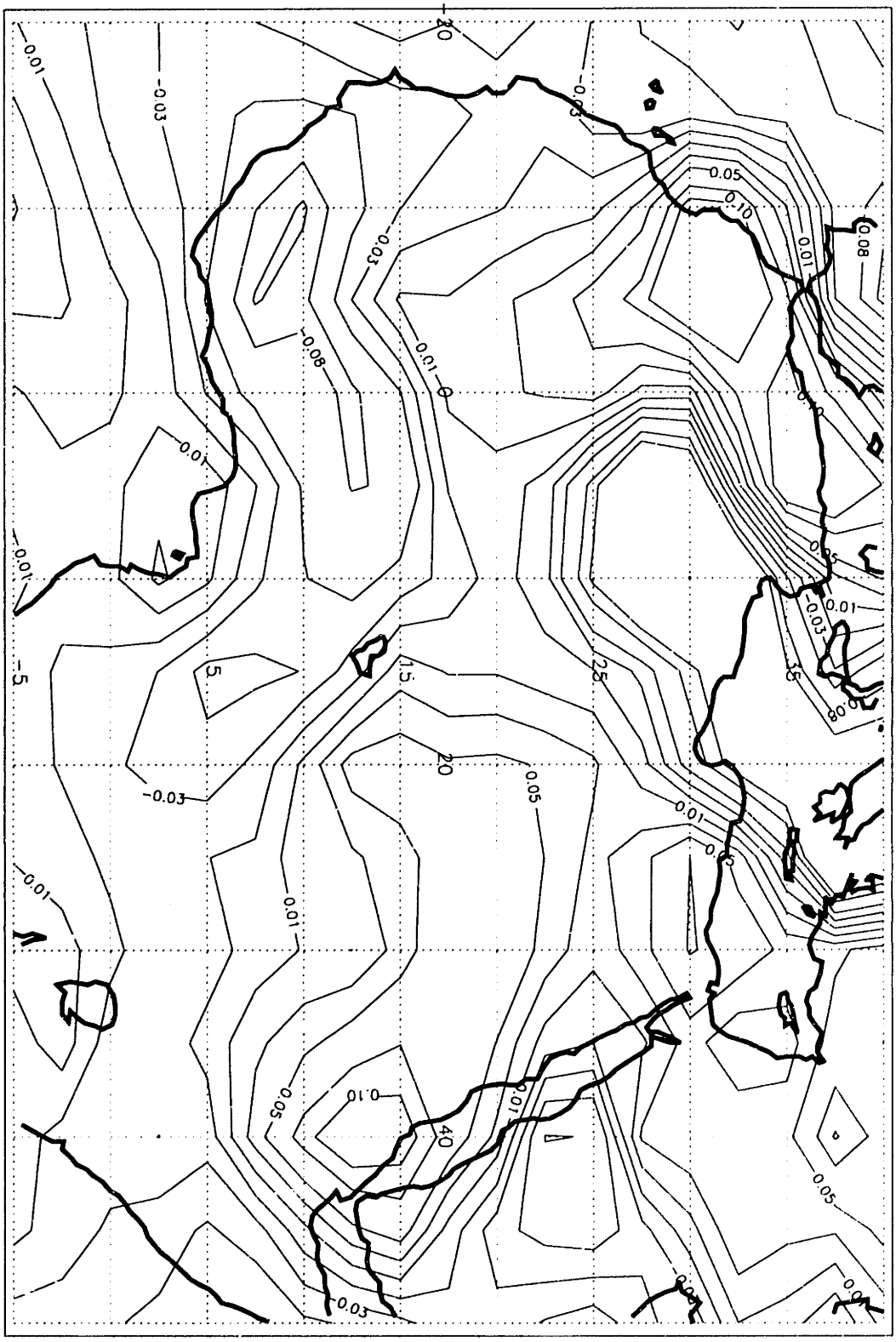

Figure 4-13: Second JJ Eigenvector Pattern

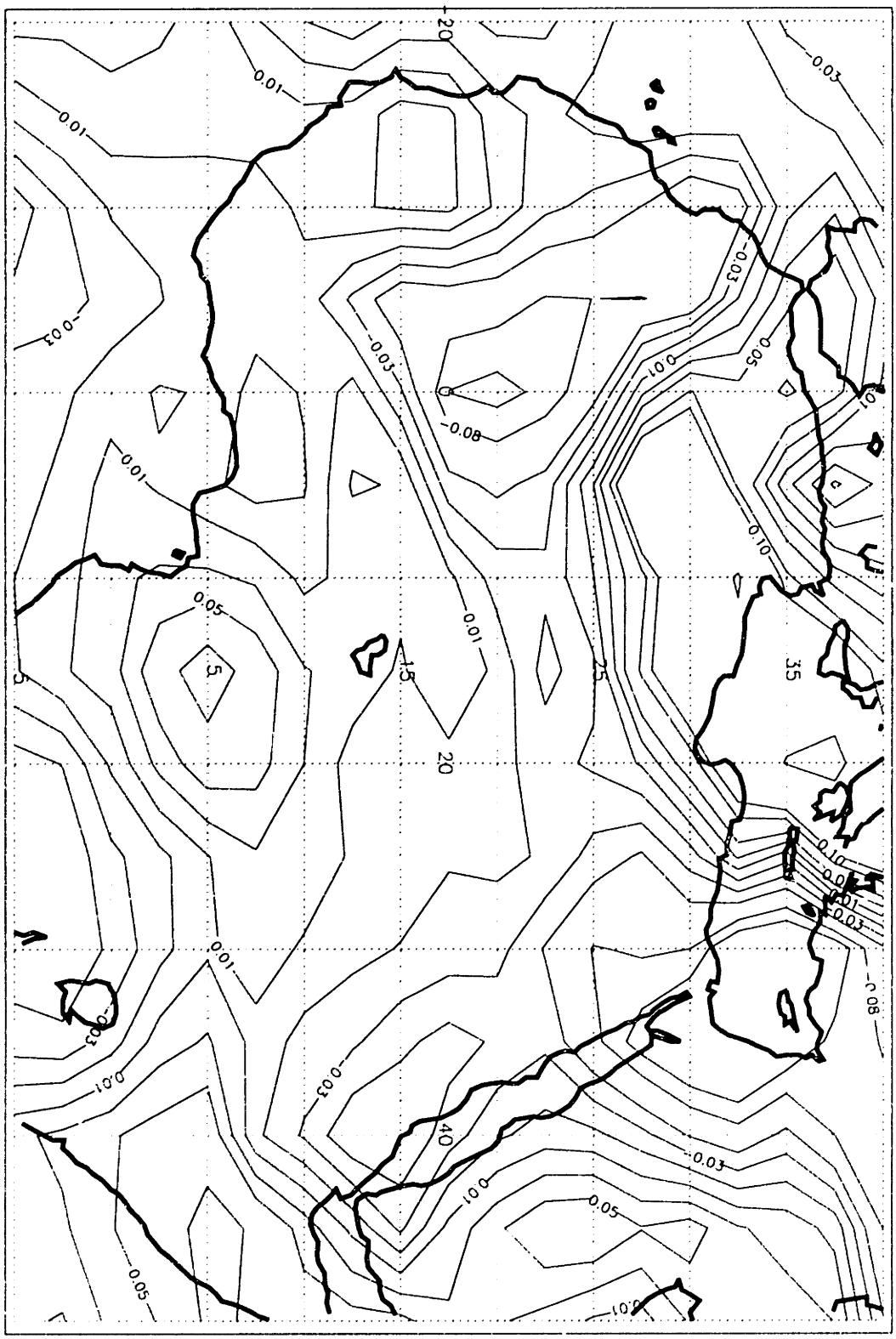

Figure 4-14: Second AS Eigenvector Pattern

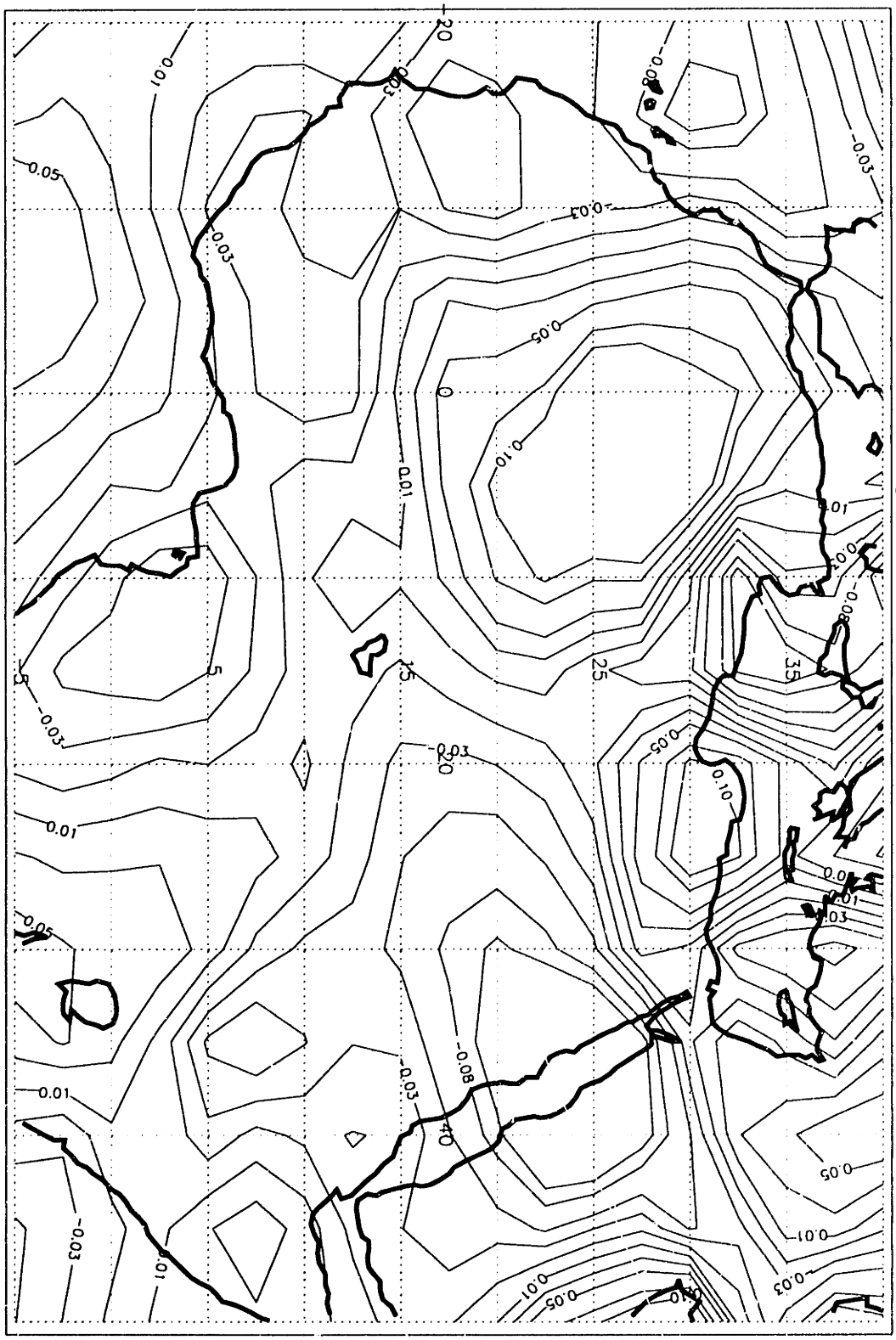

Figure 4-15: Third JJ Eigenvector Pattern

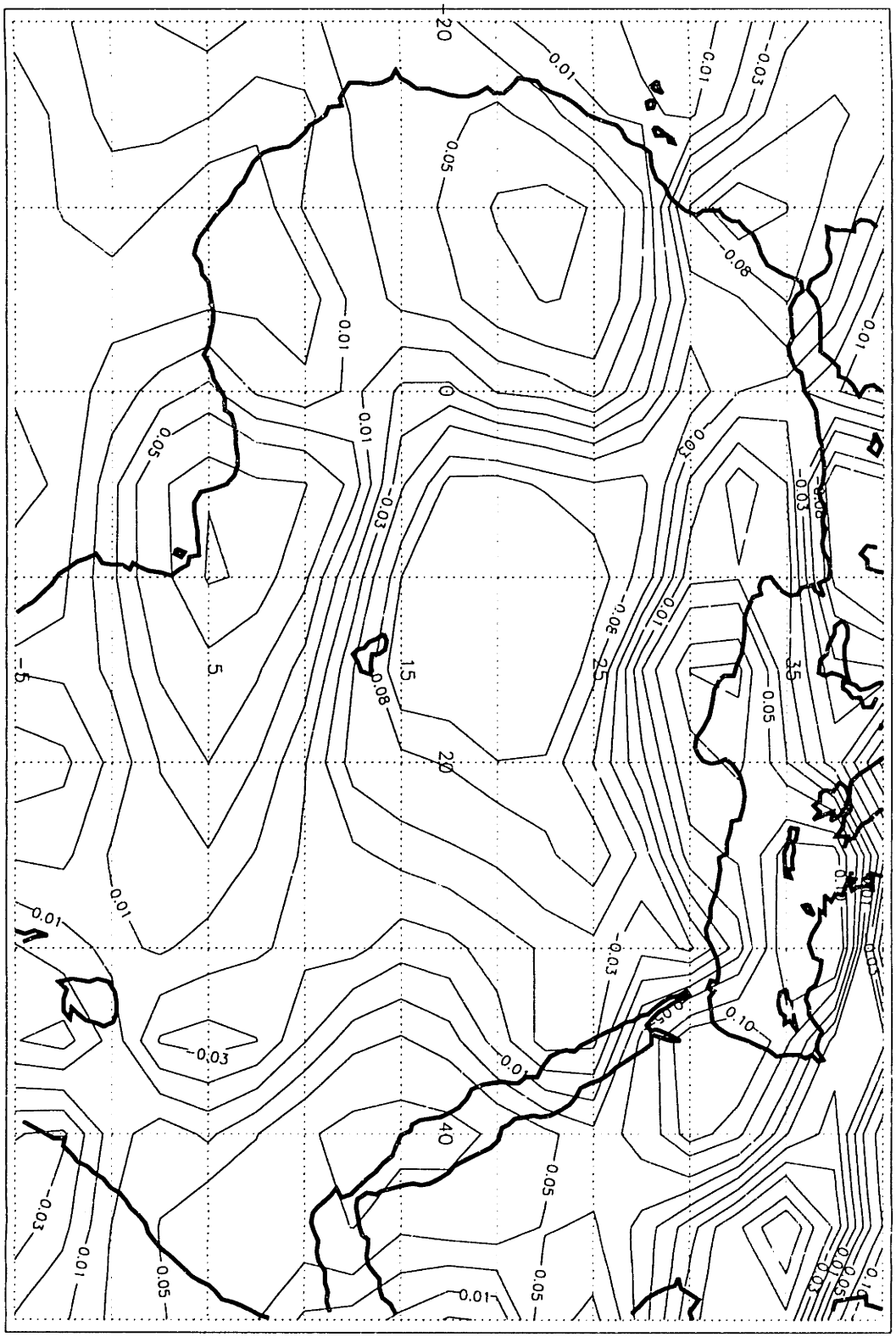

Figure 4-16: Third AS Eigenvector Pattern

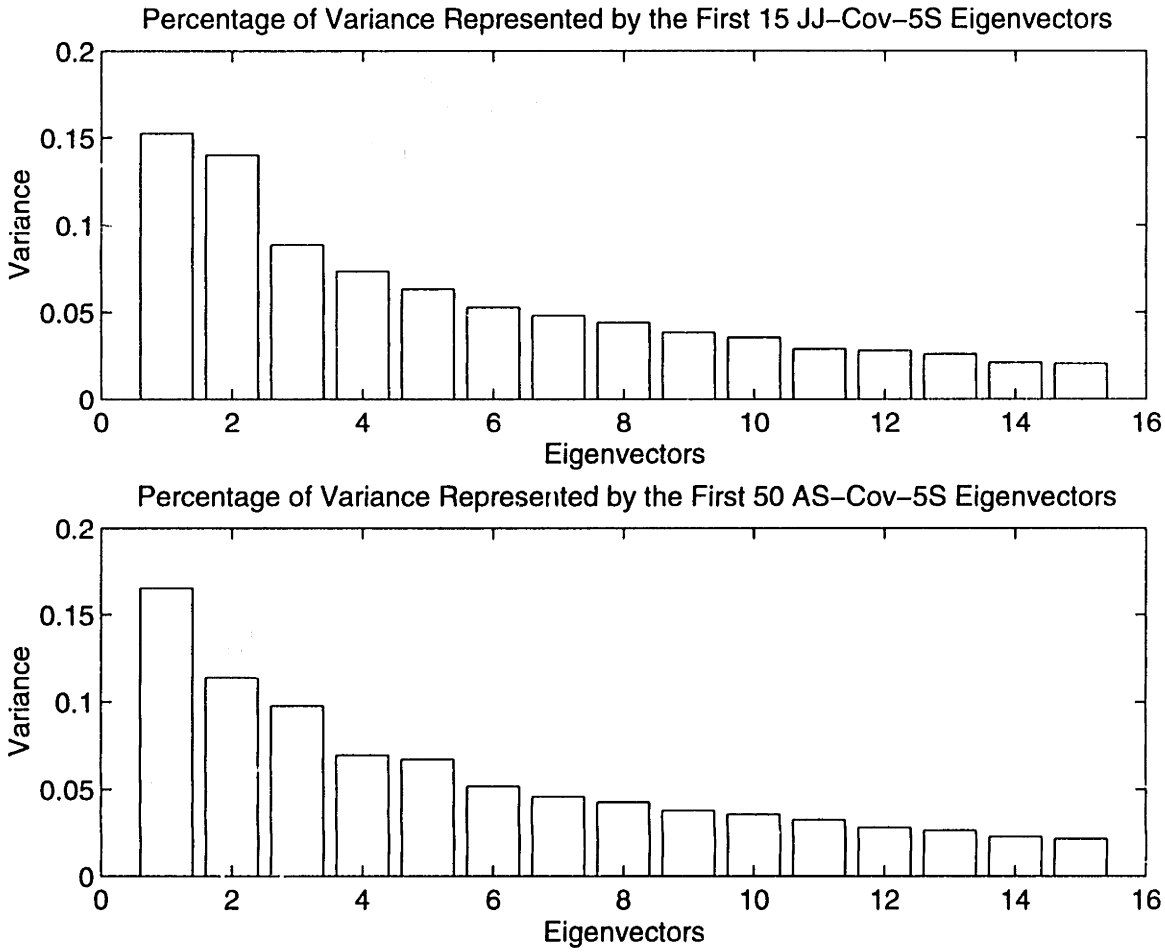

Figure 4-17: Eigenvalues for first 15 Eigenvectors

Figures 4-18 through 4-20 show JJ and AS multiplier time series for the three JJ and AS eigenvector patterns. The most prominent feature of the EOF1 time series is its strong wet and dry-year contrast. Essentially the JJ and AS time series collapse in the mid-1960s, a few years before the onset of drought in the late 1960s. The EOF2 time series in both JJ and AS exhibits a low-frequency stationary wave pattern, while the JJ and AS EOF3 time series show higher frequency fluctuation with no clear wet and dry-year distinctions.

Appendix D contains multiplier time series for rotated eigenvectors. Aside from the sign differences mentioned above, the rotated and unrotated series correspond well.

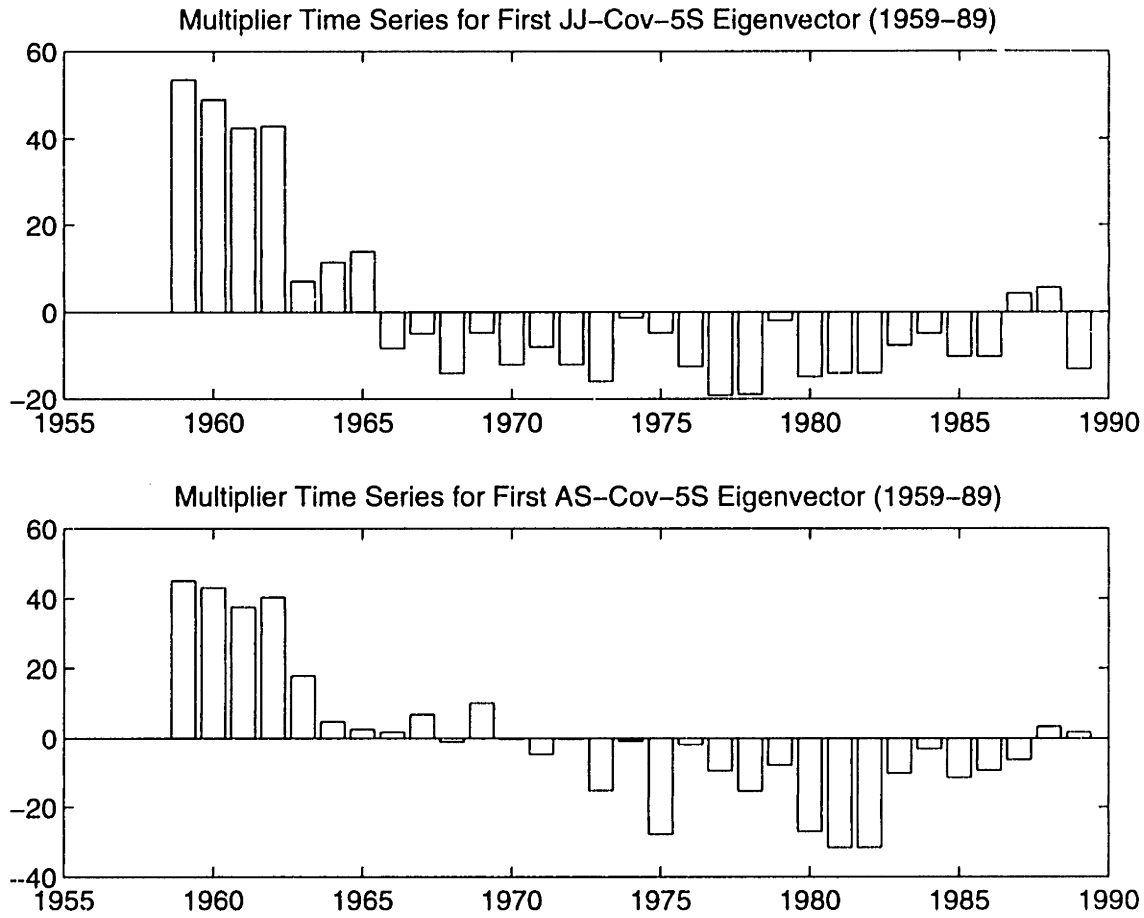

Figure 4-18: First Eigenvector Multiplier Time Series

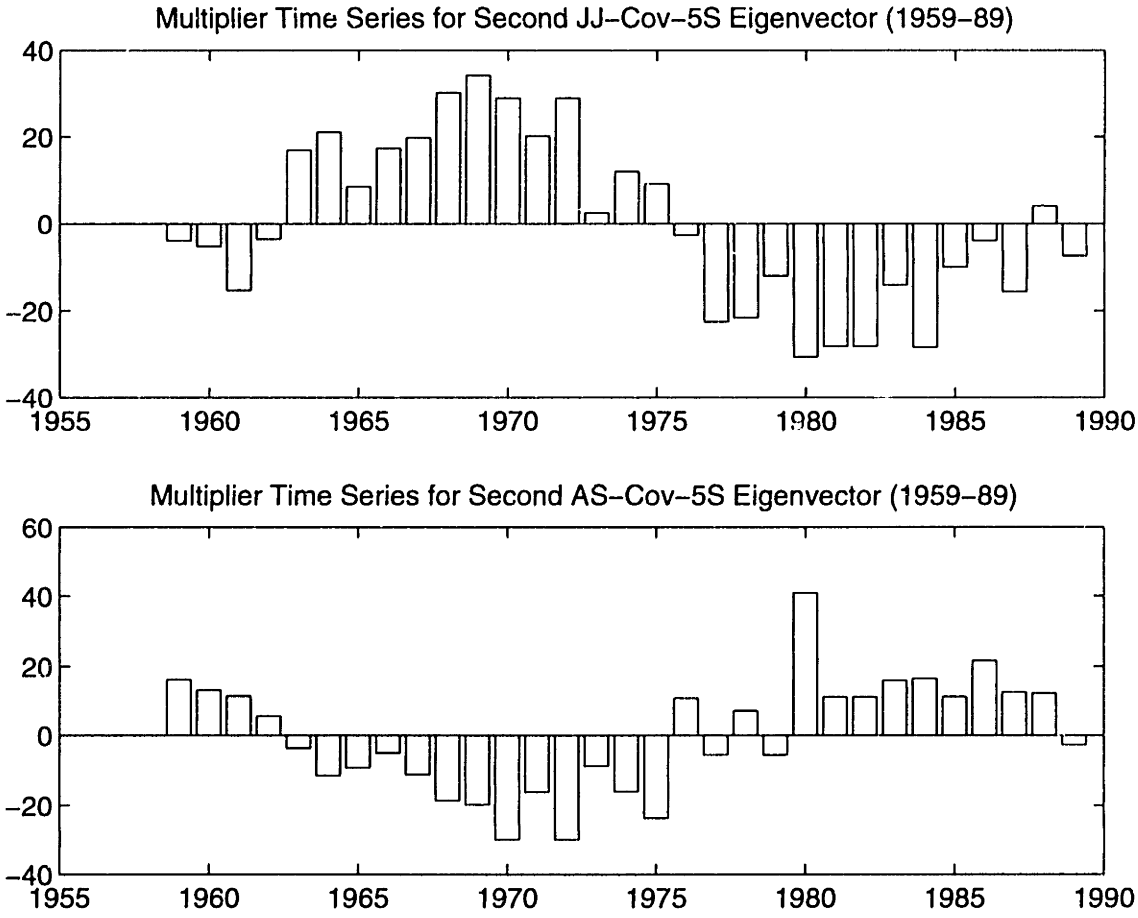

Figure 4-19: Second Eigenvector Multiplier Time Series

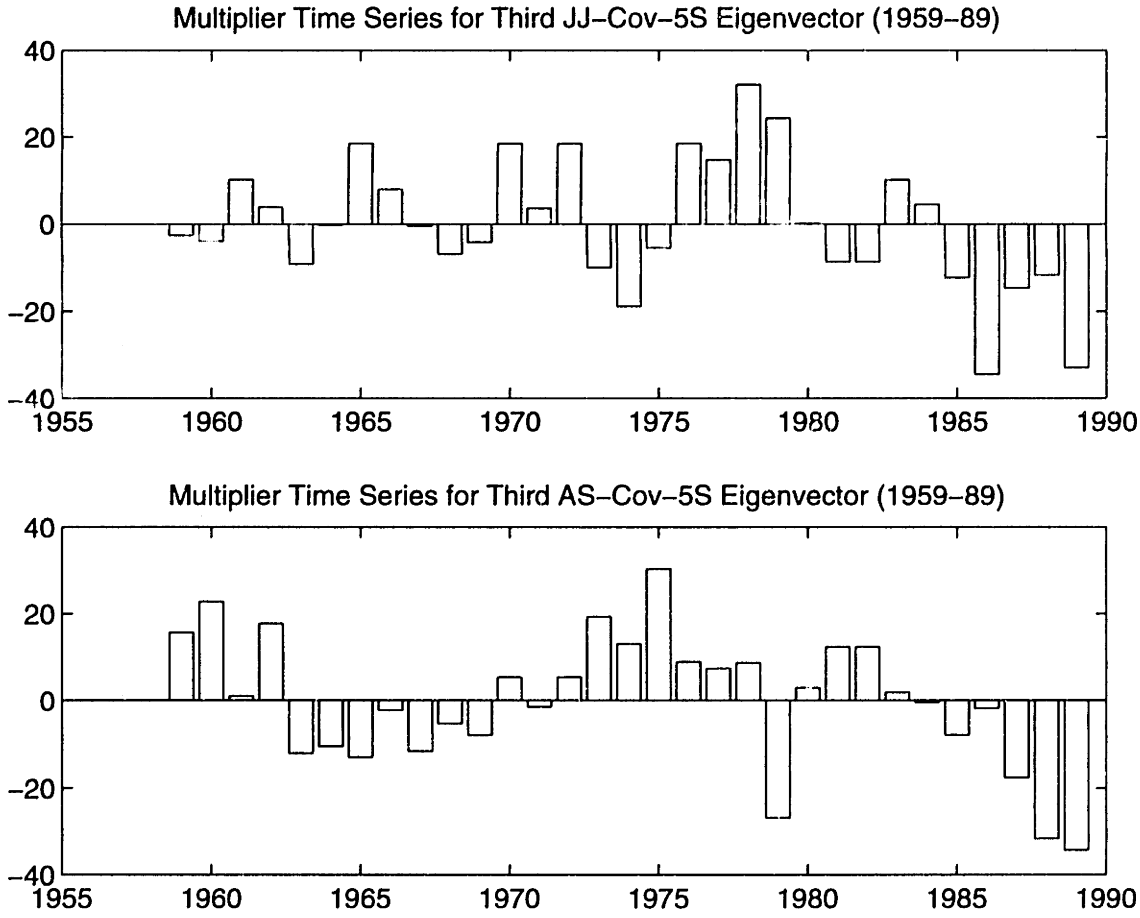

Figure 4-20: Third Eigenvector Multiplier Time Series

4.6 Correlation Coefficient and Correlation Scale Results

Relationships between rainfall, water vapor flux, and EOF time series were investigated via linear correlation coefficients and correlation scale calculations. Correlation coefficients were determined for rainfall and vapor flux times series (Section 4.6.1), for rainfall and EOF time series (Section 4.6.2), and for EOF and vapor flux time series (Section 4.6.3). Correlation scale results are presented in Section 4.6.4. Correlation scale coefficients and correlation scale results suggest possible relationships between rainfall and the general circulation and indicate possible rainfall forcing mechanisms.

4.6.1 Rain/Water Vapor Flux Correlations

Figures 4-21 and 4-22 show correlation results for rain and water vapor flux times series. The title of each graph shows the region (North or South), period (JJ or AS), and the parameters correlated. JJRAIN refers to the June/July rainfall time series. JJZON-AVG represents the June/July zonal flux time series. JJMER-BORDER designates the June/July meridional flux time series. Five correlation lag values appear along the x-axis: -2, -1, 0, 1, and 2. The sign of these values indicates which of the two parameters is leading the other. A negative number indicates that the first parameter in the title (JJRAIN on the left of Figure 4-21) lags the second parameter. A positive number indicates that the first parameter in the title leads the second. Zero indicates a one-to-one correlation, or zero lag. Correlation coefficients appear along the y-axis. The bars extending over each lag value represent the correlation coefficient associated with each lag. The dashed line represents the correlation coefficient corresponding to the 98% confidence interval. Bars that extend to or above this line show a correlation that is significant to the 98% confidence level.

North/South differences constitute the most striking features of the rain/water vapor flux correlations. In the North, JJ and AS rainfall and meridional flux are dependent (Figure 4-21), while in the South this dependence exists between AS rainfall

and zonal flux (Figure 4-22). These results suggest that meridional flux forces rain in the North only. This forcing is strongest in AS. Zonal flux forces rainfall in the South only. Zonal flux/rain forcing is also strongest during AS. A possible hypothesis may be that the ITCZ, with its North/South orientation, is responsible for the majority of rainfall in the North, while the AEJ and its attendant pressure disturbances have greater influence on southern rainfall. In both North and South, AS correlations are stronger than JJ correlations.

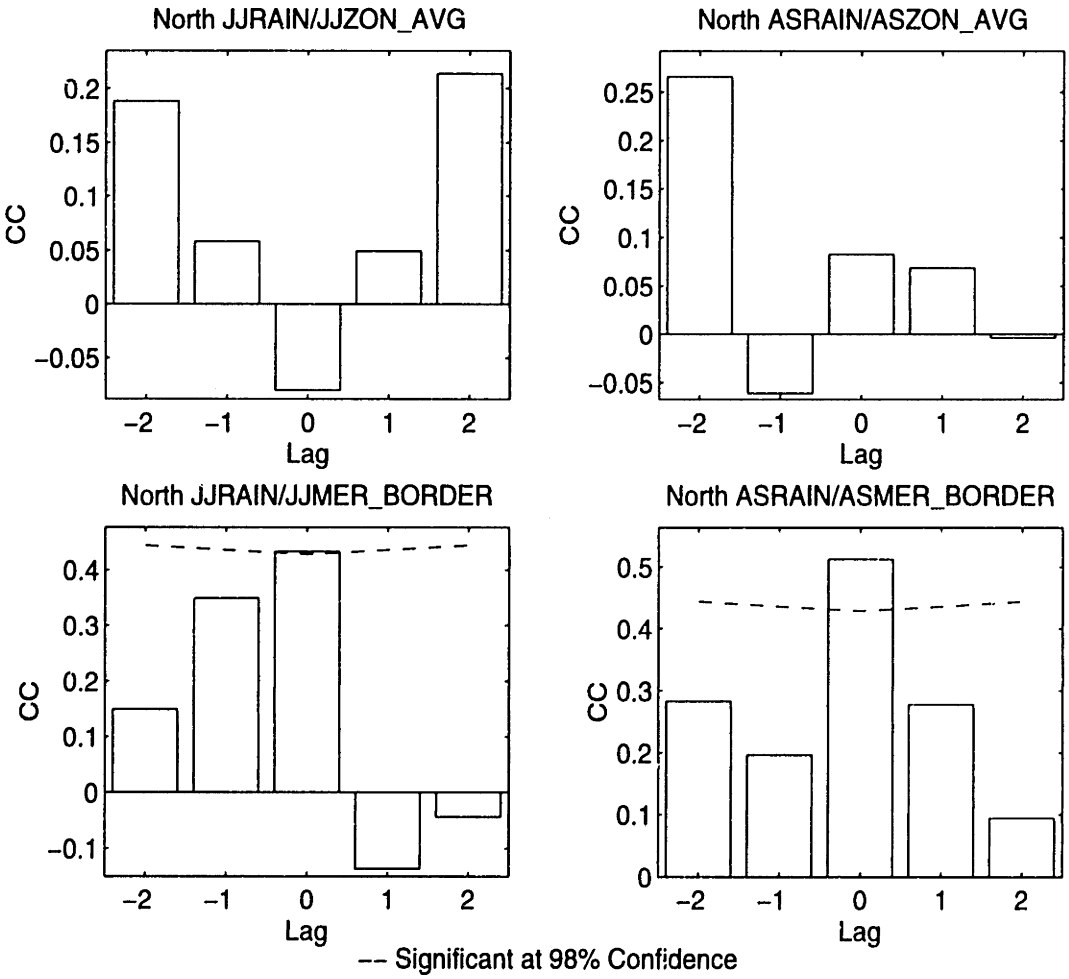

Figure 4-21: North Rain/Flux Correlations

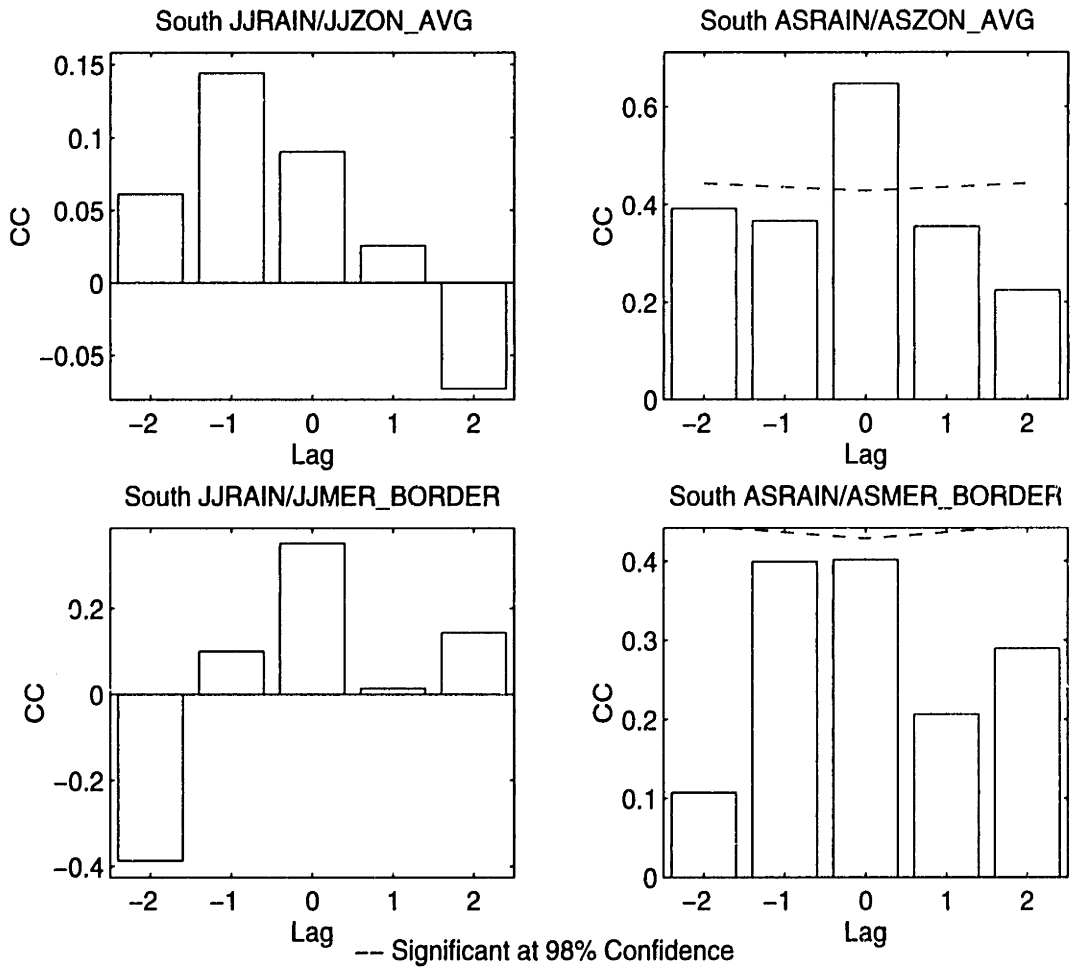

Figure 4-22: South Rain/Flux Correlations

4.6.2 Rain/EOF Correlations

Correlation coefficients were calculated in order to relate EOF time series to rainfall and vapor flux time series. Figures 4-23 through 4-28 display rain/EOF correlation plots for North and South regions in both JJ and AS. The title across the top of each graph indicates the two parameters being correlated. JJRAIN refers to the June/July rainfall series. JJEOF is the first June/July eigenvector multiplier time series.

The strongest correlations are found between EOF1 and rainfall. As shown in Figures 4-23 and 4-24, EOF1 leads rainfall by one to two years in both regions and seasons at the 98% significance level. However, as shown in Figures 4-25 through 4-28, neither EOF2 nor EOF3 are significantly correlated with rainfall at the 98% level. The strong correlation between EOF1 and rainfall along with the southeast/northwest dipole revealed in the EOF1 pattern suggest that EOF1 may reflect Hadley/Walker partitioning. According to the EOF1 time series, the strength of this dipole relationship collapses in the mid-1960s. Perhaps a weakening of the Hadley/Walker system preceded drought onset by several years.

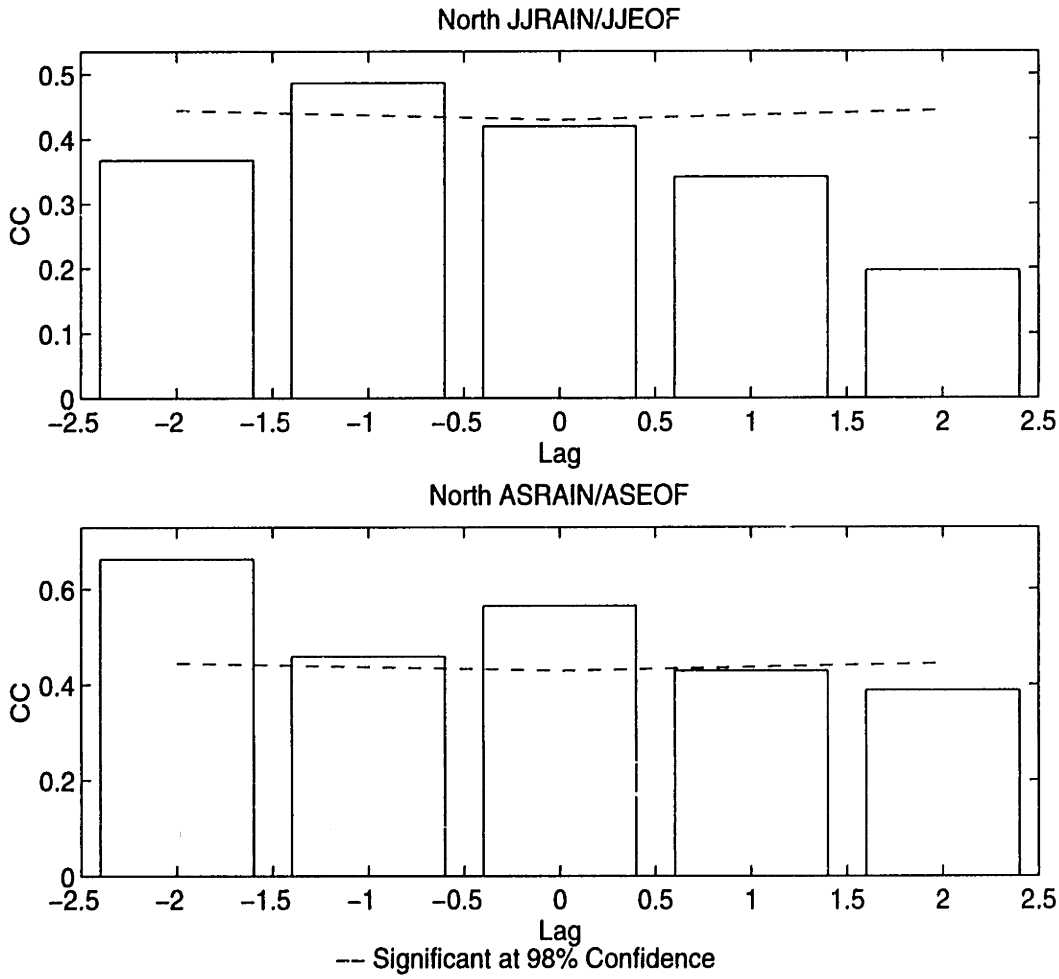

Figure 4-23: North Rain/EOF1 Correlations

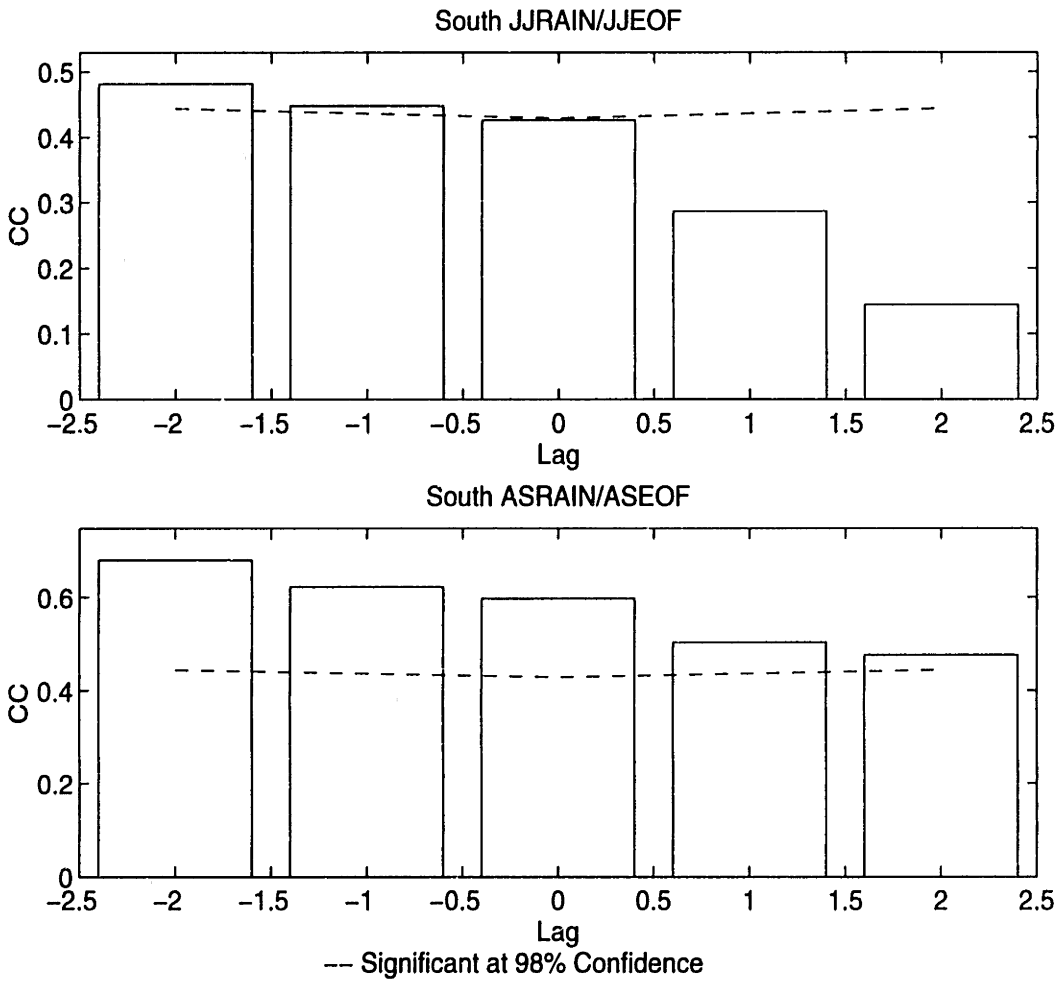

Figure 4-24: South Rain/EOF1 Correlations

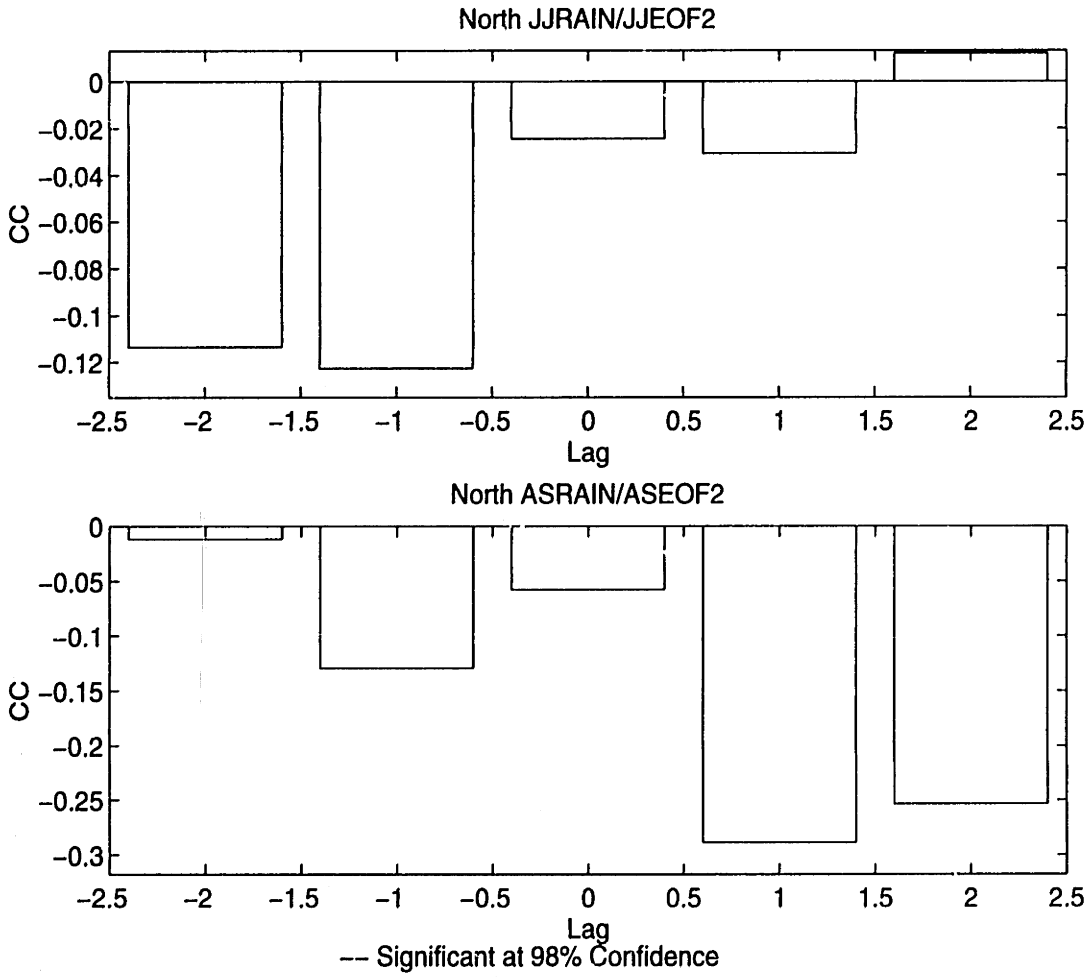

Figure 4-25: North Rain/EOF2 Correlations

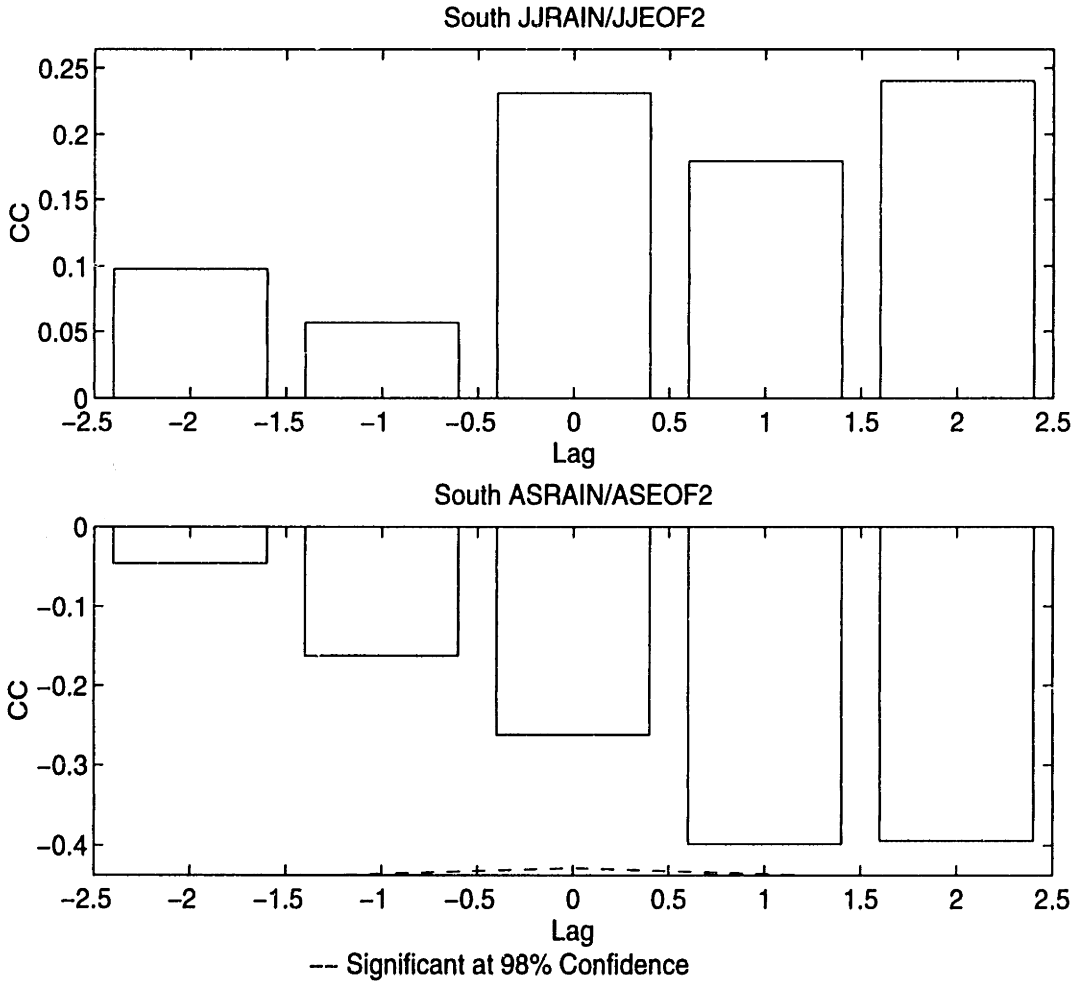

Figure 4-26: South Rain/EOF2 Correlations

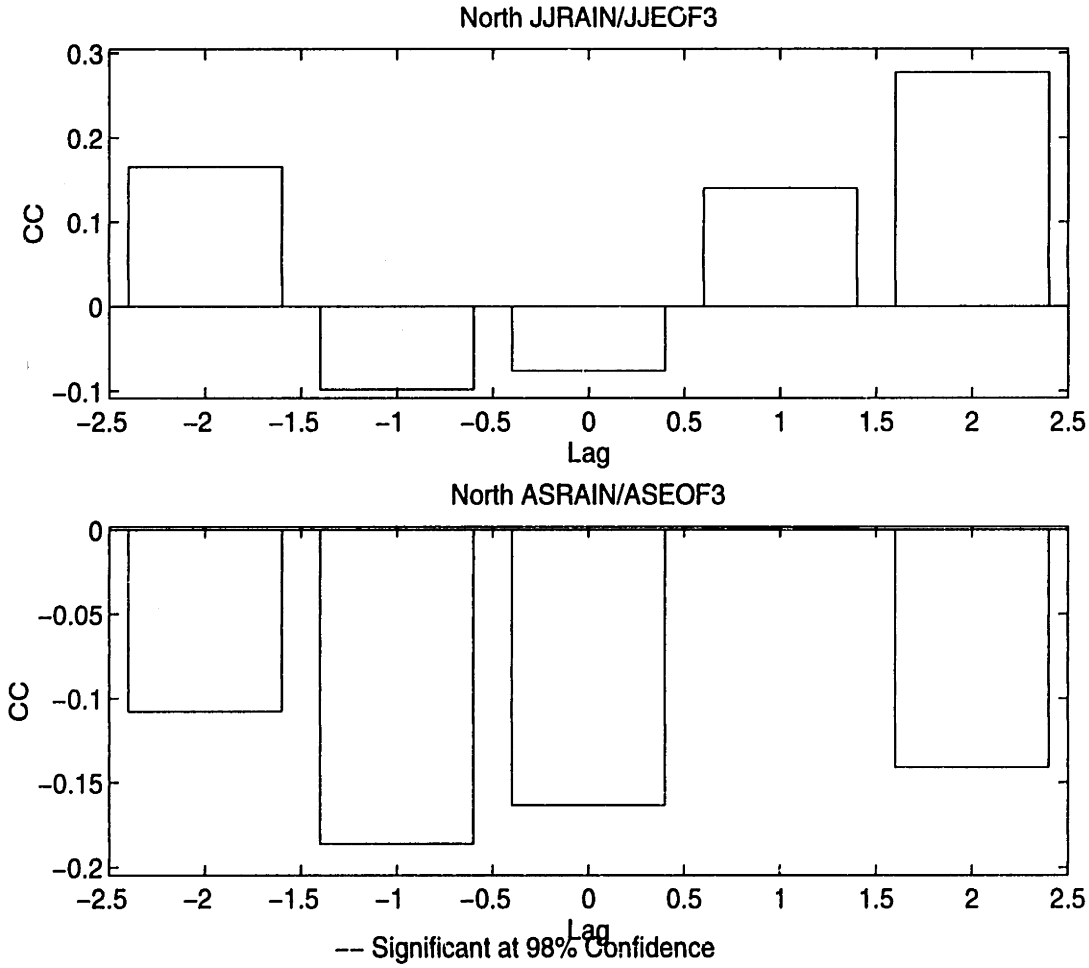

Figure 4-27: North Rain/EOF3 Correlations

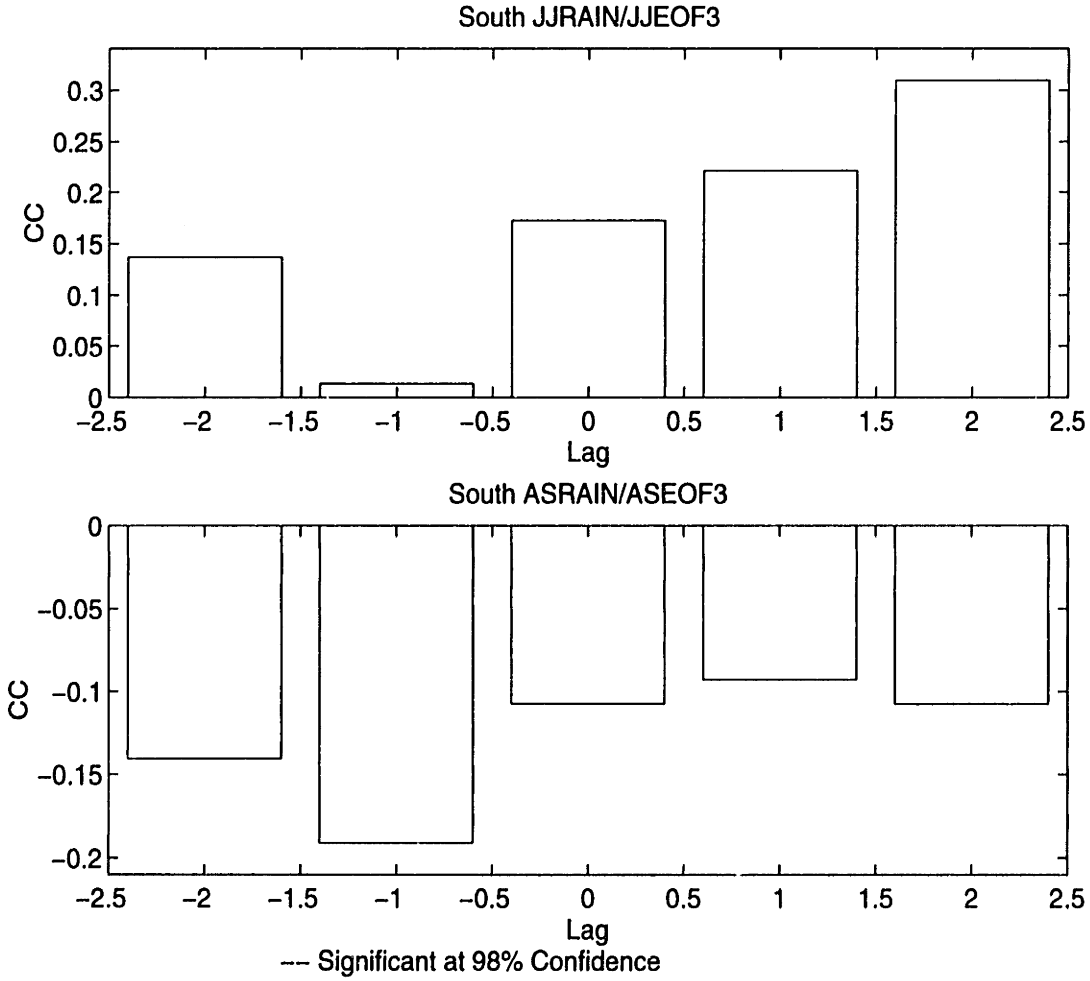

Figure 4-28: South Rain/EOF3 Correlations

4.6.3 Water Vapor Flux/ EOF Correlations

EOF time series were also correlated with water vapor flux time series. Correlation diagrams are pictured in Figures 4-29 through 4-34. Here, the strongest correlation appears between EOF2 and zonal flux. EOF2 leads northern JJ zonal flux by two seasons and northern AS zonal flux by one season. In the south, JJ EOF2 and JJ zonal flux show significant correlations at zero lag. All EOF2/zonal flux correlations are reported for the 98% confidence interval. The east/west orientation of the EOF2 patterns presented in Figures 4-13 and 4-14, the strong EOF2/zonal flow correlations, and the low-frequency stationary waves pictured in the EOF2 times series suggest that EOF2 represents the strength of the AEJ.

At slightly lower confidence intervals significant correlations appear between EOF1 and North meridional flux time series. At the 96% significance level, JJ EOF1 and JJ northern meridional vapor flux are correlated at zero lag. At the 97% confidence interval AS EOF1 and AS northern meridional vapor flux are correlated at zero lag. No significant correlations between EOF time series and meridional vapor flux appear in the South. No significant correlations exist between EOF3 and meridional or zonal vapor flux.

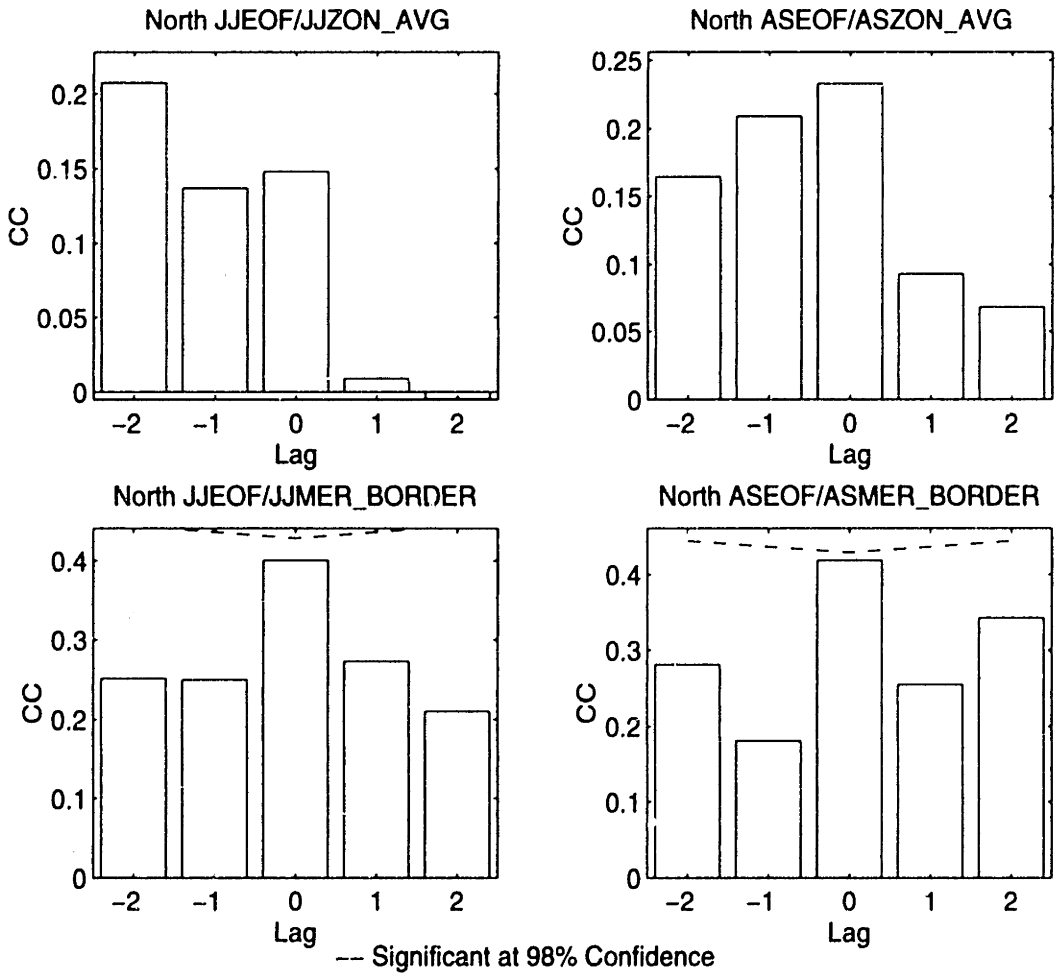

Figure 4-29: North Flux/EOF1 Correlations

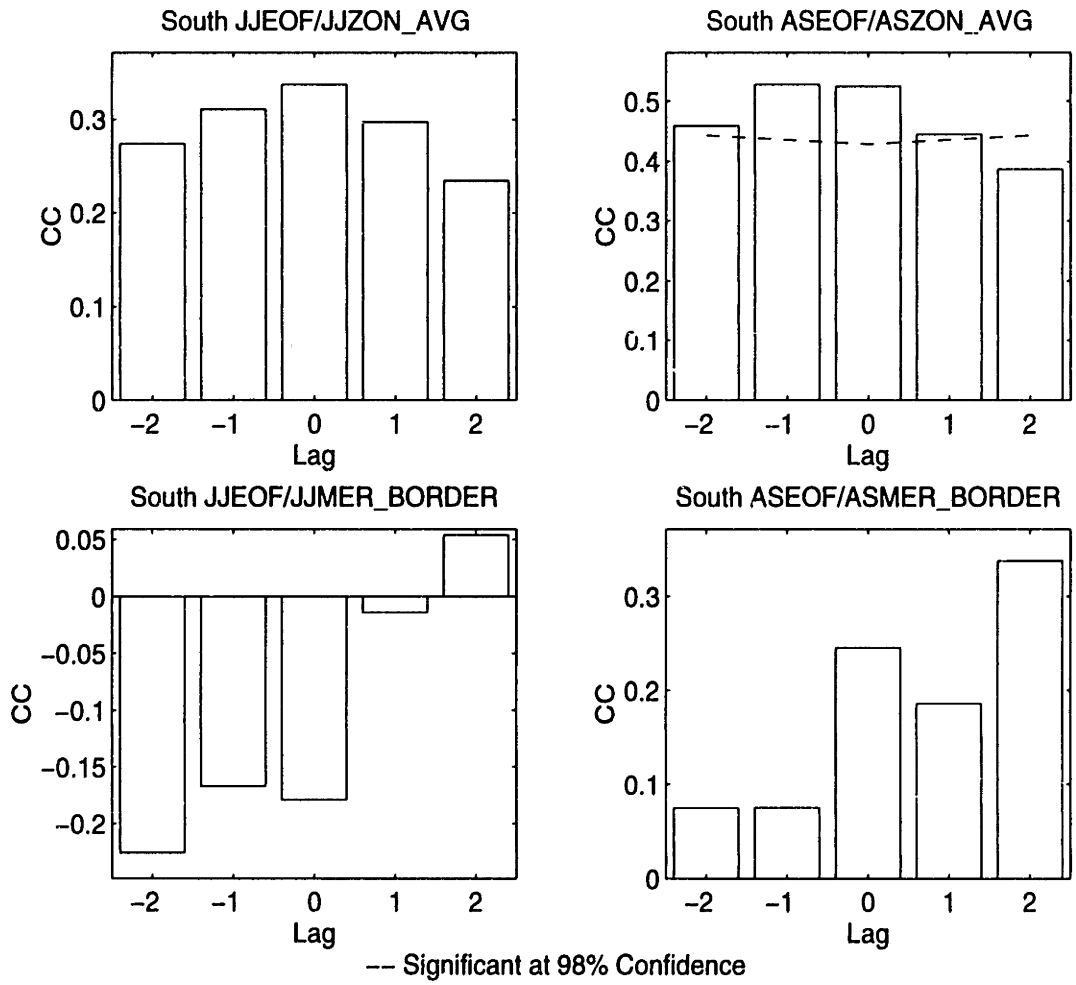

Figure 4-30: South Flux/EOF1 Correlations

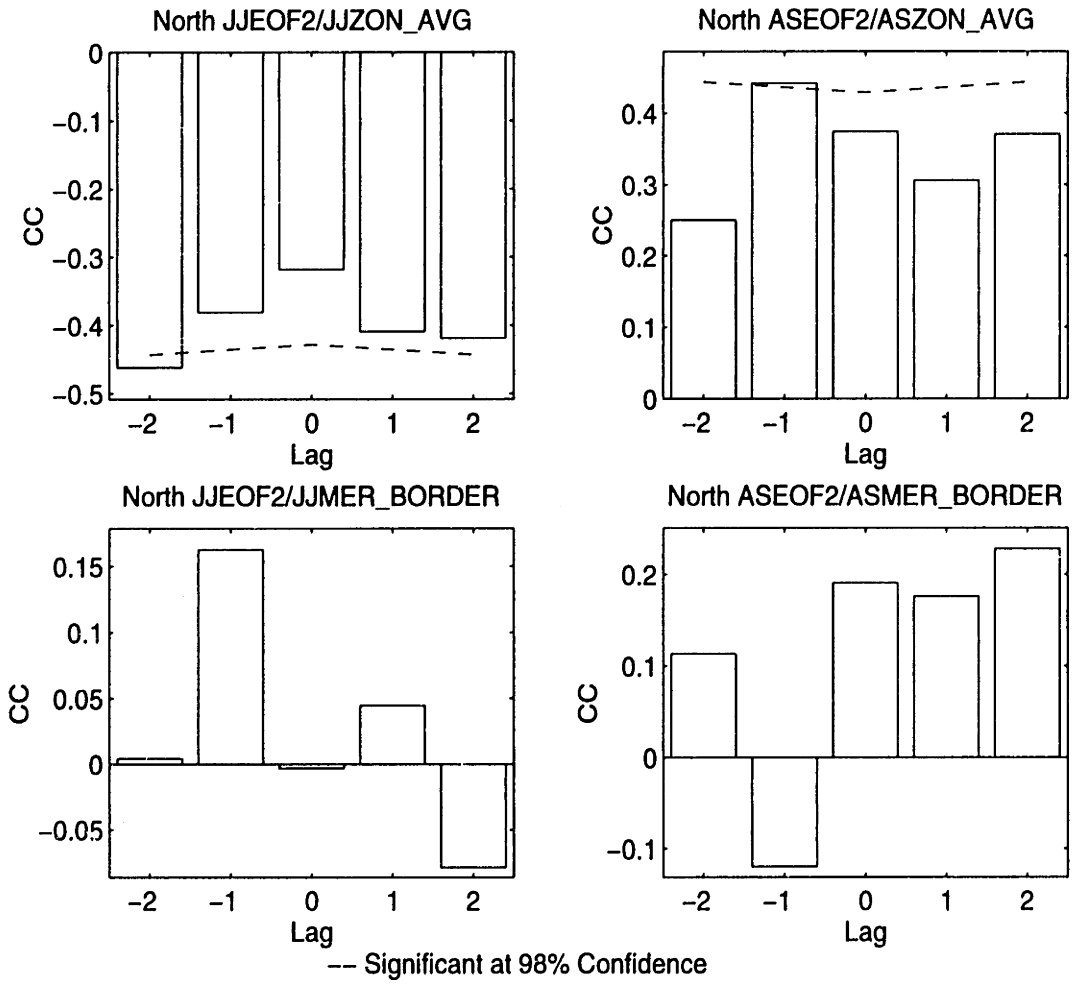

Figure 4-31: North Flux/EOF2 Correlations

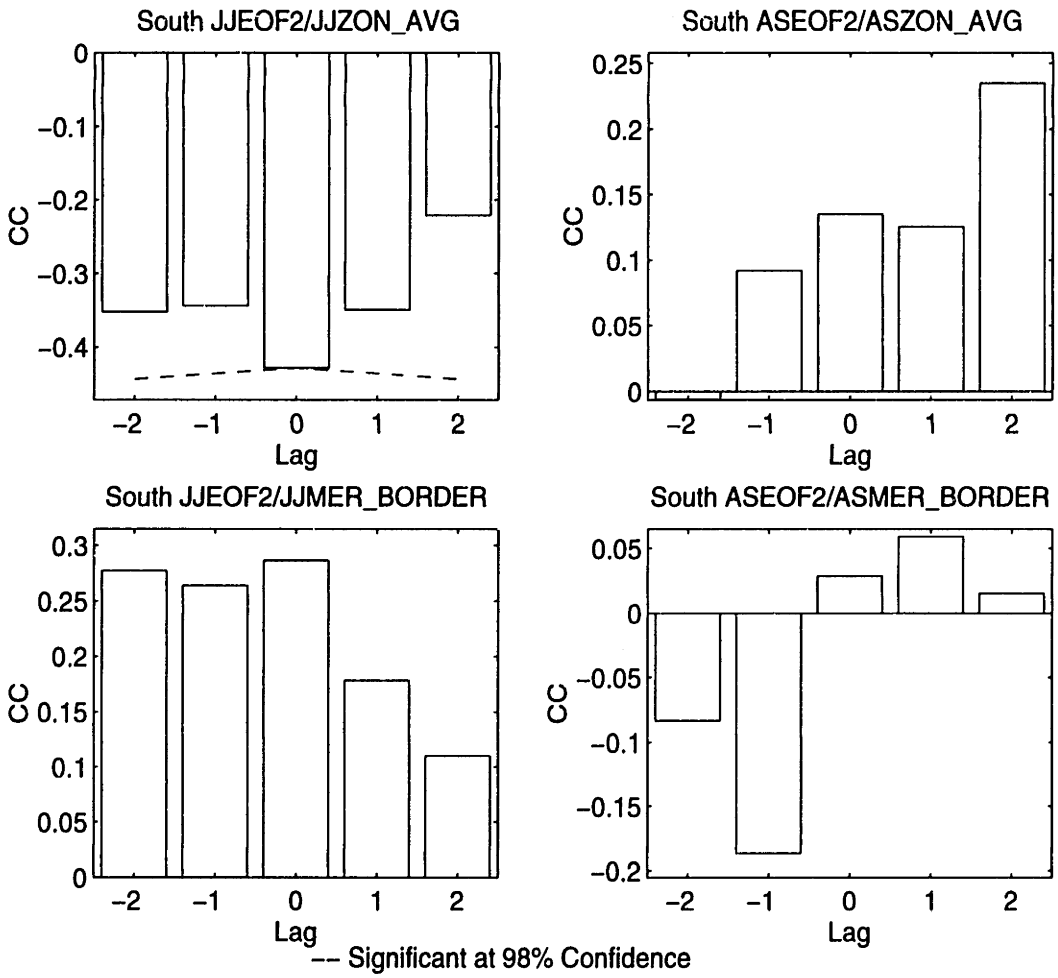

Figure 4-32: South Flux/EOF2 Correlations

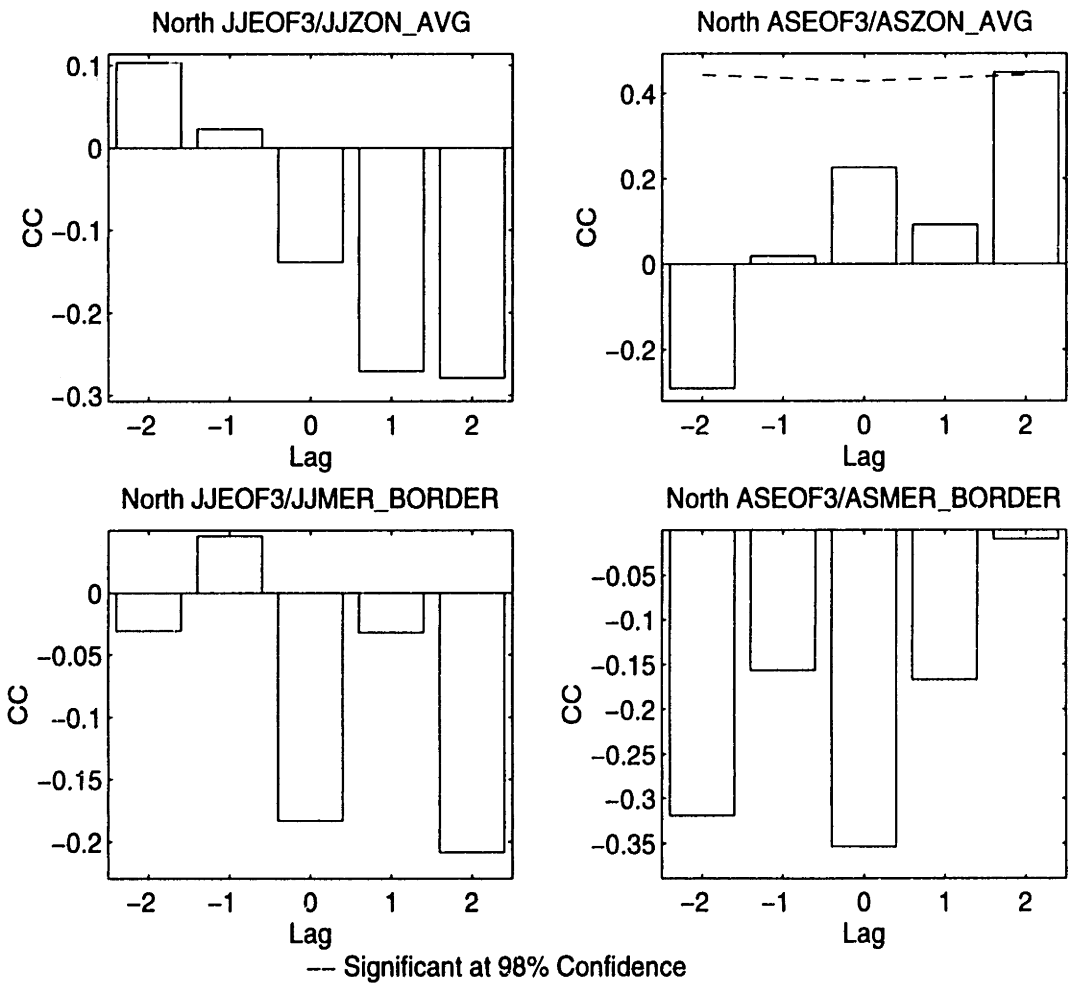

Figure 4-33: North Flux/EOF3 Correlations

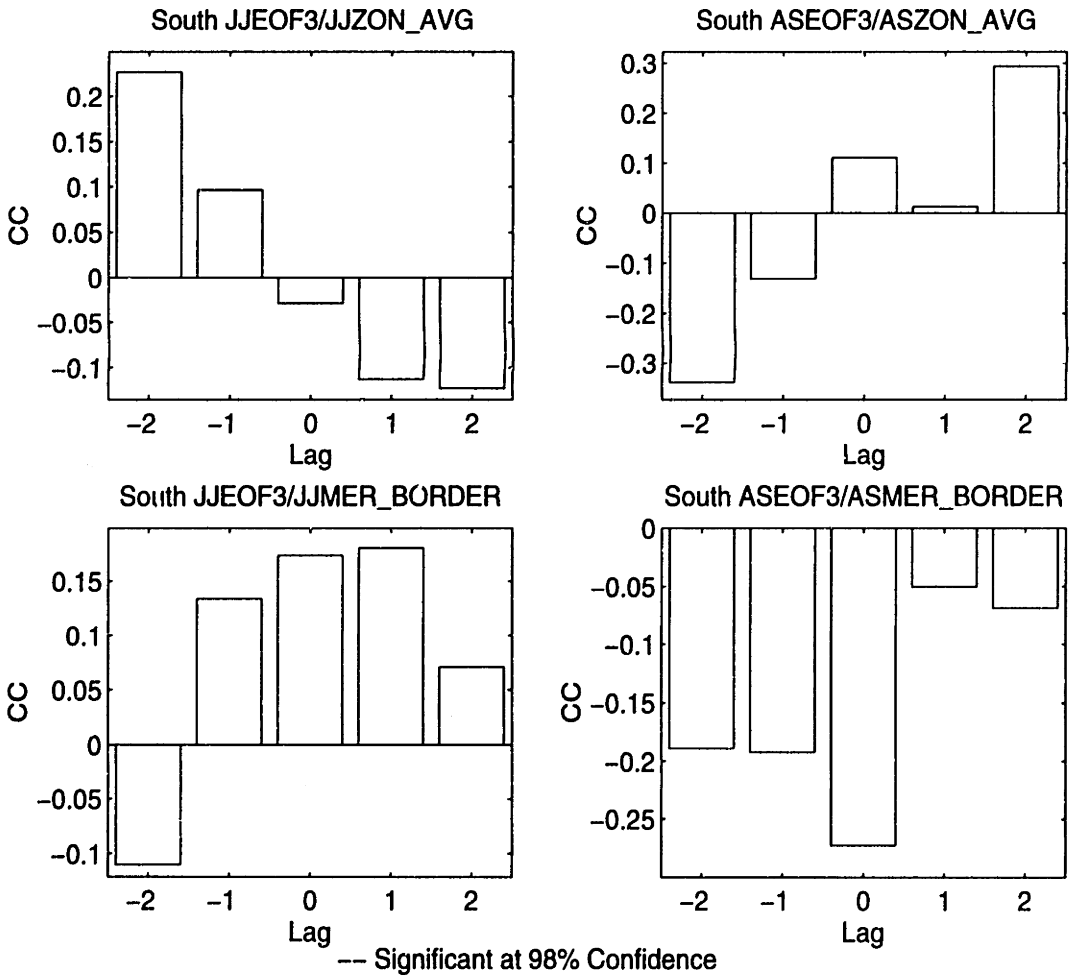

Figure 4-34: South Flux/EOF3 Correlations

4.6.4 Correlation Scale Results

While linear correlation results provide information about time series relationships at different time lags, correlation scale values reflect time series persistence. Correlation coefficients indicate dependency between rainfall, vapor flux, and a general circulation index. Correlation scale values allow comparisons regarding the frequency of variation in rainfall, flux, and EOF time series.

Correlation scale values were determined for rainfall, meridional flux, and zonal flux. Correlation scale values were calculated via the method presented in Section 4.2.2 and are found for JJ and AS in Tables 4-3 and 4-4. Correlation scale results reveal regional and seasonal differences in rainfall and water vapor flux time series. Section 4.2 addresses North/South differences in AS rainfall. This section focuses on the JJ and AS differences that characterize rainfall and vapor flux. Table 4-3 shows that both rain and water vapor flux are less persistent in JJ than in AS. This lower JJ persistence is noted in Nicholson and Palao (1993) and may be associated with the random onset of the rainy season.

JJ and AS comparisons of rain and vapor flux suggest possible drought-forcing mechanisms. During JJ, rainfall and vapor flux have equivalent time scales. The similar rainfall and flux time scales indicate that the most important rainfall forcing derives from general circulation features such as the ITCZ and AEJ which are associated with meridional and zonal vapor flux. During AS, however, rainfall persistence exceeds persistence in meridional and zonal vapor flux. This suggests that mechanisms other than the ITCZ and AEJ are impacting rainfall variability. One possible explanation involves land surface forcing. Various land-surface feedback theories are discussed below.

Parameter	JJ	
	North	South
Rain	1.3	1.3
Zonal	1.3	1.6
Meridional	1.0	1.2

Calculated at a maximum of 8 lag

Table 4.3: JJ Correlation Scale Values

Parameter	AS	
	North	South
Rain	2.8	4.1
Zonal	1.7	2.0
Meridional	1.6	1.7

Calculated at a maximum of 8 lag

Table 4.4: AS Correlation Scale Values

Several theories addressing land surface forcing mechanisms have been proposed.In a recent 1995 publication, Rowell *et al.* (1995) presents these theories and comments on their validity in relation to his own SST modeling studies. One theory involves decreased soil moisture and asserts simply that drought conditions lower soil moisture and thereby decrease the supply of evaporated moisture available for convection. However, Rowell *et al.* (1995) claims that SST forcing overshadows this mechanism on seasonal time scales. The Charney (1975) feedback hypothesis suggests that overgrazing and other land-use practices decrease vegetation and increase the surface albedo. To maintain thermodynamic equilibrium, falling motion is induced and inhibits convection. Rowell *et al.* (1995) claims that observational studies deem this theory inconclusive. Sud and Sukla (1988) propose that reduced vegetation increases surface roughness. Consequent changes in low-level wind convergence change precipitation patterns and thus, decrease rainfall (Rowell *et al.*, 1995). Other theories address increases in dust generation associated with vegetation loss (Prospero and Nees 1977). However, the linkages between dust increases and rainfall patterns are not yet established Rowell *et al.* (1995).

One problem with land-surface theories is their unrealistic year-to-year perturbations in regard to magnitude and spatial extent. Another problem involves lack of memory. As an example, soil moisture falls to zero prior to the rainy season regardless of the previous year's rainfall total. Further study regarding land-surface forcing mechanisms is necessary before these mechanisms are fully characterized.

4.7 Conclusions

Essentially, the body of scientific literature on West African drought addresses an overarching question: how do local and large-scale forcing contribute to drought? The answer to this question has major implications for dealing with the drought problem. For example, drought induced by land-use practices would require different mitigation, prediction, and future research efforts than drought caused by general circulation anomalies. The evidence to date suggests that large-scale changes in the

general circulation initiate drought, while land surface modifications may be sufficient only to intensify drought and contribute to its persistence (Nicholson 1989).

The research presented here seeks to provide information helpful in assessing the validity of this hypothesis. By correlating rainfall with vapor flux and EOF ω results, this study presents relationships between drought and the general circulation. In doing so, the study also distinguishes between the northern (Sahel) and southern (Soudan) regions of West Africa and between JJ and AS portions of the rainy season. EOF patterns reflect major circulation features. Strong EOF1/rain correlations indicate that large-scale forcing impacts rainfall anomalies. Rain/flux relationships reveal differences in JJ and AS behavior and contrast Sahel and Soudan dynamics.

EOF analysis of the 500 mb vertical wind velocity field provides an index of the general circulation via EOF patterns and associated time series. The EOF1 pattern represents the Walker/Hadley circulation and its time series collapses in the mid-1960's. This suggests a marked change in the vertical circulation regime prior to drought onset. The East-West orientation of EOF2, the low frequency fluctuations apparent in the time series, and the strong zonal flux/EOF2 correlations suggest that EOF2 reflects the position of the easterly jets traversing the West African region. These interpretations of EOF results are important in understanding correlations between rainfall, vapor flux, and EOF time series. In particular, a result that pertains to both the Sahel and Soudan involves the correlation between EOF1 and rainfall. In both regions and in both JJ and AS, EOF1 leads rainfall by one to several seasons. This indicates that large-scale forcing mechanisms operate in both regions and during both halves of the rainy season. Similar relationships are reviewed below.

In the Sahel, rainfall and meridional vapor flux exhibit a notable dependence. Time series of meridional vapor flux at 15° show a significant difference in wet and dry-year meridional vapor flux means at this latitude. In other words, changes in the mean value of meridional vapor flux at 15° between wet and dry years corresponds to changes in rainfall. Significant correlations between Sahelian meridional vapor flux and rainfall time series provide further support for this observation.

In the Soudan, the most significant relationships exist between rainfall and zonal

flux. In the South, zonal flux leads rainfall. Given the dependence between zonal flux and EOF2, it appears that strength of the easterly jets forces JJ rainfall in the Soudan, while the strength of the easterly flow forces AS rainfall. During JJ, the anomalous position of general circulation features influences the random onset of the rainy season. In AS, the position of the general circulation features is established. Thus, the strength of these features is the predominant influence on rainfall.

Correlation scale results provide further insight into rainy season dynamics. Correlation scale values reflect equivalent time scales for moisture flux and rainfall in JJ. However, AS rainfall correlation scale values exceed those for vapor flux. Lower persistence in JJ may result from the random onset of the rainy season. Higher persistence in AS may reflect the establishment of general circulation features and the positive reinforcement associated with land-surface feedback mechanisms.

Many debates continue regarding West African rainfall and the forcing mechanisms associated with it. This study attempts to relate rainfall, water vapor flux, and the general circulation. In doing so, research results reveal direct linkages between rainfall, flux, and an index of the circulation. These linkages provide new insights in drought-forcing mechanisms.

Chapter 5

Conclusion

This thesis examines water vapor transport and its relationship to other climatic factors. The North European study provides an in-depth view of water vapor dynamics by examining water vapor flux and its components, regional flux at different locations, and convergence. The West African study contains a similar analysis of water vapor flux, but also relates flux characteristics to rainfall time series and to an index of the general circulation.

The European study's intra-annual analysis reveals relationships between the different modes of water vapor movement and its wind and humidity components. The seasonal analysis also reflects the prominent weather systems in the Northern European regions. The dominant westerly flux reflects the Jet Stream and Polar Front while analysis of meridional flux illustrates the importance of transient eddies in the North-South direction. Decomposition of flux into its specific humidity and wind components shows slight variations in humidity along the meridional axis, and the importance of wind velocity in determining flux magnitude. The convergence time series suggests a possible relationship between ENSO and convergence. Regional flux time series illustrate how flux varies among the different region boundaries.

An expanded European study could provide insight into the region's water budget and its relationship to the general circulation. Analysis of precipitation, evaporation, and runoff data, for example, would lead to a more complete picture of the European water budget. Correlation of sea surface temperature with moisture flux may reveal

interesting characteristics of land/ocean/atmosphere interaction. Instead of vertically integrating the components of moisture flux, a study considering activity at the discrete pressure layers would provide further information about the behavior of wind and humidity at different altitudes. An interannual study focusing on the Mediterranean region may show an ENSO signature in the water vapor transport through this region. It would also be interesting to relate water vapor transport parameters to the energy budget.

The African study illustrates linkages between parameters not yet related in the literature. Furthermore, the analysis distinguishes between the Sahel and Sudan and between the first and second halves of the rainy season. Correlations between rainfall, water vapor, and the general circulation suggest relationships between the Walker/Hadley cells and rainfall throughout West Africa; meridional flux and rainfall in the Sahel; and zonal flux and rainfall in the Sudan. Furthermore, correlation scale results for rainfall may suggest land-surface feedback contributions to AS rainfall.

Further development of the research presented here could provide additional insight into African drought and its causes. One might, for example, investigate the ITCZ/EOF1 relationship further via an in-depth analysis of Hadley/Walker circulation. Given the wealth of information derived from intra-African rainfall studies, it might be worthwhile to expand this study to incorporate the entire African continent. Other parameters of interest include SSTs, vertical temperature gradients, and monsoonal flow. However, additional work need not be limited to atmospheric parameters only. Correlation scale differences regarding JJ and AS rainfall suggest possible avenues for land-surface interaction analysis.

Appendix A

Water Vapor Flux over Northern Europe

Figure	Season	Parameter
A-1	Annual	Total Motion Flux
A-2	DJF	Total Motion Flux
A-3	MAM	Total Motion Flux
A-4	JJA	Total Motion Flux
A-5	SON	Total Motion Flux
A-6	Annual	Mean Motion Flux
A-7	DJF	Mean Motion Flux
A-8	MAM	Mean Motion Flux
A-9	JJA	Mean Motion Flux
A-10	SON	Mean Motion Flux
A-11	Annual	Transient Eddy Flux
A-12	DJF	Transient Eddy Flux
A-13	MAM	Transient Eddy Flux
A-14	JJA	Transient Eddy Flux
A-15	SON	Transient Eddy Flux

Table A.1: Catalog of Complete Water Vapor Flux Figures

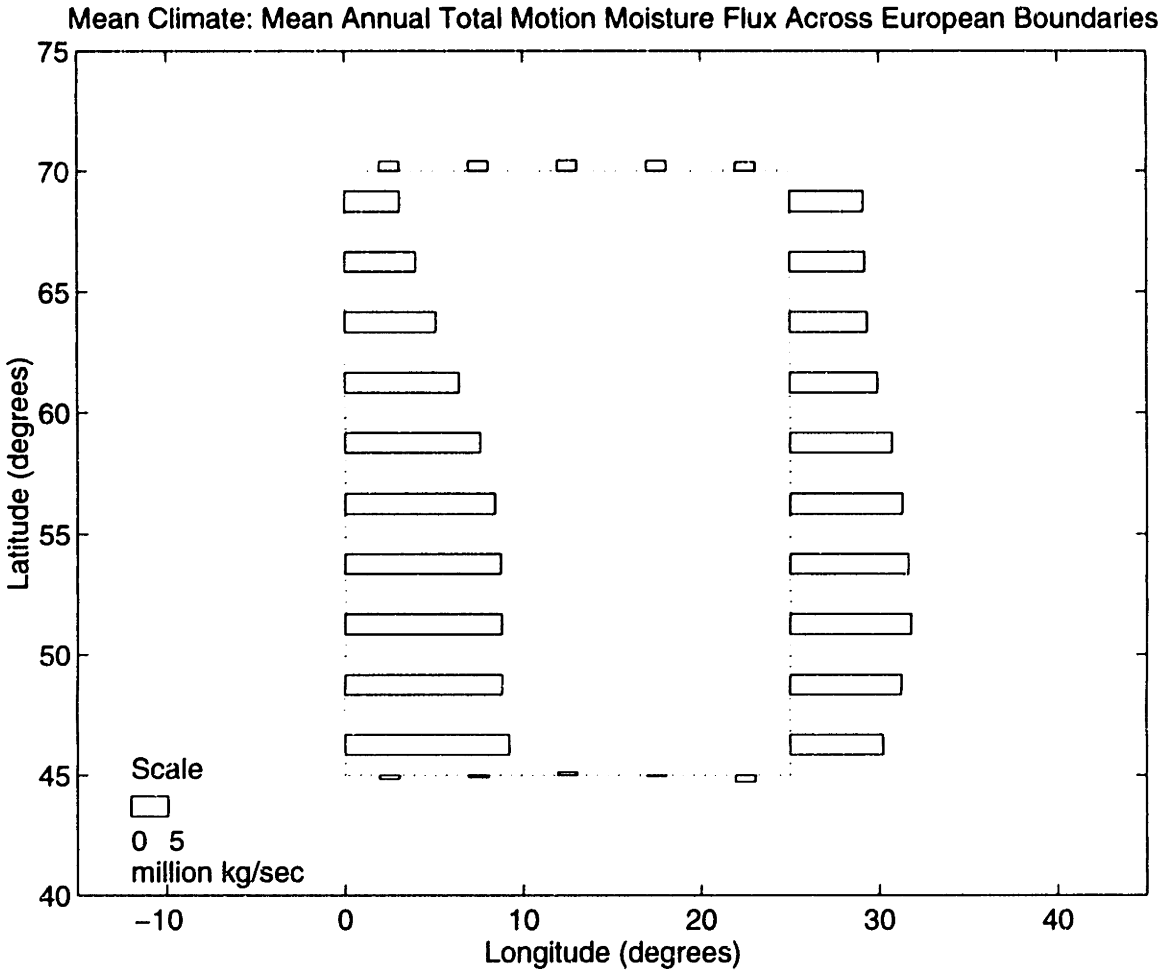

Figure A-1: Annual Mean Climate Total Motion Water Vapor Flux

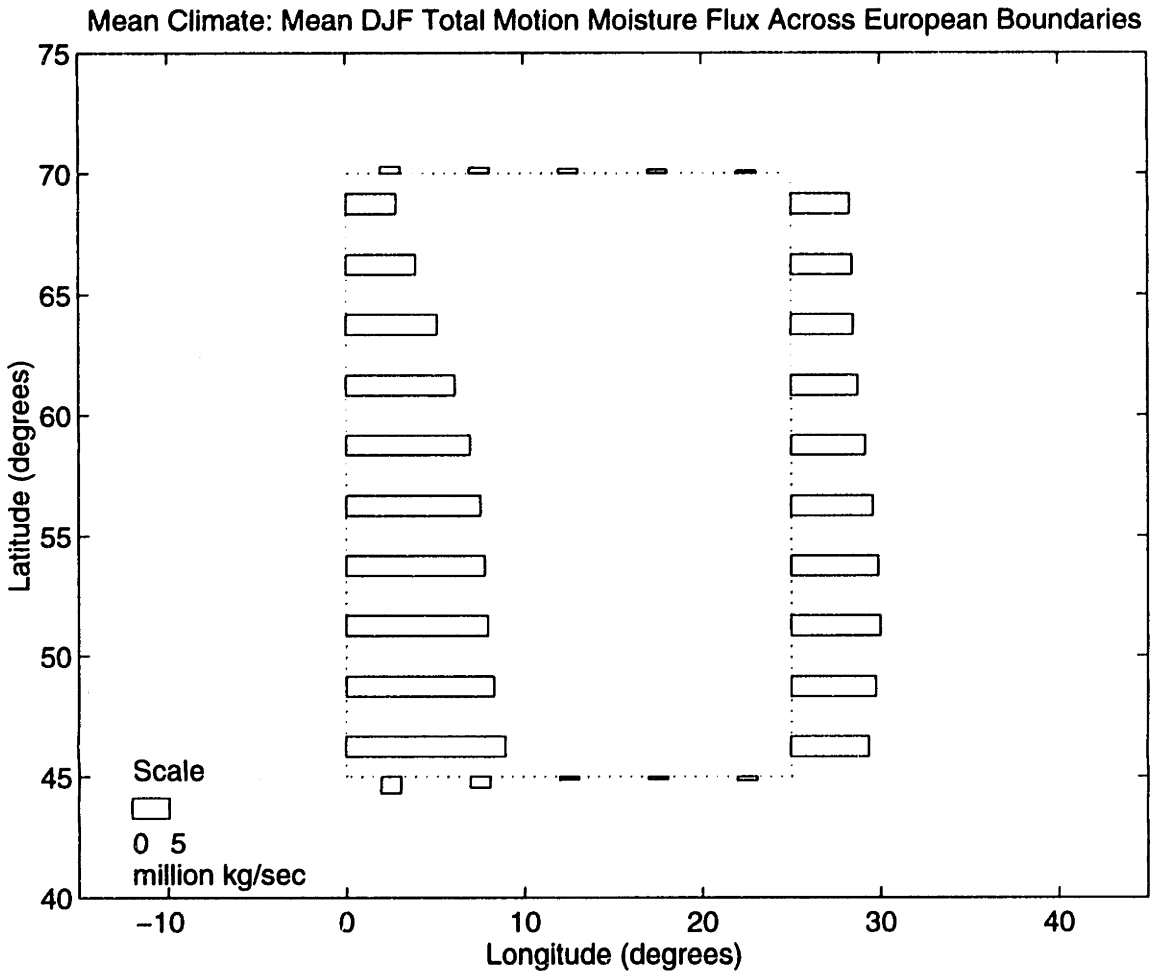

Figure A-2: DJF Mean Climate Total Motion Water Vapor Flux

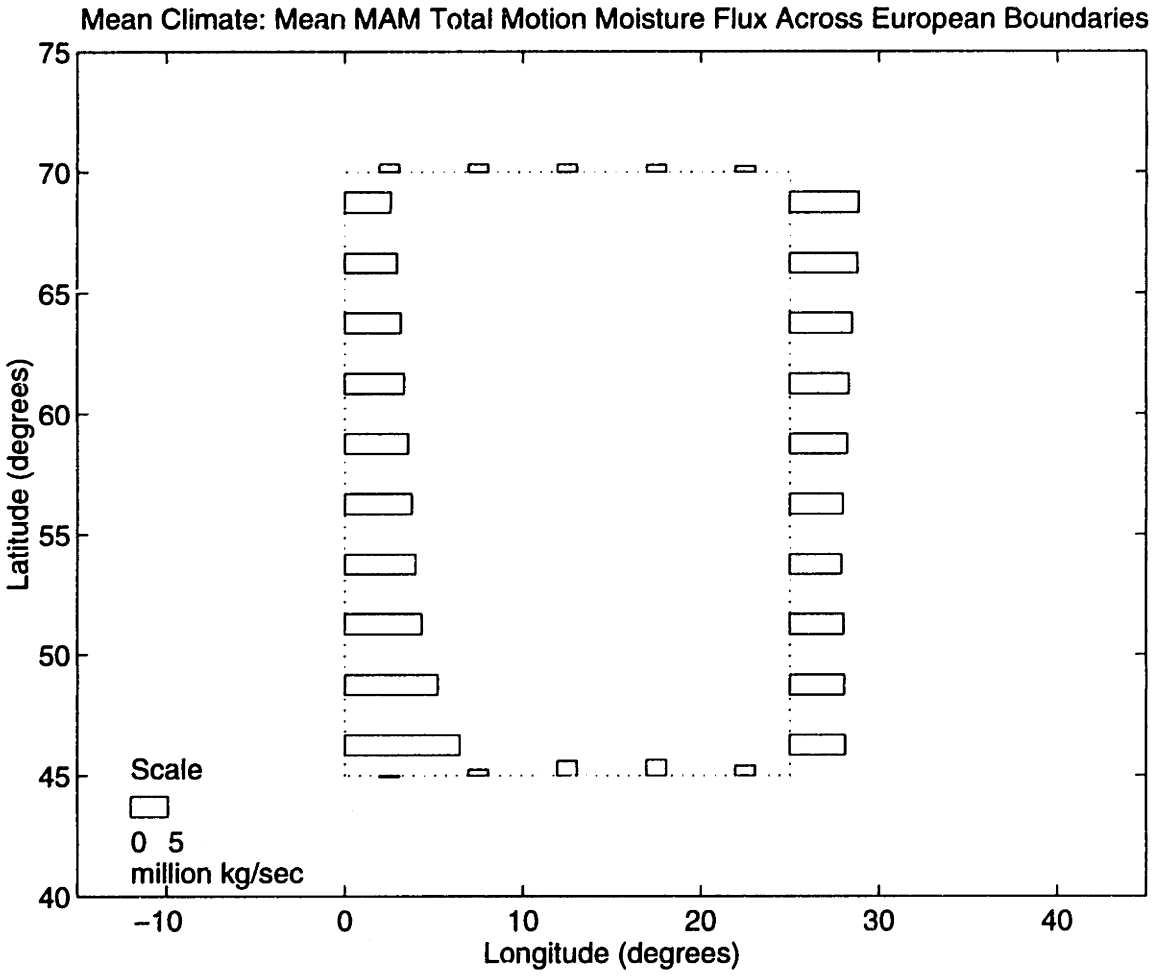

Figure A-3: MAM Mean Climate Total Motion Water Vapor Flux

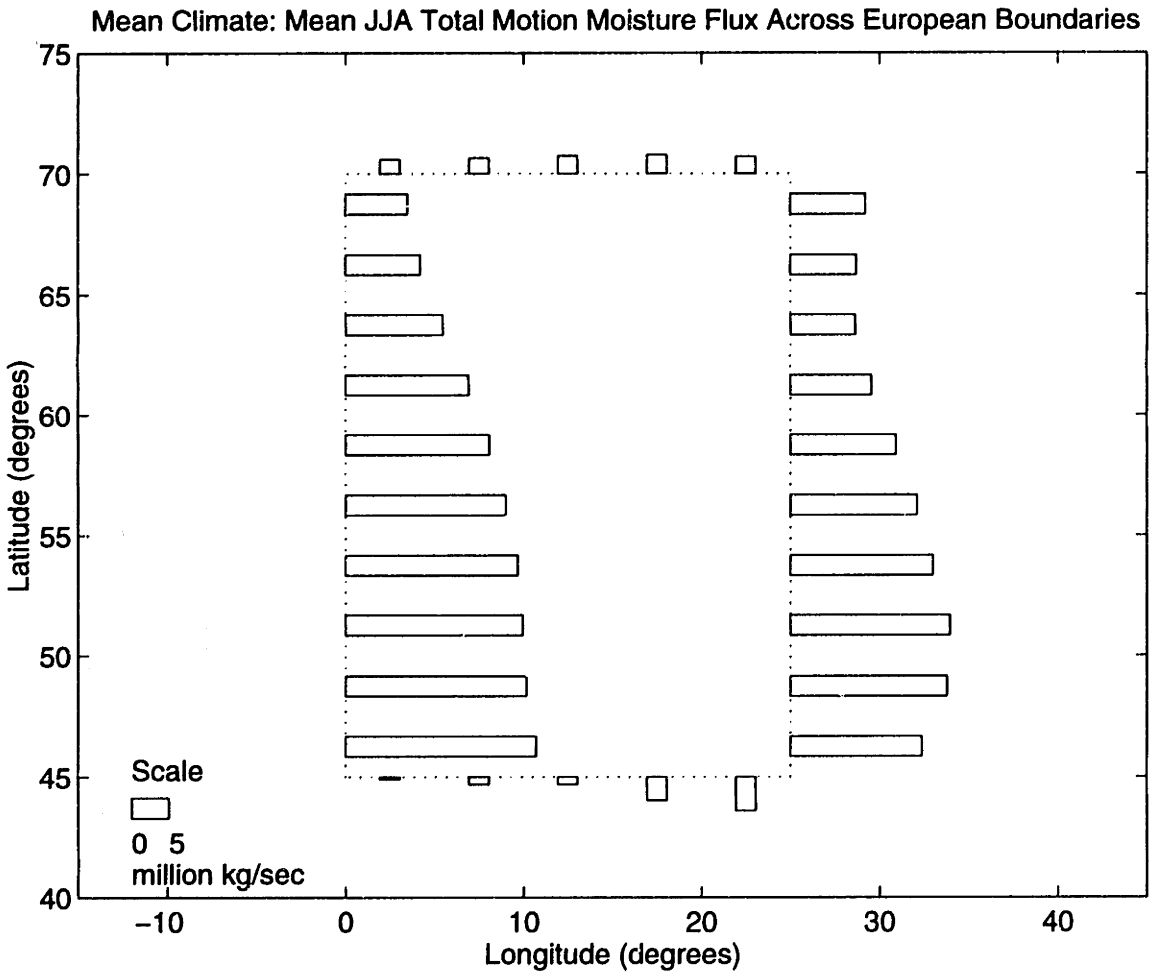

Figure A-4: JJA Mean Climate Total Motion Water Vapor Flux

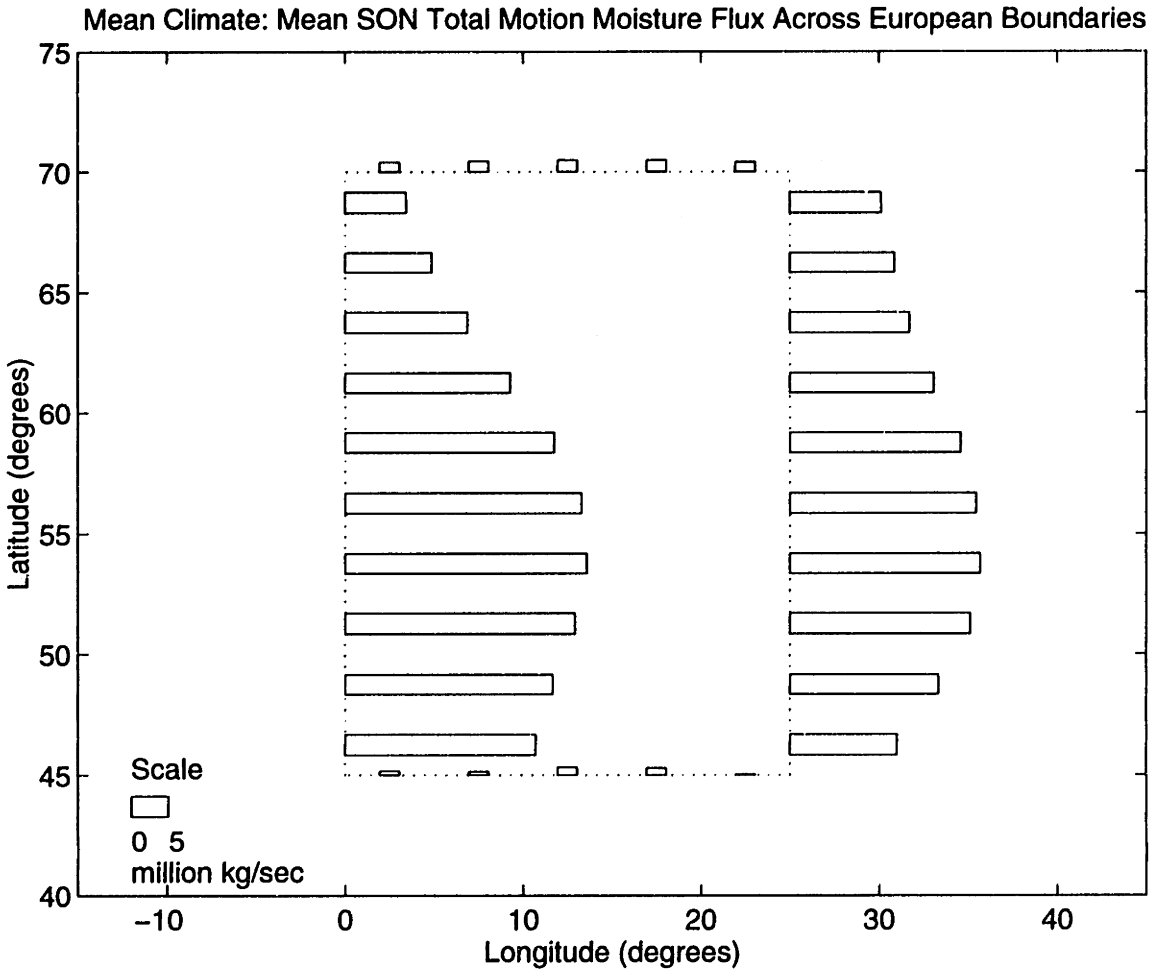

Figure A-5: SON Mean Climate Total Motion Water Vapor Flux

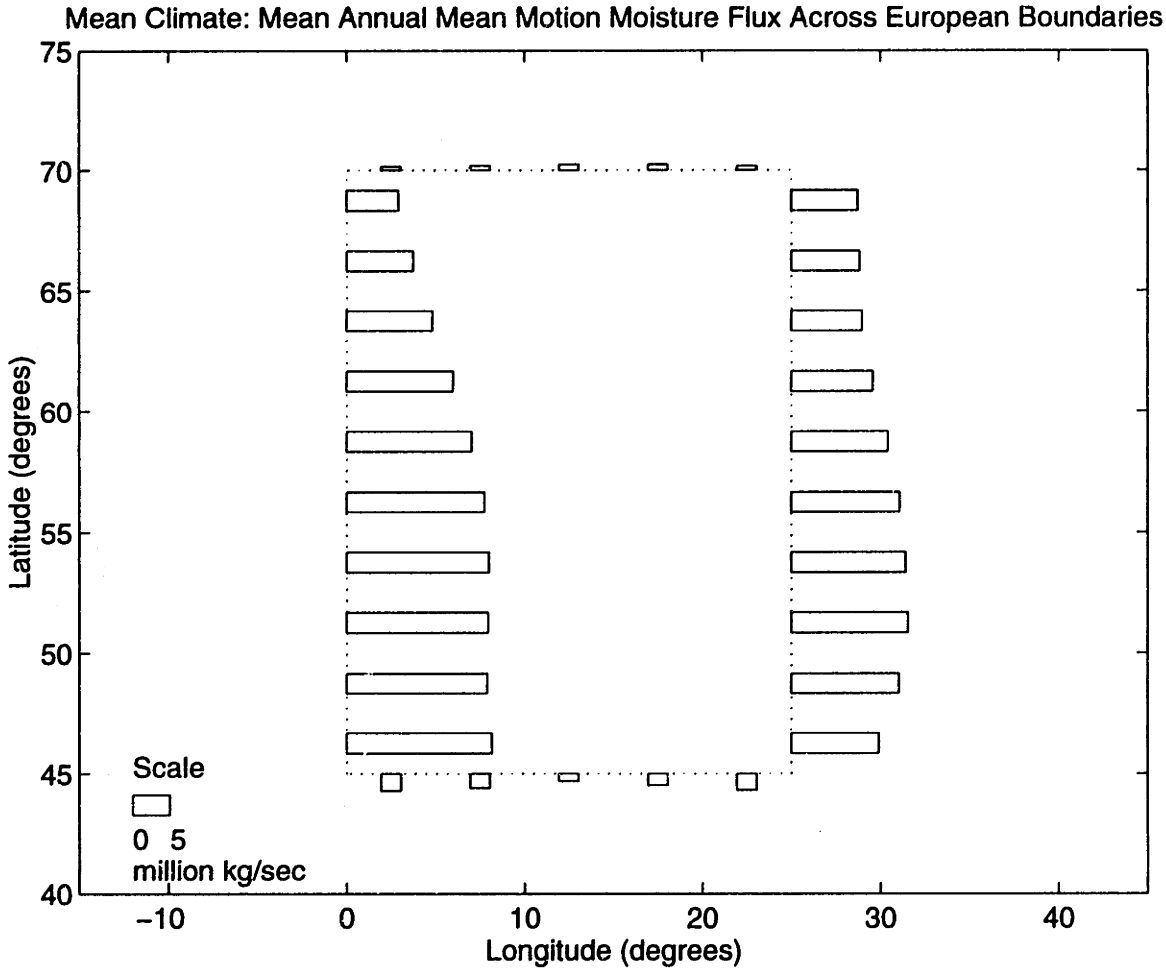

Figure A-6: Annual Mean Climate Mean Motion Water Vapor Flux

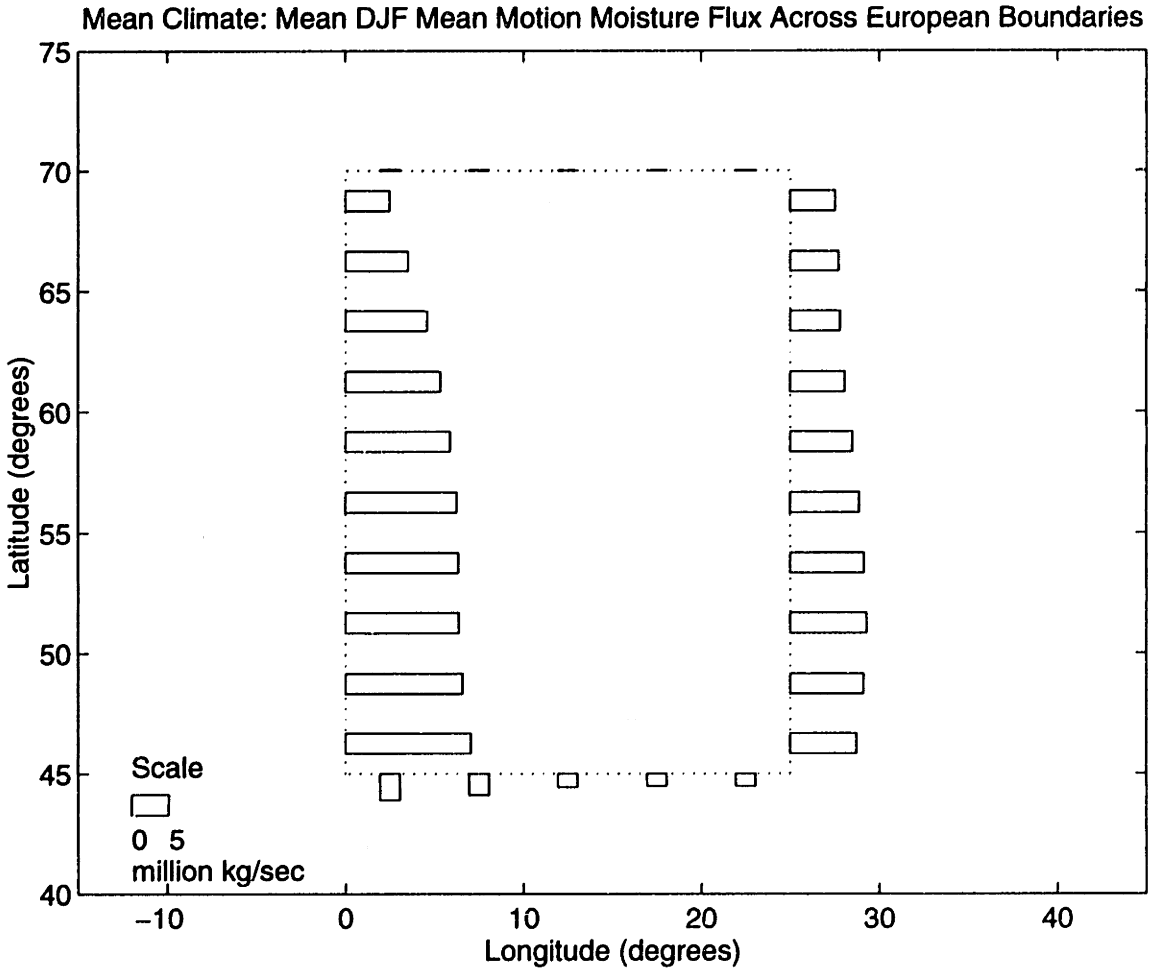

Figure A-7: DJF Mean Climate Mean Motion Water Vapor Flux

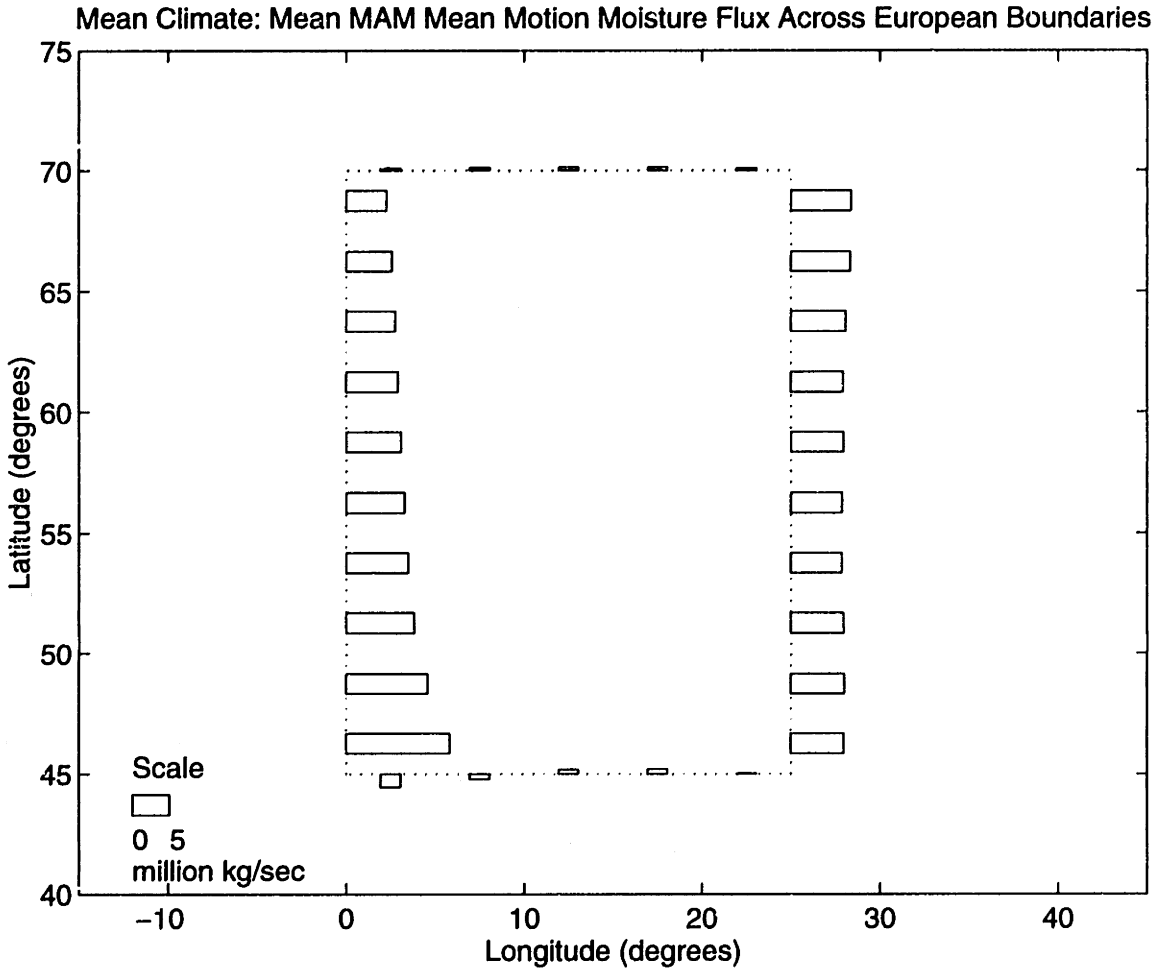

Figure A-8: MAM Mean Climate Mean Motion Water Vapor Flux

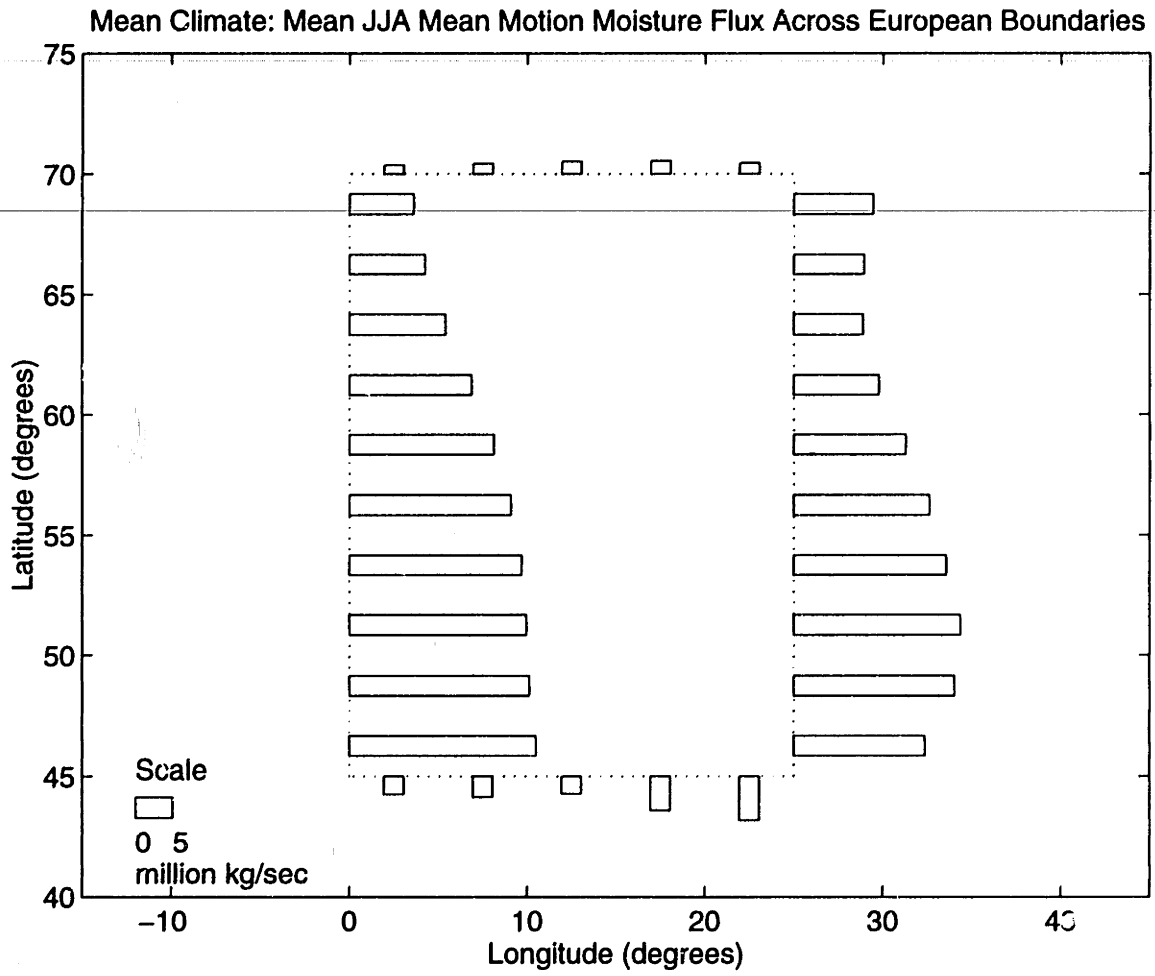

Figure A-9: JJA Mean Climate Mean Motion Water Vapor Flux

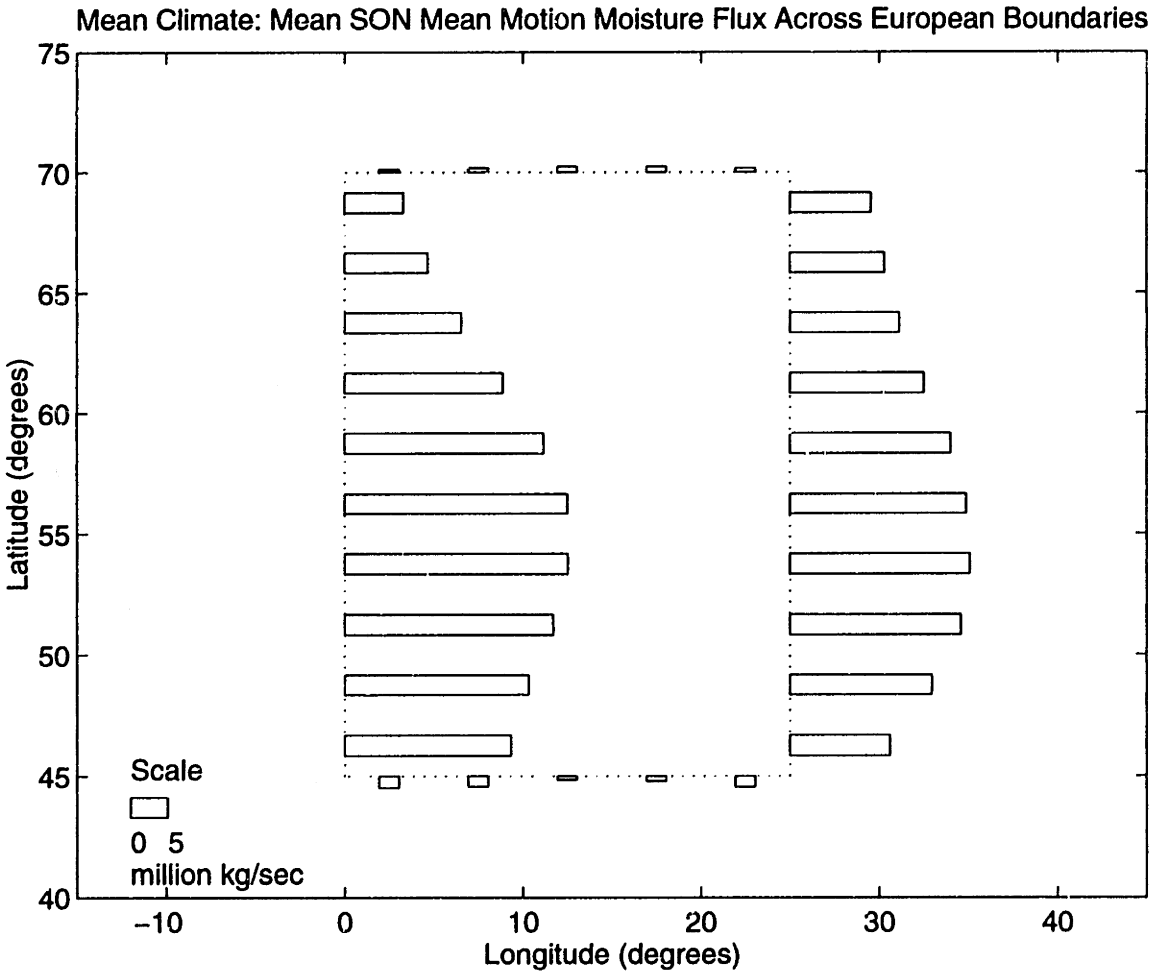

Figure A-10: SON Mean Climate Mean Motion Water Vapor Flux

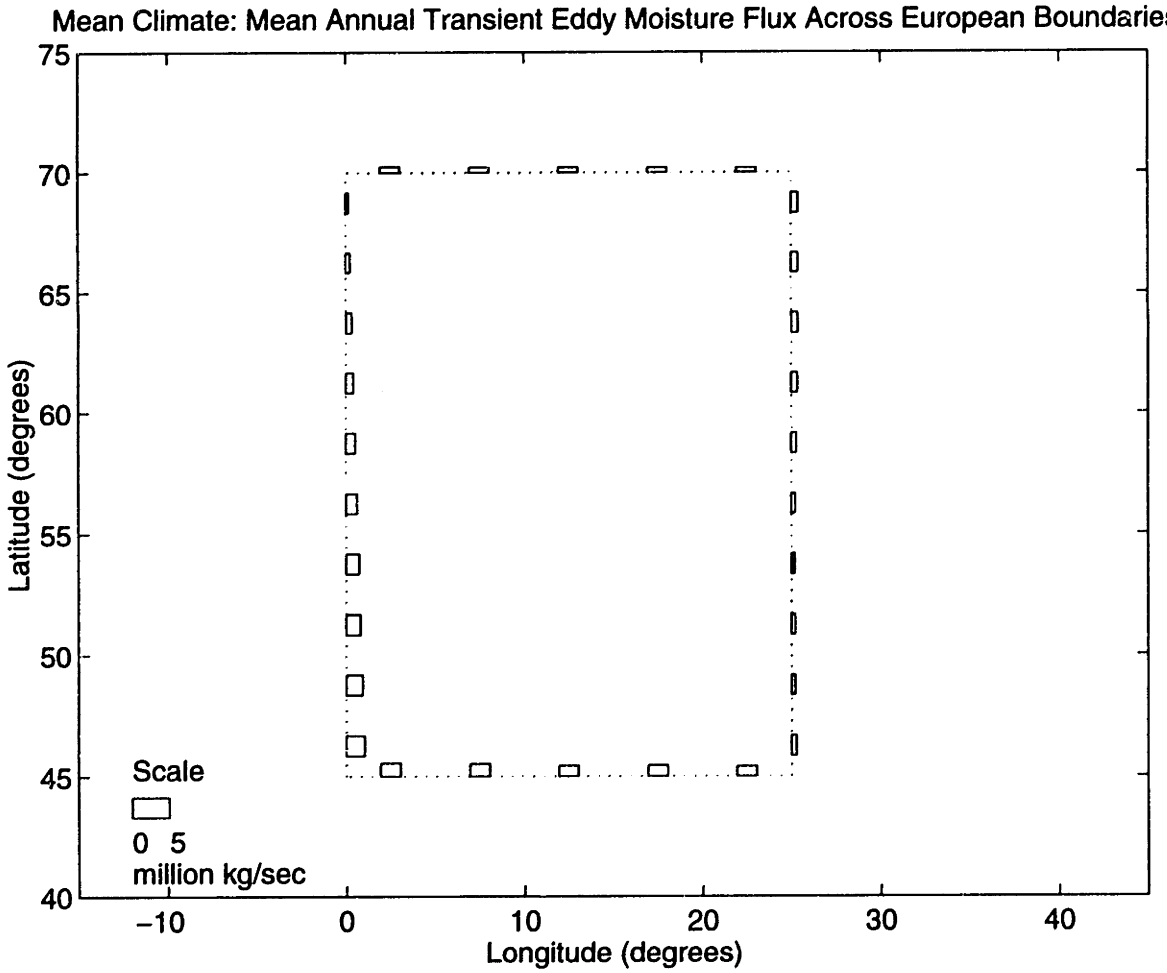

Figure A-11: Annual Mean Climate Transient Eddy Water Vapor Flux

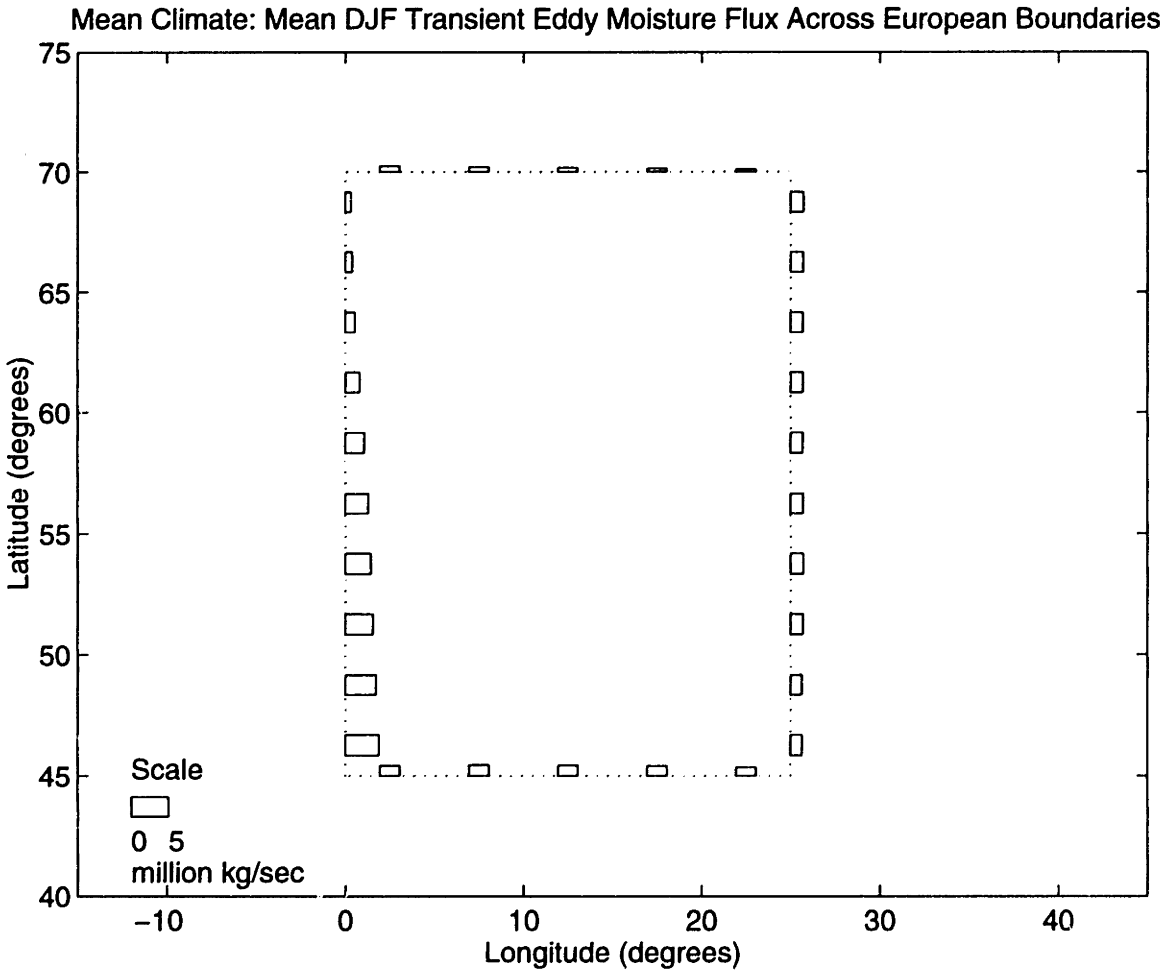

Figure A-12: DJF Mean Climate Transient Eddy Water Vapor Flux

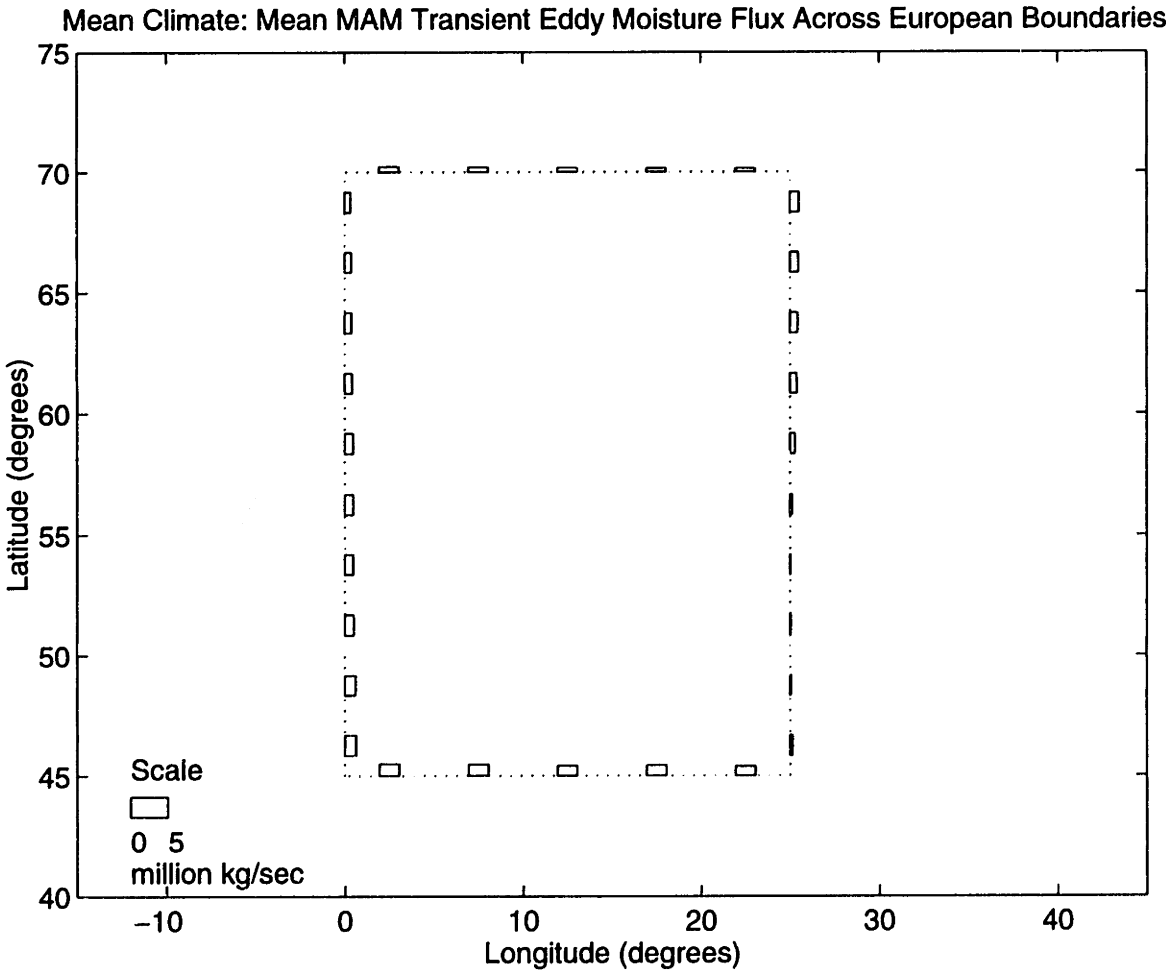

Figure A-13: MAM Mean Climate Transient Eddy Water Vapor Flux

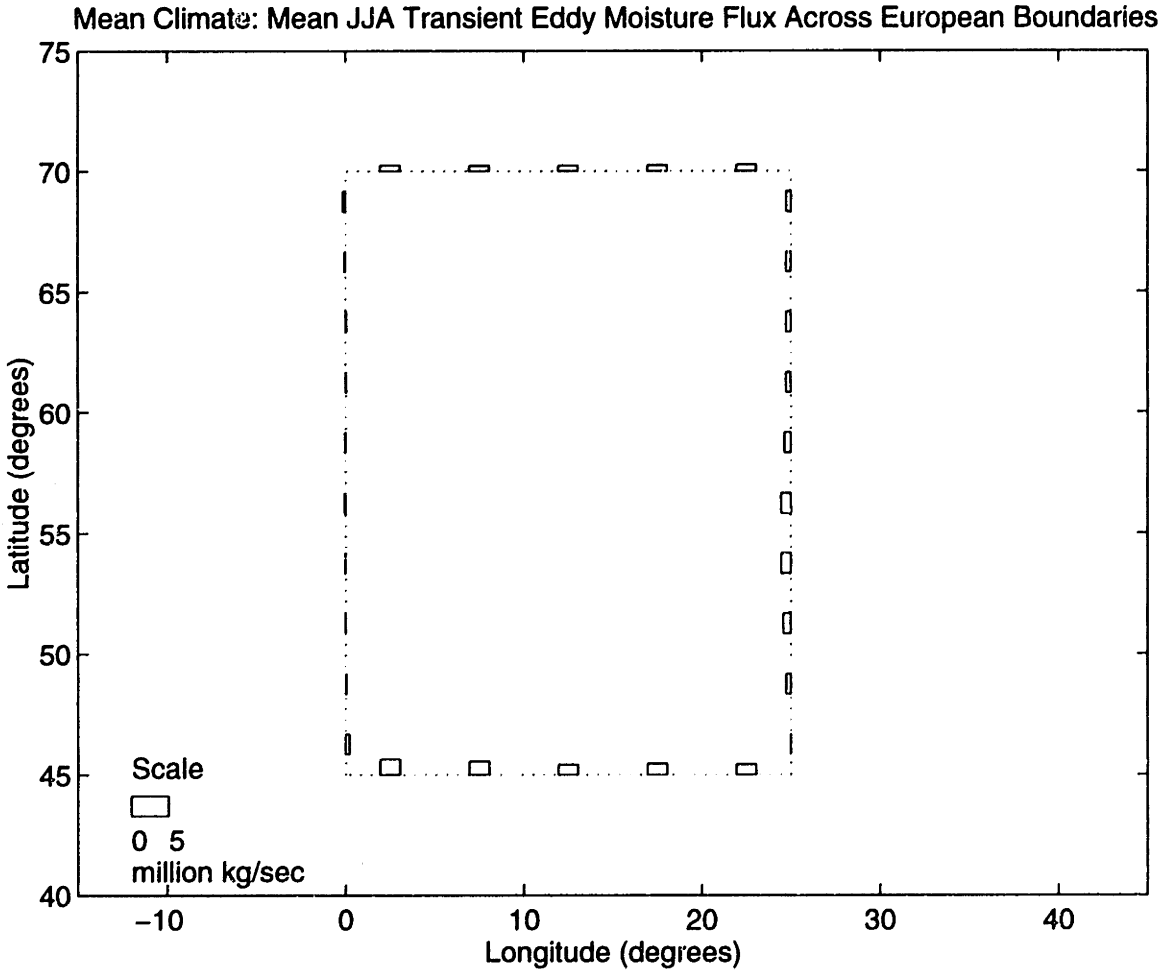

Figure A-14: JJA Mean Climate Transient Eddy Water Vapor Flux

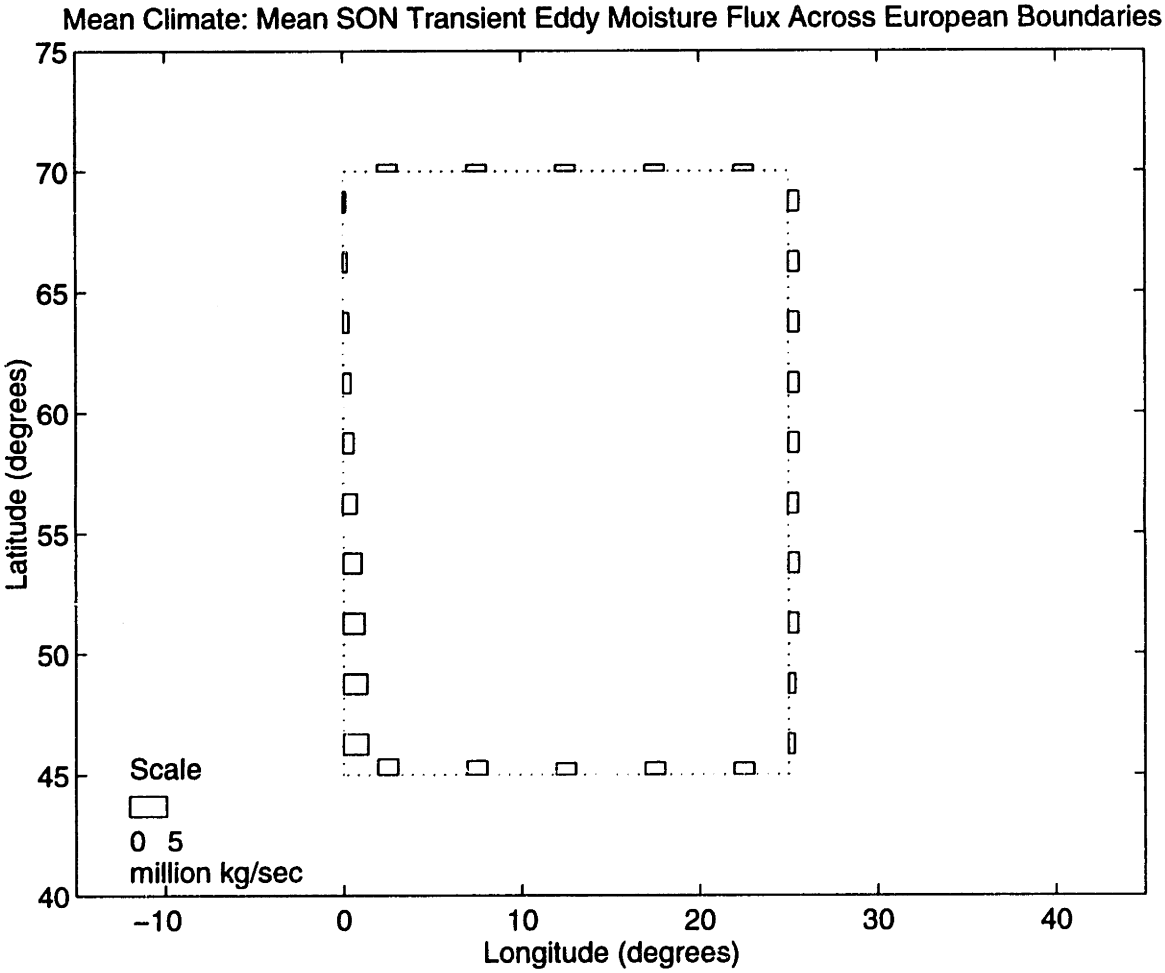

Figure A-15: SON Mean Climate Transient Eddy Water Vapor Flux

Appendix B

EOF Theory and Methodology

The following discussion is adapted from Appendix A of (Entekhabi 1988) and presents the theory underlying EOF calculations performed for this analysis. AS mentioned in Section 4.5.2, eigenvectors were constructed for 31 omega arrays, one array for each of the 31 years of the study. Each array contains omega values corresponding to 285 grid node locations. Each 285 x 1 array is represented by a column vector, $\mathbf{p}_n$, where n = 1 to 31. The 31 vectors were combined to form a 285 x 31 matrix, **P**. Thirty-one year means were removed from each element of the matrix to form matrix **F**. EOF calculations were performed on the covariance matrix formed from matrix **F** and its transpose.

The element of the **F** matrix is calculated as:

$$f_{ij} = p_{ij} - \mu_j \tag{B.1}$$

where:

$i = 1 \ldots 31$ (number of years)

$j = 1 \ldots 285$ (number of grid points)

The element of matrix **F** is represented by f_{ij}, the element of matrix **P** is represented by p_{ij}, and μ_j is the regional mean.

$\mathbf{F}$ is multiplied by its transpose to form a covariance matrix, $\mathbf{R}$ as shown below.

$$\mathbf{F}\mathbf{F}^{\mathbf{T}} = \mathbf{R} \tag{B.2}$$

The 31 columns in $\mathbf{F}$ are 31 points in a 285-dimensional space, $\mathbf{R}^{\mathbf{285}}$. The spaces that simultaneously fit the maximum possible number of the 31 points in $\mathbf{R}$ are the eigenvectors or principal components. Thus, the position of the first eigenvector must be such that the length of lines extending from each of the 31 points and perpendicular to the eigenvector are minimized. If a_i represents the length of the perpendicular line then the objective is to minimize

$$\sum_{i=1}^{n} a_i^2 \tag{B.3}$$

By substituting using Pythagorean's theorem this becomes the minimization of

$$\sum_{i=1}^{n} c_i^2 - \sum_{i=1}^{n} b_i^2 \tag{B.4}$$

Because the points in $\mathbf{R}$ are fixed, the above procedure is equivalent to maximizing

$$\sum_{i=1}^{n} b_i^2 \tag{B.5}$$

The set of values, b_i, represent the projection of data points on the vector, $\mathbf{e}$ which indicate the direction of the "component subspace." The product $\mathbf{Ze}$ represents the summation of all projection lengths or

$$\frac{1}{N} \sum_{N=1}^{N} [\mathbf{f}_n \cdot \mathbf{e}]^2 \tag{B.6}$$

This can be written as the maximization of

$$\frac{1}{N}[\mathbf{e}^T F F^T \mathbf{e}] = \mathbf{e}^T R \mathbf{e} \tag{B.7}$$

subject to

$$\mathbf{e}^T \mathbf{e} = 1 \tag{B.8}$$

The above constraint defines $\mathbf{e}$ as the unit vector.

Solving by the Lagrange method yields

$$\Xi = \mathbf{e}^T R \mathbf{e} - \lambda \mathbf{e}\mathbf{e}^T \tag{B.9}$$

Differentiating produces

$$\frac{\partial \Xi}{\partial \mathbf{e}} = \frac{\partial(\mathbf{e}^T \mathbf{R} \mathbf{e})}{\partial \mathbf{e}} - \lambda \frac{\partial(\mathbf{e}^T \mathbf{e}}{\partial \mathbf{e})} \tag{B.10}$$

$$= (\mathbf{R}\mathbf{e} + \mathbf{R}^T \mathbf{e}) - 2\lambda \mathbf{e} \tag{B.11}$$

$$= 2\mathbf{R}\mathbf{e} - 2\lambda \mathbf{e} \tag{B.12}$$

Or

$$\mathbf{R}\mathbf{e} = \lambda \mathbf{e} \tag{B.13}$$

This equation can be expressed as:

$$(\mathbf{R} - \lambda \mathbf{I})\mathbf{e} = 0 \tag{B.14}$$

Here, **e** corresponds to the characteristic value λ and **I** is a 285 x 285 identity matrix.

This produces a system of 285 equations with 285 unknowns. Nontrivial solutions are possible only if

$$determinant(\mathbf{R} - \lambda\mathbf{I}) = 0 \tag{B.15}$$

Generalizing Equation (A.15) for j = 1. . .285 produces

$$\lambda = \mathbf{E}^{-1}\mathbf{R}\mathbf{E} \tag{B.16}$$

subject to $\mathbf{E}\mathbf{E}^T = \mathbf{I}$

The values, r_{jj} values represent the variance of $\mathbf{z}_j$ vectors. The elements λ_{jj} are the eigenvalues of matrix **R** and thus, indicate the variance explained by the j-th eigenvector.

$$\sum_{j=1}^{p} \lambda_{jj} = \sum_{j=1}^{p} r_{jj} = p \tag{B.17}$$

Thus the each successive principal component captures the maximum fraction of the total variance possible while maintaining orthogonality.

An eigenvector multiplier can be thought of as the scalar quantity which, if multiplied, by an eigenvector matrix will yield the original data matrix, **F**. In this analysis, multipliers obtained for each eigenvector represent the "importance" of the given eigenvector in a given year.

$$\mathbf{M} = \mathbf{E}^{\mathbf{T}}\mathbf{F} \tag{B.18}$$

Appendix C

Rotated Eigenvector Patterns

Figure	Season	Eigenvector Pattern	Number of Eigenvectors Rotated
C-1	JJ	First	3
C-2	JJ	Second	3
C-3	JJ	Third	3
C-4	AS	First	3
C-5	AS	Second	3
C-6	AS	Third	3
C-7	JJ	First	5
C-8	JJ	Second	5
C-9	JJ	Third	5
C-10	AS	First	5
C-11	AS	Second	5
C-12	AS	Third	5
C-13	JJ	First	10
C-14	JJ	Second	10
C-15	JJ	Third	10
C-16	AS	First	10
C-17	AS	Second	10
C-18	AS	Third	10
C-19	JJ	First	80
C-20	JJ	Second	80
C-21	JJ	Third	80
C-22	AS	First	80
C-23	AS	Second	80
C-24	AS	Third	80

Table C.1: Catalog of Rotated Eigenvector Patterns

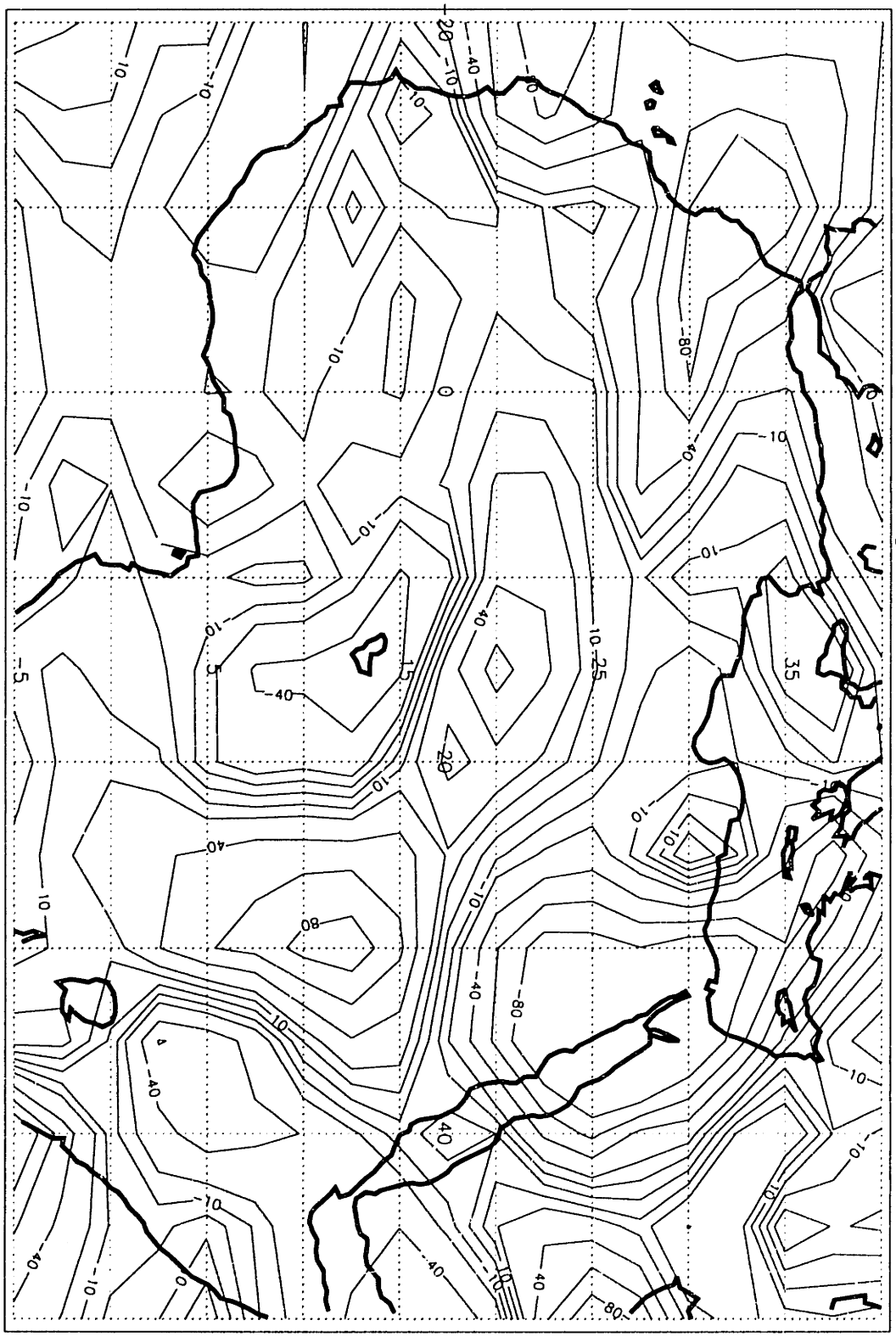

Figure C-1: First JJ Eigenvector - Based on Rotation of First Three Vectors

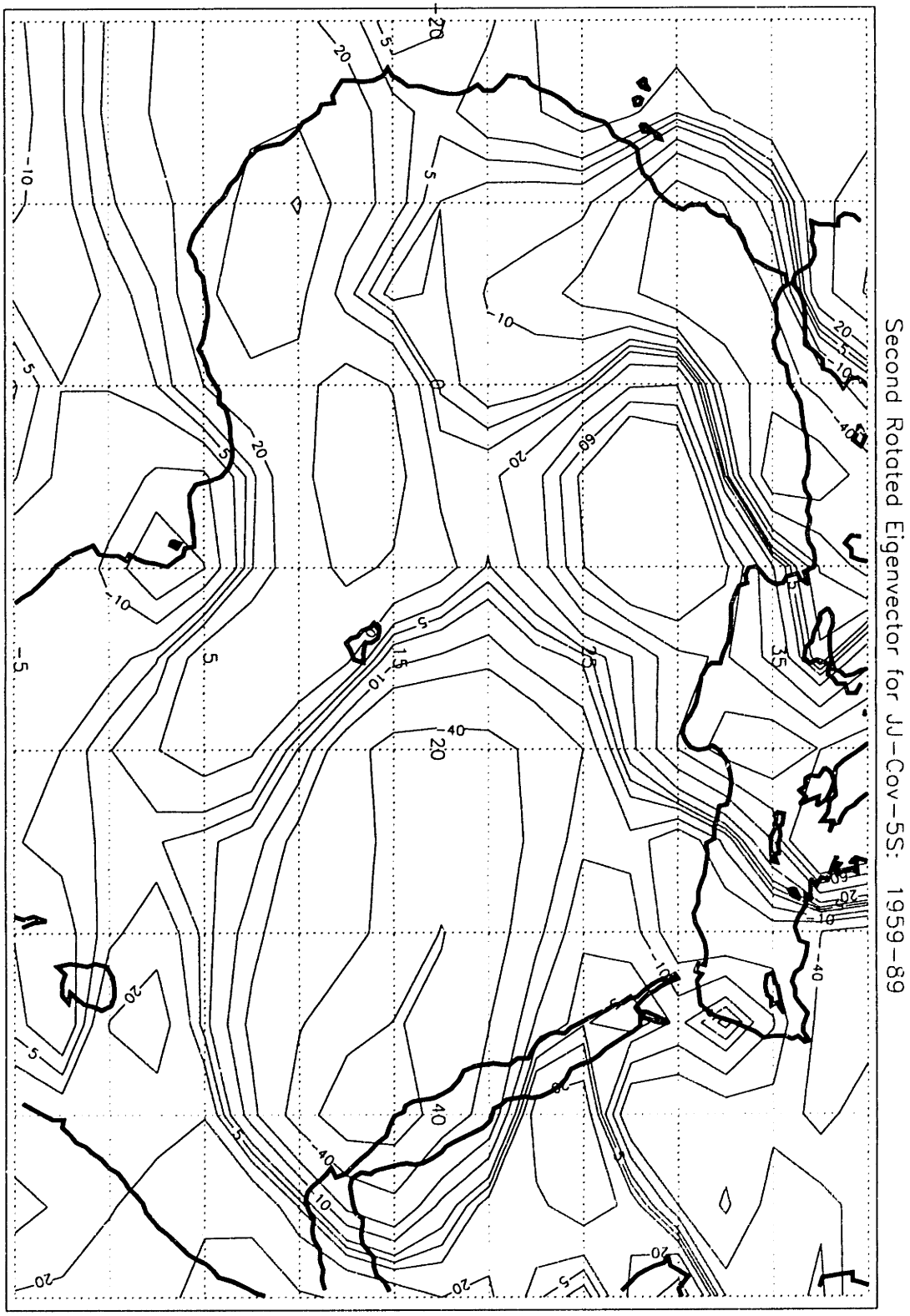

Figure C-2: Second JJ Eigenvector - Based on Rotation of First Three Vectors

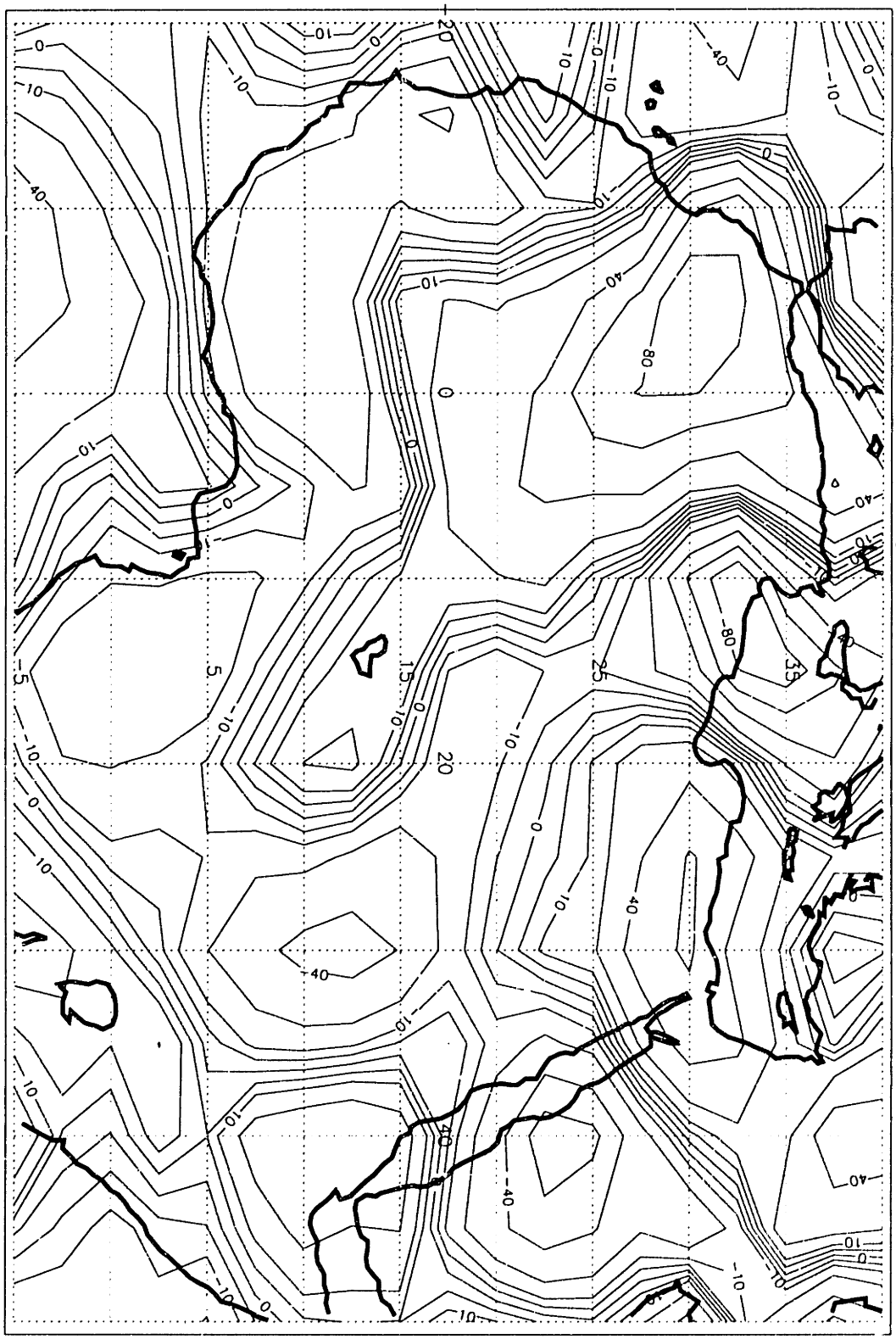

Figure C-3: Third JJ Eigenvector - Based on Rotation of First Three Vectors

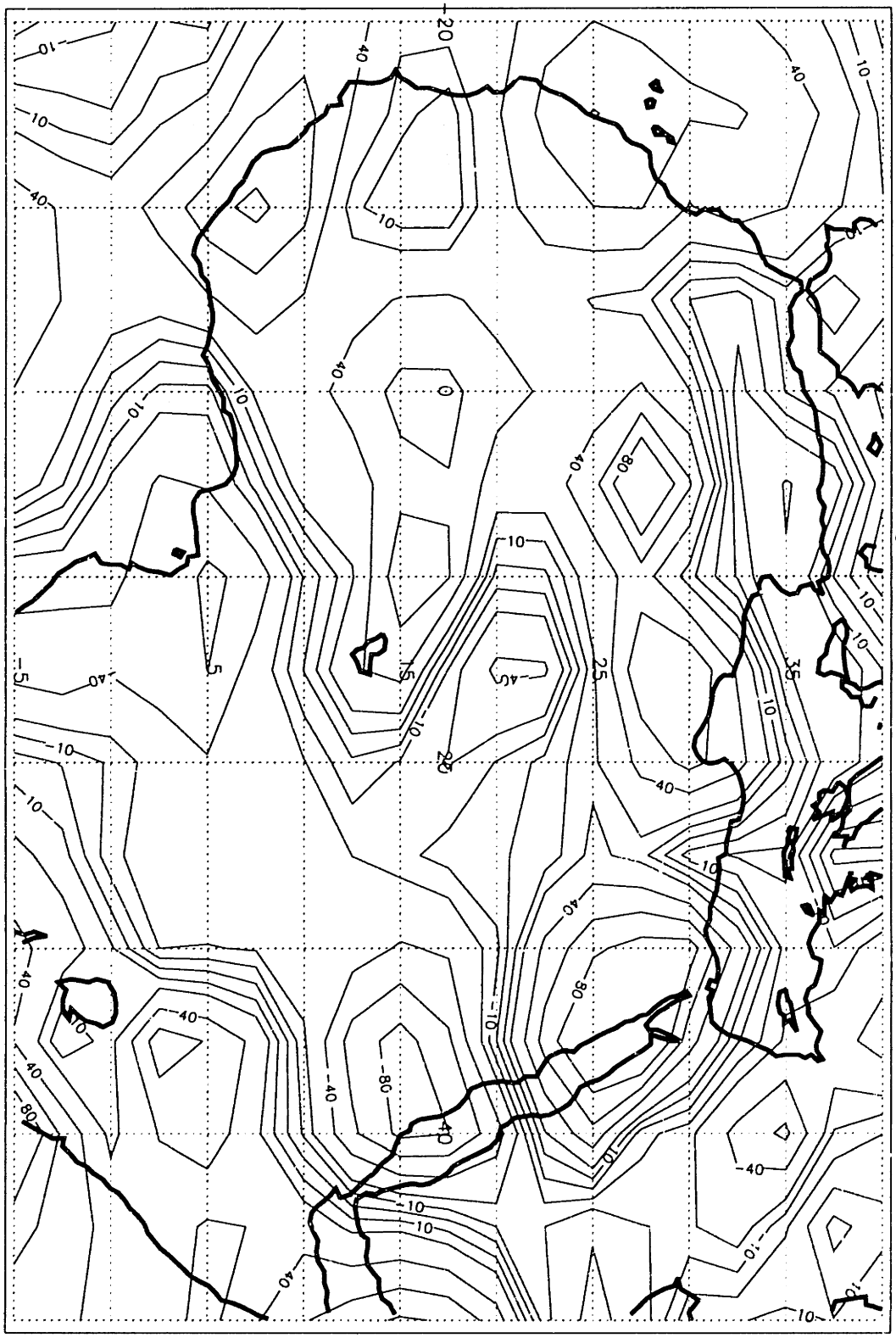

Figure C-4: First AS Eigenvector - Based on Rotation of First Three Vectors

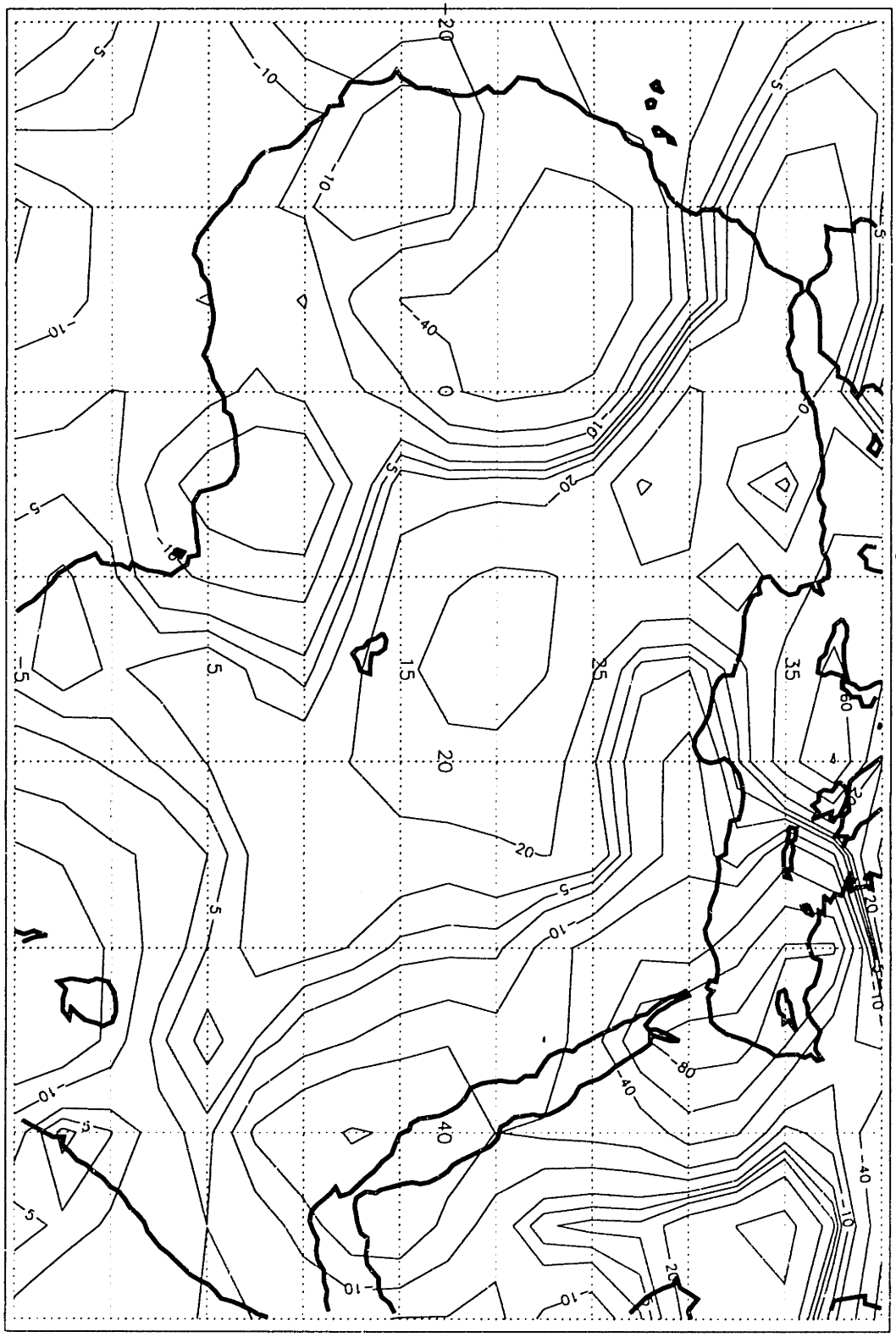

Figure C-5: Second AS Eigenvector - Based on Rotation of First Three Vectors

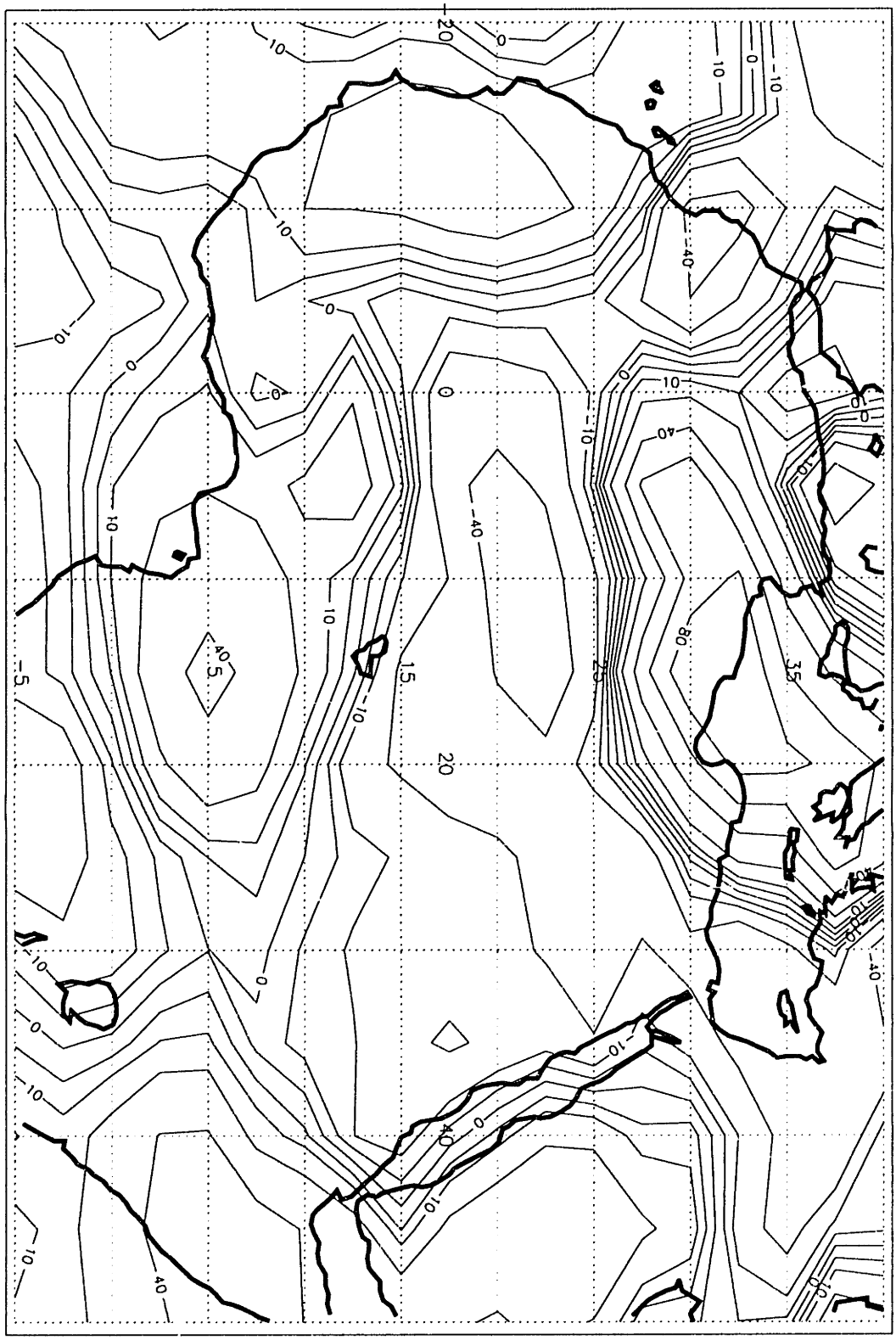

Figure C-6: Third AS Eigenvector - Based on Rotation of First Three Vectors

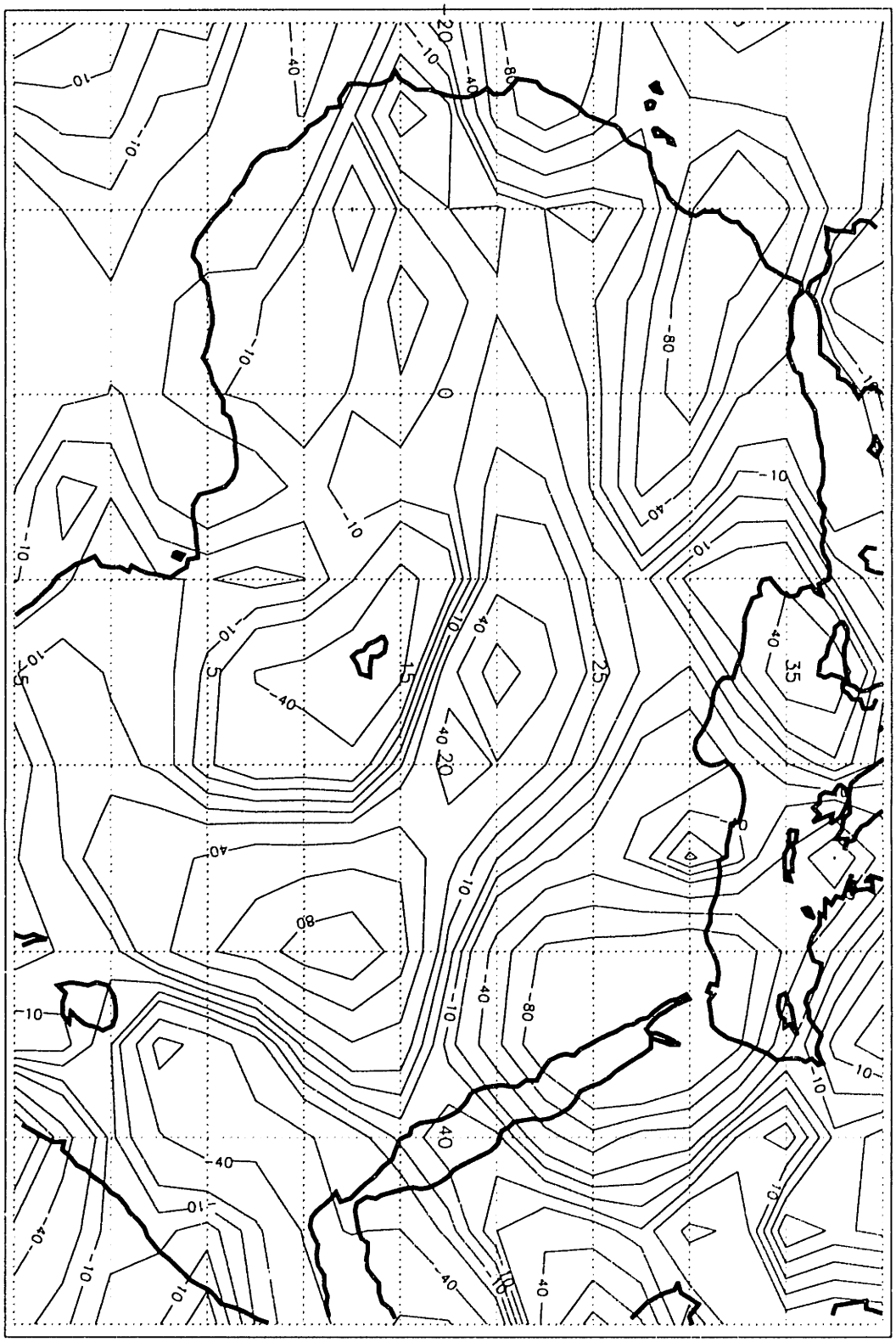

Figure C-7: First JJ Eigenvector - Based on Rotation of First Five Vectors

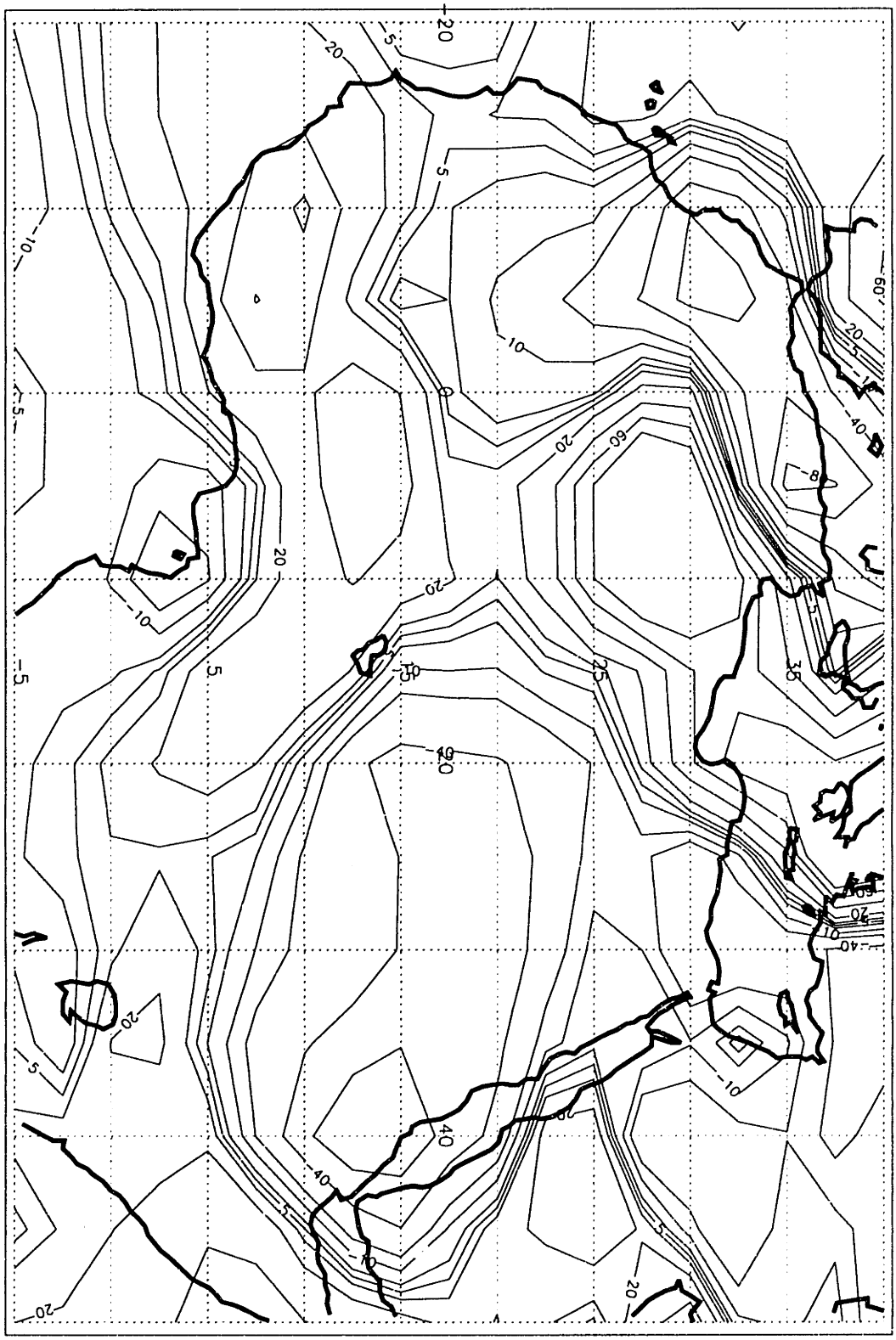

Figure C-8: Second JJ Eigenvector - Based on Rotation of First Five Vectors

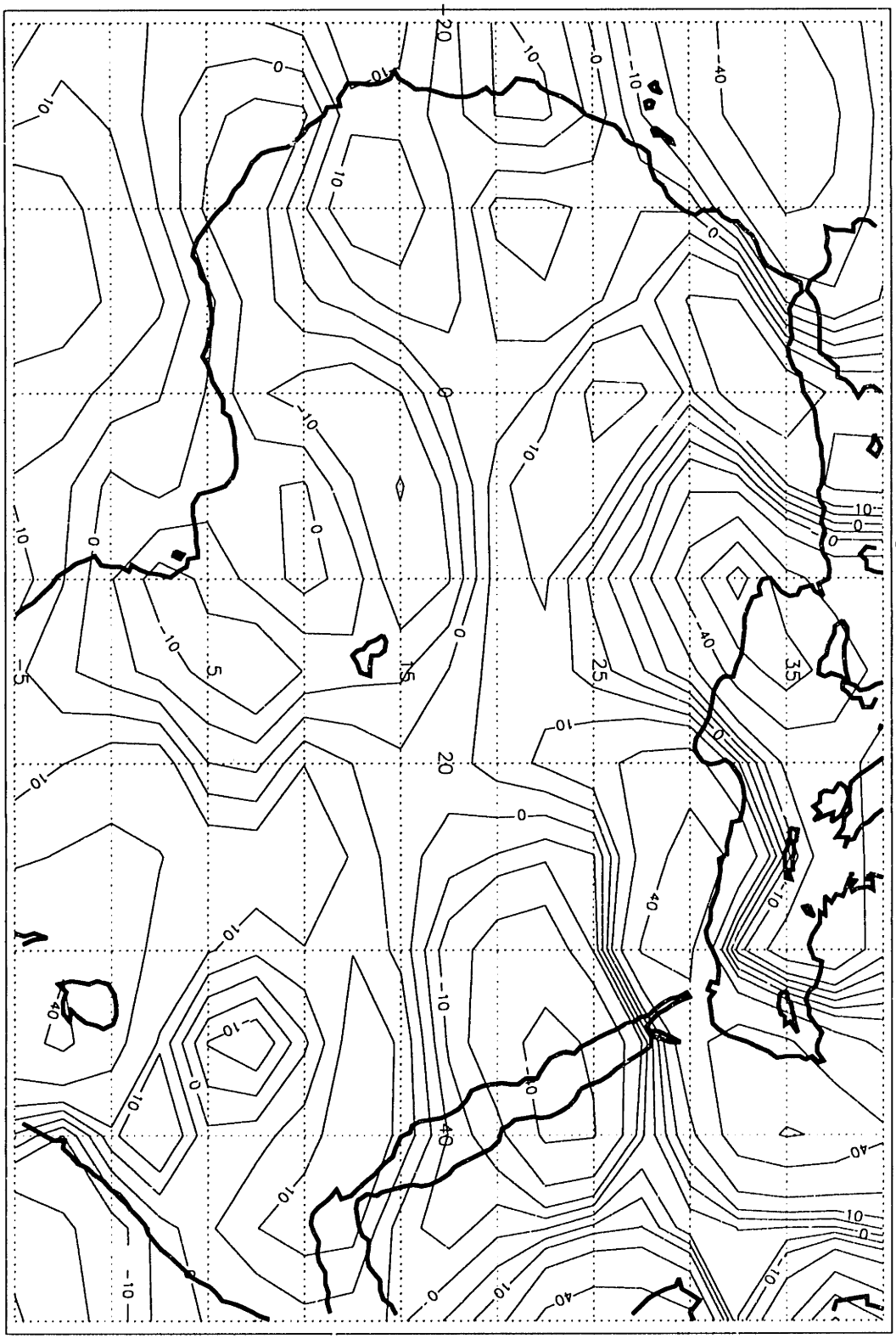

Figure C-9: Third JJ Eigenvector - Based on Rotation of First Five Vectors

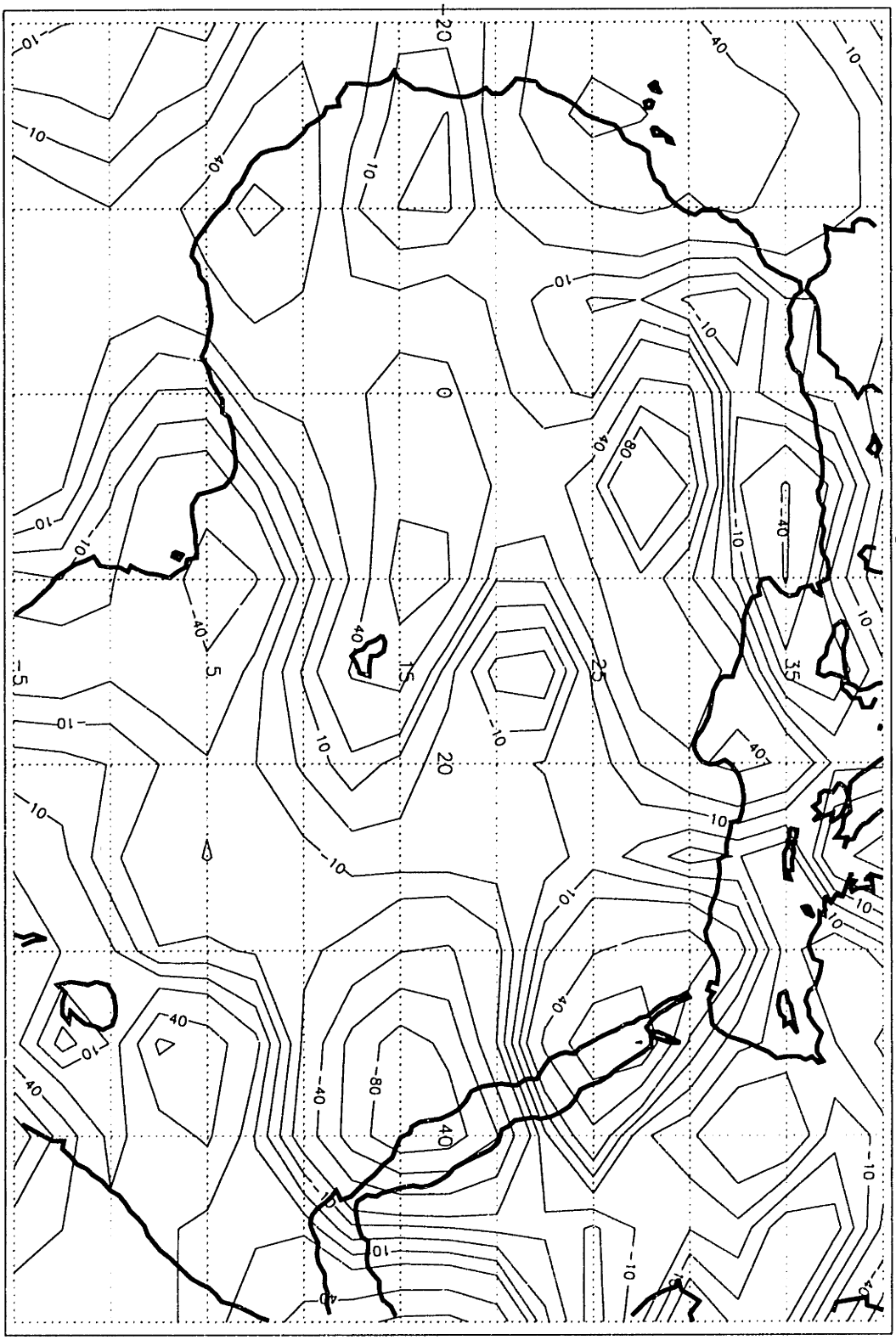

Figure C-10: First AS Eigenvector - Based on Rotation of First Five Vectors

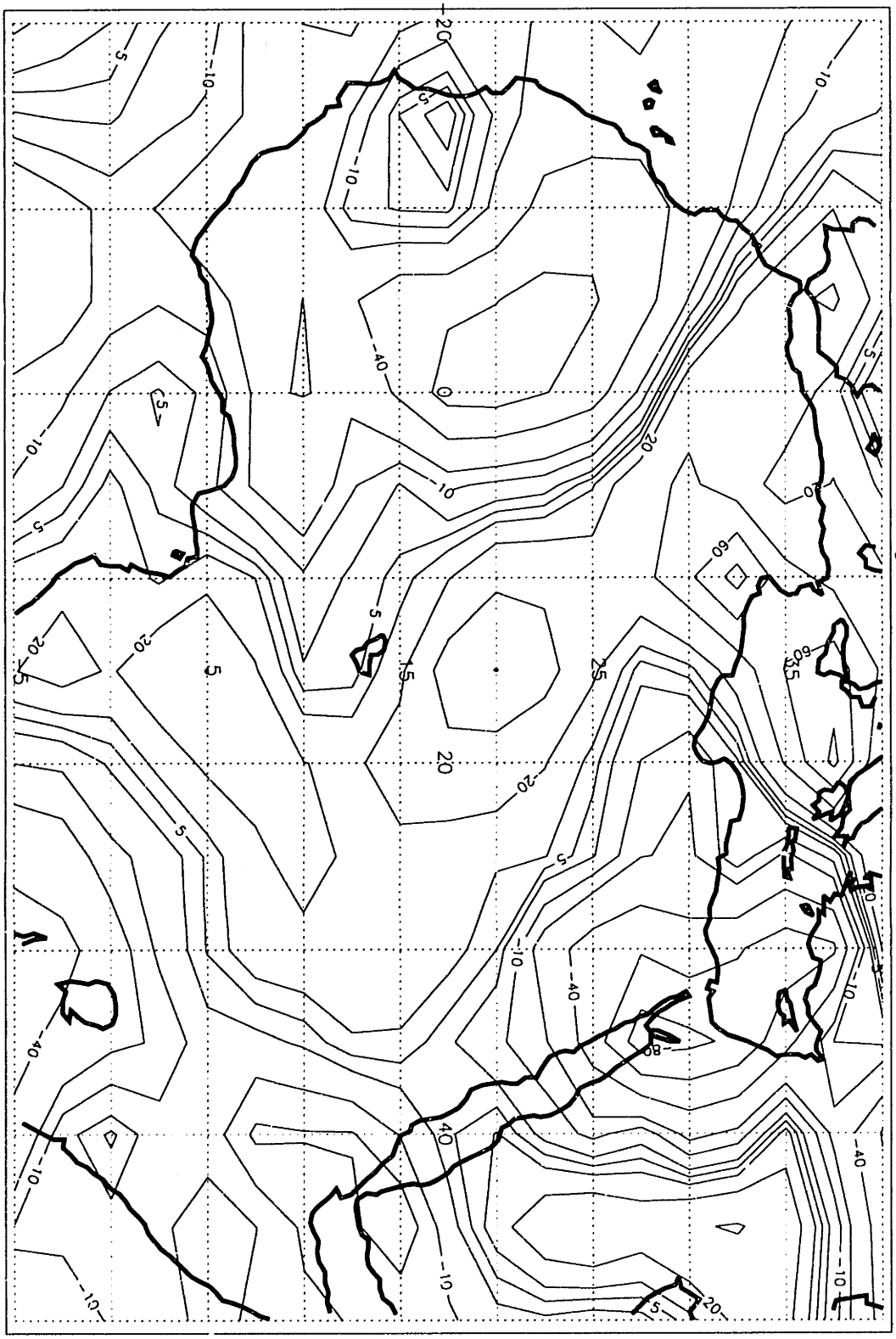

Figure C-11: Second AS Eigenvector - Based on Rotation of First Five Vectors

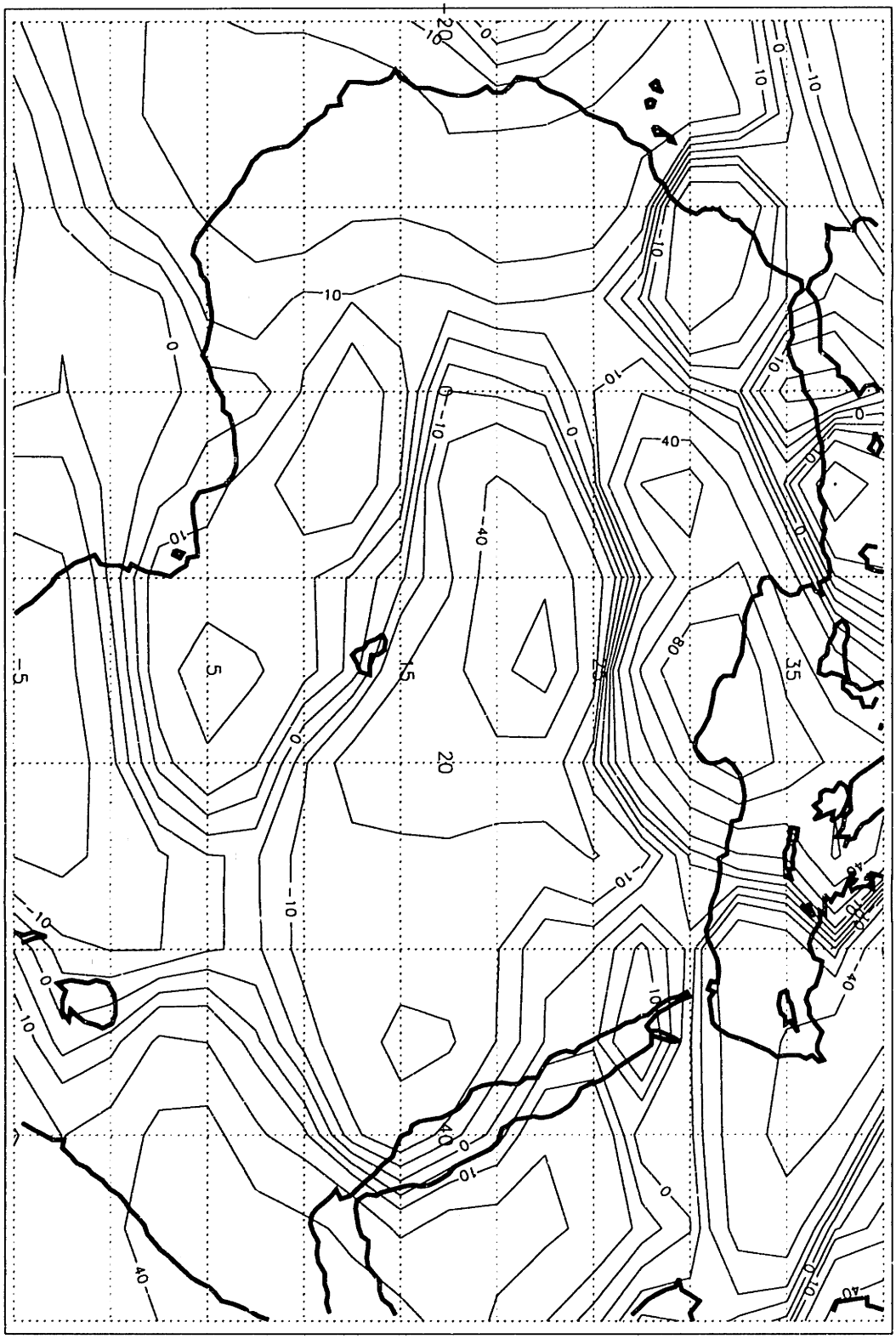

Figure C-12: Third AS Eigenvector - Based on Rotation of First Five Vectors

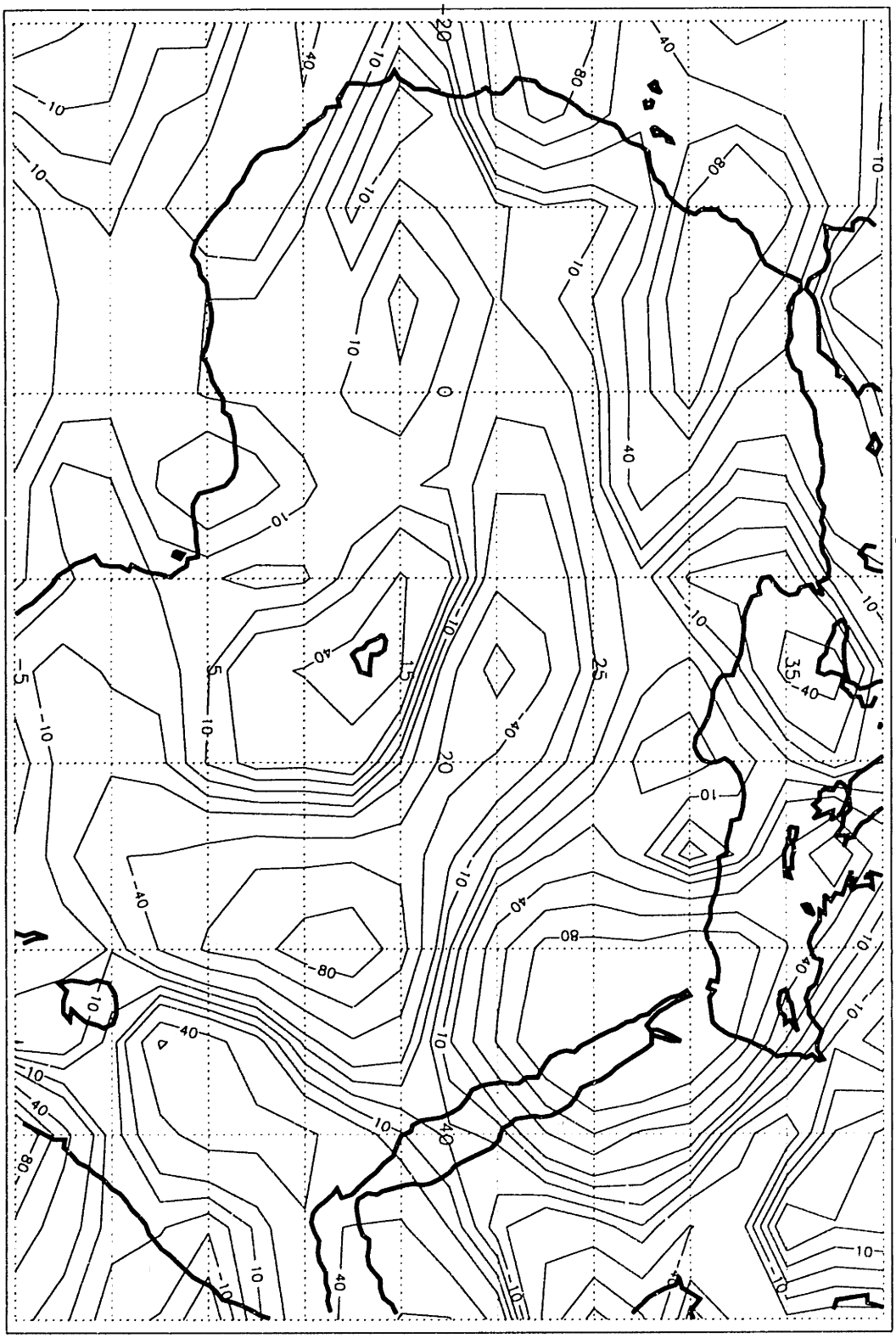

Figure C-13: First JJ Eigenvector - Based on Rotation of First Ten Vectors

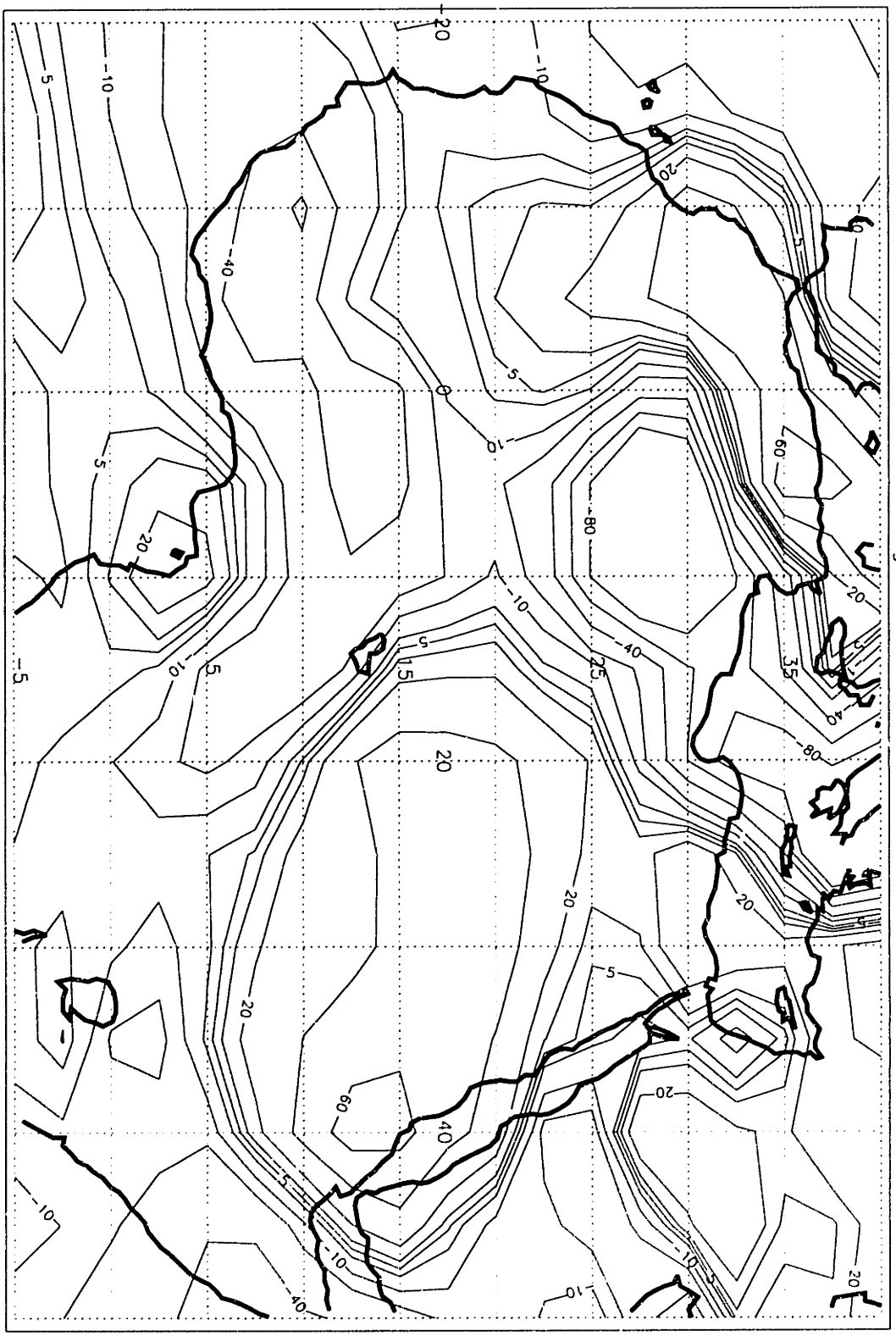

Figure C-14: Second JJ Eigenvector - Based on Rotation of First Ten Vectors

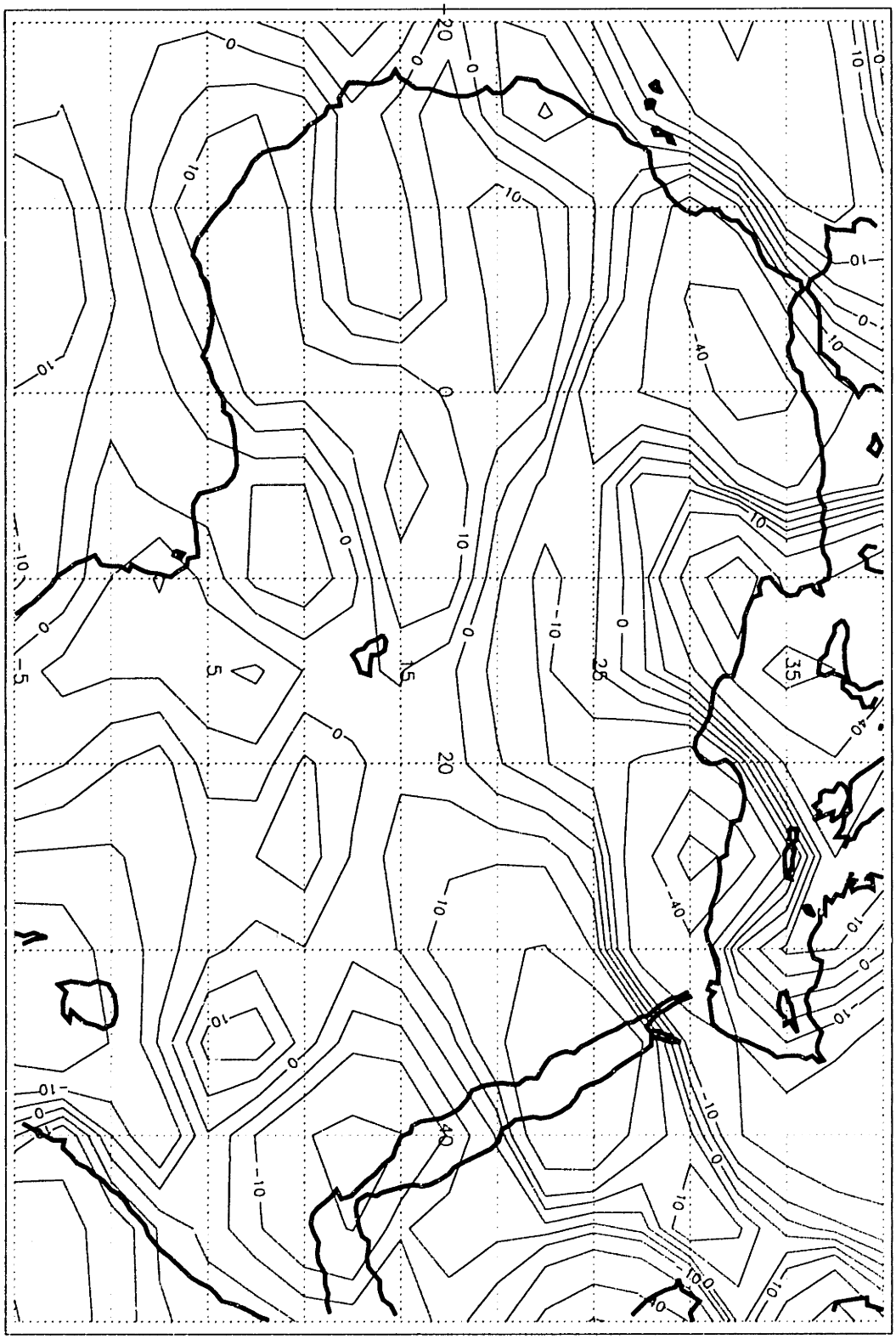

Figure C-15: Third JJ Eigenvector - Based on Rotation of First Ten Vectors

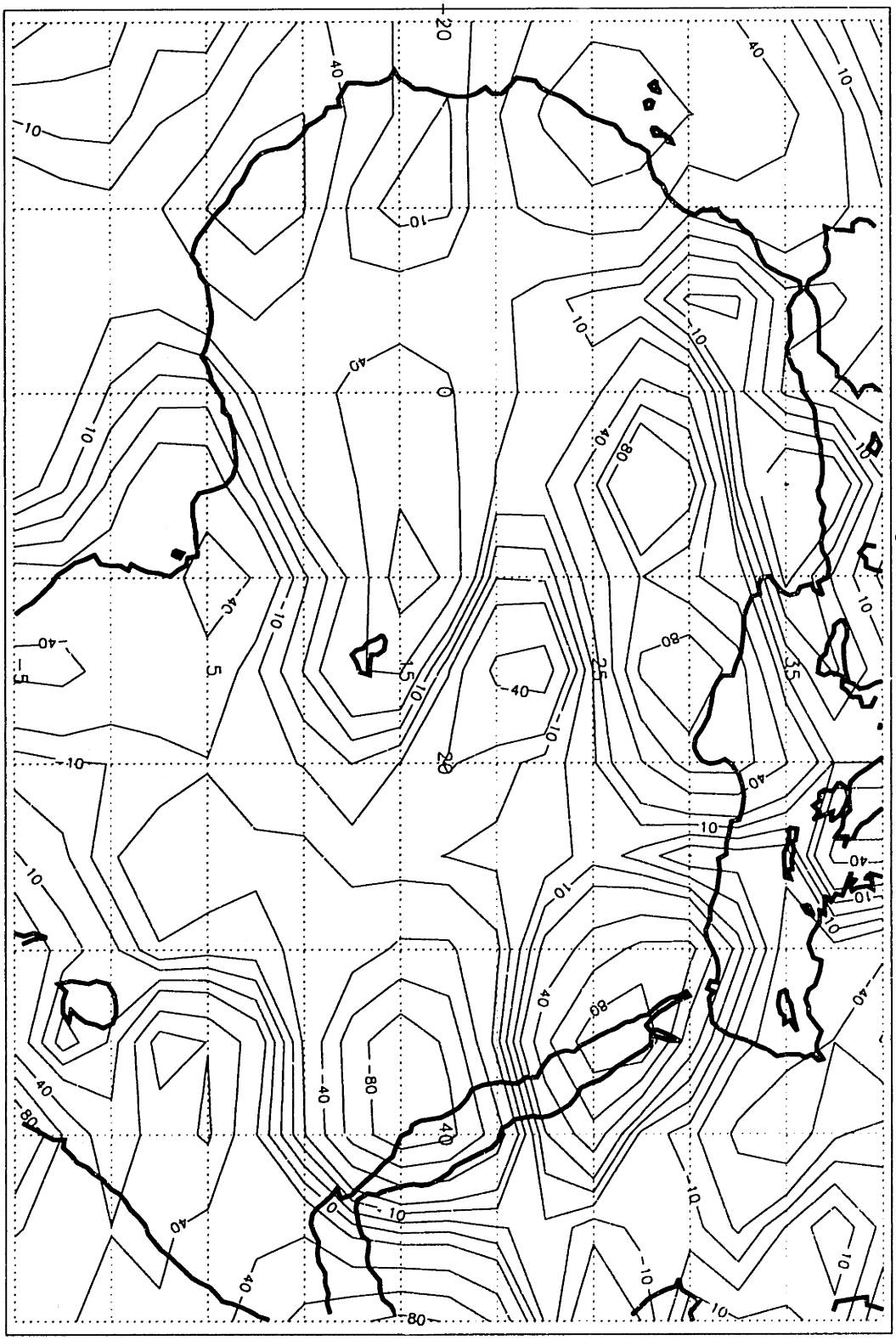

Figure C-16: First AS Eigenvector - Based on Rotation of First Ten Vectors

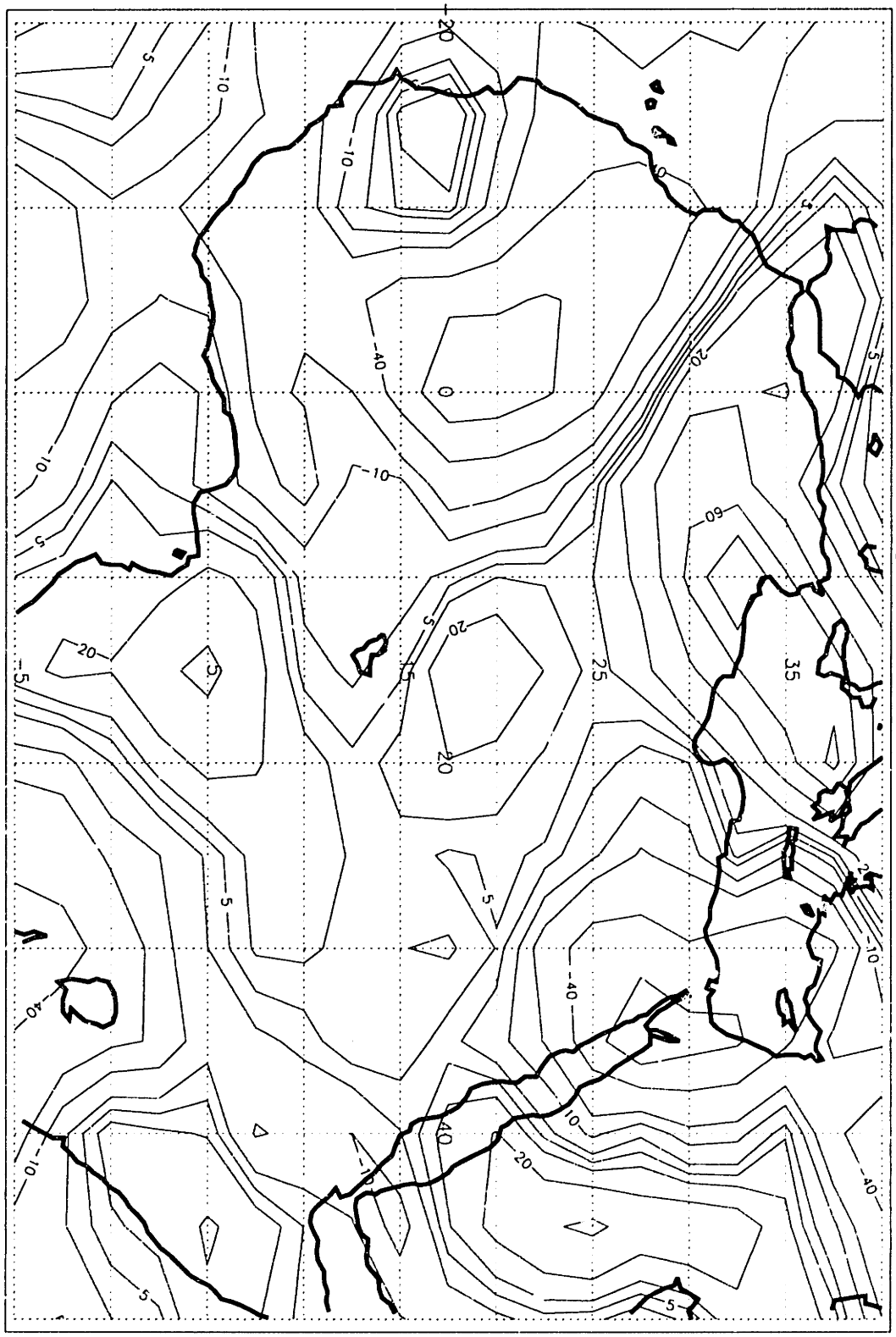

Figure C-17: Second AS Eigenvector - Based on Rotation of First Ten Vectors

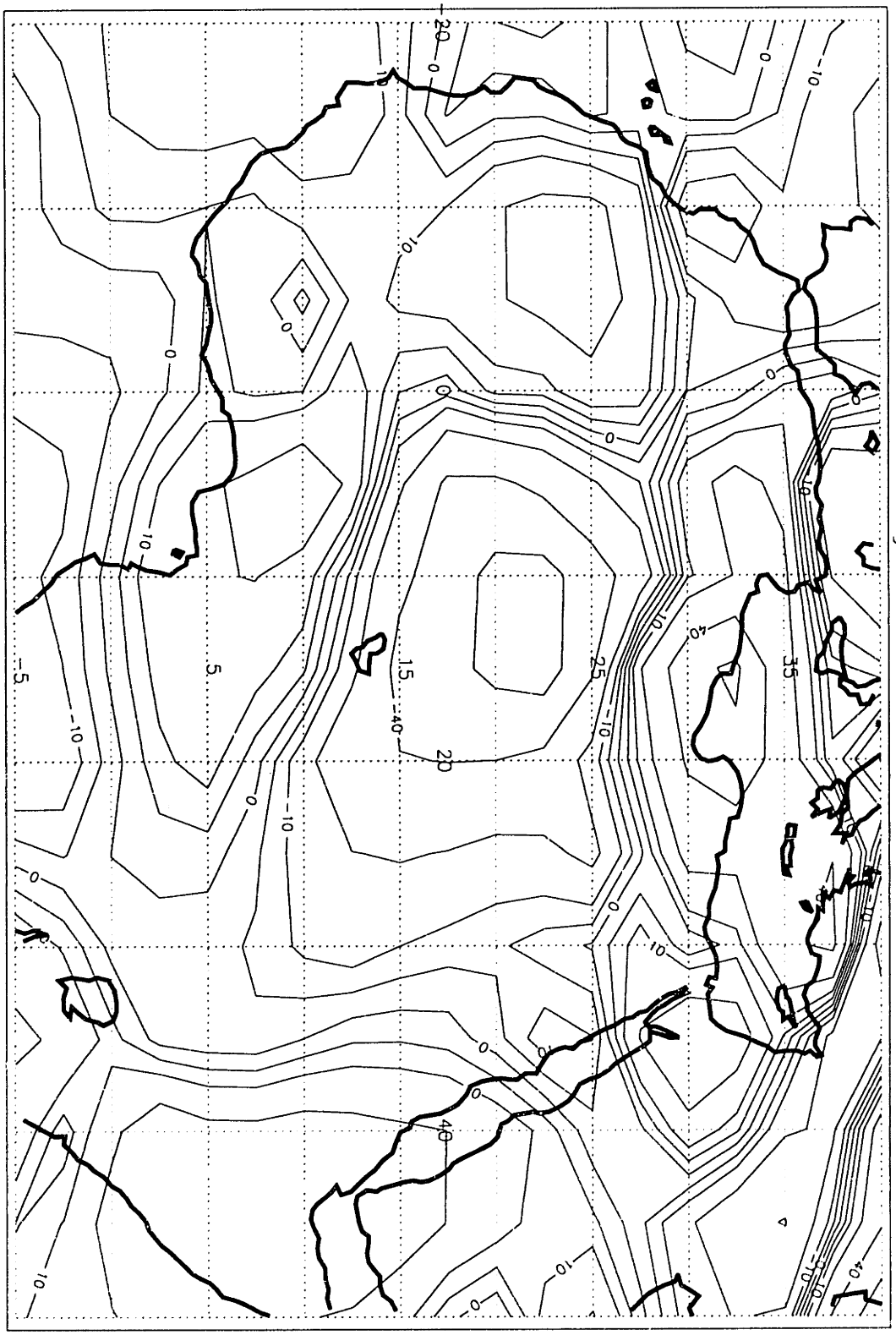

Figure C-18: Third AS Eigenvector - Based on Rotation of First Ten Vectors

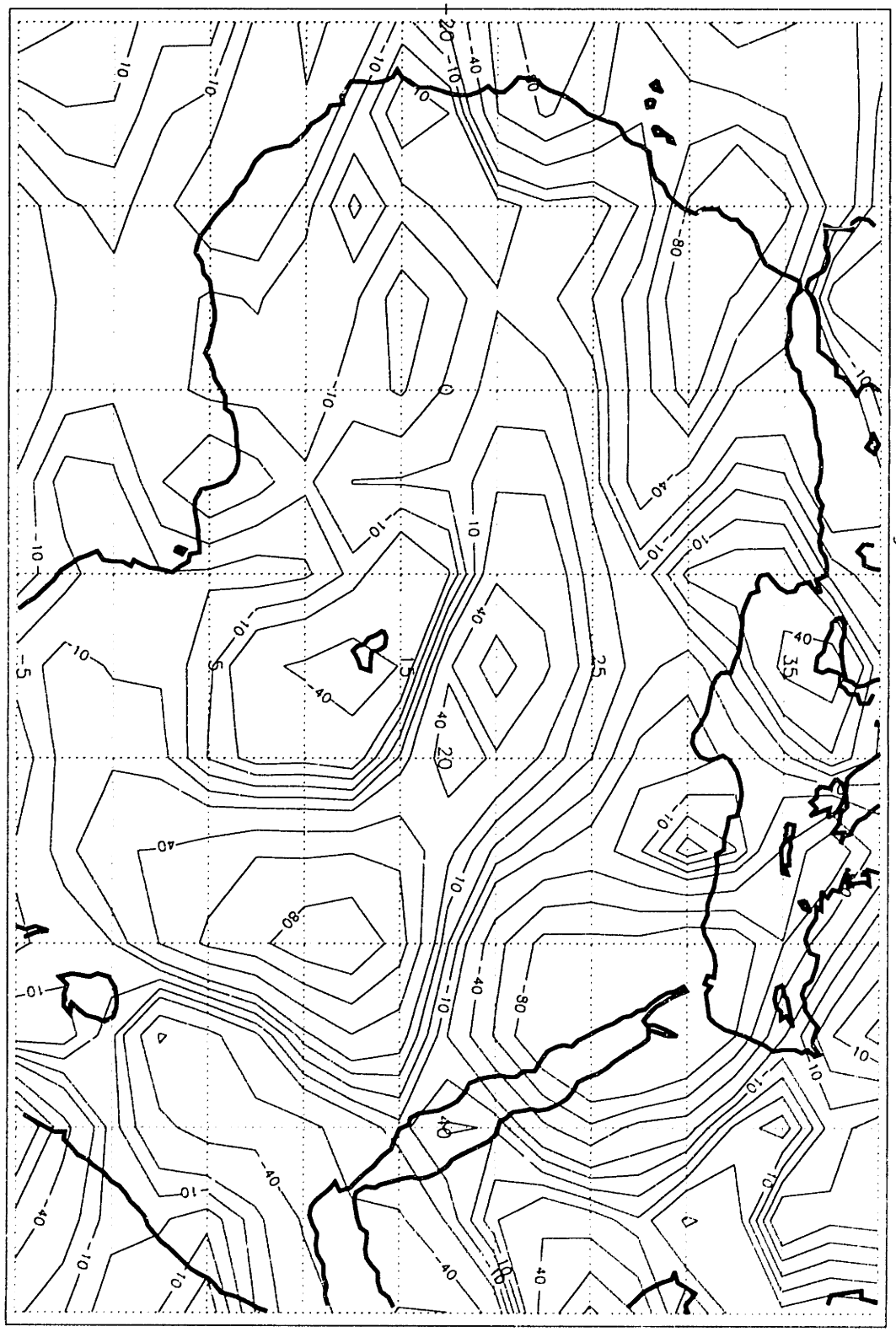

Figure C-19: First JJ Eigenvector - Based on Rotation of First 80 Vectors

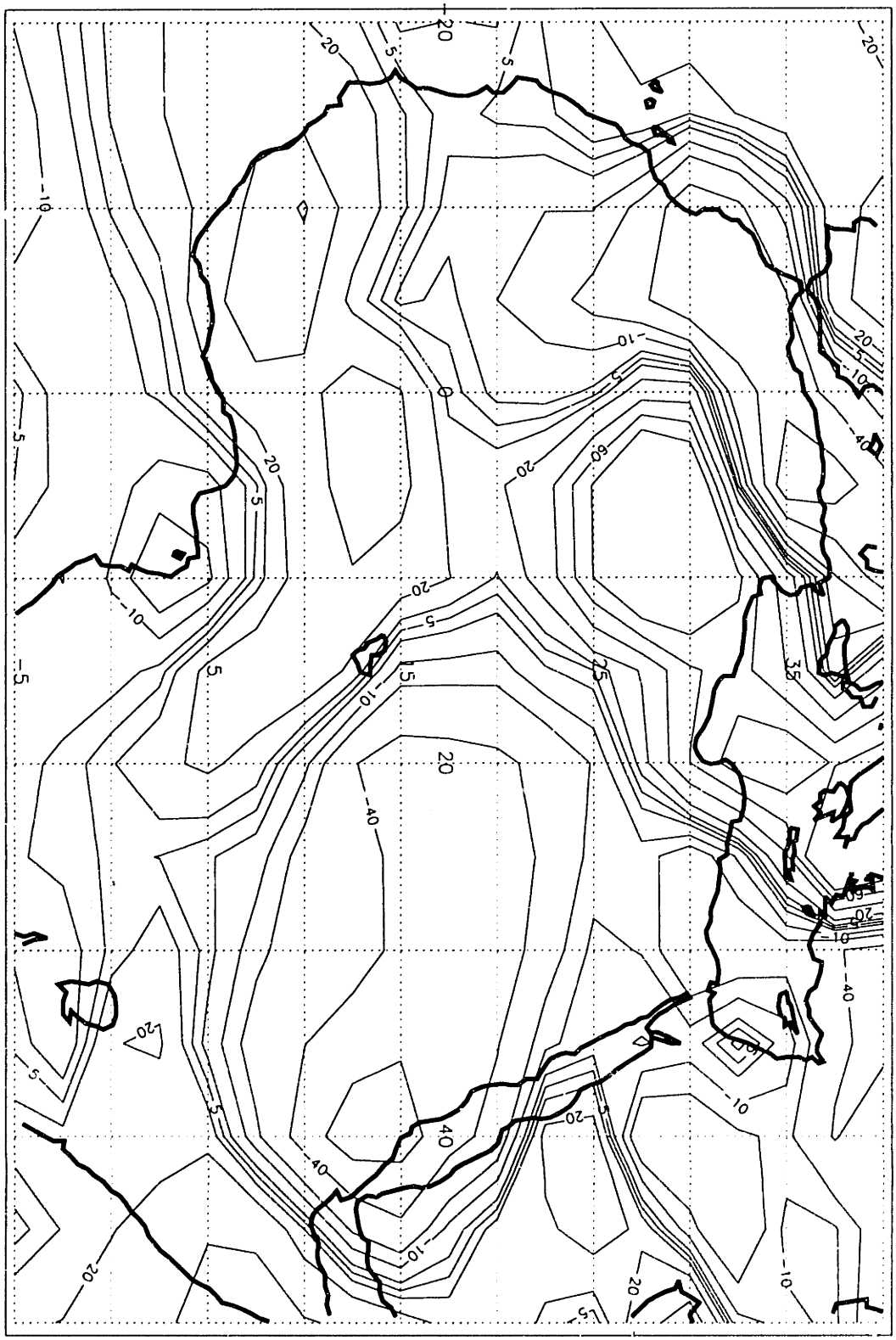

Figure C-20: Second JJ Eigenvector - Based on Rotation of First 80 Vectors

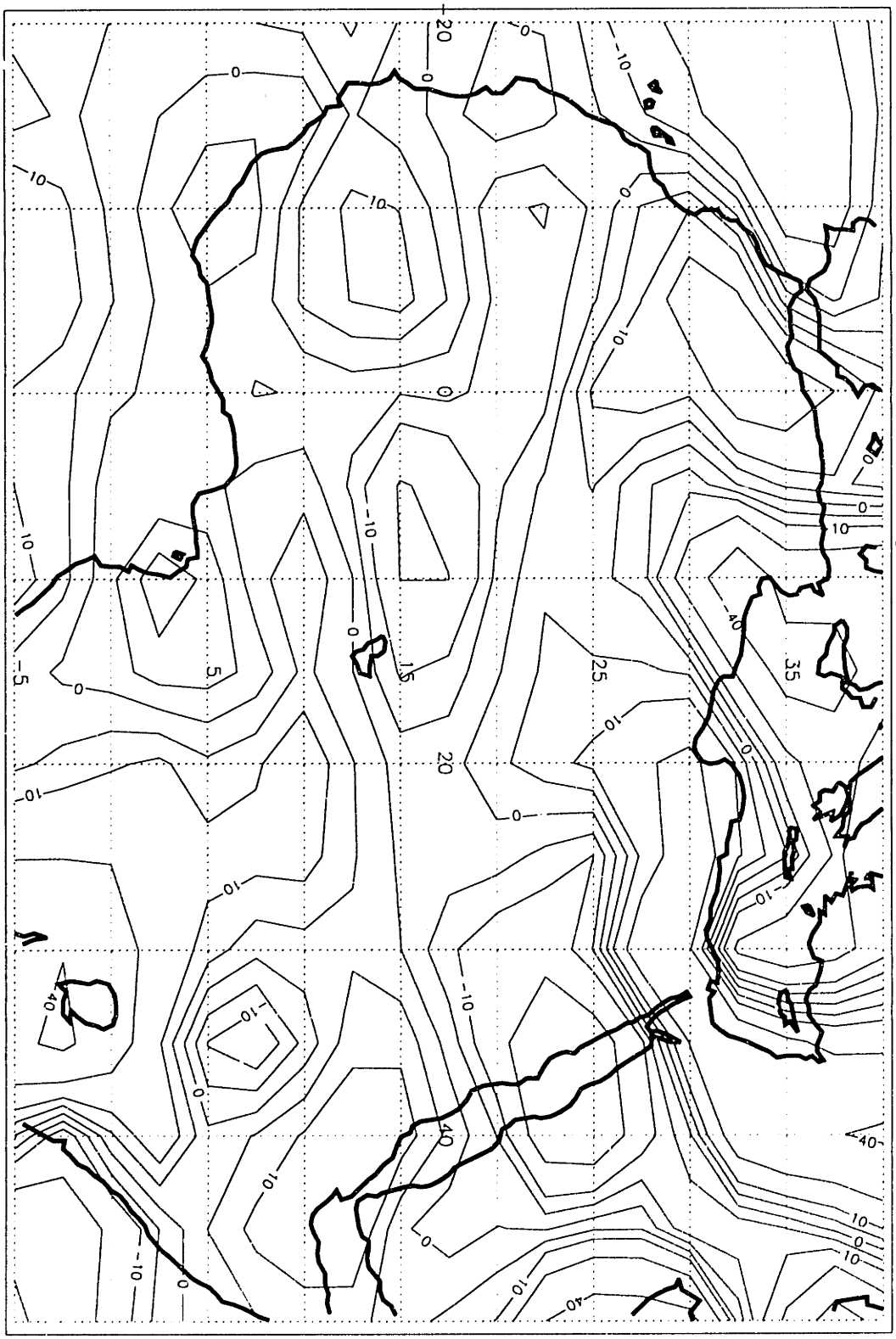

Figure C-21: Third JJ Rotated Eigenvector - Based on Rotation of First 80 Vectors

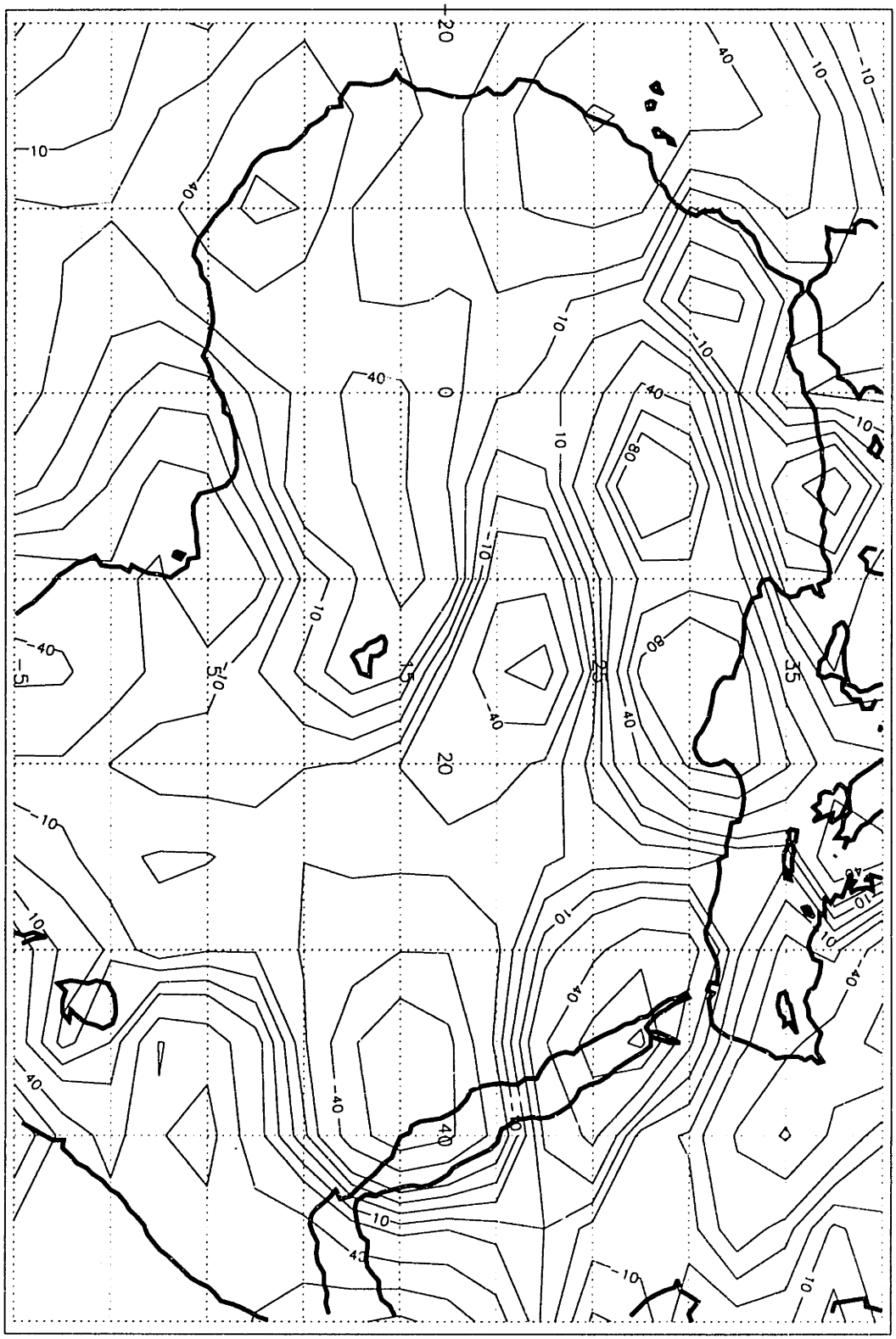

Figure C-22: First AS Eigenvector - Based on Rotation of First 80 Vectors

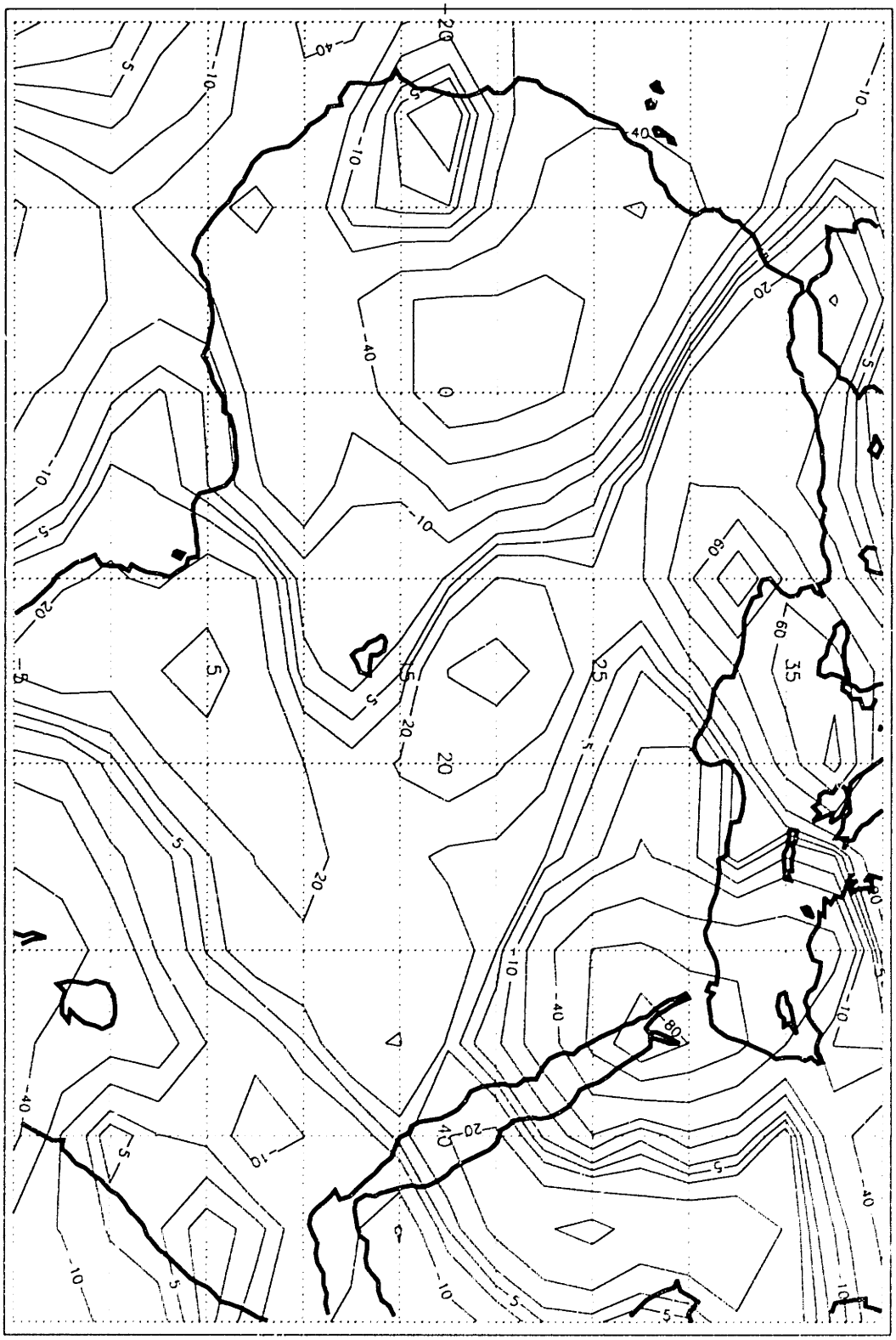

Figure C-23: Second AS Rotated Eigenvector - Based on Rotation of First 80 Vectors

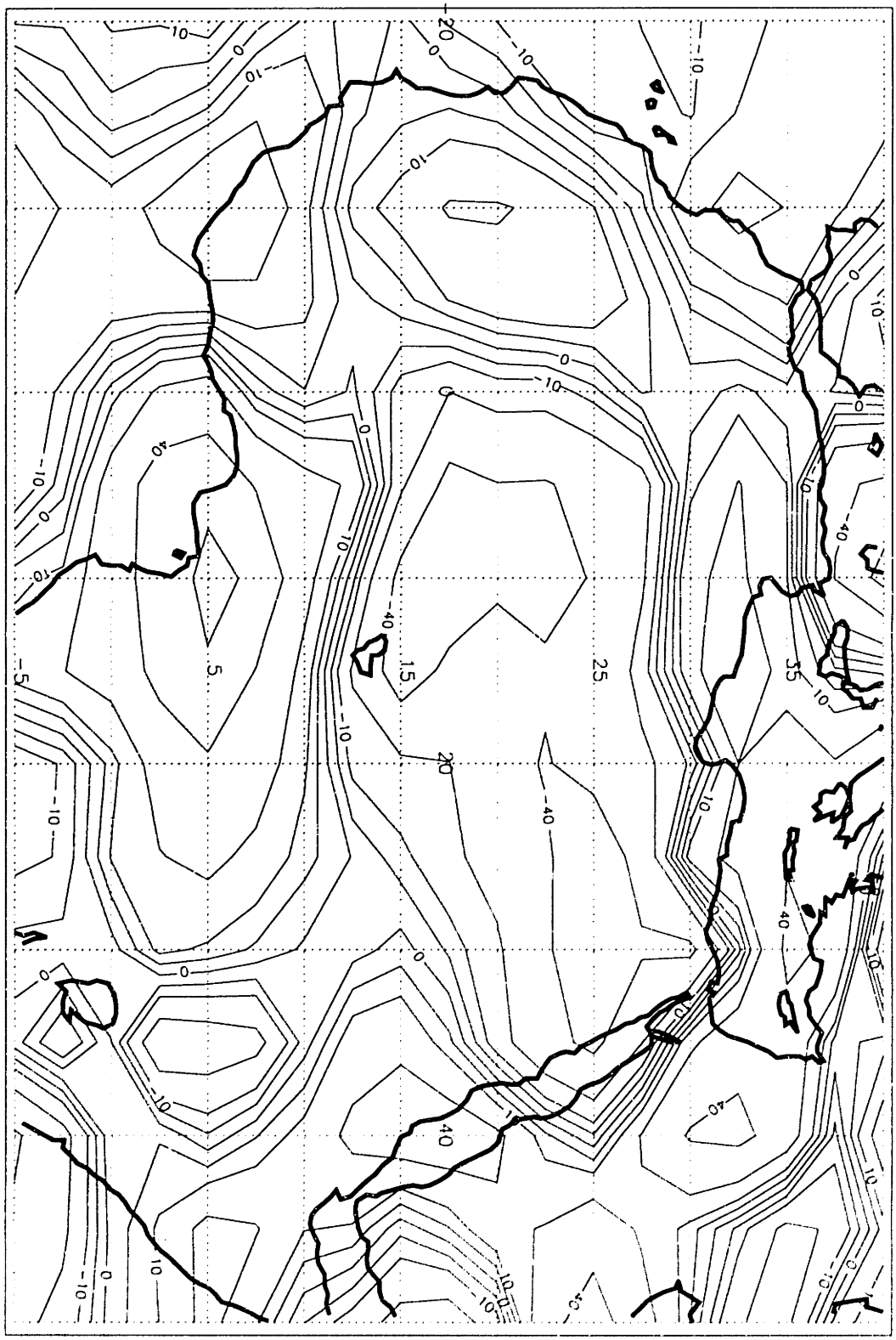

Figure C-24: Third AS Rotated Eigenvector - Based on Rotation of First 80 Vectors

Appendix D

Time Series for Rotated Eigenvector Patterns

Figure	Season	Eigenvector Time Series	Number of Eigenvectors Rotated
D-1	JJ/AS	First	3
D-2	JJ/AS	Second	3
D-3	JJ/AS	Third	3
D-4	JJ/AS	First	5
D-5	JJ/AS	Second	5
D-6	JJ/AS	Third	5
D-7	JJ/AS	First	10
D-8	JJ/AS	Second	10
D-9	JJ/AS	Third	10
D-10	JJ/AS	First	80
D-11	JJ/AS	Second	80
D-12	JJ/AS	Third	80

Table D.1: Catalog of Multiplier Time Series for Rotated Eigenvectors

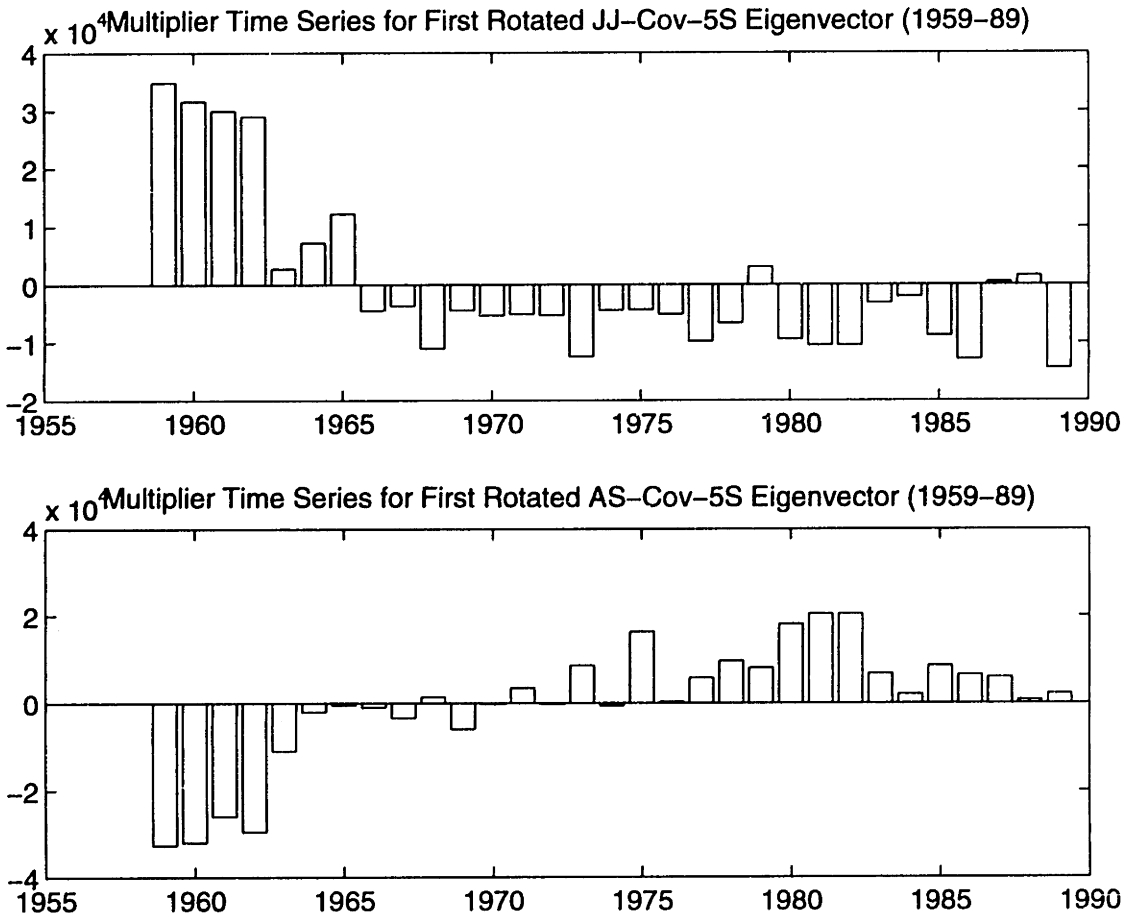

Figure D-1: First Time Series - Based on Rotation of First Three Vectors

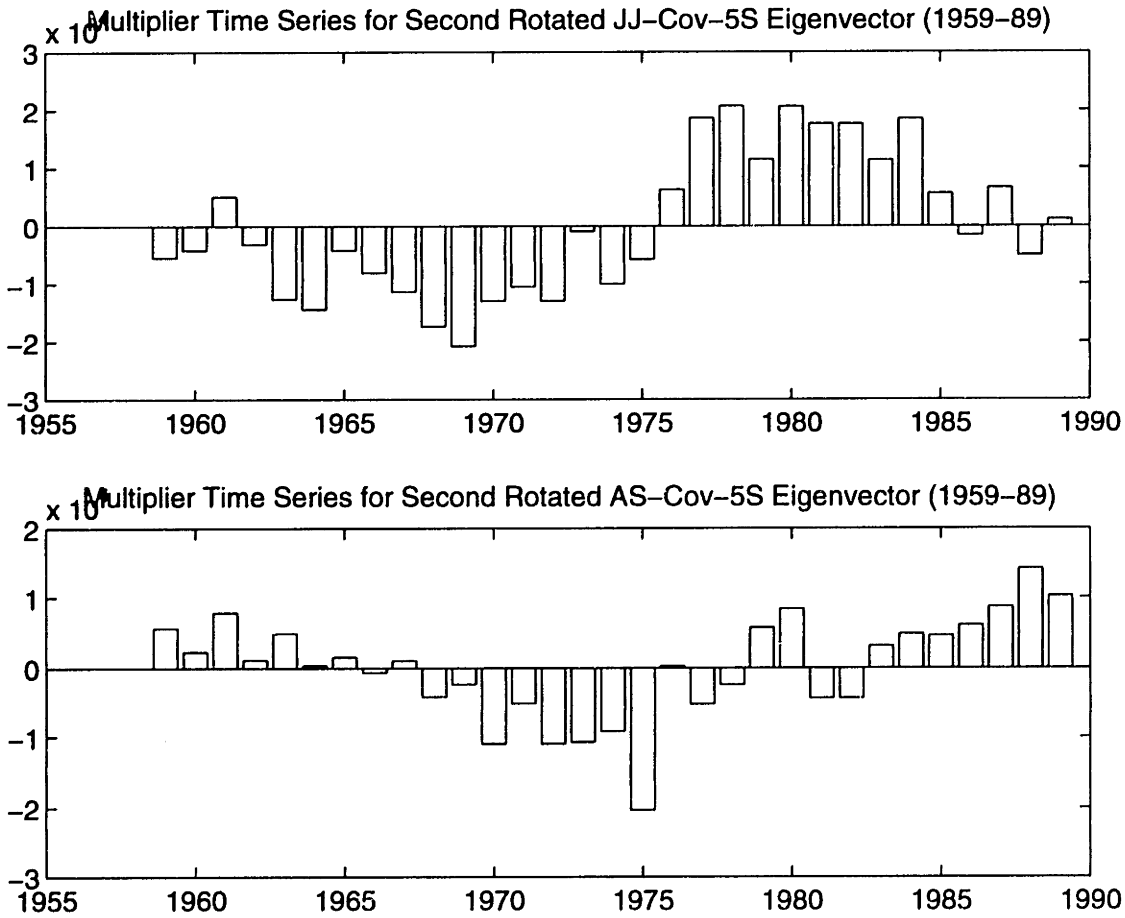

Figure D-2: Second Time Series - Based on Rotation of First Three Vectors

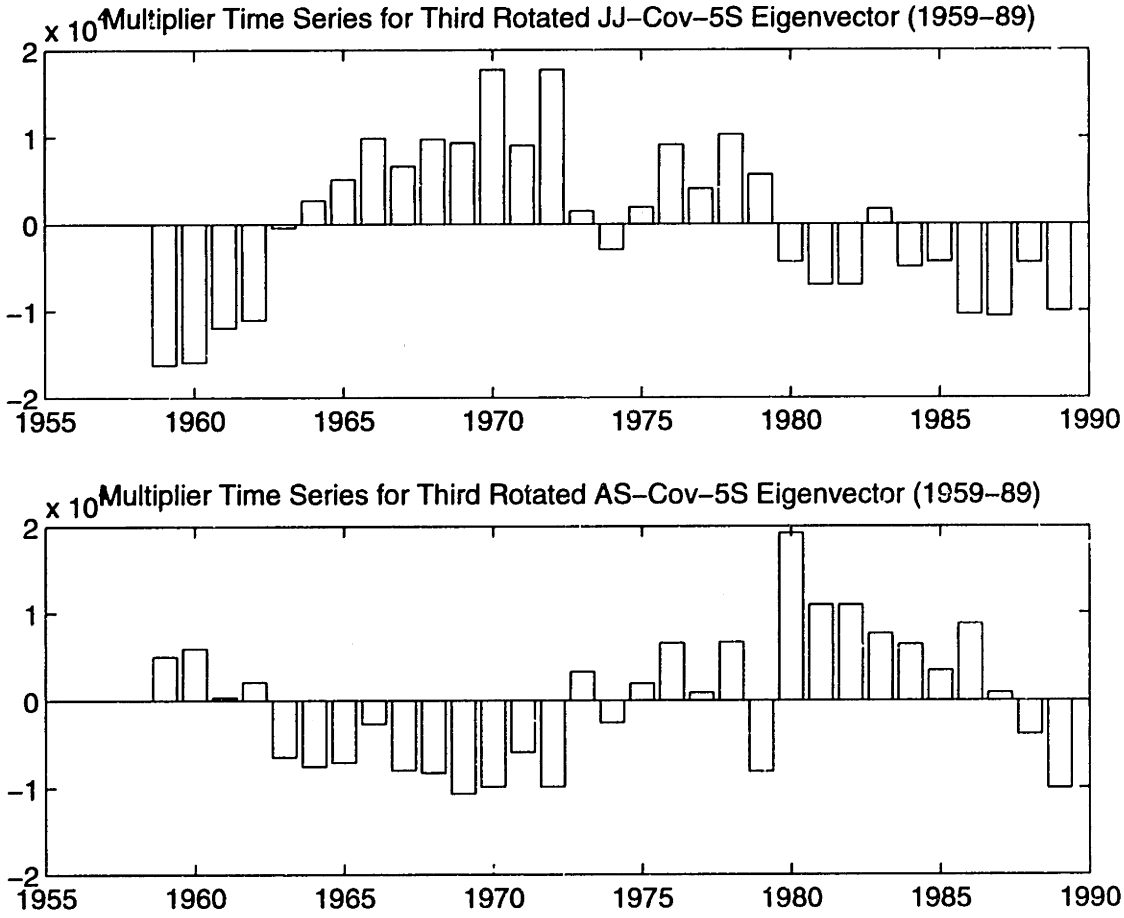

Figure D-3: Third Time Series - Based on Rotation of First Three Vectors

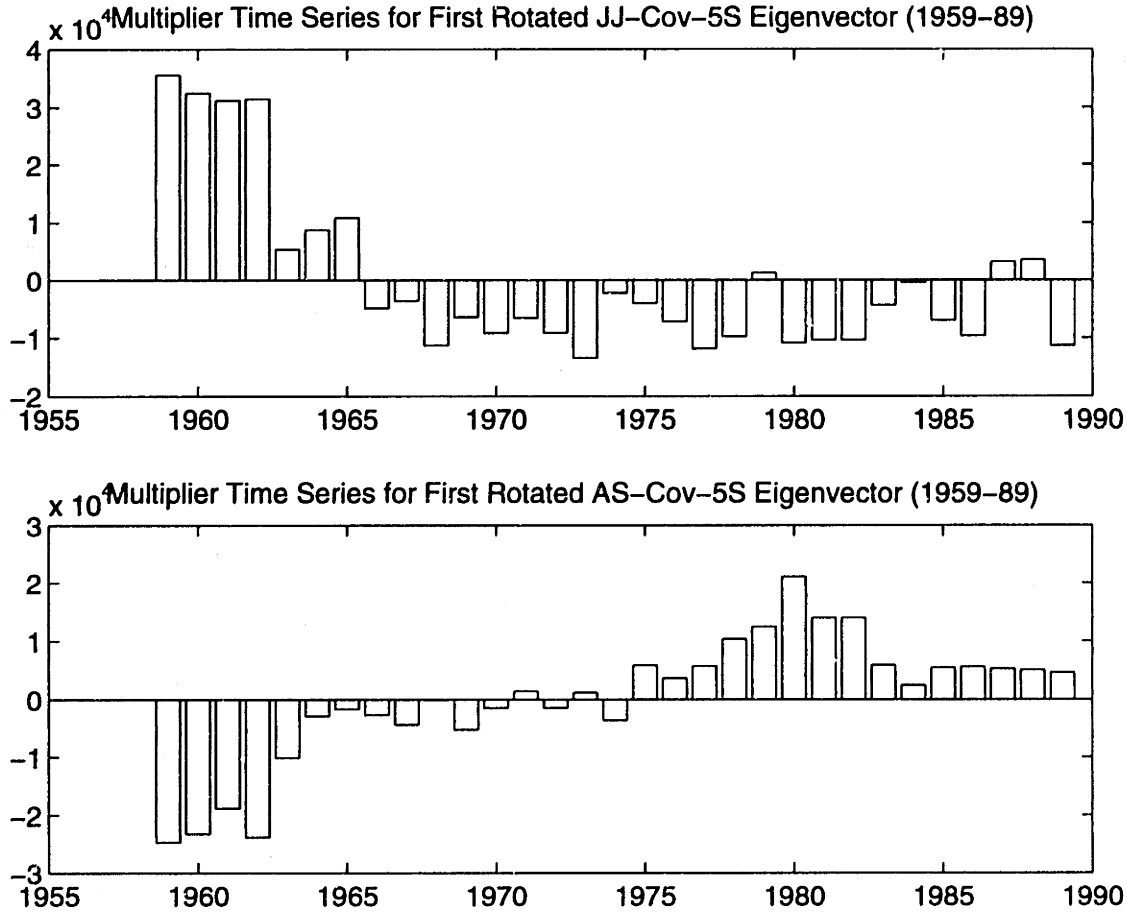

Figure D-4: First Time Series - Based on Rotation of First Five Vectors

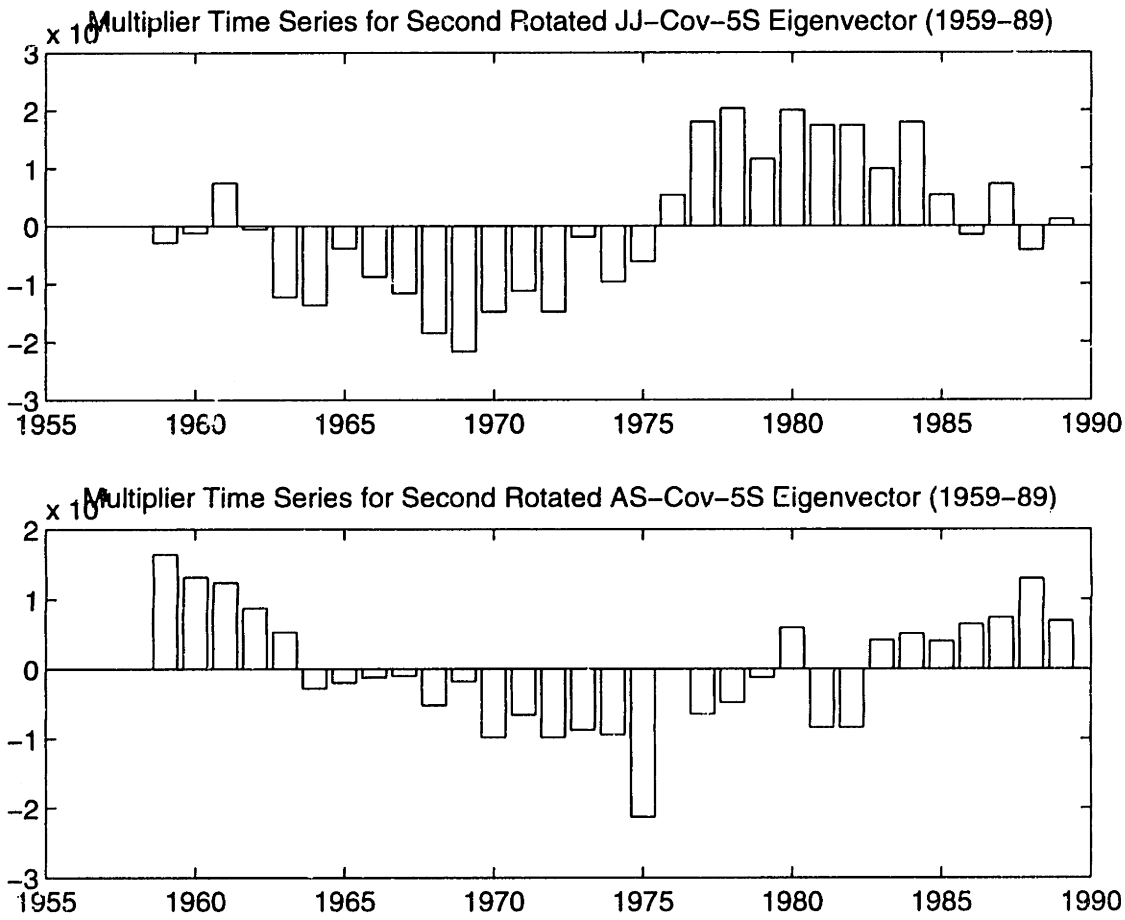

Figure D-5: Second Time Series - Based on Rotation of First Five Vectors

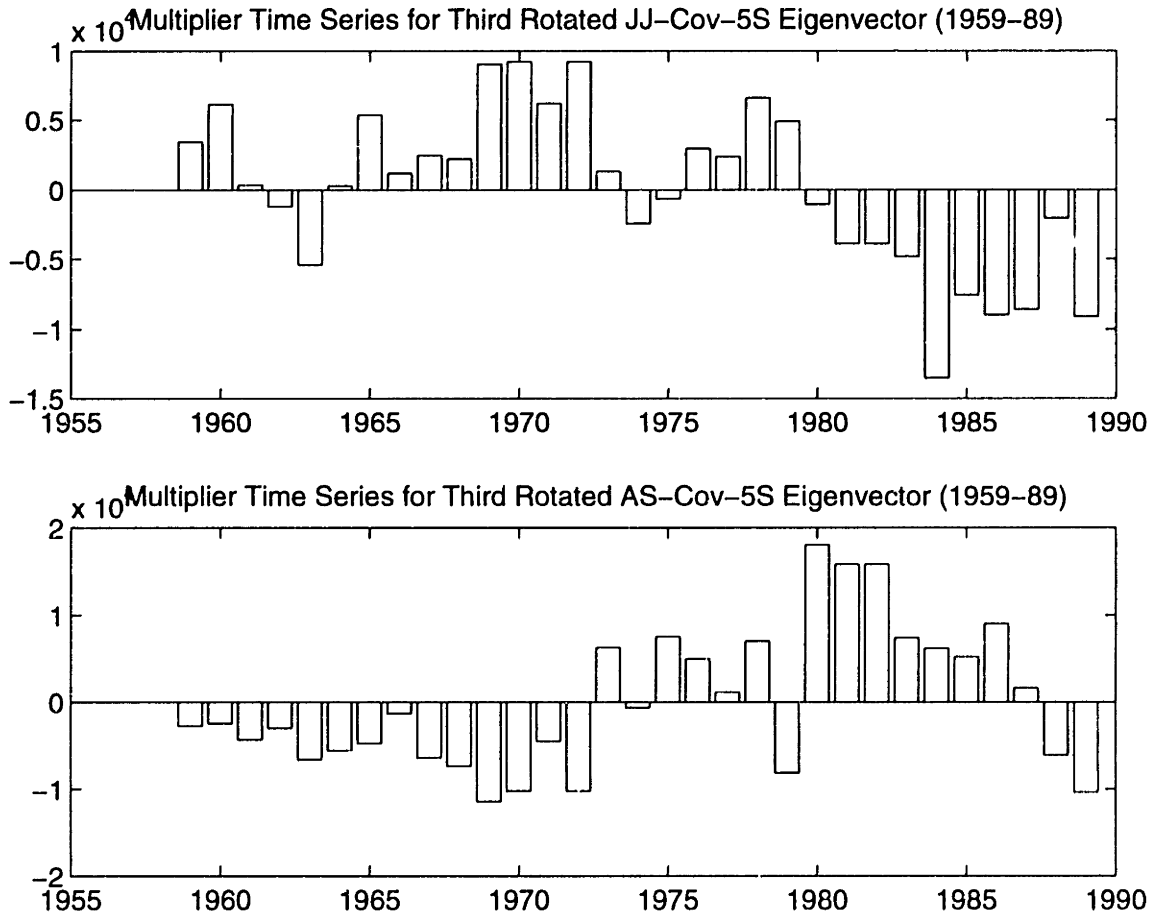

Figure D-6: Third Time Series - Based on Rotation of First Five Vectors

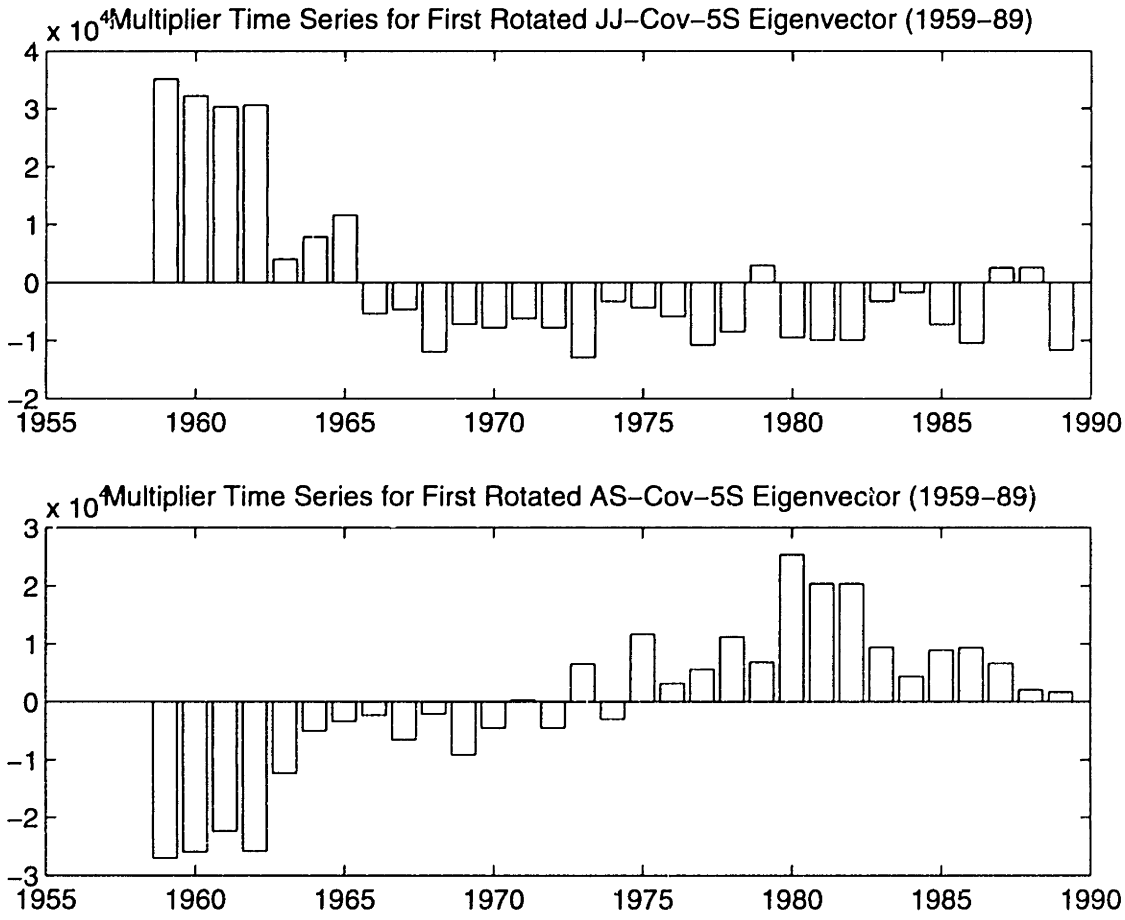

Figure D-7: First Time Series - Based on Rotation of First Ten Vectors

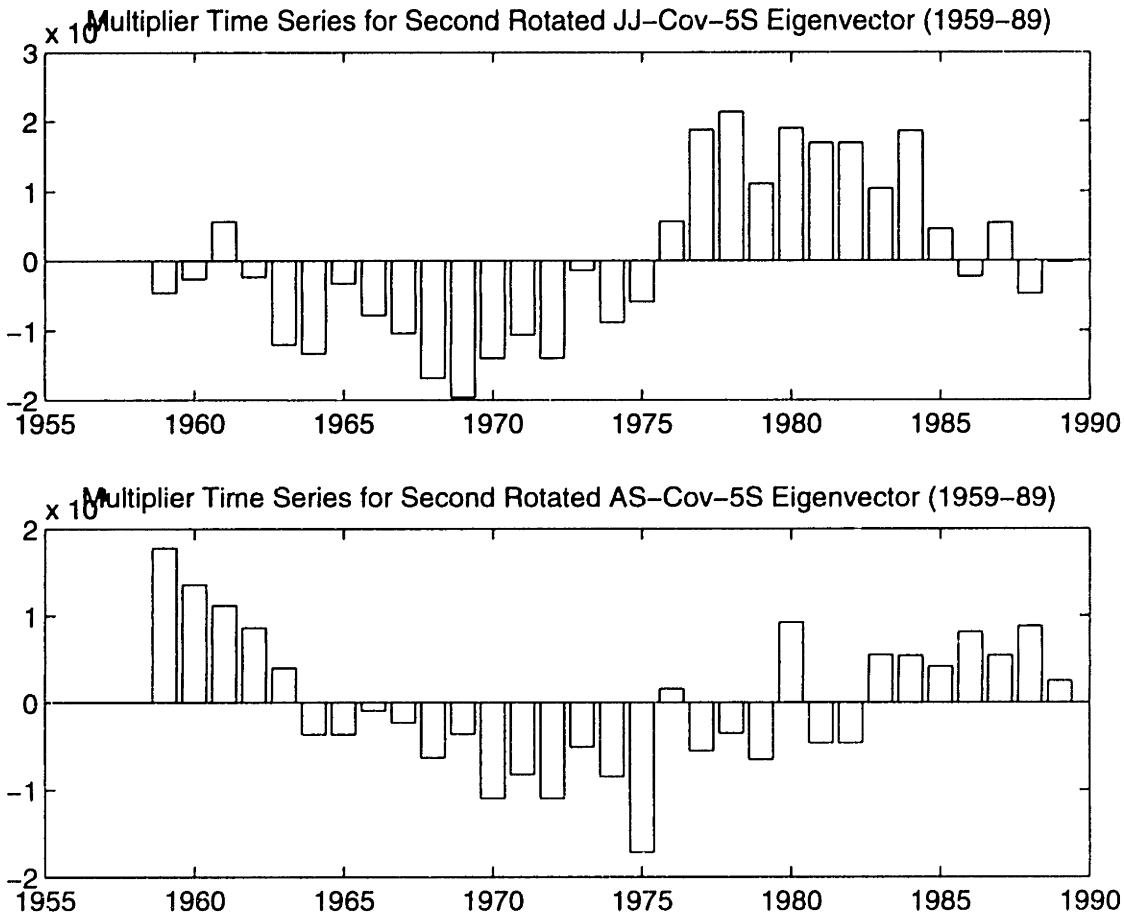

Figure D-8: Second Time Series - Based on Rotation of First Ten Vectors

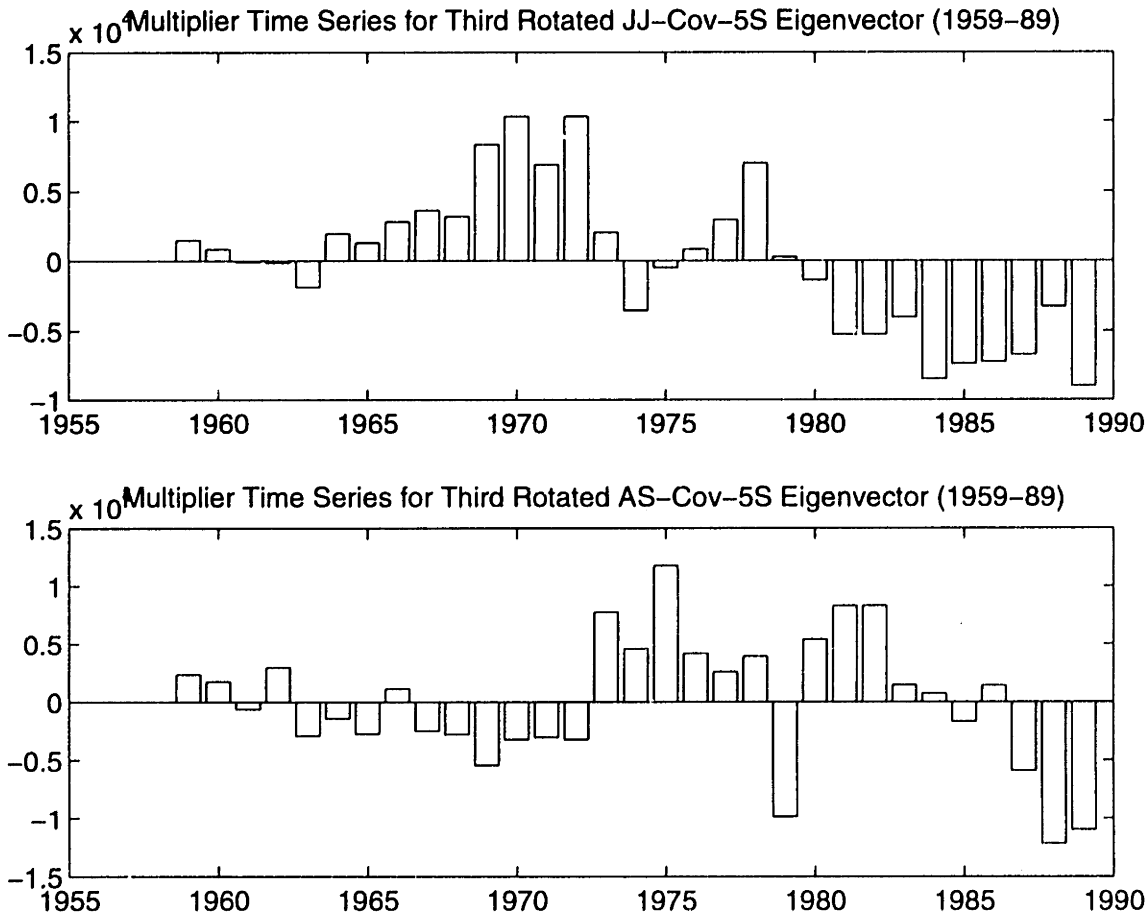

Figure D-9: Third Time Series - Based on Rotation of First Ten Vectors

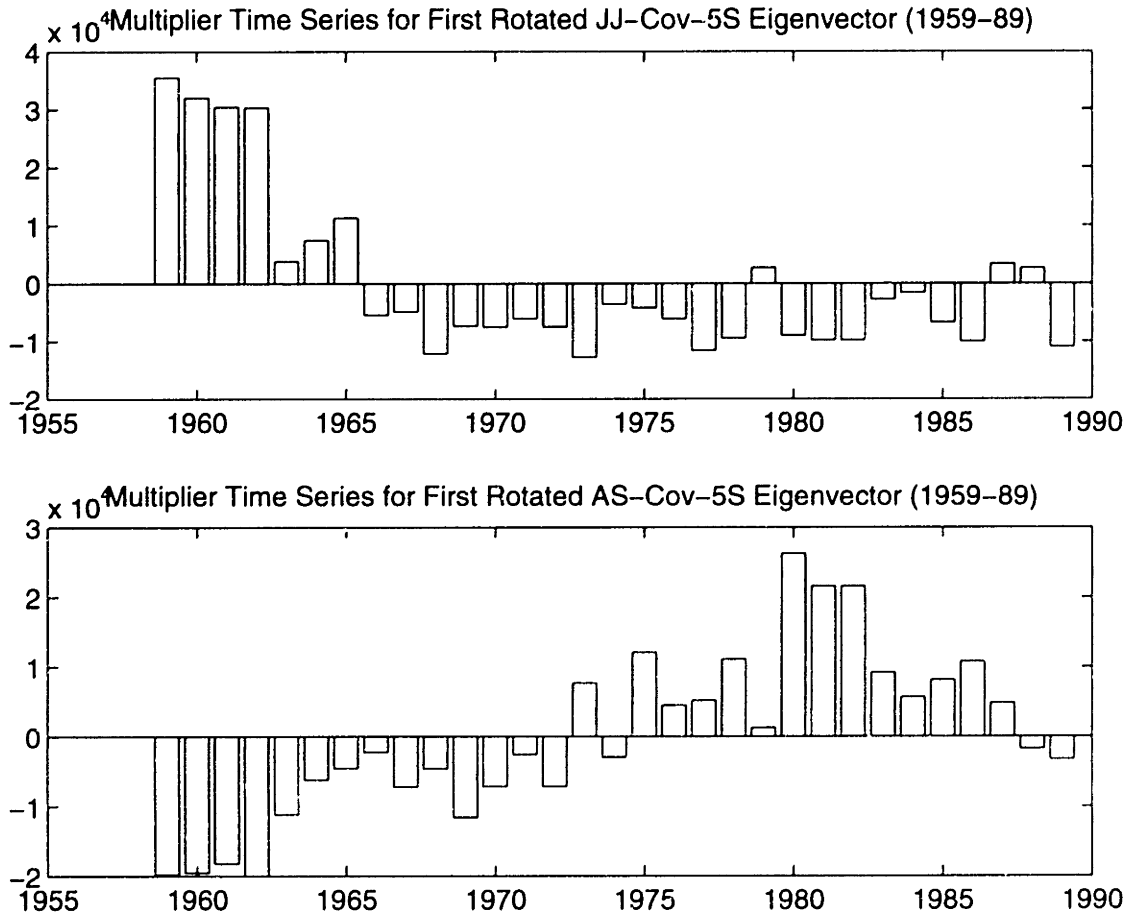

Figure D-10: First Time Series - Based on Rotation of First 80 Vectors

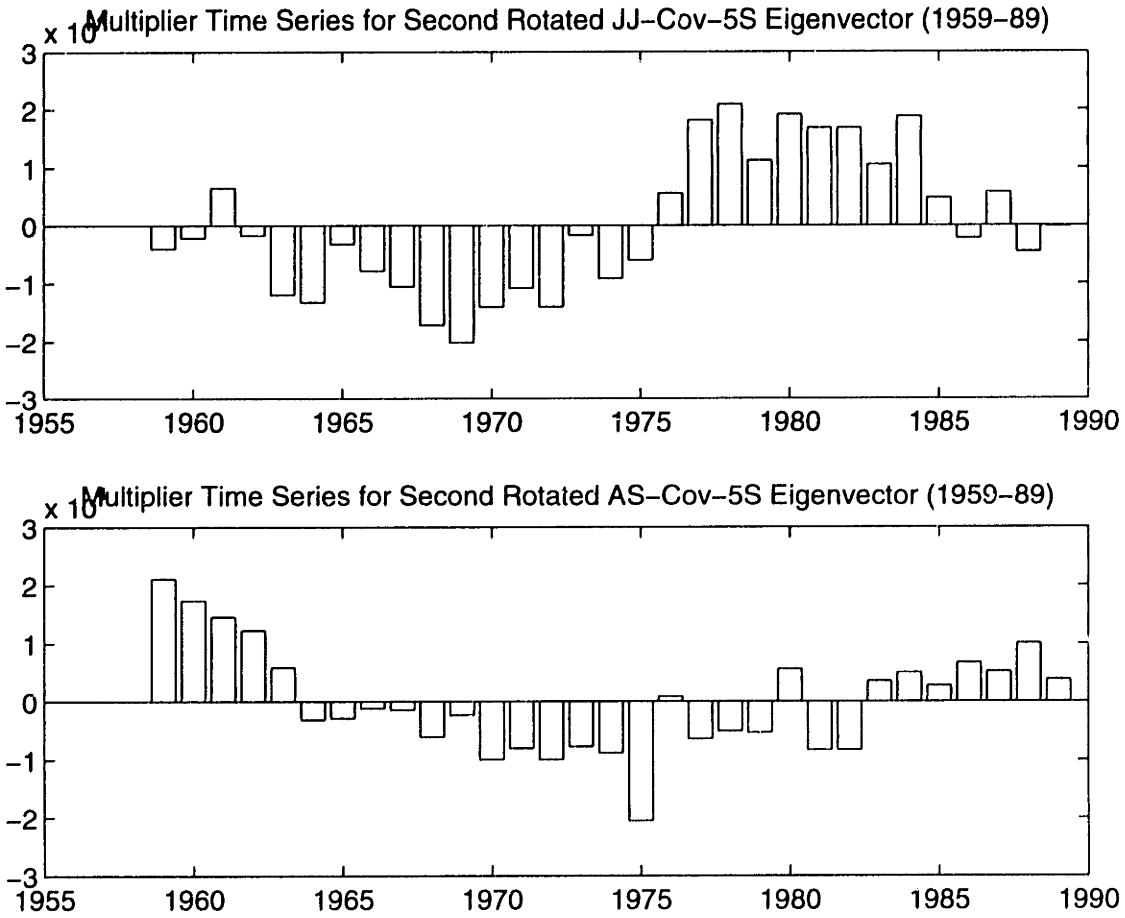

Figure D-11: Second Time Series - Based on Rotation of First 80 Vectors

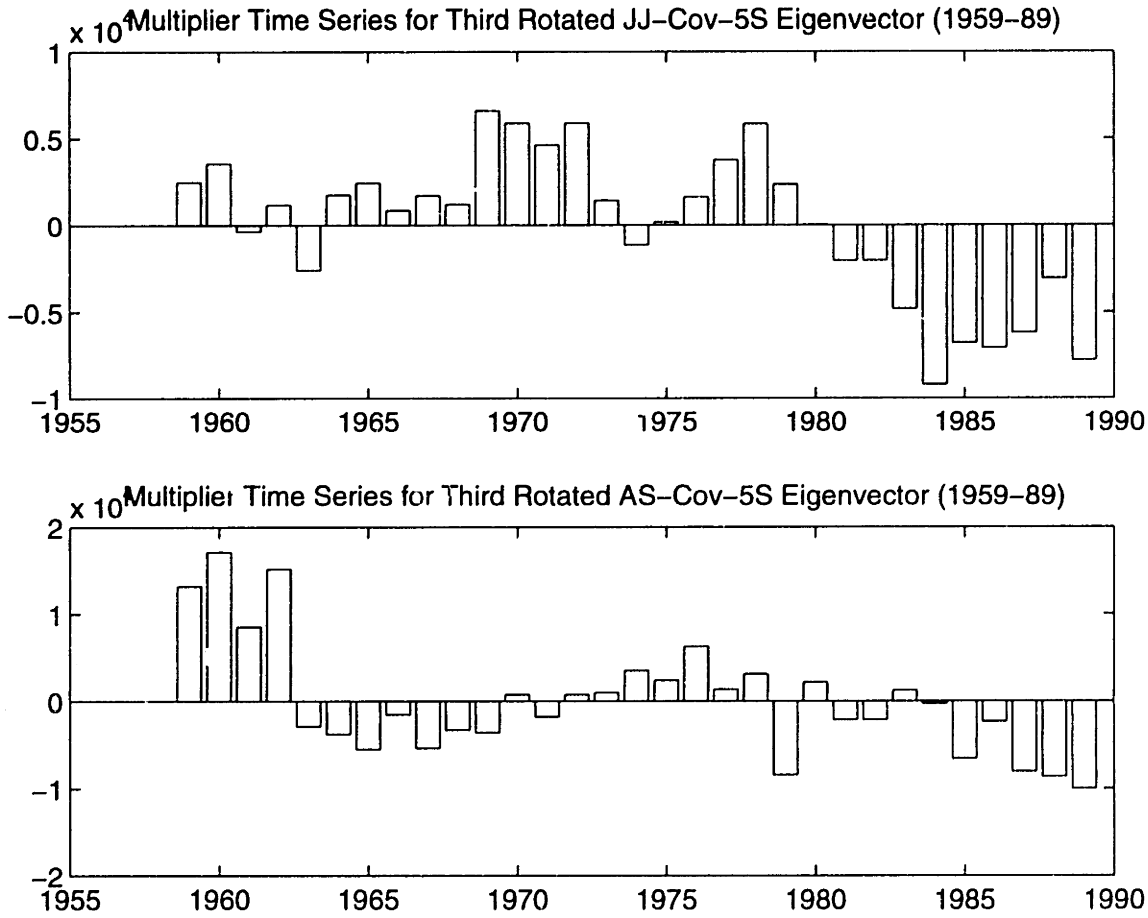

Figure D-12: Third Time Series - Based on Rotation of First 80 Vectors

Bibliography

[1] M. Alestalo. The atmospheric water budget over europe. In R. Ratcliffe A. Street-Perrott, Max Beran, editor, *Variations in the Global Water Budget*, pages 67–79. D. Reidel Publishing Company, Boston, 1983.

[2] A. Baumgartner and E. Reichel. *The World Water Balance, Mean, Annual, Global Continental and Maritime Precipitation, Evaporation, and Runoff.* Elsevier, Amsterdam, 1975.

[3] S. B. Benton, R. T. Blackburn, and V. O. Snead. The role of the atmosphere in the hydrologic cycle. *Transactions, American Geophysical Union*, 31(1):61–73, 1950.

[4] K. Brubaker, D. Entekhabi, and P. Eagleson. Atmospheric water vapor transport and continental hydrology over the Americas. *Journal of Hydrology*, 155:407–428, 1993.

[5] M. I. Budyko. *The Heat Balance of the Earth's Surface.* U. S. Weather Bureau, Washington, D. C., 1956.

[6] D. L. Cadet and N. O. Nnoli. Water vapour transport over Africa and the Atlantic Ocean during summer 1979. *Quarterly Journal of the Royal Meteorological Society*, 113:581–602, 1987.

[7] J. G. Charney. Dynamics of desert and drought in Africa. *Quarterly Journal of the Royal Meteorological Society*, 101:193–202, 1975.

[8] D. Entekhabi. Statistical-dynamical aspects of anomaly patterns of rainfall over the African continent. Master's thesis, Clark University, 1988.

[9] W. P. Elliot and D. J. Gaffen. On the utility of radiosonde humidity archives for climate studies. *Bulletin of the American Meteorological Society*, 72:1507–1520, 1991.

[10] H. Flohn and R. Fantechi. *The Climate of Europe: Past, Present, and Future.* D. Reidel Publishing Company, Boston, 1984.

[11] C. K. Folland, D. E. Parker, M. N. Ward, and A. W. Colman. Sahel rainfall northern hemisphere circulation anomalies and worldwide sea temperature changes. *Long-Range Forecasting and Climate Research*, 7, 1986.

[12] B. Fontaine and S. Janicot. Wind-field coherence and its variations over West Africa. *Journal of Climate*, 5:521–523, 1992.

[13] B. Fontaine, S. Janicot, and V. Moron. Rainfall anomaly patterns and wind field signals over West Africa in August (1958-1989). *Journal of Climate*, 8:1503–1510, 1995.

[14] A. E. Gill and E. M. Rasmussen. The 1982-83 climate anomaly in the equatorial Pacific. *Nature*, 1(17):229–234, 1983.

[15] J. W. Kidson. African rainfall and its relation to upper air circulation. *Quarterly Journal of the Royal Meteorological Society*, 103:441–456, 1977.

[16] P. J. Lamb. Case studies of tropical Atlantic surface circulation patterns during recent sub-Saharan weather anomalies: 1967 and 1968. *Monthly Weather Review*, 106:482–491, 1978.

[17] P. J. Lamb. Large-scale tropical Atlantic surface circulation patterns associated with sub-Saharan weather anomalies. *Tellus*, 299:446–47, 1978.

[18] P. J. Lamb. West African water vapor variations between recent contrasting Sub-saharan rainy seasons. *Tellus*, 35:198–212, 1983.

[19] J. M. Lough. Tropical Atlantic sea-surface temperatures and rainfall variations in Sub-saharan Africa. *Monthly Weather Review*, 114:561–570, 1986.

[20] R. Newell. Preface. In A. Street-Perrott, Max Beran, and R. Ratcliffe, editors, *Variations in the Global Water Budget.* D. Reidel Publishing Company, Boston, 1983.

[21] R. E. Newell and J. W. Kidson. African mean wind changes in Sahelian wet and dry periods. *Journal of Climatology*, 4:1–7, 1984.

[22] S. E. Nicholson. Rainfall and atmospheric circulation patterns during drought periods and wetter years in West Africa. *Monthly Weather Review*, 109:2191–2208, 1981.

[23] S. E. Nicholson. Long-term changes in African rainfall. pages 46–56, 1988.

[24] S. E. Nicholson. African drought: characteristics, causal theories and global teleconnections. *American Geophysical Union, Geophysical Monographs 52*, 7:79–100, 1989.

[25] S. E. Nicholson. An overview of African rainfall fluctuations of the last decade. *Journal of Climate*, 6:1463–1466, 1993.

[26] S. E. Nicholson, J. Kim, and J. Hoopingarner. *Atlas of African Rainfall and its Interannual Variability.* Florida State University, 1988.

[27] S. E. Nicholson and I. M. Palao. A re-evaluation of rainfall variability in the Sahel. part i. characteristics of rainfall fluctuations. *International Journal of Climatology*, 13:371–89, 1993.

[28] A. H. Oort. *Global Atmospheric Circulation Statistics, 1958-73, NOAA Professional Paper 14.* Geophysical Fluid Dynamics Laboratory, New Jersey, 1983.

[29] J. Peixoto and A. H. Oort. *Physics of Climate.* American Institute of Physics, New York, 1992.

[30] J. P. Peixoto, D. A. Salstein, and R. D. Rosen. Intra-annual variation in large-scale moisture fields. *Journal of Geophysical Research*, 86:1255–69, 1981.

[31] J. R. Philip. *Water on the Earth.* Dont know, New York, 1992.

[32] J. M. Prospero and R. T. Nees. Dust concentrations in the atmosphere of the equatorial North Atlantic: possible relationship to the Sahelian drought. *Science*, 196:1196–1198, 1977.

[33] V. B. Rao and V. D. Marques. Water vapor characteristics over northeast Brazil during two contrasting years. *Journal of Climate and Applied Meteorology*, 23:440–444, 1984.

[34] R. Reymont and K. G. Jöreskog. *Applied Factor Analysis in the Natural Sciences.* Cambridge University Press, New York, 1993.

[35] R. D. Rosen and A. S. Omolayo. Exchange of water between land and ocean in the northern hemisphere. *Journal of Geophysical Research*, 86:147–152, 1981.

[36] D. P. Rowell, C. K. Folland, K. Maskell, and N. Ward. Variability of summer rainfall over tropical north Africa (1906-92): Observations and modelling. *Quarterly Journal of the Royal Meteorological Society*, 121:669–704, 1995.

[37] D. P. Rowell and J. R. Milford. On the generation of African squall lines. *Journal of Climate*, 6:1181–1193, 1993.

[38] United Nations Educational Scientific and Cultural Organization (UNESCO). *World Water Balance and Resources of the Earth.* UNESCO, Paris, 1978.

[39] J. Shukla and Y. Xue. The influence of land surface properties on Sahel climate: part i. desertification. *Journal of Climate*, 5:2232–2245, 1993.

[40] C. Stidd. The use of eigenvectors for climate estimates. *Journal of Applied Meteorology*, 6:255–264, 1967.

[41] A. Street-Perrott, M. Beran, and R. Ratcliffe editors. *Variations in the Global Water Budget.* D. Reidel Publishing Company, Boston, 1981.

[42] Y. C. Sud and A. Molod. A gcm simulation study of the influence of Saharan evapotranspiration and surface-albedo anomalies on July circulation and rainfall. *Monthly Weather Review*, 116:2388–2400, 1988.

[43] Y. C. Sud and W. E. Smith. The influence of surface roughness of deserts on the July circulation. *Boundary-Layer Meteorology*, 33:15–49, 1985.

[44] C. C. Wallen. *Climates of Northern and Western Europe.* World Meteorological Society, Geneva, 1970.

[45] E. Yulaeva and J. M. Wallace. The signature of ENSO in global temperature field derived from the microwave sounding unit. *submitted to the Journal of Applied Meteorology*, 1993.